

**Advances in Sensing and Actuation for Turbulent Boundary Layer Control**

by

Bradley Joseph Gibeau

A thesis submitted in partial fulfillment of the requirements for the degree of

Doctor of Philosophy

Department of Mechanical Engineering  
University of Alberta

© Bradley Joseph Gibeau, 2023

# Abstract

The fluid mechanics literature suggests that the ability to manipulate the very-large-scale motions (VLSMs) that exist within turbulent boundary layers (TBLs) would provide influence over the unwanted drag forces, noise, and vibrations associated with these flows. The ability to suppress these negative effects would then allow for greatly improving the function of various engineering systems. Consequently, the work documented within this thesis focuses on developing sensing and actuation capabilities for the targeted control of VLSMs in physical systems.

Wall-mounted pressure sensors are the most practical sensor type for real-world flow control applications. However, it is not known whether such sensors can be used for the targeted control of VLSMs because the relationship between wall pressure and the VLSMs has not been identified. To remedy this, a pressure measurement system capable of capturing wall-pressure fluctuations in a noisy wind tunnel environment is developed. Simultaneous measurements of wall pressure and velocity are then used to identify the relationship between wall pressure and the VLSMs for the first time. It is found that the wall-normal velocity component of the VLSMs is responsible for producing wall-pressure fluctuations at low frequencies via suction and splatting at the wall. This result suggests that it is possible to use the low-frequency wall-pressure signal to identify VLSMs in real time for the purpose of targeted control.

Targeted actuation of the VLSMs has been explored in previous work using jets, spanwise surface motion, and (numerical) body forces. In contrast, the present work considers actuation using active surface deformations applied locally in the wall-normal direction. An “active surface” is developed to produce simple surface deformations over a range of actuation frequencies and amplitudes. An initial evaluation of the device is then conducted using a laminar boundary layer (LBL) to form a baseline understanding of the actuation strategy in a steady flow. This initial evaluation reveals that the active surface is capable of producing both high- and low-speed streamwise velocity fluctuations

with similar magnitudes. Actuation at low frequencies is found to be the most promising for flow control because the resulting motions are stronger, more stable, and concentrated along the centreline of the actuator. Moreover, a linear modelling technique is found to adequately describe the input-output dynamics of the actuated flow, thus suggesting that the actuation strategy is amenable to the powerful tools of modern control theory.

The active surface is then deployed beneath a TBL where it is used to actuate at the frequencies associated with the VLSMs. The device is found to be capable of producing high- and low-speed motions that are similar to synthetic VLSMs when considering their dimensions and ability to modulate the surrounding turbulence. Additionally, these motions act as a local actuation because their strength decays rapidly with streamwise distance. These characteristics indicate that the active surface may be well-suited for targeted control of the VLSMs using a feed-forward strategy. Alternatively, the turbulence-modulating properties of the actuated motions may also be appropriate for a control strategy. Most notably, the present results indicate that the high-speed motions produced by downward deformations of the active surface act to reduce turbulence production within the logarithmic layer of the TBL.

Finally, the motions produced by the active surface in the LBL and TBL are compared at low actuation frequencies. Both sets of actuated motions appear similar in form but with a few distinct differences. First, the motions produced in the TBL advect more quickly as a percentage of the freestream velocity than those produced in the LBL. Second, the motions produced in the TBL are weaker as a percentage of the freestream velocity when compared to those produced in the LBL. These differences lead to an attempt to scale the results to obtain a collapse of the data. The resulting normalizations suggest that the shape factor of the boundary layer plays a role in determining the advection velocity of the motions produced by the active surface. Similarly, the shape factor and Reynolds number may be part of what determines the strength of the actuated motions.

# Preface

The majority of the results documented in Chapters 4 and 5 of this thesis have been published in the *Journal of Fluid Mechanics* as:

**Gibeau, B.** and Ghaemi, S. (2021) Low- and mid-frequency wall-pressure sources in a turbulent boundary layer. *J. Fluid Mech.* 918, A18. doi: 10.1017/jfm.2021.339.

The Cambridge University Press is the copyright holder; the work is reproduced here with permission from the publisher.

The majority of the results documented in Chapters 6 and 7 of this thesis have been published in *Physical Review Fluids* as:

**Gibeau, B.** and Ghaemi, S. (2022) Laminar boundary layer forcing with active surface deformations. *Phys. Rev. Fluids* 7, 114101. doi: 10.1103/PhysRevFluids.7.114101.

The American Physical Society is the copyright holder; the work is reproduced here with permission from the publisher.

Reproduction of the above publications was carried out while adhering to the formatting of the present thesis. For example, the literature reviews contained within the introductions of the above publications have been moved to the appropriate chapter within this thesis.

The majority of the results documented in Chapter 8 are currently under peer review for publication as a journal article.

I was responsible for all work contained within this thesis. This includes the literature review, problem/question formulation, engineering design, experimental design, data collection, data analysis, and writing. My co-author for the above publications, Professor Sina Ghaemi, provided guidance as my doctoral supervisor.

# Acknowledgements

I would first like to express sincere gratitude to my doctoral supervisor, Professor Sina Ghaemi. The quality of your guidance has never wavered over the many years that we have been working together. I truly could not have imagined a better match for a supervisor.

Second, I would like to thank the committee members for my candidacy and final examinations: Professors David Nobes, Jaime Wong, Morris Flynn, Bharathram Ganapathisubramani, and Arman Hemmati. I know your time is valuable and I appreciate your evaluation of my work.

Third, I would like to acknowledge the support of the machine and electronics shops of the Mechanical Engineering Department. Dan Mooney, Andrew Campbell, and Rick Conrad have been particularly helpful over the years.

Fourth, to my friends, family, and better half: thank you for supporting me, distracting me, and humbling me. Taryn Hawkey, thank you for helping me celebrate my wins and brush off my losses. Tyler Friesen and David Gordon, I would have never made it this far without the foundations you helped me build.

And finally, I will forever be grateful to the Natural Sciences and Engineering Research Council of Canada for the Alexander Graham Bell Canada Graduate Scholarship and all other scholarships that followed as a result of that one big win. This financial support meant I did not have to worry.

# Contents

<b>Abstract</b>	<b>ii</b>
<b>Preface</b>	<b>iv</b>
<b>Acknowledgements</b>	<b>v</b>
<b>Contents</b>	<b>vi</b>
<b>List of Tables</b>	<b>x</b>
<b>List of Figures</b>	<b>xi</b>
<b>List of Symbols</b>	<b>xiv</b>
<b>List of Abbreviations</b>	<b>xviii</b>
<b>I Background</b>	<b>1</b>
<b>1 Introduction</b>	<b>2</b>
1.1 Motivation and Challenges . . . . .	2
1.2 Approach and Objectives . . . . .	5
1.3 Thesis Overview . . . . .	8
<b>2 Boundary Layers</b>	<b>10</b>
2.1 Definitions . . . . .	10
2.2 Equations of Motion . . . . .	13
2.3 Turbulent Boundary Layers . . . . .	15
2.3.1 Coherent Motions . . . . .	15
2.3.2 Velocity Statistics . . . . .	21
2.3.3 Wall-Pressure Fluctuations . . . . .	23
2.4 Control . . . . .	29
2.4.1 Moving-Surface Actuators . . . . .	29
2.4.2 Targeting Very-Large-Scale Motions . . . . .	34

<b>3</b>	<b>Experimental Methods</b>	<b>36</b>
3.1	Wind Tunnel Facility . . . . .	36
3.1.1	Specifications . . . . .	36
3.1.2	Generating a Turbulent Boundary Layer . . . . .	36
3.1.3	Generating a Laminar Boundary Layer . . . . .	38
3.2	Particle Image Velocimetry . . . . .	39
3.2.1	Working Principle . . . . .	39
3.2.2	Measurements in a Plane . . . . .	40
3.2.3	Equipment and Software . . . . .	42
3.3	Real-Time System . . . . .	43
3.3.1	Simulink Real-Time and Target Machine . . . . .	43
3.3.2	Data Synchronization . . . . .	44
<b>II</b>	<b>Sensing</b>	<b>45</b>
<b>4</b>	<b>Development of the Pressure Measurement System</b>	<b>46</b>
4.1	Measurement Requirements . . . . .	46
4.2	Sensor Selection . . . . .	46
4.3	Avoiding Spatial Filtering . . . . .	47
4.4	Correction of Helmholtz Resonance . . . . .	48
4.5	Background Noise Removal . . . . .	53
<b>5</b>	<b>Low-Frequency Wall-Pressure Sources in a Turbulent Boundary Layer</b>	<b>57</b>
5.1	Experimental Setup . . . . .	58
5.1.1	Turbulent Boundary Layer Configuration . . . . .	58
5.1.2	Wall-Pressure Measurements . . . . .	58
5.1.3	Particle Image Velocimetry . . . . .	58
5.2	Previously-Established Statistics . . . . .	61
5.2.1	Single-Point Wall-Pressure and Velocity Statistics . . . . .	61
5.2.2	Space-Time Pressure-Velocity Correlations . . . . .	65
5.3	Frequency-Dependent Pressure-Velocity Coupling . . . . .	69
5.3.1	Coherence Between Wall Pressure and Velocity . . . . .	71
5.3.2	Very-Large-Scale Coupling . . . . .	75
5.3.3	Large-Scale Coupling . . . . .	81
5.4	Further Discussion . . . . .	89
5.4.1	Decomposition of the Pressure-Velocity Correlations . . . . .	89
5.4.2	Very-Large-Scale Motions and Wall Pressure . . . . .	89
5.4.3	Hairpin Packets and Wall Pressure . . . . .	90
5.4.4	Conceptual Model of the Low- and Mid-Frequency Wall-Pressure Sources . . . . .	91
5.5	Summary . . . . .	91

<b>III</b>	<b>Actuation</b>	<b>95</b>
<b>6</b>	<b>Development of the Active Surface</b>	<b>96</b>
6.1	Actuation Requirements . . . . .	96
6.2	Actuator Selection . . . . .	96
6.3	Active Surface Assembly . . . . .	97
6.4	Shape of the Surface Deformations . . . . .	99
6.5	Tuning and Performance . . . . .	99
<b>7</b>	<b>Laminar Boundary Layer Forcing with Active Surface Deformations</b>	<b>103</b>
7.1	Experimental Setup . . . . .	103
7.1.1	Laminar Boundary Layer Configuration . . . . .	103
7.1.2	Particle Image Velocimetry . . . . .	104
7.1.3	Base Flow . . . . .	105
7.1.4	Actuation Cases . . . . .	108
7.1.5	Phase Averaging . . . . .	109
7.2	Motions Produced by Periodic Forcing . . . . .	110
7.2.1	Spatial Structure . . . . .	110
7.2.2	Strength and Stability . . . . .	116
7.3	Data-Driven Modelling of the Actuated Flow . . . . .	124
7.3.1	Modelling with Nonparametric Linear Transfer Functions . . . . .	124
7.3.2	Model Evaluation . . . . .	129
7.4	Further Discussion . . . . .	133
7.4.1	Comparison with Past Results . . . . .	133
7.4.2	Linearity of the Actuated Flow . . . . .	134
7.5	Summary . . . . .	134
<b>8</b>	<b>Turbulent Boundary Layer Forcing with Active Surface Deformations</b>	<b>136</b>
8.1	Experimental Setup . . . . .	136
8.1.1	Turbulent Boundary Layer Configuration . . . . .	136
8.1.2	Wall-Pressure Measurements . . . . .	137
8.1.3	Particle Image Velocimetry . . . . .	137
8.1.4	Base Flow . . . . .	138
8.1.5	Actuation Cases . . . . .	140
8.1.6	Phase Averaging and Triple Decomposition . . . . .	141
8.2	Periodic Motions Produced by Actuation . . . . .	143
8.2.1	Phase Averages . . . . .	143
8.2.2	Structure and Strength . . . . .	146
8.2.3	Visualization of the Induced Motions . . . . .	151
8.3	Manipulation of Turbulence . . . . .	153

8.3.1	Mean Velocity and Reynolds Stresses . . . . .	154
8.3.2	Phase-Averaged Reynolds Stresses . . . . .	154
8.3.3	Feed-Forward of the Wall-Pressure Signal . . . . .	159
8.4	Further Discussion . . . . .	165
8.4.1	Potential for Flow Control . . . . .	165
8.4.2	Scaling Between Different Boundary Layers . . . . .	167
8.5	Summary . . . . .	169
<b>IV</b>	<b>Closing</b>	<b>171</b>
<b>9</b>	<b>Conclusions</b>	<b>172</b>
9.1	Sensing with Wall Pressure . . . . .	172
9.2	Actuation with Active Surface Deformations . . . . .	173
9.3	Recommendations for Future Work . . . . .	175
	<b>Bibliography</b>	<b>177</b>
	<b>Appendices</b>	<b>187</b>
A	Uncertainty Analysis . . . . .	187
B	MATLAB Code . . . . .	194

# List of Tables

5.1	Turbulent boundary layer parameters . . . . .	59
5.2	Frequency ranges associated with the quartiles of the LSP band . . . . .	84
7.1	Laminar boundary layer parameters . . . . .	107
8.1	Turbulent boundary layer parameters . . . . .	139
A.1	Estimated bias uncertainties and random errors for all PIV measurements . . . . .	190
A.2	Estimated uncertainties, velocity statistics of Chapter 5 . . . . .	191
A.3	Estimated uncertainties, pressure-velocity correlations of Chapter 5 . . . . .	192
A.4	Estimated uncertainties, base velocity statistics of Chapter 8 . . . . .	193
A.5	Estimated uncertainties, actuated velocity statistics of Chapter 8 . . . . .	193
A.6	Estimated uncertainties, feed-forward Reynolds stresses of Chapter 8 . . . . .	193
A.7	Estimated uncertainties, phase-averaged Reynolds stresses of Chapter 8 . . . . .	193

# List of Figures

1.1	Visualization of a turbulent boundary layer . . . . .	2
2.1	The Blasius boundary layer solution . . . . .	16
2.2	Schematic of a hairpin vortex . . . . .	17
2.3	Instantaneous visualization of the near-wall streaks . . . . .	18
2.4	Instantaneous visualization of a large-scale motion . . . . .	20
2.5	Instantaneous visualization of a very-large-scale motion . . . . .	20
2.6	Mean velocity profiles of turbulent boundary layers . . . . .	22
2.7	Reynolds stresses from a direct numerical simulation . . . . .	23
2.8	Streamwise Reynolds stress across a range of Reynolds numbers . . . . .	24
2.9	Wall-pressure spectrum beneath a turbulent boundary layer . . . . .	26
2.10	Probability density of wall pressure beneath a turbulent boundary layer . . . . .	28
2.11	Correlations between wall pressure and velocity in a turbulent boundary layer . . . . .	29
2.12	Streamwise traveling wave of spanwise surface motion . . . . .	32
2.13	Wall-normal surface deformations resulting from reactive control . . . . .	34
3.1	Photograph of the wind tunnel test section at the University of Alberta . . . . .	37
3.2	Annotated photograph of the boundary layer tripping device . . . . .	38
3.3	Photograph of the plate used to generate the laminar boundary layer . . . . .	39
3.4	Schematic representation of the planar PIV process . . . . .	41
3.5	Sample correlation of interrogation windows . . . . .	42
3.6	Block diagram of the PIV and real-time systems . . . . .	43
3.7	Annotated time series of PIV trigger signals . . . . .	44
4.1	Schematic of the thread-on pinhole attachment . . . . .	48
4.2	Photographs of the thread-on pinhole attachment . . . . .	49
4.3	Photographs of the quasi-anechoic chamber . . . . .	51
4.4	Measured frequency response of the pinhole resonator . . . . .	52
4.5	Sample signal showing Helmholtz resonance correction . . . . .	53
4.6	Annotated photograph of the freestream microphone support . . . . .	54
4.7	Power spectra of wall pressure with and without background noise . . . . .	56
5.1	Experimental schematic for the investigation of wall pressure . . . . .	60

5.2	Velocity statistics at the pressure measurement location . . . . .	62
5.3	Power spectra of the streamwise velocity fluctuations . . . . .	63
5.4	Power spectrum of the wall-pressure fluctuations . . . . .	64
5.5	Probability density of the wall-pressure fluctuations . . . . .	65
5.6	Space-time pressure-velocity correlations . . . . .	67
5.7	Vector fields of the space-time pressure-velocity correlations . . . . .	70
5.8	Coherence between the wall-pressure and velocity fluctuations . . . . .	72
5.9	Phase between the wall-pressure and velocity fluctuations . . . . .	75
5.10	The filters used to isolate the VLSP and LSP fluctuations . . . . .	76
5.11	Probability density of the filtered wall-pressure fluctuations . . . . .	77
5.12	Filtered space-time pressure-velocity correlations (VLSP) . . . . .	78
5.13	Vector fields of the filtered space-time pressure-velocity correlations (VLSP) . . . . .	80
5.14	Filtered space-time pressure-velocity correlations (LSP) . . . . .	82
5.15	The filters used to isolate quartiles of the LSP band . . . . .	85
5.16	Filtered space-time pressure-velocity correlations (LSP quartiles) . . . . .	86
5.17	Vector fields of the filtered space-time pressure-velocity correlations (LSP) . . . . .	88
5.18	Conceptual model of the low- and mid-frequency wall-pressure sources . . . . .	92
6.1	Cross-sectional schematics of the active surface assembly and deformation . . . . .	98
6.2	Photographs of the active surface assembly . . . . .	100
6.3	Measured profiles showing the geometry of the active surface deformation . . . . .	101
6.4	Sample time series of the active surface tracking a random input signal . . . . .	102
7.1	Schematic of the laminar boundary layer forcing experiment . . . . .	104
7.2	Mean boundary layer profiles for the base flow . . . . .	106
7.3	Mean streamwise velocity during static deformation . . . . .	108
7.4	Phase averages of the active surface displacement . . . . .	110
7.5	Phase averages of the fluctuating streamwise velocity in the $x$ - $y$ plane . . . . .	112
7.6	Streamwise wavelengths and advection velocities of the modes produced by actuation	114
7.7	Phase averages of the fluctuating streamwise velocity in the $x$ - $z$ plane . . . . .	115
7.8	Combined phase-averaged visualizations of the motions formed by the active surface	117
7.9	Instantaneous visualizations of streamwise velocity fluctuation in the $x$ - $y$ plane . . .	119
7.10	Strength of the streamwise velocity fluctuations produced by actuation . . . . .	120
7.11	Estimated relative locations of the Stokes and critical layers . . . . .	123
7.12	Power spectral density of the system identification input . . . . .	127
7.13	Characteristics of the POD-reconstructed velocity fluctuations . . . . .	128
7.14	Samples of the identified transfer functions and impulse responses . . . . .	130
7.15	Correlation coefficients between the measured and estimated velocity fluctuations . .	131
7.16	Sample spectra and time series of the estimated and measured velocity fluctuations .	132
8.1	Schematic of the turbulent boundary layer forcing experiment . . . . .	137

8.2	Velocity statistics of the base flow . . . . .	140
8.3	Pre-multiplied spectra of streamwise velocity for the base flow . . . . .	141
8.4	Phase averages of the active surface displacement . . . . .	142
8.5	Phase averages of the fluctuating streamwise velocity in the $\phi$ - $y$ plane . . . . .	144
8.6	Phase averages of the fluctuating streamwise velocity in the $\phi$ - $z$ plane . . . . .	146
8.7	Advection velocities of the motions produced by actuation . . . . .	148
8.8	Streamwise wavelengths of the motions produced by actuation . . . . .	149
8.9	Strength of the motions produced by actuation . . . . .	150
8.10	Model of the streamwise velocity fluctuations produced by actuation in the $x$ - $y$ plane	152
8.11	Model of the streamwise velocity fluctuations produced by actuation in the $x$ - $z$ plane	153
8.12	Mean velocity and Reynolds stresses of the actuated flow . . . . .	155
8.13	Modulation of the streamwise Reynolds stress in the $\phi$ - $y$ plane . . . . .	157
8.14	Modulation of the wall-normal Reynolds stress in the $\phi$ - $y$ plane . . . . .	158
8.15	Modulation of the Reynolds shear stress in the $\phi$ - $y$ plane . . . . .	160
8.16	PSD of wall pressure compared to that from real-time background noise removal . .	162
8.17	Real-time filter used to isolate low-frequency wall pressure . . . . .	164
8.18	Sample tracking of the feed-forward signal . . . . .	165
8.19	Reynolds stresses with and without feed-forward actuation applied . . . . .	166

# List of Symbols

$\langle \cdot \rangle$	Ensemble average of a quantity
$\langle \cdot \rangle_{\text{VLS}}$	Ensemble average of a quantity filtered to isolate the very-large scales
$\langle \cdot \rangle_{\phi}$	Phase average of a quantity
$\Delta \langle \cdot \rangle_{\phi}$	Difference between a phase-averaged and ensemble-averaged quantity
$\mathcal{F}\{\cdot\}$	Fourier transform of a quantity
$\tilde{\cdot}$	Fourier transform of a quantity, short hand
$\mathcal{H}\{\cdot\}$	Hilbert transform of a quantity
$\hat{\cdot}$	Estimation of a quantity
$A$	Actuation amplitude
$A_p$	Cross-sectional area of the microphone pinhole
$b$	Exponential constant
$c$	Filter coefficient
$\mathbf{c}$	Vector of filter coefficients
$c_1$	Power-law constant
$C$	Constant offset for the logarithmic law of the wall
$C_{pu_i}$	Coherence between $p$ and $u_i$
$d$	Diameter of the rigid actuator disk
$d_p$	Diameter of the microphone pinhole
$d_t$	Diameter of a tracer particle
$D$	Diameter of the flexible actuator disk
$D_m$	Diameter of the microphone
$E_c$	Convergence uncertainty
$E_p$	Propagation uncertainty
$E_r$	Random error
$\mathcal{E}$	Total uncertainty
$f$	Frequency
$f_a$	Actuation frequency
$f_o$	Optical focal length
$f^*$	Helmholtz resonant frequency
$g$	Impulse response of the Helmholtz resonator
$g_{hu}$	Impulse response from $h$ to $u$
$G$	Transfer function of the Helmholtz resonator

$G_{hu}$	Transfer function from $h$ to $u$
$h$	Height of the active surface deformation
$h_m$	Height of the microphone lip
$h_r$	Reference signal for operation of the active surface
$H$	Boundary layer shape factor
$k$	High-amplitude pressure peak threshold factor
$k_x$	Streamwise wavenumber of $u$
$\ell_p$	Length of the microphone pinhole
$m$	Filter order
Ma	Mach number
$N$	Total number of samples
$N_{\text{eff}}$	Effective number of independent samples
$p$	Fluctuating pressure
$p_0$	Helmholtz-corrected pressure signal
$p_b$	Background noise
$p_{\text{LS}}$	Fluctuating wall pressure filtered to isolate the large scales
$p_{\text{LS}_q}$	Fluctuating wall pressure filtered to isolate the $q^{\text{th}}$ quartile of the large-scale band
$p_n$	Noise field signal
$p_p$	Pressure beneath the microphone pinhole
$p_r$	Reference pressure signal
$p_{\text{rms}}$	Root-mean-square value of $p$
$p_{\text{VLS}}$	Fluctuating wall pressure filtered to isolate the very-large scales
$P$	Instantaneous pressure
$\mathcal{P}$	Turbulence production
$q$	Index denoting a quartile of the large-scale pressure band
$r$	General correlation coefficient
$r_h$	Autocorrelation coefficient of $h$
$r_{hu}$	Cross-correlation coefficient between $h$ and $u$
$\mathbf{r}_{hu}$	Cross-correlation vector between $h$ and $u$
$r_{p_n}$	Autocorrelation coefficient of $p_n$
$r_{p_n p_0}$	Cross-correlation coefficient between $p_n$ and $p_0$
$\mathbf{r}_{p_n p_0}$	Cross-correlation vector between $p_n$ and $p_0$
$r_{u\hat{u}}$	Cross-correlation coefficient between $u$ and $\hat{u}$
$Re_D$	Reynolds number computed using $D$ and $U_\infty$
$Re_{\delta^*}$	Reynolds number computed using $\delta^*$ and $U_\infty$
$Re_\theta$	Reynolds number computed using $\theta$ and $U_\infty$
$Re_\tau$	Reynolds number computed using $\lambda$ and $U_\tau$
$\mathbf{R}_h$	Toeplitz autocorrelation matrix of $h$
$\mathbf{R}_{p_n}$	Toeplitz autocorrelation matrix of $p_n$
$\mathbf{R}_{p u_i}$	Space-time correlation between $p$ and $u_i$

$\mathbf{R}_{pu_i}^+$	Space-time correlation between $p > 0$ and $u_i$
$\mathbf{R}_{pu_i}^-$	Space-time correlation between $p < 0$ and $u_i$
$\mathbf{R}_{pu_i}^{\text{LS}}$	Space-time correlation between $p_{\text{LS}}$ and $u_i$
$\mathbf{R}_{pu_i}^{\text{LS}+}$	Space-time correlation between $p_{\text{LS}} > 0$ and $u_i$
$\mathbf{R}_{pu_i}^{\text{LS}-}$	Space-time correlation between $p_{\text{LS}} < 0$ and $u_i$
$\mathbf{R}_{pu_i}^{\text{LS}_q}$	Space-time correlation between $p_{\text{LS}_q}$ and $u_i$
$\mathbf{R}_{pu_i}^{\text{LS}_q+}$	Space-time correlation between $p_{\text{LS}_q} > 0$ and $u_i$
$\mathbf{R}_{pu_i}^{\text{LS}_q-}$	Space-time correlation between $p_{\text{LS}_q} < 0$ and $u_i$
$\mathbf{R}_{pu_i}^{\text{VLS}}$	Space-time correlation between $p_{\text{VLS}}$ and $u_i$
$\mathbf{R}_{pu_i}^{\text{VLS}+}$	Space-time correlation between $p_{\text{VLS}} > 0$ and $u_i$
$\mathbf{R}_{pu_i}^{\text{VLS}-}$	Space-time correlation between $p_{\text{VLS}} < 0$ and $u_i$
$S^-$	Strength of the low-speed actuated motions
$S^+$	Strength of the high-speed actuated motions
$S_{\text{max}}$	Peak strength of the actuated motions
$St$	Strouhal number computed using $D$ and $U_\infty$
$t$	Time coordinate
$\Delta t$	Change in time coordinate
$t_i$	$i^{\text{th}}$ time instance
$t_p$	Thickness of the pinhole material
$u$	Fluctuating streamwise velocity
$u_i$	Fluctuating $i^{\text{th}}$ component of velocity
$u'_i$	Remainder of $u_i$ following a triple decomposition
$\langle u \rangle_\phi^m$	Model for visualization of the actuated motions
$U$	Instantaneous streamwise velocity
$U_c$	Advection velocity
$U_i$	Instantaneous $i^{\text{th}}$ component of velocity
$U_s$	Speed of sound
$U_t$	Velocity of a tracer particle
$\Delta U_t$	Velocity difference between a tracer particle and the surrounding fluid
$U_\tau$	Friction velocity
$U_\infty$	Freestream velocity
$v$	Fluctuating wall-normal velocity
$V$	Instantaneous wall-normal velocity
$V_c$	Volume of the cavity beneath the microphone pinhole
$w$	Fluctuating spanwise velocity
$W$	Instantaneous spanwise velocity
$x$	Streamwise coordinate
$\Delta x$	Change in streamwise coordinate
$x_i$	$i^{\text{th}}$ coordinate
$\Delta x_i$	Change in $i^{\text{th}}$ coordinate

$x_m$	Measurement location
$y$	Wall-normal coordinate
$\Delta y$	Change in wall-normal coordinate
$z$	Spanwise coordinate
$\Delta z$	Change in spanwise coordinate
$\alpha_p$	Pinhole angle
$\delta$	Boundary layer thickness
$\delta_X$	Boundary layer thickness based on $0.XU_\infty$
$\delta^*$	Displacement thickness
$\epsilon$	Bias uncertainty of calibration
$\theta$	Momentum thickness
$\kappa$	Von Kármán constant for the logarithmic law of the wall
$\lambda$	Viscous lengthscale
$\lambda_x$	Streamwise wavelength of the actuated motions
$\Lambda_x$	Streamwise wavelength of $u$
$\mu$	Dynamic viscosity
$\nu$	Kinematic viscosity
$\xi$	Damping ratio of the Helmholtz resonator
$\rho$	Density
$\Delta\rho$	Density difference between a tracer particle and the surrounding fluid
$\sigma$	Standard deviation
$\tau_w$	Shear stress at the wall
$\phi$	Phase of actuation
$\Delta\phi$	Phase shift
$\phi'$	Modified phase of actuation
$\Phi_h$	Power spectral density of $h$
$\Phi_p$	Power spectral density of $p$
$\Phi_{pu_i}$	Cross spectral density between $p$ and $u_i$
$\Phi_{u_i}$	Power spectral density of $u_i$
$\omega$	Angular frequency
$\omega_a$	Angular actuation frequency

# List of Abbreviations

3D	Three-dimensional
FOV	Field of view
HAPP	High-amplitude pressure peak
LBL	Laminar boundary layer
LSM	Large-scale motion
LSP	Large-scale pressure
NLTF	Nonparametric linear transfer function
PIV	Particle image velocimetry
POD	Proper orthogonal decomposition
PSD	Power spectral density
RAM	Random-access memory
RANS	Reynolds-averaged Navier-Stokes
SSD	Solid-state drive
TBL	Turbulent boundary layer
VLSM	Very-large-scale motion
VLSP	Very-large-scale pressure

Part I

Background

# Chapter 1

## Introduction

### 1.1 Motivation and Challenges

A multitude of engineering systems feature fluid flowing over a solid surface. Adhesion of the fluid molecules to the surface leads to the no-slip boundary condition, which enforces the velocity of the surface onto the fluid elements that are immediately adjacent to it. Viscous forces then lead to a layer of the fluid exhibiting a gradient over which the fluid velocity transitions from that of the surface to that of the freestream. This affected layer of fluid is known as a *boundary layer*. When the fluid velocity is low, the surface exposed to the flow is small, and the system is free of disturbances, the boundary layer can remain laminar. However, the high fluid velocities, large surfaces, and disturbances found in most physical systems result in the amplification of instabilities, causing the boundary layer to quickly transition into chaos and irregularity as is illustrated by the flow visualization of Figure 1.1. The resulting *turbulent boundary layer* (TBL) significantly influences the forces, vibration, heat transfer, mixing, and acoustic noise affecting a given system, thus elevating the scenario from an interesting physics problem to one of immense practical importance to the engineering community.

Considerable scientific effort has been expended towards understanding the dynamics of TBLs and how these dynamics can be exploited or mitigated to improve various systems. Despite the progress, there is still much that is not understood about TBLs, and there are several reasons for

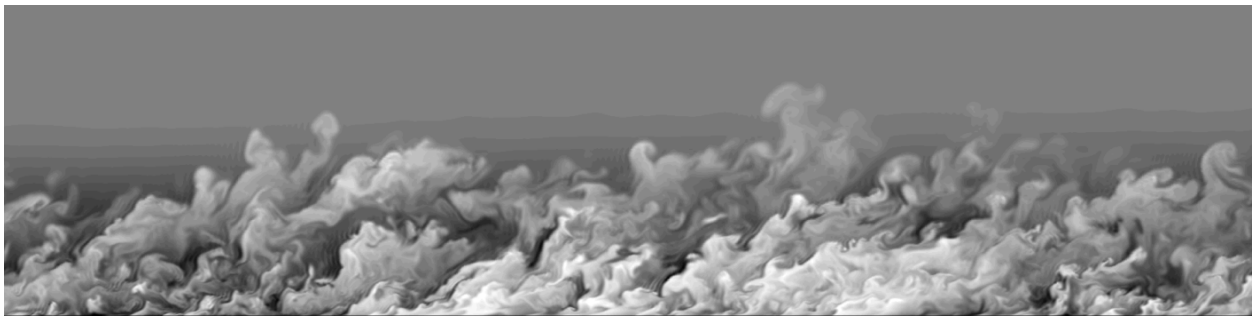


Figure 1.1: Visualization of a turbulent boundary layer. Adapted from Pirozzoli and Bernardini (2011) with permission from Cambridge University Press.

this. First, the governing equations of fluid dynamics are coupled, nonlinear, partial differential equations, which are mathematically intractable for realistic flow situations. Direct numerical simulation of the discretized equations is one route to solution that yields dense information about the velocity and pressure fields. However, such simulations are limited by the currently available computational power and are therefore unable to resolve flows with a high *Reynolds number*, i.e., the parameter used to describe how turbulent a fluid flow is. Experimental facilities can achieve much higher Reynolds numbers, but measurements are not nearly as fruitful as simulation results. Current image-based particle velocimetry techniques can produce reliable velocity field measurements in a single plane or within small volumes, but such measurements require significant labour and the resulting data is far less rich than that of a simulation. Moreover, measurements of the fluctuating pressure field have been historically difficult to execute and are only reliably obtained as point measurements at the moment. The lack of sufficient computational power for high-Reynolds-number simulations and the difficulty obtaining measurements in experiments have made it challenging to advance our understanding of TBLs.

Although our understanding of TBLs is incomplete, sufficient progress has been made to take advantage of the dynamics in some applications. For example, the boundary layer over the wing of an aircraft is sometimes forced to transition prematurely so that the diffusive properties of turbulence can be exploited. High-momentum fluid farther from the surface diffuses into regions much closer to it, allowing the boundary layer to overcome an adverse pressure gradient and prevent flow separation. This allows the wing to operate at higher angles of attack to increase lift, but comes at the cost of increased drag as sustaining the turbulent motions requires additional energy. In contrast, there is no benefit extracted from the turbulent flow over the fuselage of the aircraft. Here, the boundary layer transitions to turbulence naturally, resulting in an increase of the drag forces that must be overcome by the propulsion system and a worsening of the induced vibrations and noise experienced by passengers. In this scenario and many others it would be immensely beneficial to have the ability to control the drag, noise, and vibrations associated with the TBL – an outcome that is significantly more difficult to achieve. Despite the challenges, the outcome is likely worth the trouble because “modern turbulence control has applications of epic proportion” (Brunton and Noack, 2015). Again considering the example of an aircraft, it is estimated that roughly half of the energy required to propel such a vehicle is consumed by the drag forces from its TBLs (Goldhammer, 2009). Reducing the drag by only 1% would result in reducing fuel costs by \$100 million annually in the United States alone (Gad-el-Hak et al., 1998). These fuel savings would of course be accompanied by a large reduction in greenhouse gas emissions; some estimates indicate that the same 1% drag reduction would lower global CO<sub>2</sub> emissions by 9 million tonnes annually (Leschziner et al., 2011).

To improve the systems affected by TBLs (less drag, noise, vibration, etc.), strategies must be developed that allow for the manipulation of the flow to produce a more desirable outcome. Such flow control strategies can be considered in two broad categories: passive and active (Gad-el-Hak, 2000). Passive strategies, for example the use of surface modifications (Abu Rowin et al.,

2018) or fluid additives (Warwaruk and Ghaemi, 2021), are attractive because they do not require energy input. However, these strategies can only be applied in specific scenarios and therefore the applications are quite limited. In contrast, active strategies are more widely applicable because they make use of sensing and actuation to enhance the performance of a system. They come with the expense of increased complexity, but also open the door to control theory and machine learning. As a result, active strategies often have more potential upside than passive strategies, and this is why the present thesis focuses on the active control of TBLs. Unfortunately, active strategies are not straightforward to implement in practice. Why this is the case becomes clear when considering the complicated physics of TBLs in the context of the four components required to formulate an active control strategy: the desired state, sensors, actuators, and controller. The challenges associated with each of these components are discussed below.

*Desired state.* The desired state of the TBL must be known so that the control system can be designed to drive the TBL to this state. At first, this appears to be the most straightforward component of the control strategy since it is clear that a state of reduced drag, noise, etc., is desirable. According to Gad-el-Hak et al. (1998), such a state can be achieved relatively easily using classical flow control techniques, for example global suction at the wall. However, these strategies typically require more energy to function than is saved by the flow modification. The desired state of a TBL is therefore one that can be produced efficiently while still yielding a benefit for a given system. Gad-el-Hak et al. (1998) go on to suggest that such a state may be achievable by targeting coherent structures in the flow: “One ponders, what would become of wall turbulence if specific coherent structures are to be targeted, by the operator through a reactive control scheme, for modification? ... If such structures are nonintrusively detected and altered ... net performance gain might be achieved.” Determining whether desirable TBL states can be achieved efficiently with targeted control is an active area of research today.

*Sensing.* Sensors must be used to observe the current state of the TBL so that the controller can be informed about which action to take next. It is crucial that they are placed at or within the surface so that they do not cause a protrusion into the flow and a worsening of the turbulent state. The sensors must therefore be able to accurately represent the state of the flow at a distance. Whether measurements of velocity, pressure, or both are being used for this purpose, knowing how these sensor signals relate to the state of the TBL is a significant challenge. The velocity of a fluid is a local quantity, and so velocity sensors placed at or near the surface cannot directly measure the state of the velocity field farther from the surface. In contrast, the pressure signal at the surface contains useful information about the state of the velocity field at a distance because pressure is a global quantity (Pope, 2000). However, pressure signals contain information about all motions in the flow, and so using such a signal to infer the state of a TBL is complicated. The above make it clear that sensing for the purpose of TBL control is not straightforward.

*Actuation.* Actuators must be able to reliably force the TBL to the desired state and maintain that state over time. Just like sensors, actuators should be incorporated into the surface if possible so that they do not cause significant protrusions into the boundary layer. They must therefore

be able to function while embedded in a surface and have authority over the flow at a distance. Additionally, they must be able to operate efficiently to improve the likelihood that the control strategy will achieve a net performance gain. Many types of actuators have been explored for targeted control with the most popular being fluidic actuators (e.g., jets) and plasma actuators. Both types of actuators have disadvantages such as the need for fluid storage, high voltages, etc. As concluded in the review by Cattafesta and Sheplak (2011), “the future is bright for active flow control, but the search for the perfect actuator continues”. This statement remains true more than a decade later and highlights the ever-present difficulty of selecting an appropriate actuator for a flow control application.

*Controller.* The controller takes as input the sensor signals representing the state of the TBL and determines how the actuators should be operated to reach or maintain the desired state. Controller design typically relies on an accurate model of the actuated system, which allows for developing the control law using theory and simulation. While modern control theory provides a massive suite of tools for developing controllers, the most powerful and commonly used of these tools are largely limited to linear systems of low dimension (Chen, 1999). Unfortunately, turbulent flows are nonlinear systems with tremendous dimensionality. As a result, the degree to which actuated TBLs can be represented using linear models with low dimension is not yet clear. Moreover, simulating actuated TBLs using the full governing equations for the purpose of trial-and-error control design is prohibitively expensive, computationally speaking. There are therefore immense hurdles in the way of those looking to develop effective controllers for manipulating TBLs to produce a more desirable outcome.

None of the components discussed above are trivial in the context of TBL control. This can be contrasted with a more typical control application: a robotic arm. Such a device will include several joints, the positions of which are sensed and actuated directly using commonly available hardware. The equations of rigid-body dynamics then readily provide low-order models for controller design and simulation (Lynch and Park, 2017). This contrast in difficulty is why factories are filled with effective robots but aircraft do not have drag- and noise-reduced TBLs. It is therefore important to continue improving our ability to apply active control to TBLs so that the affected systems can be made more efficient and effective in the future.

## 1.2 Approach and Objectives

The present thesis focuses on developing sensing and actuation capabilities based around a control strategy for TBLs that is both novel and promising. Following the suggestion of Gad-el-Hak et al. (1998), the strategy involves targeting a subset of the coherent motions within TBLs that are dynamically important. The motions in question and the approach to sensing and actuating these motions are discussed next.

## Targeting the Very-Large-Scale Motions

Focusing on the largest motions that exist within TBLs is the primary theme associated with the present thesis. These are the so-called *very-large-scale motions* (VLSMs), which are also known as *superstructures*, that occupy the logarithmic layer of the flow (Kim and Adrian, 1999; Hutchins and Marusic, 2007a). These motions are characterized as long, meandering regions of high and low streamwise velocity fluctuation that have been observed to extend beyond 20 times the boundary layer thickness in length (Hutchins and Marusic, 2007a). Although the VLSMs are a recent discovery relative to the long history of TBL research, they have emerged as being critical to the dynamics of the flow. They carry a considerable amount of kinetic energy and shear stress (Balakumar and Adrian, 2007; Lee and Sung, 2011), are responsible for modulating the amplitude and frequency of near-wall fluid motions (Hutchins and Marusic, 2007b; Mathis et al., 2009; Ganapathisubramani et al., 2012), and are associated with extreme wall-shear events (Hutchins et al., 2011; Pan and Kwon, 2018). They are a desirable target for a control strategy for three primary reasons. First, the characteristics described above suggest that the ability to control the VLSMs would provide influence over the energy, turbulence production, and drag associated with TBLs. Second, they become increasingly important to the dynamics of the flow as Reynolds number is increased (Smits et al., 2011), and real-world applications typically feature TBLs at high Reynolds numbers. Finally, the elongated nature of these motions places their influence in the lowest frequency range of the turbulence spectrum. This makes it easier to develop a suitable actuator and also increases the likelihood that a control strategy will produce a net performance gain since low-frequency actuation consumes less energy. The targeted control of VLSMs is clearly worth investigating, but has only been the subject of a handful of studies to date. They therefore serve as the target for the sensing and actuation capabilities developed in the present work.

## Sensing with Wall-Pressure Measurements

The sensing capabilities developed here focus on whether the VLSMs can be identified in real time using the pressure signal at the surface beneath a TBL, i.e., the *wall pressure*. This choice was made because pressure sensors are by far the most practical for implementation into physical systems. However, there are challenges associated with the use of wall pressure as an indication of the state of the velocity field. First, pressure measurements are easily corrupted by acoustic noise sources (Willmarth, 1975; Bull, 1996; Tsuji et al., 2012), which there is no shortage of within engineering systems. The pressure measurement system utilized must therefore be designed to account for acoustic noise in real time while remaining sensitive to the pressure fluctuations of the VLSMs in the low-frequency range. Second, pressure is a global quantity as mentioned previously. More specifically, the solution to the Poisson pressure equation, which is valid for incompressible, Newtonian fluids, reveals that pressure fluctuations are dictated by the velocity field throughout the entire domain (Pope, 2000). This means that all turbulent motions contribute to the pressure fluctuations at any given point in the flow, not just those that are being targeted. The relationship between the pressure signal and the target motions must therefore be well-understood in order to

use the signal to inform a controller. The relationship between wall pressure and the VLSMs was not known prior to the present work and therefore two chapters of this thesis are dedicated to developing a suitable pressure measurement system and identifying this relationship for the first time.

## **Actuation with Active Surface Deformations**

The actuation capabilities developed here focus on targeting the VLSMs using active surface deformations applied in the wall-normal direction. This actuation strategy was primarily motivated by the results of two previous studies. First, the earlier work of Carlson and Lumley (1996) showed that one type of wall-normal surface deformation, a “Gaussian bump”, could be used to target streaky structures in wall-bounded flows. They found that raising the Gaussian deformation below a high-speed streak pushes the high-speed fluid away from the wall which in turn allows the adjacent low-speed region to expand, resulting in a lower shear stress at the wall. Conversely, raising the deformation below a low-speed streak resulted in the expansion of the adjacent high-speed region and an increase in shear stress at the wall. These results reveal a possible mechanism for targeting streaky structures such as VLSMs using active surface deformations. The second motivating study is that of Luhar et al. (2015), who used a resolvent analysis to evaluate the potential of pressure-driven compliant surfaces to control wall-bounded turbulence. They found that these passive surfaces can be optimized to effectively suppress modes resembling VLSMs, but that such a surface also produces effects elsewhere in spectral space that are detrimental to the control goal. A passive compliant surface may therefore not be the best option for targeting VLSMs. However, a surface that relies on deliberate actuation to produce local wall-normal deformations may be capable of targeting VLSMs without being accompanied by detrimental side effects. Actuation with active surface deformations has been largely overlooked in the flow control literature (Cattafesta and Sheplak, 2011), and so three chapters of the present thesis are dedicated to developing an active surface and determining how it affects boundary layer flows.

## **Objectives**

Considering the motivation, challenges, and approach outlined above, the primary objectives of this thesis can be stated:

1. Design, construct, and test a pressure measurement system capable of sensing the wall-pressure fluctuations of the VLSMs within a noisy environment.
2. Identify the relationship between wall pressure and the VLSMs within a TBL.
3. Design, construct, and test an active surface with the geometric and frequency response characteristics necessary for targeting the VLSMs.
4. Determine how the active surface influences boundary layer flows in general and whether it is a viable actuator for targeting the VLSMs.

## 1.3 Thesis Overview

This thesis is organized into four parts: Background, Sensing, Actuation, and Closing. These parts and the chapters within are described below.

### Part I: Background

- Chapter 1: Introduction

This chapter has outlined the motivation, challenges, objectives, and organization of the present thesis.

- Chapter 2: Boundary Layers

An overview of boundary layers is presented which includes common definitions, the equations of motion, and a literature review of TBLs in the context of the present work. This review covers coherent motions, velocity statistics, wall-pressure fluctuations, moving-surface actuators, and previous attempts at targeting the VLSMs.

- Chapter 3: Experimental Methods

The major details of the experiments are covered. This includes the wind tunnel used for experiments and how the desired boundary layers are generated. The velocity measurement technique and data acquisition systems are also discussed. The particulars of the individual experiments associated with the results chapters are provided within those chapters.

### Part II: Sensing

- Chapter 4: Development of the Pressure Measurement System

The development of the pressure measurement system is documented. The measurement requirements, sensor selection, component design, algorithm design, and testing of the system are discussed.

- Chapter 5: Low-Frequency Wall-Pressure Sources in a Turbulent Boundary Layer

Simultaneous wall-pressure and velocity measurements are used to investigate the pressure-velocity coupling at low frequencies within a TBL. The measurements are validated by comparison to the literature, revealing excellent agreement. The relationship between wall-pressure and the VLSMs is then identified for the first time.

### Part III: Actuation

- Chapter 6: Development of the Active Surface

The development of the active surface is documented. The actuation requirements, actuator selection, assembly design, surface deformation characteristics, and tuning of the device are discussed.

- Chapter 7: Laminar Boundary Layer Forcing with Active Surface Deformations

The active surface is used to force a laminar boundary layer (LBL) and the impact on the

flow is evaluated using measurements of the velocity field. The primary analyses determine the effects of actuation frequency and amplitude. Linear modelling of the actuated flow is then explored using a data-driven technique.

- Chapter 8: Turbulent Boundary Layer Forcing with Active Surface Deformations

The active surface is used to force a TBL and the impact on the flow is evaluated using measurements of the velocity field. The analyses reveal the average motions produced by the actuation technique and their impact on the surrounding turbulence. Comparison with the LBL results allows for estimating how the active surface may effect a wide range of boundary layers.

#### **Part IV: Closing**

- Chapter 9: Conclusions

The thesis is concluded with a synthesis of the present contributions and suggestions for future work.

- Appendix A: Uncertainty Analysis

The uncertainties are estimated for the instantaneous measurements conducted for this thesis and for various statistical quantities presented in the primary results chapters.

- Appendix B: MATLAB Code

The MATLAB codes for non-trivial algorithms used throughout this thesis are documented.

## Chapter 2

# Boundary Layers

Boundary layers found in engineering systems are exposed to a wide range of conditions. Each of these conditions, e.g., a pressure gradient, can influence the dynamics of the flow. To facilitate comparison, researchers focus on the canonical case unless otherwise stated: an incompressible boundary layer formed from a Newtonian fluid over a smooth, flat surface with minimal disturbances or gradients of any kind. This type of basic boundary layer is the focus of the present thesis and therefore also the focus of this section. Note that many of the equations discussed here will not be associated with a specific reference since they are considered common equations of fluid dynamics. Such equations can be found in texts such as Pope (2000) or Schlichting and Gersten (2017).

### 2.1 Definitions

Decades of research and engineering concerned with boundary layers have produced various definitions that can be found throughout the literature. Some are so common that they are never introduced, and others seem to be defined one way or another using one symbol or another as a matter of preference. Here the boundary layer definitions that are used in the present work are briefly introduced to avoid any confusion. To begin, the fluid density is  $\rho$ , the dynamic viscosity is  $\mu$ , and the kinematic viscosity is  $\nu = \mu/\rho$ .

A Cartesian coordinate system is used where  $x$ ,  $y$ , and  $z$  denote the streamwise, wall-normal, and spanwise directions, respectively. The origin of the coordinate system is always placed at the surface over which the boundary layer forms and therefore  $y = 0$  is the wall location. The instantaneous velocity components in the  $x$ ,  $y$ , and  $z$  directions are  $U$ ,  $V$ , and  $W$  while the instantaneous pressure is  $P$ . The brackets  $\langle \cdot \rangle$  are used to denote an ensemble average in time. The Reynolds decomposition is

$$U = \langle U \rangle + u, \tag{2.1a}$$

$$V = \langle V \rangle + v, \tag{2.1b}$$

$$W = \langle W \rangle + w, \tag{2.1c}$$

$$P = \langle P \rangle + p, \tag{2.1d}$$

where  $u$ ,  $v$ , and  $w$  are the fluctuating velocity components and  $p$  is the fluctuating pressure. The subscripts  $i = 1, 2, 3$  will sometimes be used as vector notation for velocity ( $U_i, u_i$ ) and the coordinate directions ( $x_i$ ) to indicate that all three components are relevant. Einstein notation applies in these cases.

The uniform flow sufficiently far from the wall such that it is not affected by viscous forces is referred to as the freestream and moves at a velocity  $U_\infty$ . The boundary layer begins at the wall and ends at the boundary layer thickness  $\delta$  where the mean velocity has become sufficiently close to  $U_\infty$ . Since the transition from the boundary layer to the freestream is continuous and quite gradual, the actual value of  $\delta$  can be a bit ambiguous. One common approach to computing  $\delta$  is to use the point at which  $\langle U \rangle = 0.99U_\infty$ . This value is typically denoted as  $\delta_{99}$  and is used when dealing with both LBLs and TBLs. A second approach specifically for TBLs is to compute  $\delta$  by fitting the mean velocity profile to a modified version of Coles' law of the wake (Perry et al., 2002). This approach produces values that are roughly 20% larger than  $\delta_{99}$  for a given TBL (Hutchins et al., 2011). Errors can therefore be introduced when comparing boundary layer properties between studies that have employed a different definition of  $\delta$ . To partially remedy this, the thickness of the TBL studied in the present thesis is defined as the point at which  $\langle U \rangle = 0.995U_\infty$ . This produces values of  $\delta$  that are roughly half way between what is produced by the two previous definitions and therefore the error is minimized when comparing to the literature as a whole.

Integral measures of the boundary layer thickness are also frequently reported. The displacement thickness of an incompressible boundary layer is defined as

$$\delta^* = \int_0^\infty \left(1 - \frac{\langle U \rangle}{U_\infty}\right) dy, \quad (2.2)$$

and represents the distance that the wall would need to be displaced in a frictionless flow to obtain the same mass deficit as the boundary layer. Similarly, the momentum thickness of an incompressible boundary layer is defined as

$$\theta = \int_0^\infty \frac{\langle U \rangle}{U_\infty} \left(1 - \frac{\langle U \rangle}{U_\infty}\right) dy, \quad (2.3)$$

and represents the thickness of a layer of fluid with velocity  $U_\infty$  for which the momentum flux is equal to the momentum deficit of the boundary layer. Notice that neither  $\delta^*$  nor  $\theta$  depends on the definition of  $\delta$  and therefore they can be compared between studies without ambiguity. Both parameters can be used to define the shape factor as

$$H = \frac{\delta^*}{\theta}. \quad (2.4)$$

The shape factor is an indication of how much momentum is present near the wall.

The shear stress at the wall is defined as

$$\tau_w = \mu \left. \frac{\partial \langle U \rangle}{\partial y} \right|_{y=0}, \quad (2.5)$$

and represents the average force per unit area exerted by the fluid on the wall. This quantity is used to compute the friction velocity of a boundary layer which is defined as

$$U_\tau = \sqrt{\frac{\tau_w}{\rho}}, \quad (2.6)$$

and is typically used as the velocity scale for the near-wall region of the flow where viscous effects are dominant. Similarly, the viscous lengthscale is defined as

$$\lambda = \frac{\nu}{U_\tau}. \quad (2.7)$$

The quantities  $U_\tau$  and  $\lambda$  are often referred to as the inner scales whereas  $U_\infty$  and  $\delta$  are referred to as the outer scales.

Finally, the Reynolds number is a dimensionless parameter that is used to quantify how turbulent a flow is. There are three definitions that are commonly used for boundary layers. First, the Reynolds number can be computed using either  $\delta^*$  as

$$Re_{\delta^*} = \frac{U_\infty \delta^*}{\nu}, \quad (2.8)$$

or using  $\theta$  as

$$Re_\theta = \frac{U_\infty \theta}{\nu}. \quad (2.9)$$

Both of these definitions represent a ratio between inertial forces and viscous forces within a boundary layer. In contrast, the Reynolds number can also be computed using the inner and outer lengthscales as

$$Re_\tau = \frac{U_\tau \delta}{\nu} = \frac{\delta}{\lambda}. \quad (2.10)$$

This particular definition is known as the friction Reynolds number and is more well-understood as the ratio between the largest and smallest lengthscales in a TBL as is demonstrated by the right-most side of the above equation. It remains an indication of how turbulent the flow is because the separation between the smallest and largest scales in a flow increases as the flow becomes more turbulent.

## 2.2 Equations of Motion

Although not used explicitly in the present work, the equations of motion for an incompressible Newtonian fluid will be briefly reviewed to inform the reader and to reveal a few insights they provide. The equations are derived by applying the conservation of mass and momentum to a fluid element along with a few assumptions about viscous stress. For the conservation of mass this yields

$$\frac{\partial U_i}{\partial x_i} = 0. \quad (2.11)$$

The above is known as the continuity equation and it captures the solenoidal nature of the instantaneous velocity field and by extension also the fluctuating velocity field. Similarly, the conservation of momentum yields

$$\frac{\partial U_i}{\partial t} + U_j \frac{\partial U_i}{\partial x_j} = -\frac{1}{\rho} \frac{\partial P}{\partial x_i} + \nu \frac{\partial^2 U_i}{\partial x_j \partial x_j}. \quad (2.12)$$

The above is simply referred to as the momentum equation and represents the application of Newton's second law of motion to a fluid element. Together, Equations (2.11) and (2.12) constitute the incompressible Navier-Stokes equations. They completely describe the motion of incompressible Newtonian fluids, which makes them incredibly useful, and they are nonlinear partial differential equations, which makes them notoriously difficult to work with. The intractability of these governing equations is what impedes the application of control theory to fluid-dynamical systems.

There are two manipulations of the Navier-Stokes equations that reveal details about the nature of turbulent flows. First, the Reynolds decomposition can be applied and followed by a time average to obtain the Reynolds-averaged Navier-Stokes (RANS) equations as

$$\langle U_j \rangle \frac{\partial \langle U_i \rangle}{\partial x_j} = -\frac{1}{\rho} \frac{\partial \langle P \rangle}{\partial x_i} + \nu \frac{\partial^2 \langle U_i \rangle}{\partial x_j \partial x_j} - \frac{\partial \langle u_i u_j \rangle}{\partial x_j}. \quad (2.13)$$

Notice that the RANS equations are similar in form to Equation (2.12) but without the time derivative and with a new term featuring the Reynolds stress tensor  $\langle u_i u_j \rangle$ . These equations can be used to solve for the mean velocity and pressure of a turbulent flow if the new term can be modelled as a function of  $\langle U_i \rangle$  and  $\langle P \rangle$ ; this is referred to as the closure problem and has been the subject of study for decades. Progress on this problem is what stands in the way of the efficient and accurate determination of average flow fields at high Reynolds numbers – an ability that has the potential to revolutionize engineering design. Unfortunately, the Reynolds stress term in the RANS equations cannot be neglected without significant error. Taking a closer look, it is clear that the Reynolds stress term is the divergence of the Reynolds stress tensor. This indicates that it captures the degree to which the stresses resulting from turbulent fluctuations act as sinks or sources of momentum (i.e., forces). The turbulent fluctuations then act to force the RANS equations, and therefore the mean flow, despite the fact that  $\langle u_i \rangle = 0$  by definition, therefore highlighting the

complex nature of turbulent flows in general. As will be discussed later in Section 2.3, the Reynolds stresses reveal where turbulence is produced within TBLs and how the dominant motions vary as Reynolds number is increased.

The second manipulation requires taking the divergence of the Navier-Stokes equations followed by applying the continuity equation to yield

$$\frac{1}{\rho} \frac{\partial^2 P}{\partial x_j \partial x_j} = - \frac{\partial U_i}{\partial x_j} \frac{\partial U_j}{\partial x_i}. \quad (2.14)$$

This particular equation is referred to as the Poisson pressure equation and it is typically used to couple the pressure and velocity fields. The Reynolds decomposition can be applied to obtain a version of the equation for the fluctuating pressure with two source terms as

$$\frac{1}{\rho} \frac{\partial^2 p}{\partial x_j \partial x_j} = -2 \frac{\partial \langle U_i \rangle}{\partial x_j} \frac{\partial u_j}{\partial x_i} - \frac{\partial^2}{\partial x_i \partial x_j} (u_i u_j - \langle u_i u_j \rangle). \quad (2.15)$$

The first term on the right-hand-side of the above is referred to as the rapid pressure because it responds immediately to a change in the mean velocity profile. The term is linear with respect to the fluctuating velocity field and reflects the interaction between the turbulent motions and the mean flow. As a result, it dominates where the mean velocity gradient is strong, for example very close to the wall in a TBL. In contrast, the second term is referred to as the slow pressure and is nonlinear. It contains the Reynolds stress tensor and reflects the turbulence-turbulence interactions in the flow. Overall, Equation (2.15) reveals that the fluctuating pressure field in a turbulent flow results from the complex interaction of the fluctuating velocity field with the mean flow and with itself.

The solution to a Poisson equation requires integration over the entire relevant domain. Considering the equations above, this reveals that the pressure at any one point depends on the velocity field at every other point in the flow. The inspection of the Poisson pressure equation therefore reveals two key pieces of information: i) pressure is related to the velocity field in a nonlinear manner, and ii) pressure is a global quantity. Both of these facts make it difficult to use pressure sensors as inputs to a controller that seeks to act on the velocity field.

Finally, the Navier-Stokes equations can also be used to derive the Blasius boundary layer solution for the LBL profile. Assuming steady, two-dimensional flow with zero pressure gradient, the Navier-Stokes equations reduce to

$$\frac{\partial \langle U \rangle}{\partial x} + \frac{\partial \langle V \rangle}{\partial y} = 0, \quad (2.16a)$$

$$\langle U \rangle \frac{\partial \langle U \rangle}{\partial x} + \langle V \rangle \frac{\partial \langle U \rangle}{\partial y} = \nu \frac{\partial^2 \langle U \rangle}{\partial y^2}. \quad (2.16b)$$

The above are a form of the boundary layer equations and can be transformed into a nonlinear ordinary differential equation and solved numerically. The resulting Blasius solution is shown in

Figure 2.1. The solution is self-similar and so profiles with varying  $U_\infty$  and  $\delta_{99}$  will overlap as long as the profile is normalized with these parameters. The Blasius profile is used in Chapter 7 to validate the LBL produced for the evaluation of the active surface.

## 2.3 Turbulent Boundary Layers

This section provides an overview of the velocity and pressure fields of TBLs. While the present thesis does not focus on the unactuated velocity field, the well-established velocity characteristics are used to validate the present measurements and to confirm that the experimental facility produces the desired flow field. Moreover, the discussions throughout the results chapters frequently reference various features of the velocity field that the reader may not be familiar with. Therefore, the characteristics of the velocity field that are relevant to the present work will be briefly reviewed before discussing what is known about the wall-pressure fluctuations. Note that some of the studies cited here consider channel or pipe flows instead of boundary layer flows because some aspects of wall-bounded turbulence are universal.

### 2.3.1 Coherent Motions

Contrary to popular belief, turbulence is not random chaos as it features distinct patterns that remain coherent over space and time. These so-called coherent motions (or coherent structures, eddies) are paramount to the dynamics of TBLs and the associated statistics (Robinson, 1991; Smits et al., 2011). Of course, the VLSMs that this thesis focuses upon are the largest coherent motions that exist within TBLs. However, the present discussion of coherent motions begins by considering what is referred to as the *hairpin vortex*, which is another essential element of TBLs (Adrian, 2007). Note that a commonly-accepted and rigorous definition of a vortex does not exist (Jeong and Hussain, 1995). However, the definition of Robinson (1991) is straightforward and reasonable for the following discussion: “A vortex exists when instantaneous streamlines mapped onto a plane normal to the vortex core exhibit a roughly circular or spiral pattern, when viewed from a reference frame moving with the center of the vortex core.”

A schematic of an idealized hairpin vortex is shown in Figure 2.2. Its apt name comes from the hairpin loop structure depicted in the schematic, which features a head and two legs in its complete form. The head of the vortex is located away from the wall while the legs trail behind, resulting in an overall inclination of roughly  $45^\circ$  to the wall (Head and Bandyopadhyay, 1981; Ganapathisubramani et al., 2006). The mean shear of the boundary layer supports the rotational direction of the vortex which acts to eject fluid between its legs and sweep fluid around its outside. Here, an *ejection* refers to fluid motion that is up and back with respect to the mean flow ( $u < 0$ ,  $v > 0$ ) while a *sweep* refers to fluid motion that is down and forward ( $u > 0$ ,  $v < 0$ ) (Corino and Brodkey, 1969; Wallace et al., 1972). Both ejections and sweeps are also considered important coherent motions within TBLs. The ubiquity of hairpin vortices and their tendency to produce ejections and sweeps help explain the observation that instantaneous  $u$  and  $v$  within TBLs have opposite signs more often than not (more on this in Section 2.3.2).

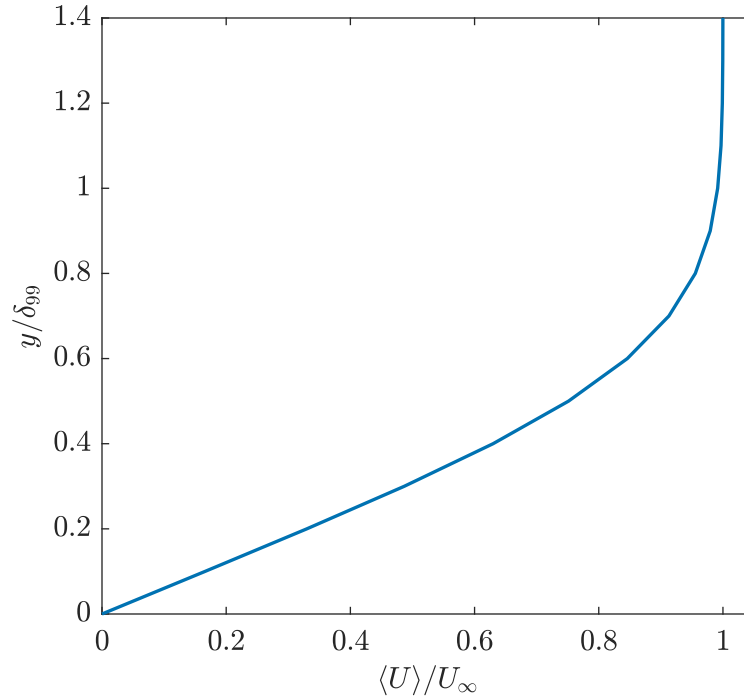


Figure 2.1: The Blasius solution for a steady, two-dimensional boundary layer with zero pressure gradient.

Hairpin vortices are rarely symmetric as depicted in Figure 2.2 because the surrounding turbulence distorts them. They are also not always found in their complete form. Instead, it is common to observe distorted, partial hairpins that may be missing one portion or another of the complete structure. For example, the structure could be missing one leg to produce a “cane” or be missing both legs to produce an “arch” (Adrian and Liu, 2002; Ghaemi and Scarano, 2011; Dennis and Nickels, 2011a). Vortices resembling single legs of hairpins, which are often referred to as quasi-streamwise vortices, are also prevalent (Robinson, 1991). Any of these partial hairpin vortices can exist alone. However, they are typically found within *packets* consisting of a series of hairpin or partial hairpin vortices aligned in the streamwise direction (Head and Bandyopadhyay, 1981; Adrian et al., 2000; Marusic, 2001; Ganapathisubramani et al., 2003; Tomkins and Adrian, 2003; Dennis and Nickels, 2011a). Packets are thought to form as a result of the “autogeneration mechanism” which causes hairpin vortices with sufficient strength to generate new hairpins on their downstream side (Zhou et al., 1996, 1999). Just like individual hairpin vortices, the packets are often inclined to the wall such that the most downstream vortices are larger. However, this inclination is not quite as steep as that of an individual hairpin vortex (Head and Bandyopadhyay, 1981; Adrian et al., 2000; Dennis and Nickels, 2011a).

The combined motions of the hairpin vortices within a packet produce specific effects. First, the series of hairpin vortices produce an alternating series of ejections and sweeps. These alternating motions oppose one another to form inclined shear layers and stagnation points (Adrian et al.,

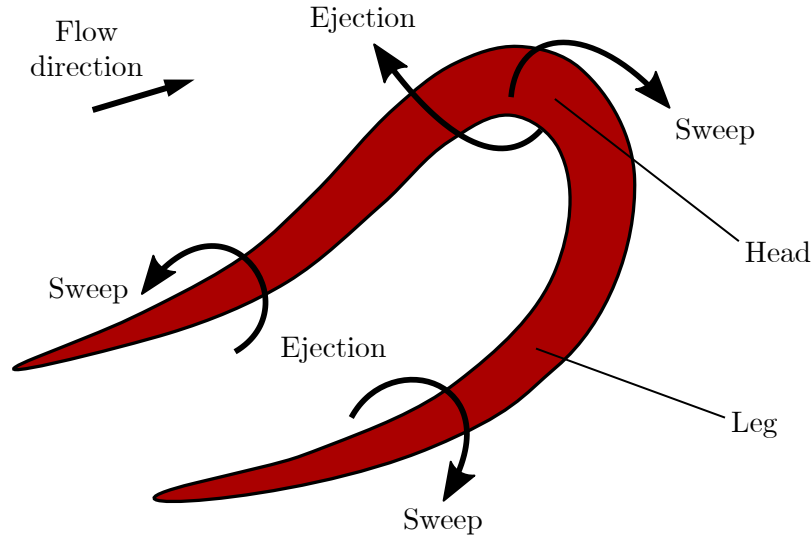


Figure 2.2: Annotated schematic of an ideal hairpin vortex showing the associated sweep ( $u > 0$ ,  $v < 0$ ) and ejection ( $u < 0$ ,  $v > 0$ ) motions.

2000). The signature produced by this process was referred to as the “bursting cycle” before hairpin packets were more well-understood (Adrian, 2007) and the associated shear layers are also considered to be coherent motions (Robinson, 1991). Second, the combined ejections and sweeps act to move momentum across the gradient of the boundary layer profile (Adrian et al., 2000; Tomkins and Adrian, 2003; Dennis and Nickels, 2011a). The ejections between the legs of the hairpins lift low-speed fluid away from the wall to form an elongated low-speed motion. That is, low-speed with respect to the local mean velocity. Similarly, the sweeps at the sides of the packets move high-speed fluid towards the wall to produce elongated high-speed motions. Such high- and low-speed *streaks* are another important type of coherent motion found within TBLs. The visualization from the measurements of Ghaemi and Scarano (2011) shown in Figure 2.3 highlights an example of these streaks. The locations of the vortices, ejections, and sweeps relative to the streaks are evident within this visualization, as is the existence of distorted, partial hairpin vortices.

Hairpin vortices and packets exist in a hierarchy of sizes across the entirety of the boundary layer thickness such that smaller vortices/packets are often nested within the larger ones (Adrian et al., 2000). At the smallest scale these hairpin vortices, both full and partial, are associated with the near-wall high- and low-speed streaks (Blackwelder and Eckelmann, 1979; Adrian and Liu, 2002; Tomkins and Adrian, 2003). Near-wall streaks with the same sign of fluctuation are typically spaced in the spanwise direction at a distance of around  $100\lambda$  (Smith and Metzler, 1983; Lin et al., 2008), making them the smallest streaks present within TBLs. The visualization of Ghaemi and Scarano (2011) shown in Figure 2.3 is an example of these near-wall streaks. When viewed in streamwise–spanwise planes, the size of the streaks that are present within a TBL increase with distance from the wall. The streaks can reach widths of up to around  $0.5\delta$  (Tomkins and Adrian, 2003; Dennis and Nickels, 2011b), which indicates that the maximum spanwise spacing between

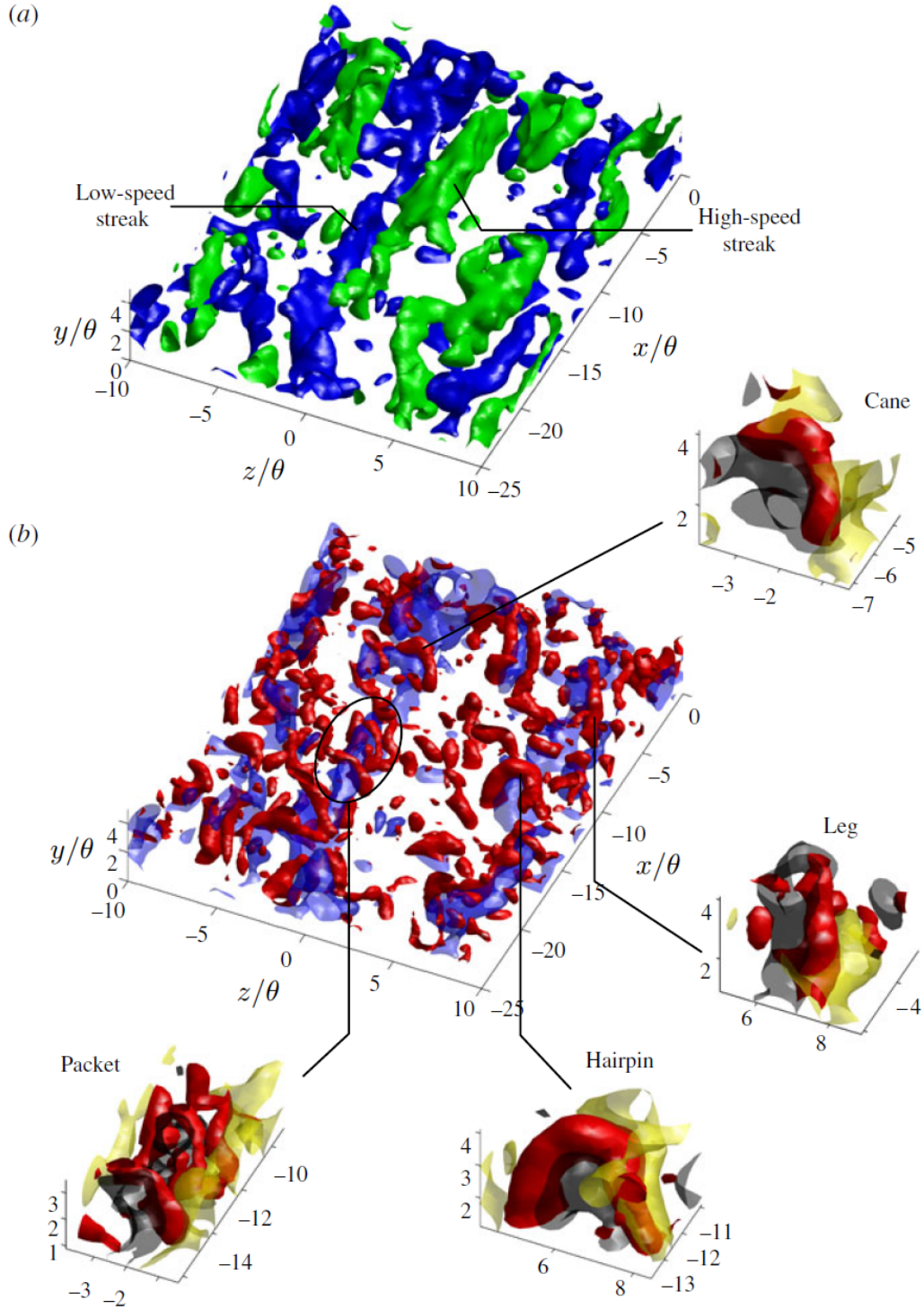


Figure 2.3: Instantaneous visualization of the near-wall streaks and the associated vortical structures. In (a), the high-speed streaks are shown with green while the low-speed streaks are shown with blue. In (b), only the low-speed streaks are shown with blue while the vortical structures are shown with red. The magnified details of (b) also show sweeping motions in yellow and ejection motions in grey. Adapted from Ghaemi and Scarano (2011) with permission from Cambridge University Press.

streaks of the same sign of fluctuation is  $\sim\delta$ . It is therefore the case that high- and low-speed streaks that scale on both inner ( $\lambda$ ) and outer ( $\delta$ ) variables exist within TBLs.

The high- and low-speed coherent motions within TBLs with streamwise lengths ranging from roughly  $1-3\delta$  are considered to be large-scale motions (LSMs) (Balakumar and Adrian, 2007). Due to the inclination of the associated packets, the LSMs can extend through most of the boundary layer thickness. The packets extending to near the outer edge of the boundary layer likely explain the outer “bulges” at the interface between the boundary layer and freestream described in earlier investigations of TBLs (Robinson, 1991). A visualization highlighting the hairpin packet and streaks associated with an LSM from the measurements of Dennis and Nickels (2011a) is shown in Figure 2.4. The distorted, partial structures of the hairpin vortices in the packet are visible and can be seen to increase in size with downstream distance to produce the characteristic inclination discussed previously. The high- and low-speed streaks formed by the collective ejection and sweeping motions of the hairpin vortices are also visible. Coherent motions with the sizes necessary to be considered LSMs, such as the one shown in Figure 2.4, are common within TBLs (Adrian et al., 2000; Ganapathisubramani et al., 2003; Dennis and Nickels, 2011b).

The coherent motions considered for targeted control in the present work are high- and low-speed streaks with streamwise lengths greater than  $3\delta$  (Balakumar and Adrian, 2007). These so-called VLSMs (Kim and Adrian, 1999) or “superstructures” (Hutchins and Marusic, 2007a) are believed to form due to the concatenation and merging of the LSMs (Balakumar and Adrian, 2007; Lee and Sung, 2011; Dennis and Nickels, 2011b; Lee et al., 2014; Kevin et al., 2019). They have been observed to extend upwards of  $20\delta$  in the streamwise direction (Hutchins and Marusic, 2007a) and typically do not surpass  $\sim 0.5\delta$  in height or width (Dennis and Nickels, 2011b). A key characteristic of the VLSMs is their meandering behaviour which masks their true length when not accounted for in measurements (Hutchins and Marusic, 2007a; Kevin et al., 2019). These motions are an attractive target for a control strategy because they carry a considerable amount of kinetic energy and shear stress (Balakumar and Adrian, 2007; Lee and Sung, 2011), are responsible for modulating the amplitude and frequency of near-wall fluid motions (Hutchins and Marusic, 2007b; Mathis et al., 2009; Ganapathisubramani et al., 2012), and are associated with extreme wall-shear events (Hutchins et al., 2011; Pan and Kwon, 2018). A visualization of a low-speed VLSM from the measurements of Dennis and Nickels (2011a) is shown in Figure 2.5. The coherent motion is surrounded by hairpin and partial hairpin vortices and can be seen to extend more than  $7\delta$  in the streamwise direction.

The coherent motions reviewed here include hairpin and partial hairpin vortices, ejections, sweeps, shear layers, and streaks. These motions are arranged in predictable patterns and exist across a large range of scales. Considering that the smallest and largest streaks are spaced in the spanwise direction by roughly  $100\lambda$  and  $\delta$ , respectively, it can be concluded via Equation (2.10) that the ratio of the largest to smallest streaks in a TBL vary by a factor of  $\sim Re_\tau/100$ . The near-wall streaks and VLSMs can therefore have sizes differing by several orders of magnitude in high-Reynolds-number TBLs – an observation that is commonly referred to as the *separation of*

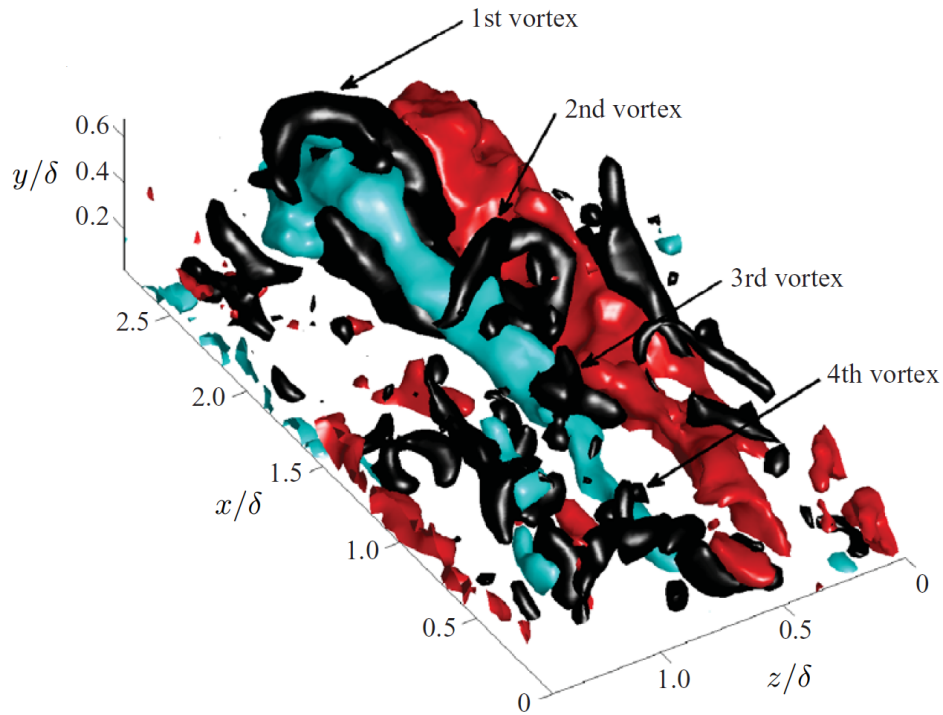


Figure 2.4: Instantaneous visualization of an LSM with the vortices of the associated hairpin packet labelled. The low-speed motions are shown with blue, the high-speed motions are shown with red, and the vortical motions are shown with black. Adapted from Dennis and Nickels (2011a) with permission from Cambridge University Press.

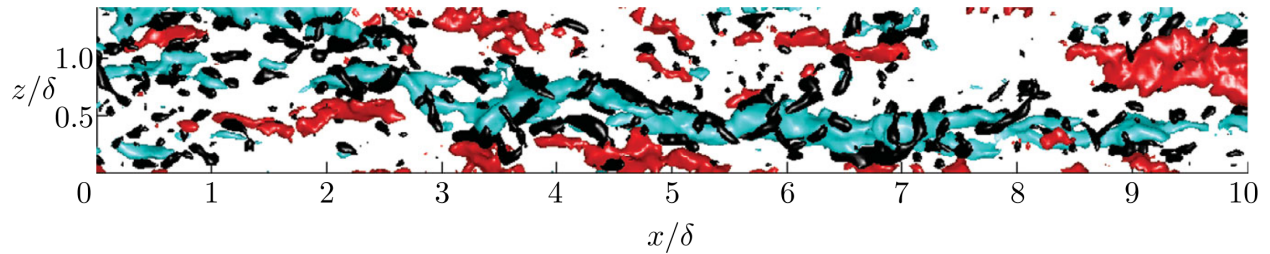


Figure 2.5: Instantaneous visualization of a low-speed VLSM (blue) and the associated vortical structures (black). Adapted from Dennis and Nickels (2011a) with permission from Cambridge University Press.

*scales*. Despite this, they are strikingly similar in form as is evident when comparing the near-wall streaks in Figure 2.3 to the VLSM in Figure 2.5. Scale separation by several orders of magnitude suggests that it is unlikely that the near-wall streaks simply grow into the VLSMs (Hutchins and Marusic, 2007a). However, the similarity between the near-wall streaks and VLSMs has prompted researchers to ponder whether the same process is responsible for producing and maintaining streaky motions at all scales within wall-bounded turbulence (Kevin et al., 2019). Whether this is true or not remains an unanswered question for the time being.

### 2.3.2 Velocity Statistics

The most commonly-discussed and well-understood velocity statistics for TBLs are the mean velocity profile and Reynolds stresses. Both are briefly covered here because they are used throughout the results chapters of this thesis. First considering the former, the *law of the wall* for the mean velocity profile leads to the relationships

$$\frac{\langle U \rangle}{U_\tau} = \begin{cases} y/\lambda & y/\lambda \lesssim 5, \\ (1/\kappa)\ln(y/\lambda) + C & y/\lambda \gtrsim 30, \end{cases} \quad (2.17)$$

where  $\kappa$  and  $C$  are constants. The region defined by  $y/\lambda \lesssim 5$  is referred to as the *viscous sublayer* while the region  $y/\lambda \gtrsim 30$  (up to a point) is referred to as the *logarithmic layer*. The intermediate region  $5 \lesssim y/\lambda \lesssim 30$  is referred to as the *buffer layer*. The values of the constants have been obtained from experiments and are typically found to be  $\kappa = 0.41$  and  $C = 5.0$  for smooth walls.

The relationships in Equation (2.17) have been shown to hold up well in experiments despite being formulated using simple scaling arguments. The mean velocity profiles of TBLs across a large range of Reynolds numbers are shown on semi-logarithmic axes in Figure 2.6, where both relationships are highlighted relative to collected data. Excellent overlap is observed between the data closer to the wall. However, this is not the case for the outer-most portion of each velocity profile as there is a point at which the profile deviates from the logarithmic law. The outer region characterized by a deviation from the logarithmic law is often referred to as the wake region (Coles, 1956). Upon closer inspection, it is clear that the start of the wake region, which is also the end of the logarithmic region, is dependent on the Reynolds number. More specifically, the logarithmic layer becomes increasingly extended at higher Reynolds numbers. As a result, the dynamics that characterize the logarithmic layer become more dominant as Reynolds number is increased.

The Reynolds stresses are shown for a simulated TBL in Figure 2.7. The streamwise normal Reynolds stress  $\langle u^2 \rangle$  features a distinct peak within the buffer layer. This peak can be attributed to the near-wall streaks and “bursting” (Robinson, 1991), which are of course directly tied to hairpin and partial hairpin vortices (Adrian, 2007). Following the near-wall peak,  $\langle u^2 \rangle$  tapers off gradually in the logarithmic layer before reducing steeply near the outer edge of the boundary layer. Different behaviour is observed for the wall-normal Reynolds stress  $\langle v^2 \rangle$  and spanwise Reynolds stress  $\langle w^2 \rangle$ , neither of which feature a distinct peak but instead appear to be hump-shaped. Similarly, the Reynolds shear stress  $\langle uv \rangle$  is also hump-shaped, but, in contrast, is always negative. These Reynolds

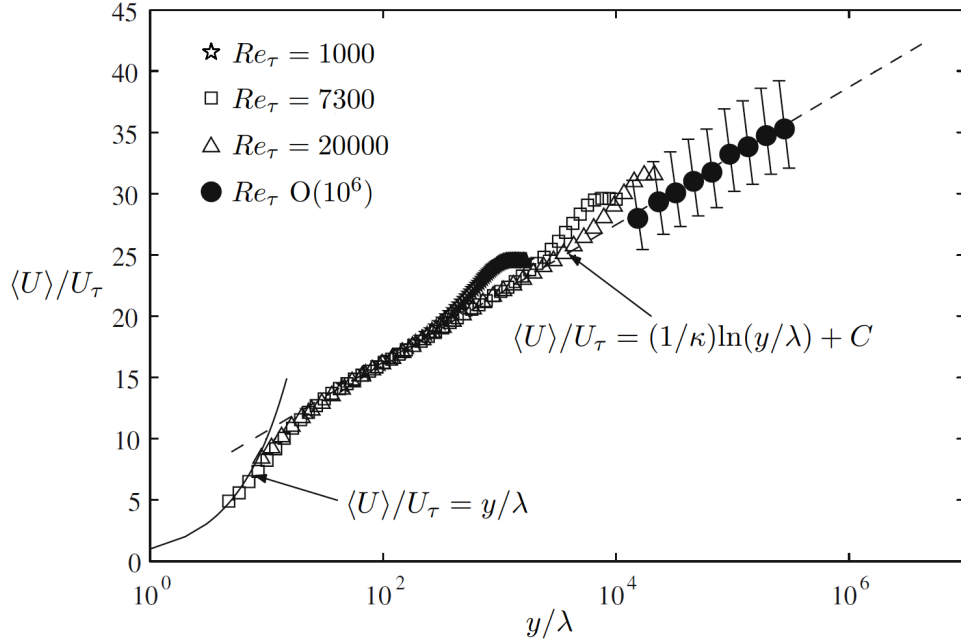


Figure 2.6: Mean velocity profiles of TBLs across a large range of Reynolds numbers. Adapted from Marusic and Hutchins (2008) with permission from Springer Nature.

stresses are generally representative of those observed in all TBLs, although there are differences as Reynolds number is increased. The scaling of the peak locations and peak values of the Reynolds stresses as a function of Reynolds number have been considered in detail by Buschmann et al. (2009).

The negative Reynolds shear stress observed in Figure 2.7 is an indication of the prevalence of ejection and sweeping motions within TBLs. These motions are related to the production of turbulence, which can be observed directly in the production term from the turbulent kinetic energy equation with the boundary layer approximation applied:

$$\mathcal{P} = -\langle uv \rangle \frac{\partial \langle U \rangle}{\partial y}. \quad (2.18)$$

Although the peak Reynolds shear stress occurs in the logarithmic layer, the steep velocity gradient near the wall results in the peak turbulence production occurring within the buffer layer. Despite this, the total contribution of turbulence production becomes dominated by the logarithmic layer as Reynolds number is increased (Smits et al., 2011). This is a direct result of the emergence of VLSMs within the flow as Reynolds number is increased and is a key reason why the VLSMs are considered attractive for targeted control.

The influence of the VLSMs on the streamwise Reynolds stress is clear when viewing  $\langle u^2 \rangle$  over increasing Reynolds numbers. Such data are presented in Figure 2.8, which contains results from laboratory-scale TBLs all the way up to atmospheric flows. The buffer-layer peaks align when

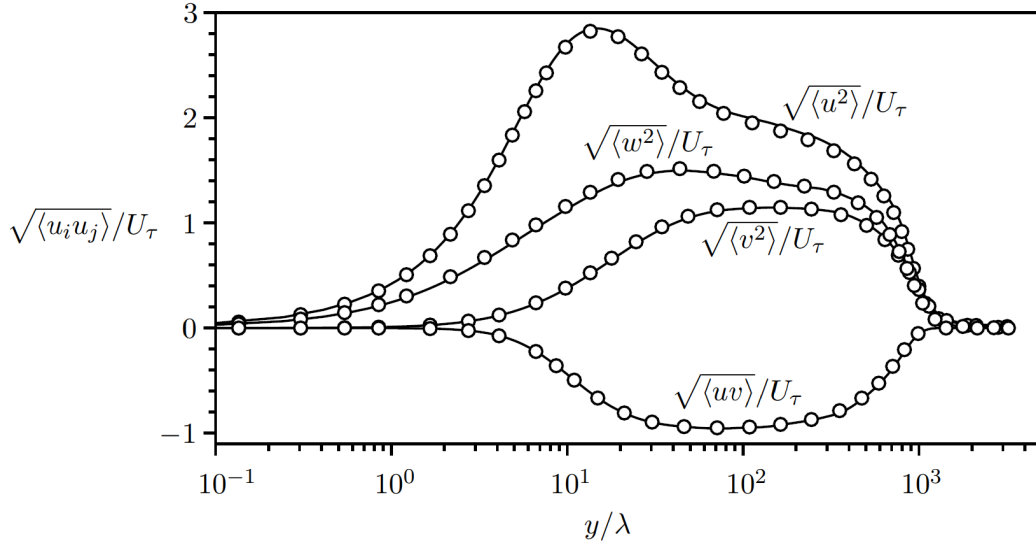


Figure 2.7: Square root of the Reynolds stresses from a direct numerical simulation of a TBL at  $Re_\theta = 3000$ . Adapted from Hwang and Sung (2017) with permission from Cambridge University Press.

the horizontal axis is plotted as  $y/\lambda$ . However, the height of the peaks increase with Reynolds number despite  $\langle u^2 \rangle$  being normalized by  $U_\tau$ . This indicates that the peak is not only a function of the inner scales. In fact, the amplitude modulation caused by the VLSMs is responsible for increasing the intensity of the near-wall motions (Hutchins and Marusic, 2007b; Mathis et al., 2009; Ganapathisubramani et al., 2012), thus leading to larger  $\langle u^2 \rangle$  in the buffer layer. The increasing strength and influence of the VLSMs with increasing Reynolds number is therefore visible in both the heightening of the near-wall peak and also the increase of  $\langle u^2 \rangle$  in the logarithmic layer where the VLSMs exist. As demonstrated in Figure 2.8, the portions of the  $\langle u^2 \rangle$  curves beyond the buffer layer collapse when the horizontal axis is plotted as  $y/\delta$ , indicating an outer-layer scaling for the VLSMs. Since the VLSMs scale with outer-layer variables while strongly influencing the near-wall motions, it is evident that a complicated interaction exists across the scales within TBLs. This behaviour is also evident in the pre-multiplied spectra of  $u$ , which capture the total contribution of various wavelengths to  $\langle u^2 \rangle$  as a function of wall-normal location (Hutchins and Marusic, 2007a).

### 2.3.3 Wall-Pressure Fluctuations

Experimental limitations have made it difficult to study the wall-pressure fluctuations beneath TBLs in the past. The low-frequency range of pressure fluctuations is often corrupted by the background noise in experimental facilities (Willmarth, 1975; Bull, 1996; Tsuji et al., 2012) or limited by the frequency response of the measurement device, while the high-frequency range can be spatially filtered when pressure transducer dimensions are too large with respect to the lengthscale of the smallest pressure fluctuations (Schewe, 1983; Lueptow, 1995; Gravante et al., 1998). Additionally, any pinhole-type measurement device will introduce some finite error (Shaw, 1960) and also act as

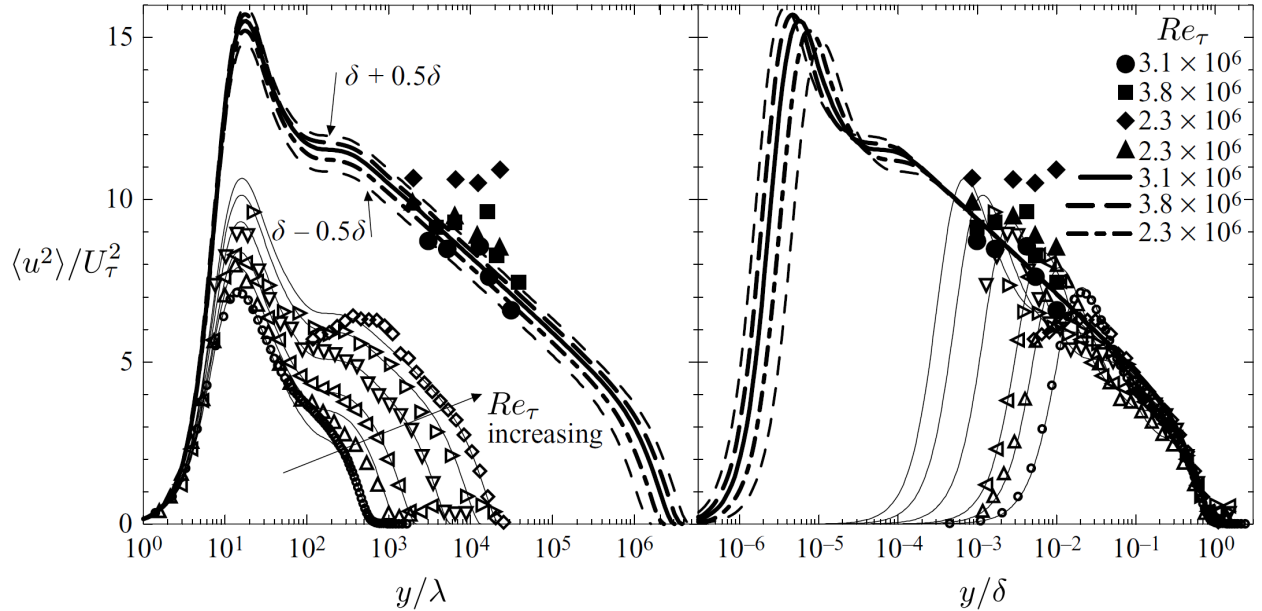


Figure 2.8: Streamwise Reynolds stress within TBLs across a range of Reynolds numbers compared using inner (left) and outer (right) scaling for the wall-normal distance. The open symbols represent data from laboratory-scale flows at  $Re_\tau = 700$  to 23000. The closed symbols represent data from atmospheric flows. Adapted from Kunkel and Marusic (2006) with permission from Cambridge University Press.

a Helmholtz resonator (Tsuji et al., 2007), which has the potential to distort measurements. The above are why the first few decades of research on the wall pressure beneath a TBL did not reach final conclusions regarding even simple single-point statistics (Bull, 1996). It is important to keep these difficulties in mind when discussing the relationship between wall pressure and the largest motions in the TBL. The size of these motions should place some portion of their influence in the low-frequency range, which is one of the extremes that is difficult to reliably measure and therefore often filtered out of measurements entirely.

A significant portion of past investigations into the wall pressure beneath a TBL focused on single-point statistics and pressure-pressure correlations (Willmarth and Wooldridge, 1962; Corcos, 1964; Bull, 1967; Panton et al., 1980; McGrath and Simpson, 1987; Farabee and Casarella, 1991; Keith et al., 1992; Tsuji et al., 2007; Klewicki et al., 2008; Palumbo, 2012). The picture that emerges from these studies is as follows. There are two distinct groups of wall-pressure fluctuations, one containing the low and mid frequencies and one containing the high frequencies of the wall-pressure power spectrum. The low and mid frequencies scale with outer variables, and the associated fluctuations have been found to advect faster, decay slower, and have a larger spanwise extent than those in the high-frequency group. These characteristics suggest that the low- and mid-frequency fluctuations are associated with larger pressure-producing motions in the outer portion of the flow. In contrast, the high-frequency group of fluctuations scale with inner variables. The motions that produce these fluctuations are likely associated with turbulence production near the

wall and the smaller structures resulting from the breakdown of larger ones. The high-frequency pressure fluctuations travel a distance proportional to their wavelength before decaying completely. This behaviour is not observed for the lowest frequencies, which appear to decay independent of their wavelength. The wall-pressure spectrum also features a region that scales with a mix between inner and outer variables, indicating that the frequencies in this region are a result of the interaction between the inner and outer scales of the flow. This region falls between the mid and high frequencies and is referred to as the “overlap” or “universal” region of the wall-pressure power spectrum.

The general characteristics of the wall-pressure power spectrum have been summarized by Hwang et al. (2009) and are shown in Figure 2.9 as a function of the angular frequency  $\omega = 2\pi f$ . The four regions of the spectrum are highlighted: the low-frequency, mid-frequency, overlap, and high-frequency regions. The spectrum climbs in magnitude from the low-frequency region until a peak is reached in the mid-frequency region. The spectrum then declines in magnitude as it passes through two segments of constant proportionality: one in the overlap region and one in the high-frequency region. The constant decay in the high-frequency region has been observed in the past to be approximately  $\omega^{-5}$  to  $\omega^{-6}$  (McGrath and Simpson, 1987; Goody, 2004; Palumbo, 2012; Van Blitterswyk and Rocha, 2017) while the decay in the overlap region is typically closer to  $\omega^{-0.7}$  (McGrath and Simpson, 1987; Goody, 2004; Tsuji et al., 2007; Van Blitterswyk and Rocha, 2017). The behaviour of the low-frequency region is not well-established at the moment. Some attempts at modelling the wall-pressure spectrum suggest that the low-frequency region should vary with  $\omega^2$  as discussed by Panton et al. (1980) and Bull (1996), while another model predicts a  $\omega^{1.1}$  to  $\omega^{1.5}$  proportionality (Panton and Linebarger, 1974). There is currently some experimental evidence to support the former (Farabee and Casarella, 1991; Palumbo, 2012), but reliable low-frequency data are difficult to obtain owing to background noise contamination and frequency response limitations of the available pressure transducers.

Integrating the power spectrum and taking the square root produces the root-mean-square wall pressure  $p_{\text{rms}}$ . This quantity is important for engineering design, experimental validation, modelling, etc. An empirical relation for  $p_{\text{rms}}$  has been derived by Farabee and Casarella (1991):

$$\left(\frac{p_{\text{rms}}}{\rho U_\tau^2}\right)^2 = 6.5 + 1.86 \ln\left(\frac{Re_\tau}{333}\right), \quad (2.19)$$

which is valid for  $Re_\tau > 333$ . This relation has been found to agree well with direct numerical simulations and experiments for  $Re_\tau$  up to roughly 20000 (Tsuji et al., 2007, 2012). Equation (2.19) is used in Chapter 5 to validate the present wall-pressure measurements.

Identifying the coherent motions responsible for the wall-pressure fluctuations has mainly been pursued using pressure-velocity correlations and conditional averaging. These techniques were used early on to show that the near-wall “bursting” was associated with a distinct wall-pressure pattern (Kim, 1983; Thomas and Bull, 1983; Kobashi and Ichijo, 1986). The pattern consists of a large wall pressure maximum with smaller pressure minimums on its upstream and downstream sides. Kim

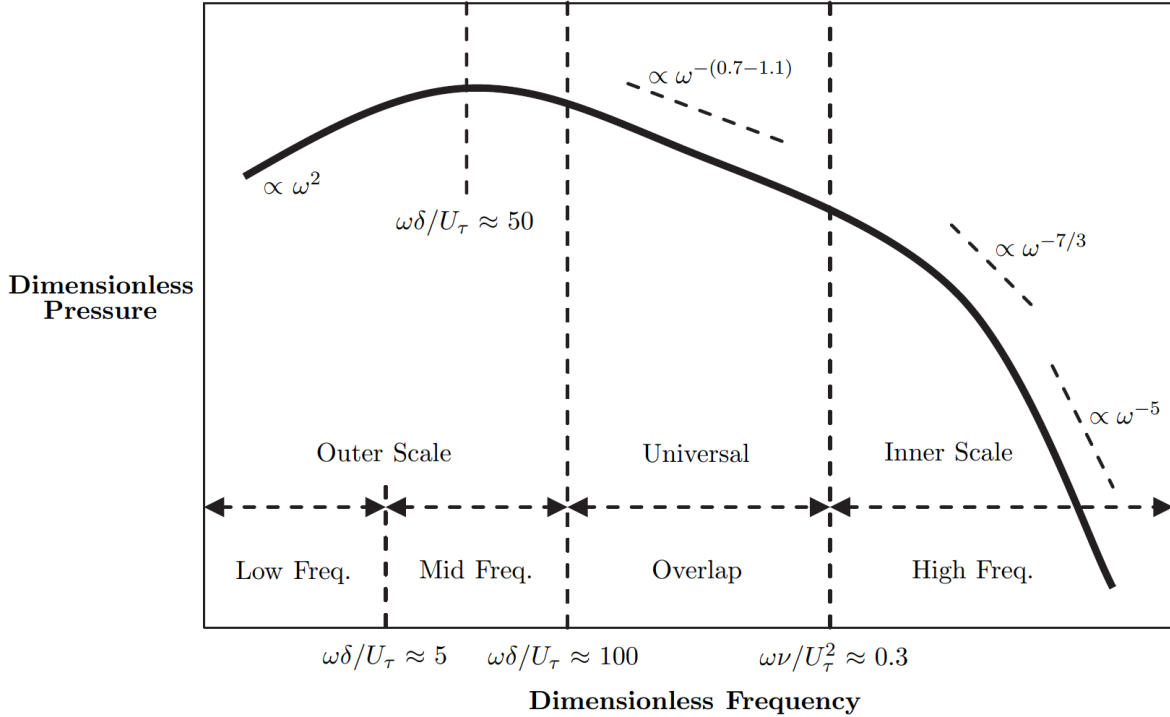


Figure 2.9: General characteristics of the wall-pressure spectrum beneath a TBL. Adapted from Hwang et al. (2009) with permission from Elsevier.

(1983) and Kobashi and Ichijo (1986) explicitly associated the bursting cycle, and therefore the convecting pattern, with inclined streamwise vortex pairs, while Thomas and Bull (1983) connected the cycle to the passage of a shear layer that forms on the upstream side of a hairpin structure. It is now known that the bursting cycle is a series of ejections and sweeps formed by hairpin packets (Adrian, 2007), which indeed feature both inclined vortex pairs and shear layer structures. Many of the studies that followed focused on the high-amplitude pressure peaks (HAPPs) at the wall, which can be positive or negative (Johansson et al., 1987; Karangelen et al., 1993; Kim et al., 2002; Ghaemi and Scarano, 2013). A HAPP is defined as  $|p| \geq kp_{\text{rms}}$  where  $k$  is typically 2 to 3. Karangelen et al. (1993) found that the HAPPs associated with  $k = 3$  are present only 5% of the time, yet they are responsible for 49% of  $p_{\text{rms}}$ , indicating that the motions associated with the HAPPs are quite important for understanding the fluctuating wall pressure. Ghaemi and Scarano (2013) measured the time-resolved, three-dimensional pressure field near the wall beneath a TBL using tomographic particle image velocimetry by integrating the Poisson pressure equation. Their results, considered along with those of the past investigators, reveal that negative HAPPs are caused by the low-pressure cores of quasi-streamwise vortices and hairpin heads, while the positive HAPPs are caused by the stagnation of shear layers formed when sweeps occur upstream from ejection events caused by hairpin or partial hairpin vortices. Considering these results along with those of Kim (1983), Thomas and Bull (1983), and Kobashi and Ichijo (1986), it is clear that hairpin

vortices are a significant source of wall-pressure fluctuations. The HAPPs caused by these hairpins are clearly visible in the wall-pressure probability density shown in Figure 2.10, the long tails of which deviate significantly from Gaussian behaviour to indicate large wall-pressure values.

Relatively few studies to date have been able to provide a detailed description of the fluid motions associated with the wall-pressure fluctuations at the lowest frequencies of the spectrum. The earlier work of Panton et al. (1980) and Farabee and Casarella (1991) associated the low-frequency fluctuations with relatively passive motions in the outer layer, but these studies were carried out prior to knowledge of the VLSMs, which have only been a focus for the last two decades. The more recent study of Beresh et al. (2013) employed Taylor’s hypothesis along with an array of pressure sensors to study the wall-pressure footprint beneath a supersonic TBL at Mach 2. Note that VLSMs have been observed in a Mach 2 TBL in past experiments at a similar Reynolds number (Elsinga et al., 2010). Beresh et al. (2013) found that highly elongated, meandering regions of positive and negative fluctuation were visible in their lowpass-filtered visualizations of the wall-pressure footprint. However, a regular alternation between positive and negative fluctuation in the spanwise direction was not observed as would be expected of the VLSMs. They also found that these highly elongated pressure footprints were much lower in magnitude than the fluctuations with higher frequencies, suggesting that any wall-pressure footprints caused by the VLSMs may be quite weak. It therefore may be the case that the expected alternation was not observed due to issues with transducer sensitivity. Similarly, Buchmann et al. (2016) investigated the relationship between velocity and wall pressure beneath a transonic TBL at Mach 0.5–0.8 ( $Re_\tau = 5100$  to  $9500$ ). They computed the space-time pressure-velocity correlations shown in Figure 2.11, revealing that positive wall-pressure fluctuations are negatively correlated with streamwise velocity in a wall-attached region extending roughly  $4\text{--}5\delta$  downstream from the wall-pressure sensor. This is larger than the minimum length defined for the VLSMs (Balakumar and Adrian, 2007) and also falls just short of the length of the VLSMs inferred from statistics (Hutchins and Marusic, 2007a; Lee and Sung, 2011). Such a large streamwise extension of the correlation is not observed for the negative wall-pressure fluctuations. Buchmann et al. (2016) concluded that the elongation of these correlations provides evidence that large-scale structures play an important role in determining the near-wall pressure field.

The most thorough investigation into the relationship between wall pressure and the largest motions in a TBL was performed by Naka et al. (2015), this time in the incompressible regime ( $Re_\tau = 2465$  to  $6390$ ). These authors extensively investigated the coupling between velocity and wall pressure as well as between velocity and field pressure throughout the height of the boundary layer. In agreement with the results of Buchmann et al. (2016), the space-time pressure-velocity correlations of Naka et al. (2015) revealed that streamwise velocity is negatively correlated with positive wall-pressure fluctuation in a highly elongated, wall-attached region downstream from the pressure measurement location. Once again, such an elongated correlation was not observed for negative wall-pressure fluctuations. Naka et al. (2015) concluded that this elongated correlation may be related to the VLSMs, but their primary conclusions focused on other features of the correlations

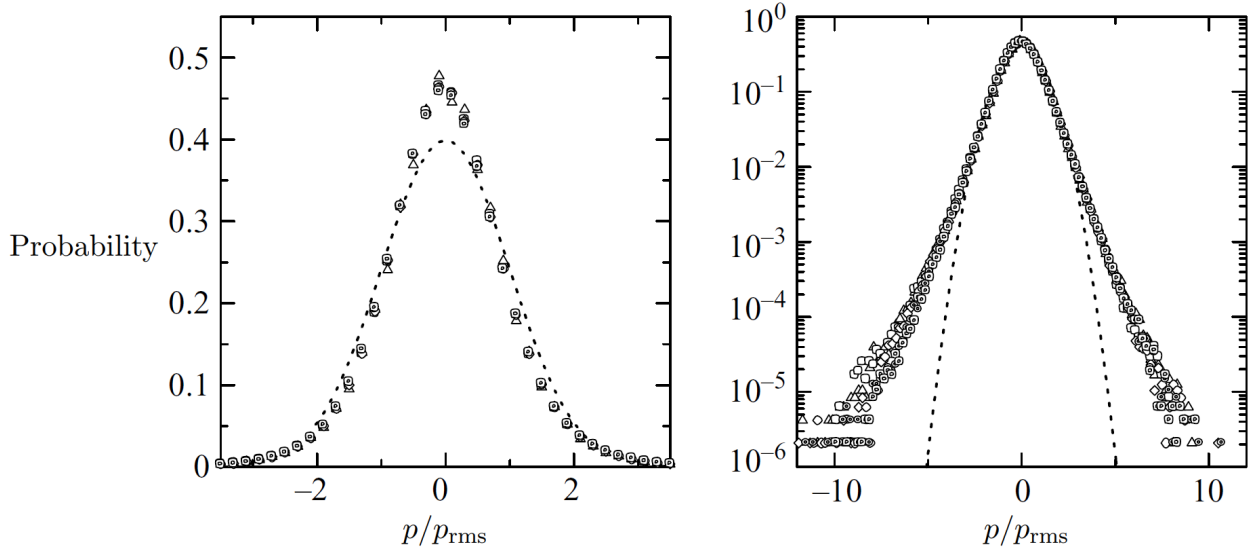


Figure 2.10: Probability density of wall pressure beneath a TBL shown on linear and logarithmic axes for  $Re_\theta = 5900$  to 16700. Adapted from Tsuji et al. (2007) with permission from Cambridge University Press.

which were much stronger. More specifically, they found that wall-pressure fluctuations occur at the edges of large ( $O(\delta)$ ) organized motions with strong wall-normal velocity components. Positive wall-pressure fluctuations were found to be associated with the leading edge of a strong sweeping motion of the splatting type. Here, “splatting” refers to a downward motion that impacts the wall and spreads out. Downstream from this sweep exists a region of positive streamwise and wall-normal velocity, which is a first-quadrant event (in the  $u$ - $v$  plane) and therefore does not fit the description of a sweep or an ejection. Conversely, negative wall-pressure fluctuations were found to be associated with a localized ejection occurring upstream from the pressure measurement location while another strong sweeping motion occurred downstream. The sweeping motions associated with both positive and negative wall-pressure fluctuations were accompanied by quasi-streamwise vortical motions. Naka et al. (2015) suggested by comparison with the results of Ghaemi and Scarano (2013) that these patterns could be related to large hairpins. However, counter-rotating quasi-streamwise vortex pairs that act to induce a sweep between them, which are present in their results for both positive and negative wall-pressure fluctuations, are not consistent with this notion. Interestingly, Naka et al. (2015) also found that field pressure, even very close to the wall, could clearly be linked to the VLSMs, while the wall pressure could not. It is not clear how the VLSMs could influence the pressure field of the whole boundary layer thickness without affecting wall pressure.

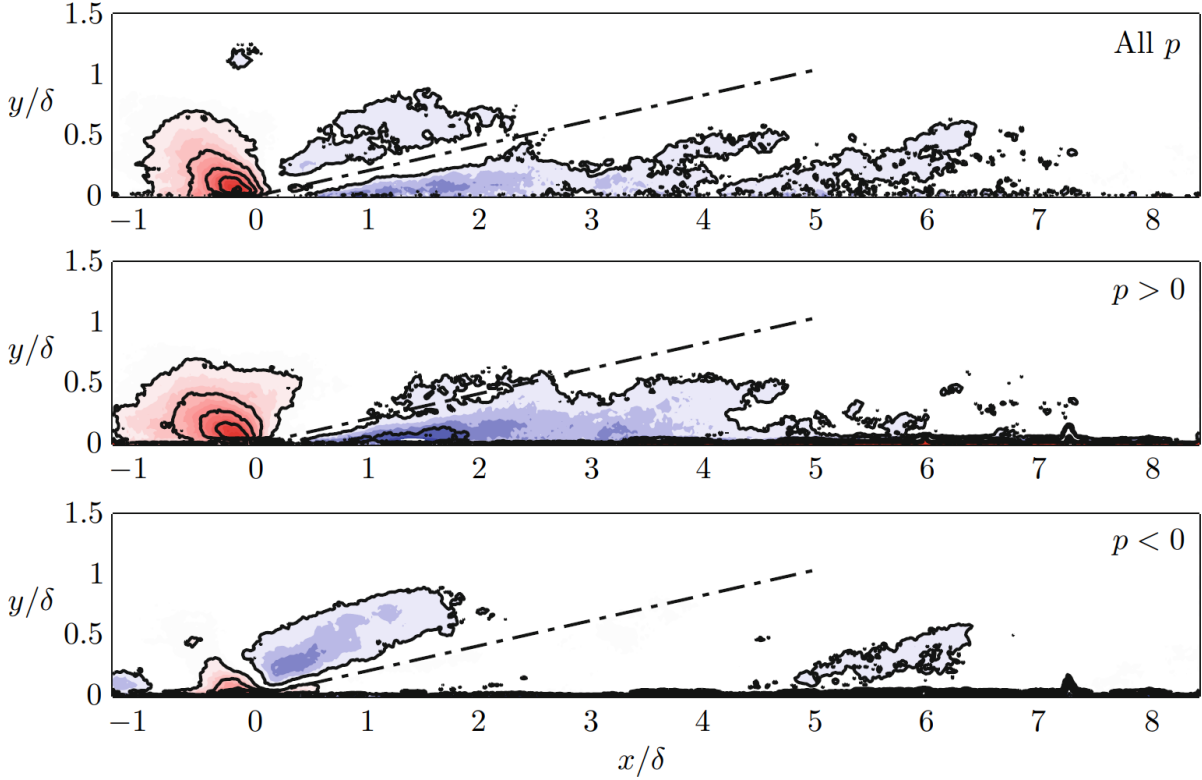


Figure 2.11: Correlations between wall pressure and velocity in a TBL at  $Re_\tau = 5100$  and  $Ma = 0.5$ . Adapted from Buchmann et al. (2016) with permission from Springer Nature.

## 2.4 Control

The body of literature regarding the control of TBLs is far too large to review here. This section will therefore focus on the two subtopics that are directly relevant to the present work: i) actuation with moving surfaces and ii) the targeting of VLSMs with active control strategies.

### 2.4.1 Moving-Surface Actuators

A wide range of moving surface actuation strategies have been investigated in the past. To simplify the discussion moving forward, these strategies can be considered in three primary groups depending on whether they utilize wall-normal surface motion, in-plane surface motion, or dynamic elements. Wall-normal and in-plane motion include techniques that utilize relatively smooth and continuous surface deformations or movements in their respective directions to interact with the flow. In contrast, dynamic elements are moving-surface actuators with discontinuous geometries, e.g., featuring gaps, steps, or abrupt protrusions at the wall. These include flush-mounted piezoelectric cantilevers (Jacobson and Reynolds, 1998; Jeon and Blackwelder, 2000; Kim et al., 2013; Bai et al., 2014; Qiao et al., 2017, 2018; Tang et al., 2019, 2021; Tang and Jiang, 2020), active vortex generators (Osborn et al., 2004; Seshagiri et al., 2009; Barth et al., 2011; Le Pape et al., 2012; Joubert et al., 2013), and some forms of dynamic roughness (Segawa et al., 2002; Jacobi and McKeon, 2011, 2017; Duvvuri

and McKeon, 2017; Gildersleeve et al., 2017; McKeon et al., 2018; Amitay and Gildersleeve, 2019; Huynh and McKeon, 2020a,b; Tang et al., 2020; Huynh et al., 2021). The former two actuator types are distinctly different from dynamic roughness because their primary effect is to form relatively organized streamwise vortices, with piezoelectric cantilevers achieving this via a mechanism similar to that of a synthetic jet (Jacobson and Reynolds, 1998; Kim et al., 2013).

Dynamic roughness interacts with the flow by introducing roughness perturbations with some form of temporal oscillation. There are two clear drawbacks associated with this type of forcing. First, the roughness has the potential to significantly increase drag locally, and so a successful control strategy will have to overcome not only the energy loss of operating the actuator, but also the energy loss associated with this excess drag. Second, the forcing is asymmetric because an effect opposite to what is produced by the roughness cannot be achieved by the actuator. In contrast, piezoelectric cantilevers and active vortex generators are more promising for many flow control applications because the resulting streamwise vortices are more useful for targeting coherent motions. These vortices can be considered a form of symmetric forcing because each streamwise vortex will induce a high- and low-speed streak at the wall. Leveraging this effect using a staggered arrangement of actuators can allow for producing both positive and negative velocity fluctuations at a target location. Despite this, both of these actuator types still feature discontinuous geometry and therefore they also must overcome excess drag. Although there are drawbacks associated with dynamic elements, they remain suitable for some applications. For example, they can be used to study how a given flow reacts to dynamic perturbations (Jacobi and McKeon, 2011, 2017; Bai et al., 2014; Duvvuri and McKeon, 2017; Tang et al., 2019, 2021; Tang and Jiang, 2020). Additionally, promising results have been achieved in the realm of separation control (Osborn et al., 2004; Le Pape et al., 2012; Joubert et al., 2013; Amitay and Gildersleeve, 2019), and piezoelectric cantilevers in particular have been employed successfully in feedback and feedforward control schemes (Jacobson and Reynolds, 1998; Qiao et al., 2017, 2018).

In-plane surface motion introduces wall-parallel fluid velocity near the surface as a result of viscous effects and the no-slip boundary condition. This technique appears to overcome the main issues associated with dynamic elements. It does not introduce any roughness at the surface, and it can be considered symmetric forcing since the surface can in theory be moved or deformed in both the positive and negative streamwise or spanwise directions. The recent review of Ricco et al. (2021) provides a near-exhaustive summary of turbulent drag reduction achieved using near-wall traverse forcing – a category that includes in-plane surface motion in the spanwise direction. This work shows that drag reductions of up to around 50% have been reported in both experimental and numerical studies of wall-bounded flows employing open-loop spanwise surface motion of various forms. The most effective form appears to be streamwise traveling waves of spanwise surface motion as depicted schematically in Figure 2.12. This type of open-loop surface motion has been the dominant form of in-plane surface motion studied in the past. Some investigations have considered streamwise surface motion (Choi et al., 1994; Hamelin and Alving, 1996; Menu and Tavoularis, 2007; Józsa et al., 2019, 2020) or rotating disks (Klewicki and Hill, 2003; Ricco and Hahn, 2013; Wise et al.,

2014; Wise and Ricco, 2014), but far less attention has been dedicated to these concepts and their implementation has been mostly numerical.

In-plane surface motion is clearly a promising actuation strategy for turbulent drag reduction applications, but there are some limitations to discuss. First, this actuation technique relies on the continuous motion of the surface. That is, a “move-and-hold” strategy is not an option like it is for other actuators such as dynamic roughness and active vortex generators, both of which can continue to influence the flow when operated statically. Second, implementing a surface that is capable of these types of motions is not straightforward in practice, especially when considering that streamwise travelling waves of spanwise surface motion seem to be the most promising strategy for drag reduction. Experimental investigations of in-plane surface motion have typically resorted to oscillating a flat plate (Laadhari et al., 1994; Choi and Clayton, 2001; Choi, 2002; Di Cicca et al., 2002; Iuso et al., 2003; Ricco, 2004; Kempaiah et al., 2020) or utilizing a flush-mounted belt system (Hamelin and Alving, 1996; Kiesow and Plesniak, 2003; Menu and Tavoularis, 2007). These strategies allow for uniform surface motion, but they do not allow for the generation of travelling waves. To obtain a travelling wave motion, some researchers have segmented the surface into thin elements that can be oscillated independent of those that are adjacent (Auteri et al., 2010; Marusic et al., 2021). Others have explored the development of flexible surfaces that can be continuously deformed using electromagnetic actuation and electroactive polymers (Gouder et al., 2013) or actuated lattice structures (Bird et al., 2018). These studies represent steps in the right direction, as it appears that much of the remaining work in this particular area is a question of how to engineer a surface capable of producing the required surface motions.

Wall-normal surface motion, which is one focus of the present thesis, can be applied at many different scales. At the small scale the surface can be actively deformed to produce dimples, pimples, or ridges to yield local actuation or another type of dynamic roughness (Arthur et al., 2006; Huebsch, 2006; Dearing et al., 2007, 2010; Huebsch et al., 2012; DeMauro et al., 2015; Ge et al., 2017). At the large scale, a major segment of the surface of a fluidic device can be actively deformed to produce morphing geometry (Munday and Jacob, 2002; Thill et al., 2008; Jones et al., 2018; Garland et al., 2019). It is also possible to use open-loop surface waves to modify the mean characteristics of wall-bounded flows (Mito and Kasagi, 1998; Itoh et al., 2006; Klumpp et al., 2010, 2011; Tamano and Itoh, 2012; Koh et al., 2015; Roggenkamp et al., 2015, 2019; Meysonnat et al., 2016; Albers et al., 2019, 2020; Fernex et al., 2020; Li et al., 2020). This strategy is similar to the in-plane surface waves discussed previously, but the drag reductions obtained by wall-normal surface waves have not been as large as those achieved by their in-plane counterpart (Ricco et al., 2021).

The present work does not consider dynamic roughness, morphing geometry, or surface waves. Instead, the goal is to determine whether it is feasible to target coherent motions within the flow using active wall-normal surface deformations applied locally. It should be stated that this actuation strategy is not without its drawbacks. For example, wall-normal actuation is also likely to increase drag locally. However, the strategy has not received much attention in the past and therefore its

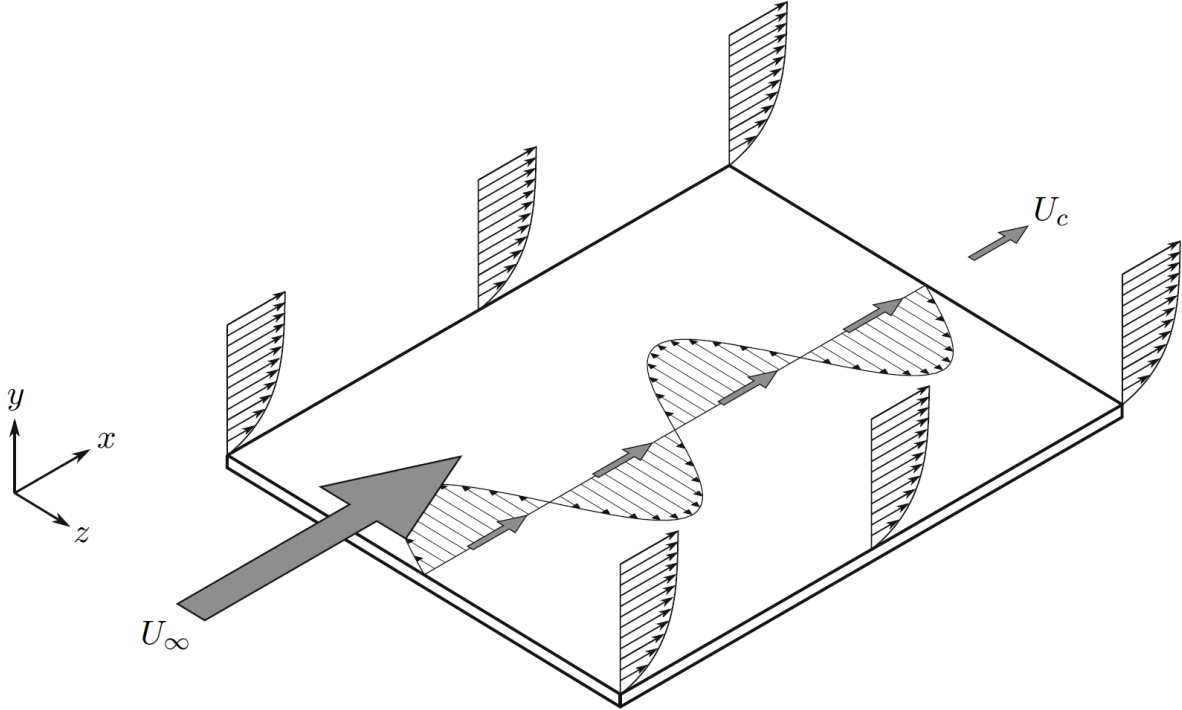


Figure 2.12: Schematic representation of a streamwise traveling wave of spanwise surface motion where  $U_c$  is the advection velocity of the wave. Adapted from Bird et al. (2018) under CC BY 4.0.

potential for flow control is unknown. The few studies that have considered such a strategy are discussed next.

In perhaps the earliest investigation of active surface deformations, Breuer et al. (1989) showed that wall-normal surface motion could produce both high- and low-speed streamwise velocity fluctuations in an LBL. Impulse-like disturbances were generated using a pressure-driven rectangular membrane and their evolution was monitored. The authors then showed that a different type of wall-normal motion, a “travelling bump”, could be used to interact with the disturbance to delay its growth to farther downstream. Later on, Hofmann and Herbert (1997) used direct numerical simulations to show that oscillating membranes of varying shapes could be used to generate disturbances in an LBL that match those that occur naturally. This work confirmed that wall-normal motion can produce both high- and low-speed streamwise velocity fluctuations in a wall-bounded flow. It also revealed that the delay of disturbance growth demonstrated by Breuer et al. (1989) could likely be improved by optimizing the shape of the wall-normal surface motion. The delay of disturbance growth using wall-normal surface motions has more recently been demonstrated by both Goldin et al. (2013) and Amitay et al. (2016).

One of the motivating studies for the present work was that of Carlson and Lumley (1996) as was discussed in Chapter 1. Their simulations showed that an outward Gaussian deformation could be used to push streaky structures away from the surface, resulting in the expansion of the opposite-signed streaks that are adjacent to the one being targeted by the deformation. They found that

the expansion of these adjacent streaks can lead to both decreases and increases in drag depending on their sign of fluctuation, thus highlighting a possible mechanism for flow control. Shortly after, Kim et al. (2003) considered periodic actuation of a circular membrane that produced wall-normal surface deformations beneath a TBL. They measured the resulting phase-averaged velocity field and found that the device produces a series of high- and low-speed regions that form above the actuator and advect downstream. They found that the upward motion of the actuator produces the low-speed regions, while the downward motion produces the high-speed regions. Kim et al. (2003) also found that their wall-normal deformations produced streamwise vortices under certain conditions, which is similar to the result obtained by Dearing et al. (2007) using active dimples in an LBL. Both Kim et al. (2003) and Dearing et al. (2007) employed circular surface deformations at a constant amplitude of 0.1 times the actuator diameter. However, the frequencies considered by Dearing et al. (2007) were 1-2 orders of magnitude higher than those considered by Kim et al. (2003) if the frequency is normalized using the actuator diameter and freestream velocity. The results from these two studies suggest that higher frequencies are more likely to produce streamwise vortices, although it is probable that the amplitude and geometry of the deformation also play significant roles.

A collection of numerical studies have investigated controlling wall-bounded turbulence using wall-normal surface deformations that react to local variables. The investigations of Endo et al. (2000) and Kang and Choi (2000) considered control schemes that allowed for each element of the surface to deform independently. Both investigations achieved drag reduction, but the resulting surface deformations were highly complex as is shown in Figure 2.13 and are therefore impractical for application in physical systems. This is why Endo et al. (2000) extended their analysis to consider a more realistic array of active surface deformations that were elongated in the streamwise direction and responded to information from upstream shear sensors. This strategy was designed to act on the near-wall streaks and vortices and could achieve a net positive energy savings. Pamiès et al. (2011) also considered an array of active surface deformations that were somewhat elongated in the streamwise direction. The deformations were actuated according to opposition control such that the surface velocity was used to oppose the wall-normal velocity above. However, this strategy was not as successful at producing drag reduction, suggesting that the details of such a strategy are important to its success. Similarly, Zhang et al. (2016) and Ge et al. (2017) considered control strategies involving active surface deformations with pimple and dimple geometries that reacted to local variables. Some weaker drag reduction was reported, but overall these strategies appear to be less effective than that of Endo et al. (2000).

The reactive nature of the control strategies discussed above make it difficult to systematically study the effects of actuation as a function of actuator inputs such as the frequency (velocity), amplitude, and geometry of the deformations. The effects of these parameters are more appropriately studied using periodic surface deformations with simple geometries. However, this type of study has not been common, and, as a result, the literature lacks the information necessary for designing a suitable surface deformation for targeting a given flow feature in a control application.

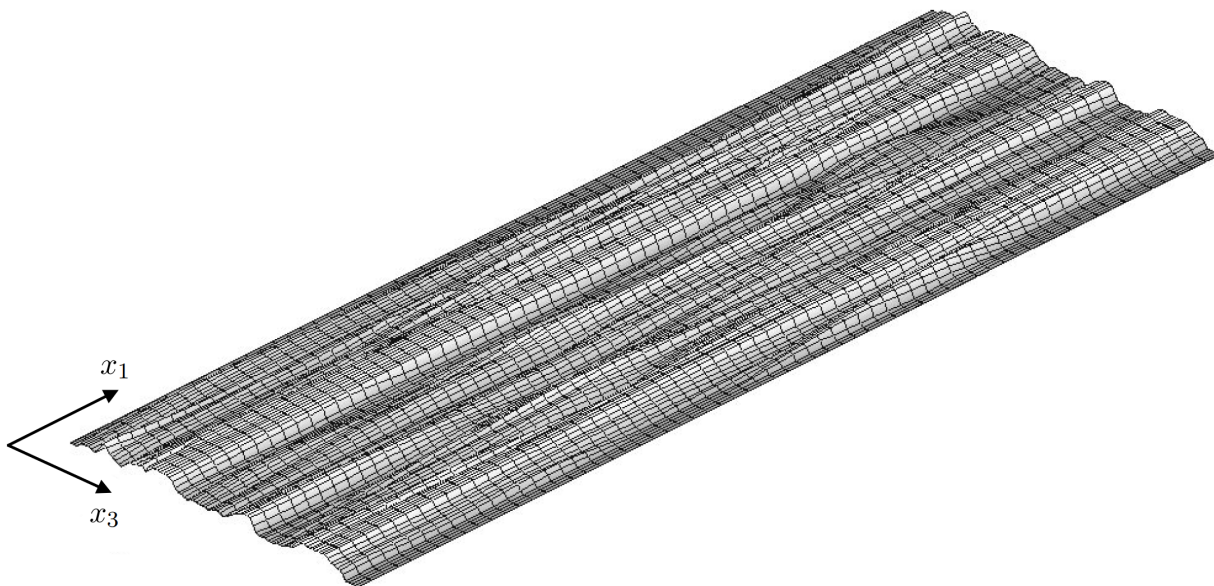


Figure 2.13: Wall-normal surface deformations resulting from a reactive control scheme that allows each surface element to deform independently. Adapted from Kang and Choi (2000) with permission from AIP Publishing.

### 2.4.2 Targeting Very-Large-Scale Motions

Only a few studies to date have sought to target VLSMs with an active control strategy. This is partly because they are a relatively new discovery within the wall-bounded turbulence community, but also because they are a high-Reynolds-number phenomenon and therefore are more difficult to produce within experiments and simulations. The first explicit attempt at targeting VLSMs with active control appears to be the experiments of Abbassi et al. (2017). The VLSMs within a boundary layer were identified in real time using their wall-shear footprints, and wall-normal jets were actuated to either oppose or reinforce the wall-normal components of the high- and low-speed VLSMs, respectively. The strategy allowed for both decreasing and increasing the streamwise turbulence intensity associated with the VLSMs and could produce a drag reduction of a few percent. A different approach was demonstrated by the experiments of Marusic et al. (2021), who used a streamwise traveling wave of spanwise surface motion to target the VLSMs within a boundary layer. This type of actuation has proved effective for drag reduction when used to target the near-wall motions, but its efficacy and practicality diminish with increasing Reynolds number (Ricco et al., 2021). Marusic et al. (2021) showed that it remains a viable drag reduction strategy at high Reynolds numbers if the parameters of the surface motion are set to target the VLSMs instead of the near-wall motions. In contrast to these experimental studies, Oehler and Illingworth (2021) applied linear control to target VLSMs in a channel flow simulated using the linearized Navier-Stokes equations. Their work suggests that actuator and sensor arrays each in a single plane (i.e., realistic hardware arrangements) are sufficient for targeting the VLSMs using linear control schemes. This result is promising because it indicates that the VLSMs might be amenable

to the tools of modern control theory, although it must be kept in mind that a linearized set of governing equations was employed in their investigation. Finally, Jacobi and McKeon (2017) used dynamic roughness to generate synthetic VLSMs for the purpose of exploring the phase relationships between the very-large and small scales. While they did not implement a targeted control scheme, it is possible that such synthetic VLSMs could be used to target the naturally-occurring VLSMs or even offset their influence on the flow.

As it stands, only Abbassi et al. (2017) and Marusic et al. (2021) have been able to target the VLSMs in experimental applications of flow control. Moreover, only the works of Abbassi et al. (2017) and Oehler and Illingworth (2021) are consistent with the targeted control concept discussed by Gad-el-Hak et al. (1998), which requires identifying and altering a specific coherent motion in real time with the goal of producing a more desirable TBL state. Identifying and altering the VLSMs in real time would of course require the ability to both sense and actuate the VLSMs, and these abilities are developed in the present work.

## Chapter 3

# Experimental Methods

This chapter presents an overview of the experimental methods that apply generally to the experiments conducted here. The following are covered: the experimental facility, generation of boundary layers, velocity measurement technique, and real-time system used to generate and acquire various signals. The specific details of the experiments associated with each results chapter are discussed within those chapters.

### 3.1 Wind Tunnel Facility

The work documented within this thesis required a facility capable of generating the boundary layer flows of interest. The large two-story wind tunnel within the Mechanical Engineering Building at the University of Alberta was selected for this purpose.

#### 3.1.1 Specifications

The wind tunnel is capable of freestream speeds of up to 35 m/s and features a turbulence intensity of less than 0.5% at speeds of 5 m/s or greater (Gibeau and Ghaemi, 2020). The test section has dimensions of 2.4 m  $\times$  1.2 m  $\times$  11 m (width  $\times$  height  $\times$  length) and a contraction ratio of 6.3:1. Previous investigations have shown that the mean freestream velocity remains uniform within  $\sim 1\%$  across the span (Johnson and Kostiuk, 2000; Gibeau et al., 2020). The side walls of the test section are acrylic for optical access, as are some sections of the upper and lower walls. A photograph of the test section is provided in Figure 3.1.

#### 3.1.2 Generating a Turbulent Boundary Layer

It is necessary for a TBL to have  $Re_\tau \gtrsim 2000$  for the VLSMs to have a strong presence (Hutchins and Marusic, 2007a). Obtaining this Reynolds number in a wind tunnel requires a long surface for the boundary layer to develop over. This can be achieved by adding a long plate to the test section. However, it is much simpler to use the existing floor, and so this is what was done here.

First, a tripping device was developed to force a transition of the boundary layer to turbulence as early as possible. The device consists of a strip of 60-grit sandpaper with irregular protrusions



Figure 3.1: The test section of the wind tunnel in the Mechanical Engineering Building at the University of Alberta.

adhered to it as shown in Figure 3.2 (only a small segment is shown). The strip extends 7 cm in the streamwise direction and spans the entire width of the test section (2.4 m). The “initial trip” labelled in Figure 3.2 consists of a line of larger protrusions with a maximum height of 5 mm. The remaining “random protrusions” are much smaller and are meant to break up any coherent motions that may form from the initial trip. The tripping device was adhered to the floor of the test section just past the end of the contraction. Following the trip, the boundary layer was allowed to develop for roughly 7.75 m before reaching the location where the TBL was utilized. Since the maximum trip height was 5 mm, there were more than 1500 trip heights between the tripping device and the location where the experiments were conducted. Elsinga and Westerweel (2012) found that the mean velocity of a boundary layer returned to uniformity roughly 40 trip heights following a zigzag tripping device, and so the present tripping configuration seems reasonable. Second, the quality of the test section floor was improved to provide a flat, smooth surface for the development of the boundary layer. This included leveling all floor panels, filling the gaps between them, and then sanding the interfaces. This was done for all panels between the tripping device and the measurement location.

The configuration described above produces a TBL with  $Re_\tau = 2600$  and  $\delta = 94$  mm at  $U_\infty = 11.8$  m/s. This Reynolds number is sufficient to have a strong presence of VLSMs. Moreover, the boundary layer thickness is large enough and the freestream velocity is low enough to enable proper measurement of the velocity field using the available equipment (see Section 3.2.3). This TBL was therefore used for all experiments within this thesis that required the presence of VLSMs.

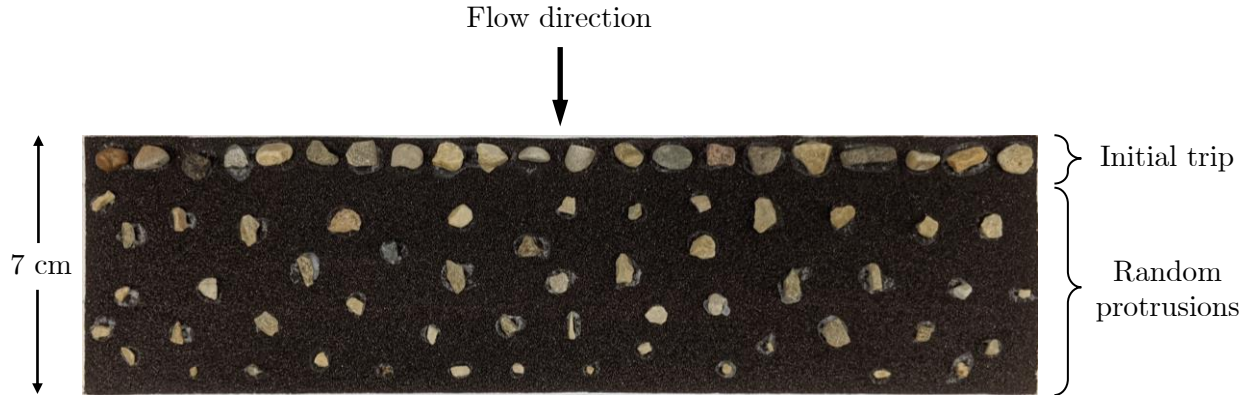


Figure 3.2: The boundary layer tripping device used to force a transition to turbulence.

### 3.1.3 Generating a Laminar Boundary Layer

An LBL was used for the initial evaluation of the active surface. Generating an LBL requires minimizing the velocity and turbulence intensity of the freestream flow as well as the development length for the boundary layer. The turbulence intensity of the present wind tunnel rises as the freestream velocity drops below 5 m/s (Gibeau et al., 2020), and so an LBL cannot be obtained simply by minimizing the freestream velocity. Moreover, the floor of the test section cannot be used because the development length leading up to the first point of measurement access would be too large. Instead, an LBL plate was constructed to allow generating a fresh boundary layer within the uniform freestream of the wind tunnel.

The LBL plate, which is shown in Figure 3.3, was machined from aluminum and features a smooth surface finish. It has a thickness of 12.7 mm, a length of 123 cm, and a width of 100 cm. The trailing edge is sharp and the leading edge is the profile from Hanson et al. (2012) which has been optimized for experimental studies of LBLs. The plate is supported by adjustable feet such that its top surface is located roughly 20 cm from the bottom wall of the test section. This places the plate well above the boundary layer that develops along the bottom wall. Several openings have been machined into the plate to accommodate sensors and actuators for a variety of boundary layer control experiments. These openings are plugged using blank inserts when not in use, thus retaining the flat and smooth surface necessary for the boundary layer. The most upstream opening was used to accommodate the active surface in the present work so that the development length was minimized.

The configuration described above produces a spatially-developing LBL with a mean velocity that matches the Blasius solution (Figure 2.1) for  $U_\infty = 4.0$  m/s. This is the lowest velocity that can be achieved before the freestream turbulence intensity rises significantly, and so this LBL was used in the present work.



Figure 3.3: Photograph of the plate used to generate the LBL.

## 3.2 Particle Image Velocimetry

Particle image velocimetry (PIV) is a non-invasive technique used to measure the velocity field of a fluid flow. PIV is briefly covered here because it is the technique of choice for obtaining velocity measurements in the present thesis. A full treatment of the topic cannot be provided and so the reader is referred to Raffel et al. (2018) for more information. The uncertainty associated with the present PIV measurements is discussed in Appendix A.

### 3.2.1 Working Principle

The basic working principle of PIV involves inferring the velocity field of a fluid flow from the movement of *tracer particles* within the flow. These particles are illuminated using a light source (typically a laser) and imaged using one or more calibrated cameras. Images are taken with a short time delay between them such that the motion of the tracer particles between subsequent images is captured. A group of particles within a small interrogation region is then considered. The distance travelled by the particles  $\Delta x_i$  and the known time between images  $\Delta t$  are used to compute the velocity vector for the interrogation region as

$$U_i = \frac{\Delta x_i}{\Delta t}. \quad (3.1)$$

This operation is applied across the imaging domain using a regular grid to produce an estimate of the velocity field.

The PIV working principle assumes that the tracer particles will faithfully follow the flow of interest. However, perfect tracing is typically not achieved. It is therefore critical to select a particle

that minimizes the tracing error while also being large enough to scatter sufficient light for imaging. Stokes' law can be used to model the dynamics of a tracer particle if the particle is assumed to be spherical with a diameter  $d_t$ . Along with Newton's second law, this produces:

$$\frac{\pi}{6}d_t^3\Delta\rho\frac{dU_t}{dt} = -3\pi\mu d_t\Delta U_t, \quad (3.2)$$

where  $\Delta\rho$  and  $\Delta U_t$  are the density and velocity differences between the tracer particle and surrounding fluid, respectively. Equation 3.2 implies that perfect tracing ( $\Delta U_t = 0$ ) can be achieved for  $\Delta\rho = 0$ , i.e., when the particle is neutrally buoyant. This is achieved in water easily due to the high fluid density, but is difficult to achieve in air (Scarano et al., 2015; Gibeau and Ghaemi, 2018). When neutral buoyancy cannot be achieved, the *time response* of the tracer particle is used to quantify the tracing fidelity. A tracer particle with a time response that is more than an order of magnitude smaller than the time scale of the flow will have tracing errors of less than 1% (Tropea et al., 2007). A fog machine is used to seed the wind tunnel with  $\sim 1\text{-}\mu\text{m}$  glycol-water droplets for the application of PIV in the present work. These droplets have time a response of  $\sim 1\ \mu\text{s}$  (Ragni et al., 2011) which renders the tracing errors negligible in the boundary layers considered here.

### 3.2.2 Measurements in a Plane

Planar PIV, which is depicted schematically in Figure 3.4, is the most common variation of PIV applied in experimental fluid mechanics. A laser sheet with a thickness on the order of 1 mm is used to illuminate a single plane which is then imaged using one or more cameras that are oriented normal to the plane. Each interrogation region is taken to be a two-dimensional interrogation window which is used to extract the in-plane components of the velocity vector that is located at the centre of the window. The distance travelled by the particles within the interrogation window is determined using a two-dimensional spatial cross-correlation between subsequent images. A sample of such a cross-correlation is shown using  $32\times 32$ -pixel interrogation windows in Figure 3.5. The associated correlation map features a distinct peak at  $\Delta x_1 = 8$  pixels representing the shift in the particles during  $\Delta t$ . Indeed, the particles in the interrogation window can be seen to have shifted in the horizontal ( $x_1$ ) direction by 8 pixels. The peak location therefore determines  $\Delta x_i$  for the application of Equation 3.1.

The above describes the simplest form of the planar PIV correlation process. In reality, typical PIV software will implement a more complex algorithm to improve the results. First, a multi-pass cross-correlation can be utilized. The first pass of cross-correlations produces values of  $\Delta x_i$  across the field of view (FOV). These values are then used to determine the starting point of the interrogation windows within the second image for the next pass of cross-correlations. This results in more common particles being captured between interrogation windows, thus improving the correlation and allowing for the use of a smaller window to yield a measured velocity field that is denser. Note that window overlap is also used to improve the density of the measured velocity field. Second, the final pass can employ an interpolation when locating the peak in the

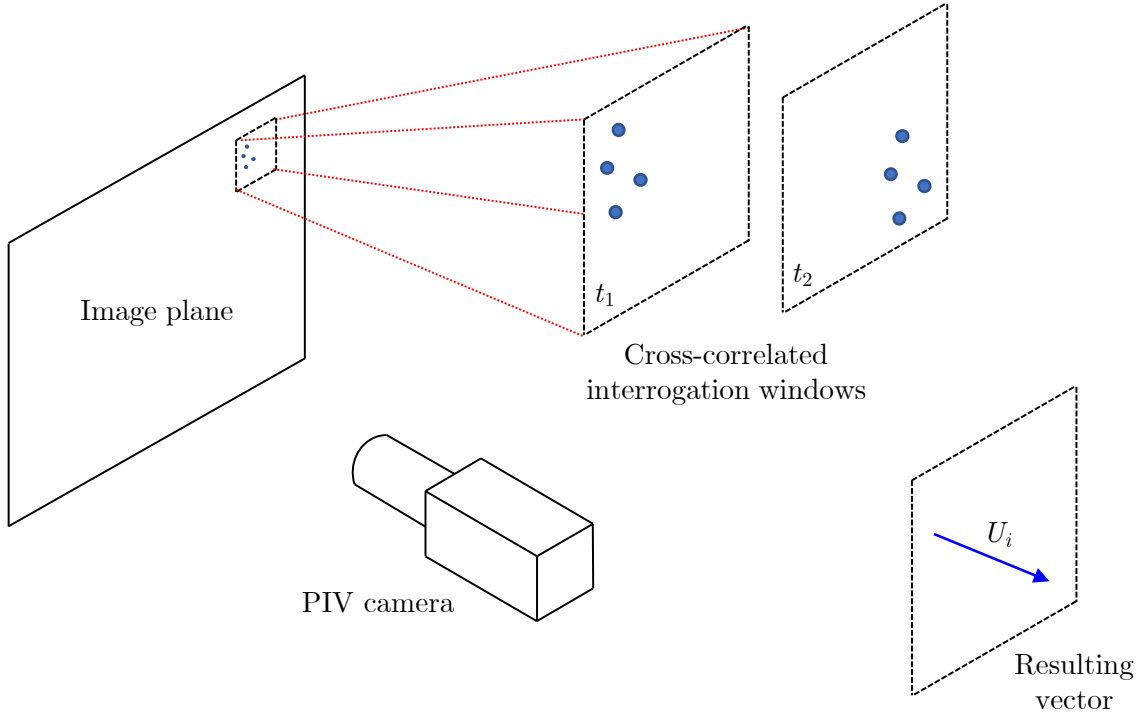


Figure 3.4: Schematic representation of the planar PIV process where  $\Delta t = t_2 - t_1$ . Adapted from Gibeau (2018) with permission.

correlation map. This provides sub-pixel accuracy for  $\Delta x_i$  and therefore also provides improved accuracy for  $U_i$ . Third, a weighting function can be applied to the interrogation windows to bias the correlation in some way that makes sense. For example, applying a Gaussian weighting will bias the correlation towards the centre of the window, which is where the final vector will be located in space. Finally, the interrogation windows can be deformed to account for local shear in the velocity field. This requires using information from a previous pass and therefore is only available when using multi-pass algorithms. Each of the algorithmic improvements discussed above are used when PIV is applied in the present work.

Planar PIV provides access to the two velocity components that are within the imaging plane of interest. However, it is sometimes necessary to have access to the out-of-plane component as is the case in the experimental campaigns documented in this thesis. This can be achieved by applying stereoscopic PIV, which makes use of two cameras placed at angles with respect to the imaging plane. This allows each camera to capture part of the out-of-plane velocity component, but also introduces additional complexities into the experimental setup. First, focusing the camera becomes more difficult because the camera sensor will no longer be oriented normal to the imaging plane. This is typically remedied by utilizing the Scheimpflug lens condition (Prasad and Jensen, 1995) along with a smaller aperture size, although the latter can also introduce issues with image intensity. Second, the relationship between the image and physical space is no longer described using a simple

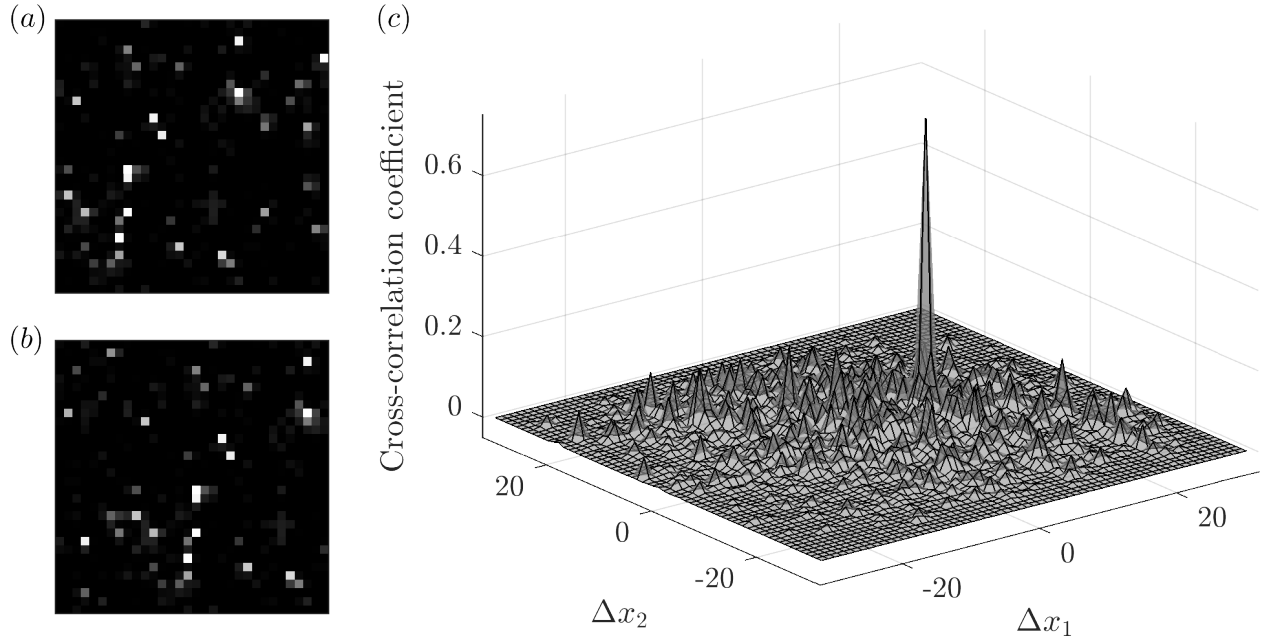


Figure 3.5: Sample correlation using  $32 \times 32$ -pixel interrogation windows: (a) the interrogation window at  $t_1$ , (b) the interrogation window at  $t_2$ , and (c) the resulting cross-correlation map. Adapted from Gibeau (2018) with permission.

calibration factor as is the case for planar PIV. Instead, it is now necessary to conduct a three-dimensional calibration to map the images to the plane of interest. This is achieved in the present work using a three-dimensional calibration target along with an additional disparity-correction step that is known as self-calibration (Wieneke, 2005). The two-dimensional cross-correlation technique described earlier is applied to the images from each camera after these images have been projected onto the plane of interest. The three desired velocity components are then obtained by applying a least-squares technique to the vectors obtained from both cameras.

### 3.2.3 Equipment and Software

The same PIV system, which is depicted in Figure 3.6, was used for all experiments conducted for the present thesis. A dual-cavity, high-speed Nd:YLF laser (Photonics Industries DM20-527-DH) was used to provide illumination. Each cavity of the laser is capable of producing light at a wavelength of 527 nm and at frequencies of up to 10 kHz. At 1 kHz, the maximum output of each cavity is 20 mJ per pulse and each pulse has a width of 170 ns. Imaging was carried out using up to four high-speed cameras (Phantom v611). Each camera features a  $1280 \times 800$ -pixel complementary metal oxide semiconductor sensor with a  $20 \mu\text{m} \times 20 \mu\text{m}$  pixel size and 12-bit resolution. The laser and cameras were controlled using a timing unit (LaVision PTU X) which was programmed using DaVis 8.4 software installed on a host computer. The same software was used for processing the images collected during experiments. The resulting velocity measurements were then transferred to MATLAB for analysis. Finally, a fog machine (American DJ Fog Fury 3000) was used to generate

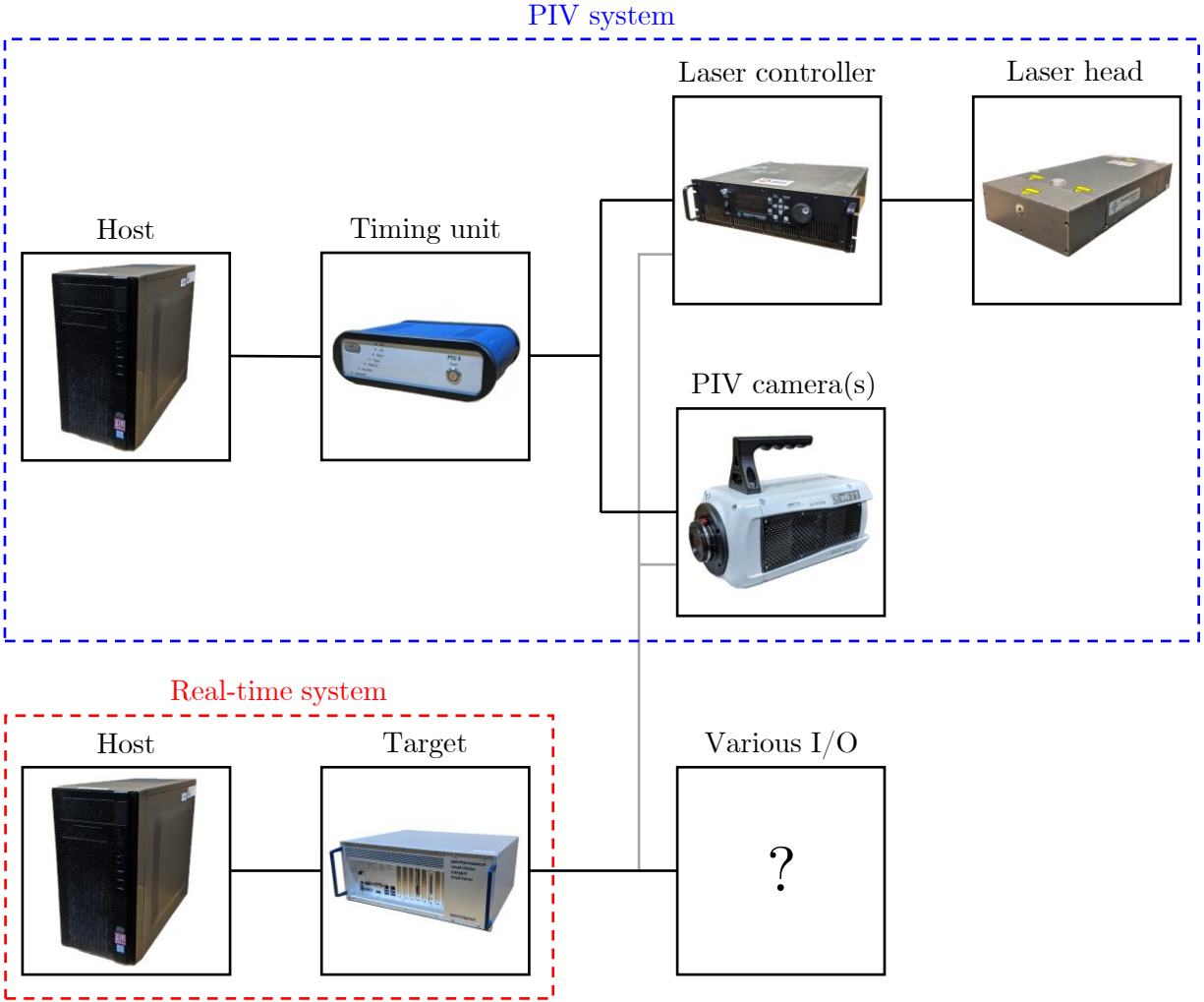


Figure 3.6: Block diagram showing the PIV system, real-time system, and their interconnections.

~1- $\mu\text{m}$  glycol-water droplets as tracer particles for all experiments.

### 3.3 Real-Time System

The experiments conducted for the present thesis required generating and acquiring voltage signals for the purpose of interacting with hardware components other than those used for PIV. This was accomplished using a real-time system as described next.

#### 3.3.1 Simulink Real-Time and Target Machine

Simulink is a MATLAB-based graphical programming language that can be used for system modelling, simulation, and analysis. Simulink Real-Time allows for the compilation of these models into real-time applications that accommodate input and output signals for the purpose of interacting with external hardware. The applications are programmed using Simulink on a host computer

and then run on a target machine that interfaces with various inputs and outputs as depicted in Figure 3.6. A Speedgoat target machine (Performance model) equipped with a 16-bit input/output module (IO135) was used to run Simulink Real-Time applications in the present work. The configuration featured an Intel Core i3-6100 processor, a 120-GB SSD, 4096 MB of RAM, and could accommodate 32 and 16 analog inputs and outputs, respectively, at up to 200 kSPS and  $\pm 10$  V.

### 3.3.2 Data Synchronization

The PIV and real-time systems were used simultaneously to acquire various data from experiments. However, these systems were operated by two different host computers. A process was therefore developed to synchronize the two data streams for later analysis. This involved using the real-time system to record the trigger signals for the PIV laser and one camera as depicted in Figure 3.6. An annotated sample of these signals is shown in Figure 3.7, revealing a train of double peaks separated by  $\Delta t$  (Equation (3.1)). These peaks correspond to the trigger signals of the first and second laser cavities and they can be seen to exist before the camera trigger occurs. This is because the laser fires for a short time before the camera begins recording images. The first set of laser pulses after the camera trigger corresponds to the first vector field recorded by the PIV camera. As a result, the time of the first PIV measurement can be taken to be the halfway point between these two pulses as is shown in Figure 3.7. The synchronized data from the real-time system is then extracted at the PIV sampling frequency beginning with this initial point.

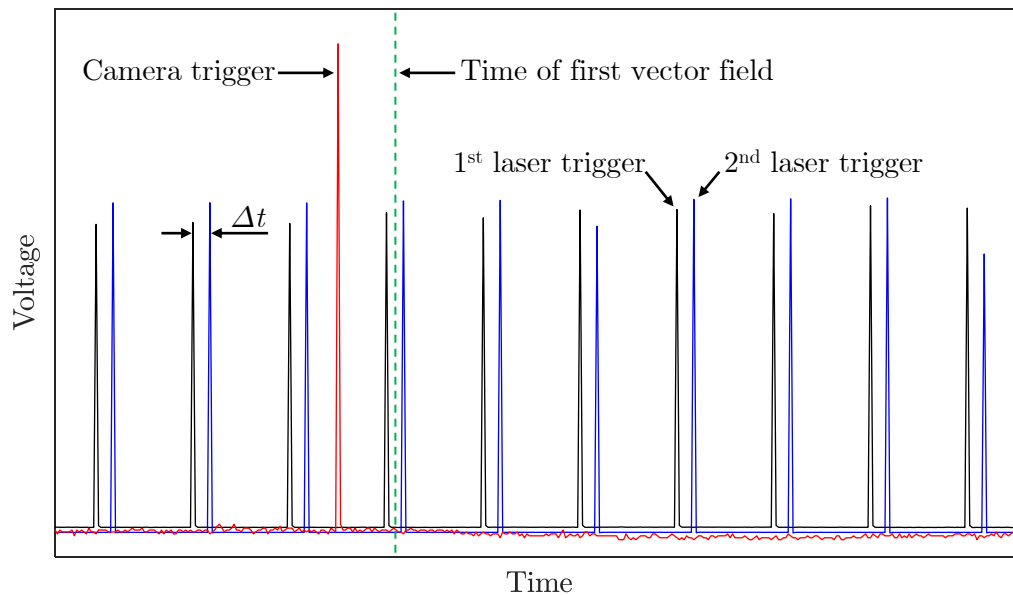


Figure 3.7: Annotated time series recorded by the real-time system showing the PIV laser and camera trigger signals and how they were used to synchronize the real-time data stream with the PIV vector fields.

**Part II**  
**Sensing**

## Chapter 4

# Development of the Pressure Measurement System

This chapter details the development of the pressure measurement system used to identify the relationship between wall-pressure and the VLSMs within a TBL. The following are covered: the measurement requirements, sensor selection, component design, algorithm design, and testing of the system.

### 4.1 Measurement Requirements

There are several requirements that the measurement system must adhere to. First, the system must allow for measuring the wall-pressure fluctuations beneath the TBL without disrupting the flow above the surface. Second, the system must be sensitive enough to capture the wall-pressure fluctuations produced by the VLSMs, which may be quite weak as suggested by the work of Beresh et al. (2013). Third, the system must be able to account for the background noise produced by the experimental facility. And finally, the system must have a flat frequency response across the frequency range of interest. The summary of Hwang et al. (2009) indicates that the low-frequency range is defined as  $\omega\delta/U_\tau \lesssim 5$ , which corresponds to  $f \lesssim 4$  Hz in the present TBL. Ideally, the system should be able to measure frequencies as low as 0.4 Hz to capture a full order of magnitude of the low-frequency range. Similarly, the work of Tsuji et al. (2007) indicates that frequencies beyond  $f\nu/U_\tau^2 \approx 0.25$  have decayed several orders of magnitude with respect to the beginning of the high-frequency range. This is a reasonable upper cutoff for the frequency range and corresponds to  $f \approx 3000$  Hz in the present TBL. The ideal frequency range for the pressure measurement system is therefore 0.4 Hz to 3 kHz.

### 4.2 Sensor Selection

The first necessary condition for capturing the frequency range of interest is acquiring a sensor that has a flat frequency response across this range. Unfortunately, many sensors that are capable of measuring very-low frequencies are not sensitive enough for use beneath a laboratory-scale TBL.

For example, piezoresistive pressure sensors can measure down to 0 Hz (i.e., they can also capture the static pressure) but typically have low sensitivity. To achieve both high sensitivity and an adequate response at low frequencies, a 1/2-inch Brüel & Kjær infrasound microphone (model 4964) was selected for the present work. This microphone has a flat frequency response from 0.02 Hz to 20 kHz ( $\pm 3$  dB). However, it must be paired with the associated pre-amplifier (Brüel & Kjær model 2669) which affects the measurable frequency range. More specifically, the  $-3$  dB point at the lower end of the frequency response for the combined measurement chain shifts to 0.7 Hz. This results in an attenuation of roughly  $-5$  dB for the ideal low-frequency cutoff of 0.4 Hz, which means that pressure fluctuations at this frequency will be measured at roughly 56% of their true value. This is sufficient for the purposes of the present work. The microphone also has a dynamic range of  $1.1 \times 10^{-4}$  to  $4.0 \times 10^2$  Pa and a nominal sensitivity of 50 mV/Pa. The empirical relation of Farabee and Casarella (1991) shown in Equation (2.19) indicates that the present TBL will produce  $p_{\text{rms}} \approx 0.75$  Pa, which is more than 6800 times larger than the smallest measurable pressure fluctuation. This microphone is therefore sufficiently sensitive for the purposes of the present work. Note that the true sensitivity values of the microphones used here have been obtained in-house using a constant-frequency calibrator at 1 kHz (Brüel & Kjær 4231). The uncertainty associated with this calibration is estimated in Appendix A.

### 4.3 Avoiding Spatial Filtering

The low-frequency response of the pressure measurement system is more-or-less guaranteed by proper sensor selection. However, the high-frequency response can be attenuated by a spatial filtering effect (Schewe, 1983; Lueptow, 1995; Gravante et al., 1998). This occurs when pressure-producing motions in the TBL are smaller than the size of the pressure sensor, resulting in the measured signal being the average of the signals from all small motions above the sensor. This type of spatial filtering is avoided by placing the pressure sensor behind a pinhole with a sufficiently small diameter. A thread-on pinhole attachment was machined from aluminum to replace the protection grid of the microphone for this purpose. A schematic of the attachment is shown in Figure 4.1. The known dimensions of the microphone and attachment as depicted in the figure are  $D_m = 12.05$  mm,  $d_p = 0.49$  mm,  $t_p = 1.17$  mm, and  $\alpha_p = 40^\circ$ . The value of  $h_m$  is difficult to determine because it depends on the height of the lip around the microphone diaphragm. This lip sits flush against the attachment during use and therefore its height determines  $h_m$ . However, the lip cannot be measured without damaging the diaphragm. A reasonable estimate is  $h_m \approx 0.5$  mm.

The thread-on attachment has been specially designed for the TBL produced for this thesis. First, the pinhole is at an angle to ensure that laser light from the PIV measurements does not pass through the pinhole and heat the diaphragm of the microphone. The present results show no indication that using an angled pinhole has affected the measurements in any way. Second, the pinhole dimensions have been chosen to minimize measurement errors. Past work suggests that the length of the pinhole  $\ell_p$  ( $= t_p/\sin(\alpha_p)$  here) must be at least twice its diameter  $d_p$  (Shaw, 1960). Furthermore, the maximum allowable pinhole diameter to avoid spatial filtering is somewhere in

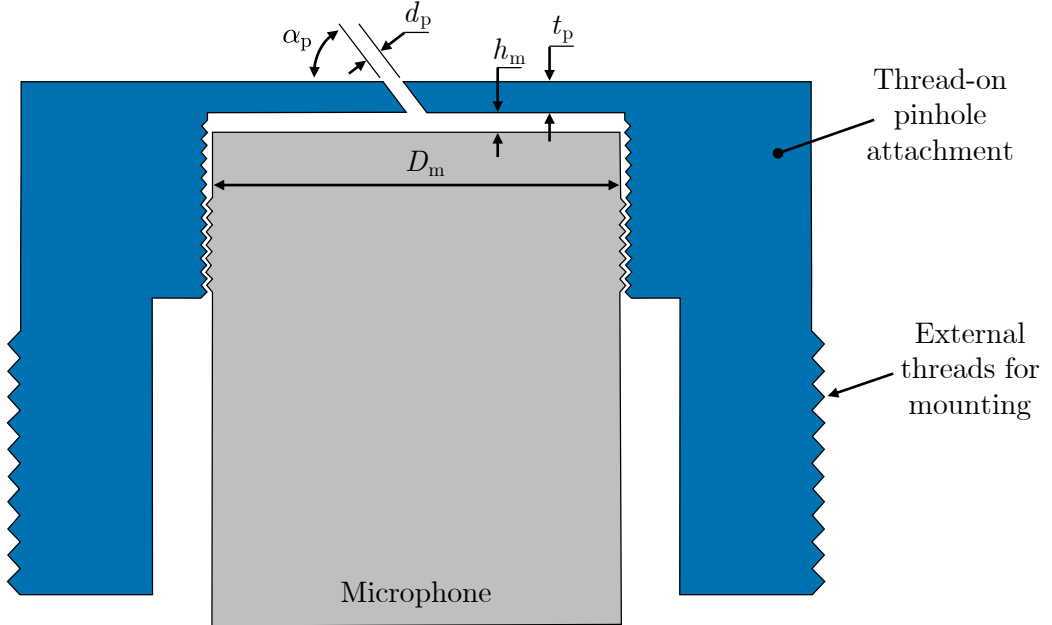


Figure 4.1: Schematic of the thread-on pinhole attachment for the microphone.

the range  $12 < d_p/\lambda < 18$  (Gravante et al., 1998). The present thread-on attachment satisfies these requirements with  $\ell_p/d_p = 3.7$  and  $d_p/\lambda = 13.4$ . Finally, the attachment features external threads so that it can be mounted to the floor of the wind tunnel test section. The attachment is threaded until it is flush with the top surface of the floor and then is locked in place using a second threaded piece. Any remaining gaps between the attachment and floor are filled and sanded to ensure a flat, smooth surface for the TBL. The actual thread-on pinhole attachment used in this work is shown in Figure 4.2.

#### 4.4 Correction of Helmholtz Resonance

The thread-on pinhole attachment is necessary for avoiding spatial filtering of the wall-pressure signal. However, the pinhole and cavity beneath it act as a Helmholtz resonator which has the potential to distort the frequency response of the pressure signal measured by the microphone. More specifically, the frequencies near the Helmholtz resonant frequency  $f^*$  will be amplified and phase-shifted while the frequencies well beyond  $f^*$  will be attenuated and phase-shifted. The theoretical resonant frequency of a typical Helmholtz resonator is

$$f^* = \frac{U_s}{2\pi} \sqrt{\frac{A_p}{V_c \ell_p}}, \quad (4.1)$$

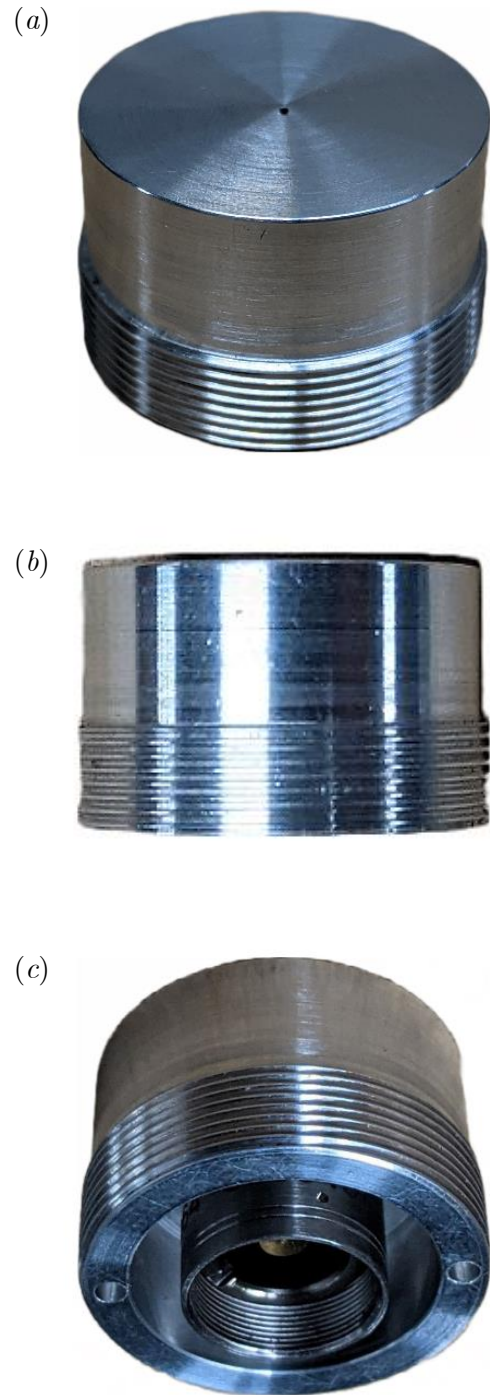


Figure 4.2: Photographs of the (a) top, (b) side, and (c) bottom of the thread-on pinhole attachment with the microphone cartridge installed (no pre-amplifier).

where  $U_s$  is the speed of sound,  $A_p$  is the cross-sectional area of the pinhole, and  $V_c$  is the volume of the cavity beneath the pinhole. Using the dimensions associated with Figure 4.1, Equation (4.1) produces  $f^* = 2340$  Hz. This value falls within the frequency range that is relevant to the present TBL and so the Helmholtz resonance must be accounted for in the wall-pressure signal.

A typical Helmholtz resonator can be modelled using a second-order transfer function for a linear, time-invariant system (Tsuji et al., 2007), which has a frequency response  $G(f)$  defined by

$$|G(f)| = \left[ \left( 1 - \left( \frac{f}{f^*} \right)^2 \right)^2 + \left( \frac{2\xi f}{f^*} \right)^2 \right]^{-1/2}, \quad (4.2a)$$

$$\angle G(f) = -\tan^{-1} \left[ \frac{2\xi(f/f^*)}{1 - (f/f^*)^2} \right], \quad (4.2b)$$

where  $\xi$  is the damping ratio of the resonator. Given that the pinhole system can be modelled as linear and time-invariant, the true input pressure  $p_0(t)$  and the vector of pressure measurements sampled behind the pinhole  $p_p(t)$  are related through a convolution with the impulse response of the system as

$$p_p(t) = g(t) * p_0(t), \quad (4.3)$$

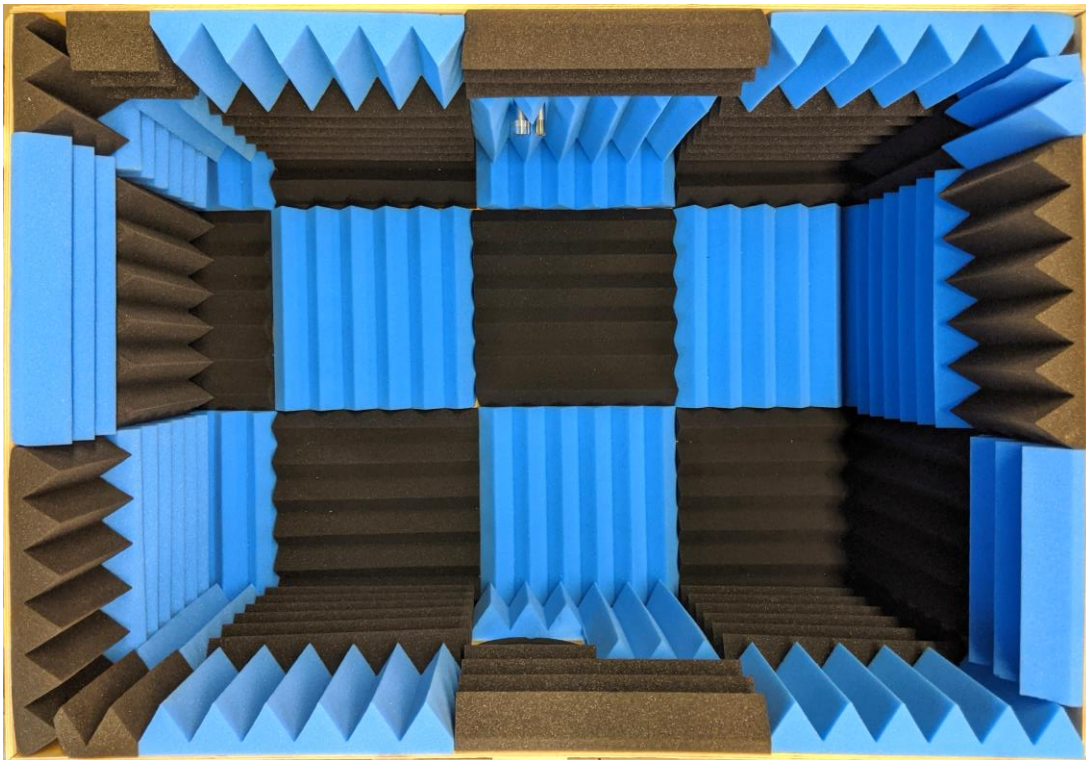
where the impulse response  $g(t)$  and the frequency response  $G(f)$  are related through the discrete Fourier transform as  $G(f) = \mathcal{F}\{g(t)\}$ . If  $G(f)$  and  $p_p(t)$  are known and  $G(f)$  is not zero anywhere, then  $p_0(t)$  can be obtained by employing the convolution theorem for Fourier transforms:

$$p_0(t) = \mathcal{F}^{-1} \left\{ \frac{\mathcal{F}\{p_p(t)\}}{G(f)} \right\}. \quad (4.4)$$

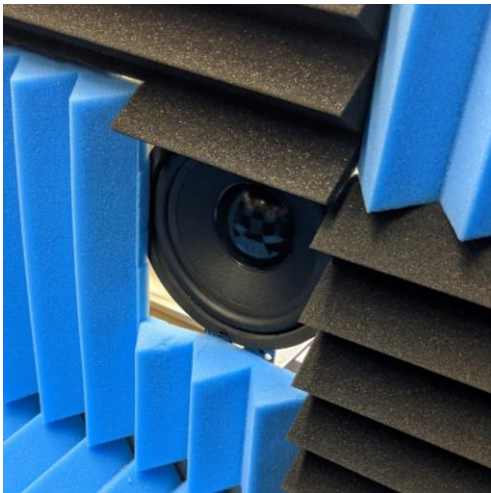
The parameters of  $G(f)$  must be determined and the function must be sampled and arranged into a two-sided spectrum with the same frequency bins as  $\mathcal{F}\{p_p(t)\}$  prior to utilizing Equation (4.4).

The parameters of Equation (4.2) have been determined for the present pinhole system using a dynamic calibration against a second identical microphone which will be referred to as the reference. A quasi-anechoic chamber that is similar to the one used by Naka (2009) has been constructed for this purpose and is shown in Figure 4.3. The pinhole and reference microphones were placed parallel to each other facing a loudspeaker within the chamber as is shown in the figure. Sound waves with frequencies ranging from 1 Hz to 5 kHz were generated and recorded by both microphones simultaneously. The Fourier coefficients of the recorded signals were used to estimate the amplitude and phase response of the pinhole resonator which were then used to fit  $G(f)$ , resulting in  $f^* = 2200$  Hz and  $\xi = 0.29$ . This resonant frequency agrees reasonably well with the theoretical value of 2340 Hz. The measured response and the fit model are shown in Figure 4.4. The plot reveals that the model captures the response of the pinhole well, but the phase response slightly deviates from that of the model for frequencies beyond  $f \approx 2000$  Hz, and the amplitude response deviates for

(a)



(b)



(c)

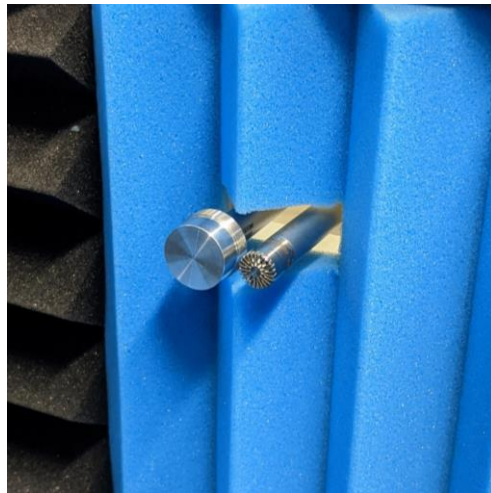


Figure 4.3: Photographs of (a) the quasi-anechoic chamber, (b) the externally supported loudspeaker, and (c) the externally supported microphones. The microphone on the right in (c) is the reference and the microphone on the left is fitted with the attachment that is to be calibrated.

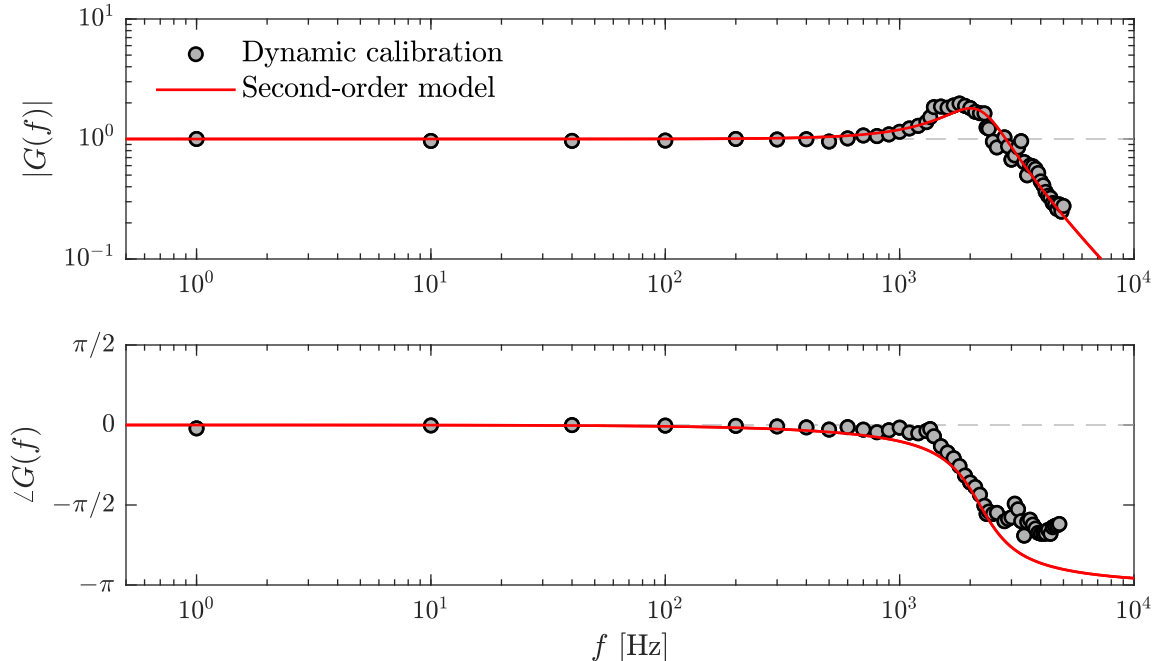


Figure 4.4: Measured frequency response of the pinhole resonator compared to the second-order model given by Equation (4.2).

frequencies beyond  $f \approx 3000$  Hz. Moreover, both responses show some differences at  $f \approx 1500$  Hz. These discrepancies may be attributable to the geometry of the current pinhole and microphone cavity, as they do not exactly match the standard Helmholtz resonator. Similar differences between the measured response and the second-order system were also reported by Tsuji et al. (2007). As will be discussed shortly, these discrepancies do not significantly affect the signal correction.

The frequency response shown in Figure 4.4 reveals that high frequencies are significantly attenuated by the Helmholtz resonator. Since a signal correction using Equation (4.4) requires dividing by the frequency response, the correction process has the potential to amplify noise at high frequencies beyond those relevant to the present TBL. This is undesirable, and so a lowpass filter must be applied after the correction. The cutoff frequency of this filter was selected to be 3 kHz to match the upper cutoff of the frequency range of interest. This filter has been applied such that the group delay is compensated for, i.e., there is no time delay introduced by the filtering process. Note that this sort of delay-compensated filter is only possible in post-processing and therefore cannot be implemented in real time.

The Helmholtz correction has been tested in the quasi-anechoic chamber using a white noise signal containing frequencies up to 3 kHz. The pinhole signal, before and after correction, is compared to the reference signal in Figure 4.5, and it is evident that the reference and corrected signals match quite well. The correlation coefficient between the two signals is 0.97, in contrast to 0.58 prior to correction. It is therefore evident that the corrected pinhole measurements can

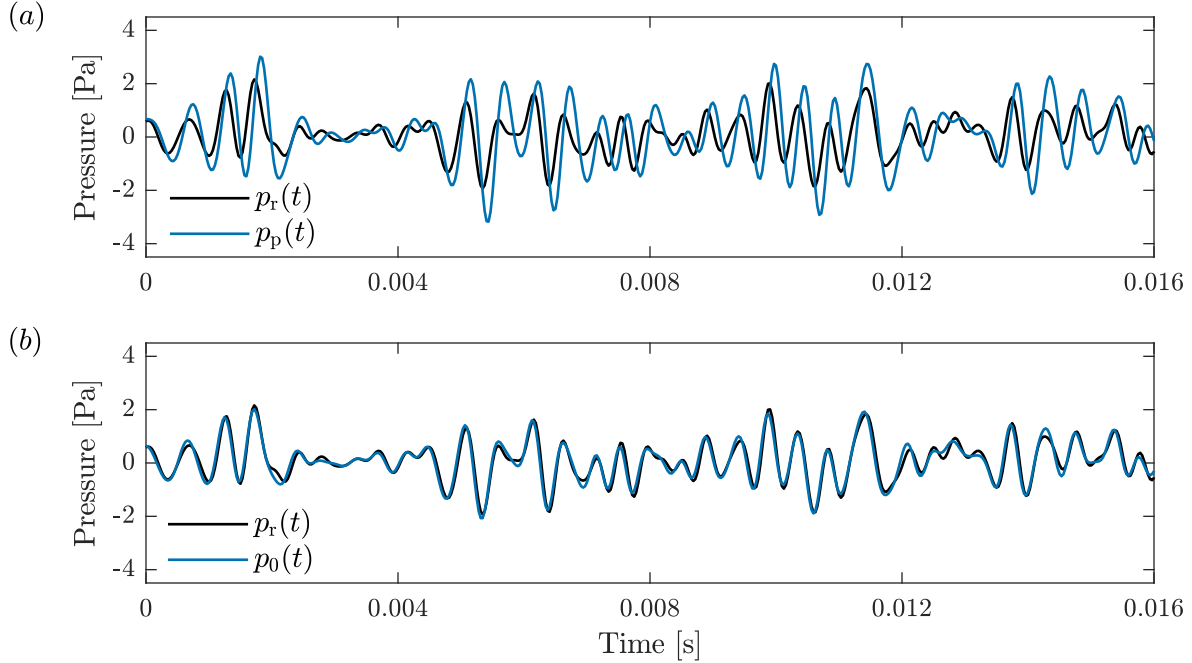


Figure 4.5: Sample signal of white noise containing frequencies up to 3 kHz: (a) the pinhole microphone signal  $p_p(t)$  compared to the reference microphone signal  $p_r(t)$  and (b) the Helmholtz-corrected signal  $p_0(t)$  compared to  $p_r(t)$ .

reliably capture pressure fluctuations up to 3 kHz, which is sufficient to capture the relevant pressure fluctuations in the present TBL. The MATLAB code used to implement the Helmholtz resonance correction is provided in Appendix B.

## 4.5 Background Noise Removal

Finally, the background noise of the wind tunnel must be removed from the wall-pressure measurements. This has been achieved using a Wiener noise cancelling filter as outlined by Hayes (1996), which requires a simultaneous measurement of the noise field along with the wall pressure. This has been accomplished using the second microphone supported in the freestream and fitted with a nose cone. The support structure for this microphone consists of two pieces: one 3D-printed and one machined from aluminum. The overall design goal of the structure was to permit measurement of the background noise without disturbing the flow. A photograph of the structure being used to support the second microphone in the freestream of the wind tunnel is shown in Figure 4.6.

The Wiener noise cancelling filter is posed as an estimation problem of the form

$$p_0(t) = p(t) + p_b(t), \quad (4.5)$$

where, in the present case,  $p_0(t)$  is the Helmholtz-corrected signal measured through the pinhole,

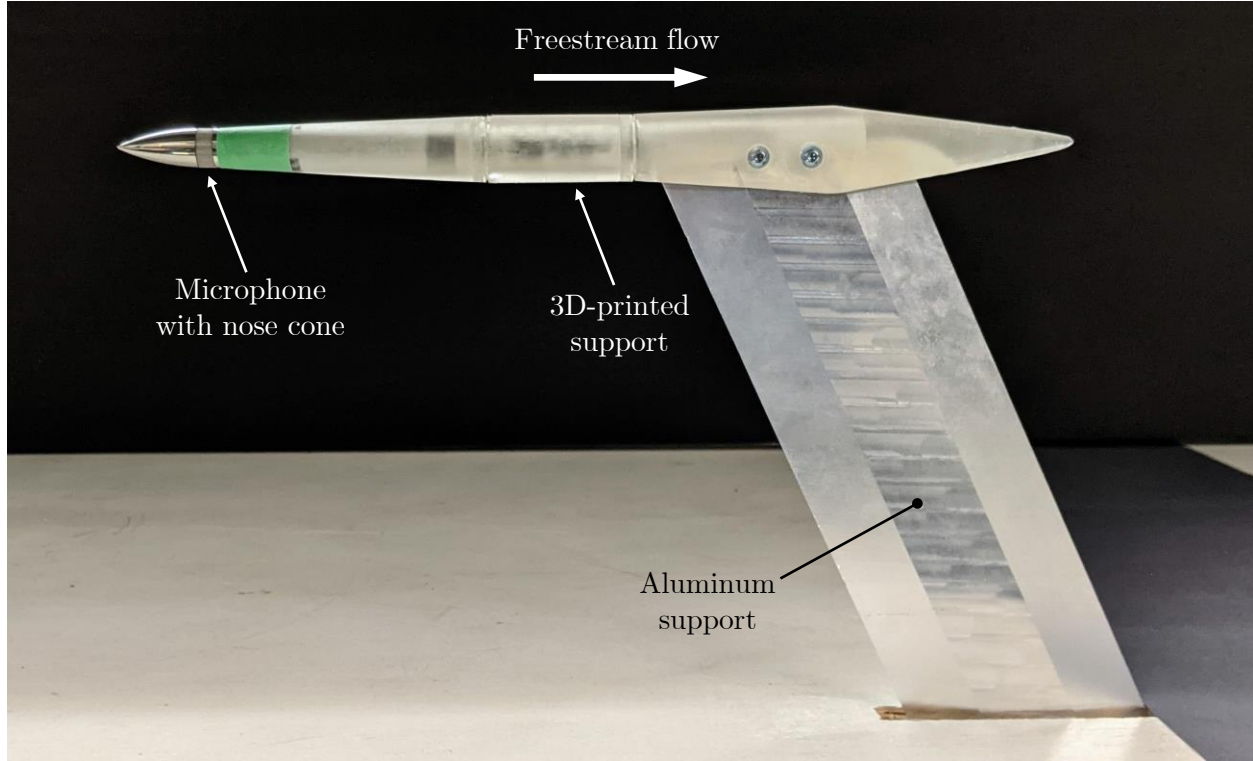


Figure 4.6: Annotated photograph of the freestream microphone support installed in the test section of the wind tunnel.

$p(t)$  is the true wall pressure, and  $p_b(t)$  is the background noise. The filter provides an estimate for  $p_b(t)$  so that it can be subtracted from  $p_0(t)$  to obtain an estimate for the true wall pressure

$$\hat{p}(t) = p_0(t) - \hat{p}_b(t). \quad (4.6)$$

The ‘hat’ notation used here denotes an estimate. It is important to note that simply subtracting the measurement of the noise field does not fully remove the background noise from the wall-pressure signal. This can be due to many reasons, for example slight differences between the microphones, different propagation paths between the noise sources and microphones, or leakage of the boundary layer fluctuations into the noise field signal. For this reason, the background noise  $p_b(t)$  and the noise field signal  $p_n(t)$  are distinguished. The latter is the signal recorded by the microphone in the freestream.

The Wiener filter is applied as a digital filter whose coefficients  $\mathbf{c}$ , which represent the impulse response of the filtering system, are obtained by solving the following set of Wiener-Hopf equations:

$$\mathbf{R}_{p_n} \mathbf{c} = \mathbf{r}_{p_n p_0}. \quad (4.7)$$

Here,  $\mathbf{R}_{p_n}$  is a Toeplitz matrix containing the autocorrelations of  $p_n(t)$  and  $\mathbf{r}_{p_n p_0}$  is a vector containing the cross-correlations between  $p_n(t)$  and  $p_0(t)$ . The compact notation of Equation (4.7) can

be expanded to better see the contents:

$$\begin{bmatrix} r_{p_n}(0) & r_{p_n}(1) & \dots & r_{p_n}(m-1) \\ r_{p_n}(1) & r_{p_n}(0) & \dots & r_{p_n}(m-2) \\ r_{p_n}(2) & r_{p_n}(1) & \dots & r_{p_n}(m-3) \\ \vdots & \vdots & & \vdots \\ r_{p_n}(m-1) & r_{p_n}(m-2) & \dots & r_{p_n}(0) \end{bmatrix} \begin{bmatrix} c(0) \\ c(1) \\ c(2) \\ \vdots \\ c(m-1) \end{bmatrix} = \begin{bmatrix} r_{p_n p_0}(0) \\ r_{p_n p_0}(1) \\ r_{p_n p_0}(2) \\ \vdots \\ r_{p_n p_0}(m-1) \end{bmatrix}. \quad (4.8)$$

Note that  $m$  is the selected filter order. As is evident in Equation (4.8), the filter coefficients can be obtained using only the noise field signal  $p_n(t)$  and the Helmholtz-corrected pinhole signal  $p_0(t)$ . The estimated background noise  $\hat{p}_b(t)$  is then obtained through a convolution of the filter coefficients with the noise field signal

$$\hat{p}_b(t) = \mathbf{c} * p_n(t). \quad (4.9)$$

The background noise can then be subtracted following Equation (4.6) to obtain the estimated true wall-pressure signal. The Wiener noise cancelling filter has been implemented in the present investigation using a filter order of  $m = 16000$ . The order of this filter was selected by iterating until the power spectrum converged. Figure 4.7 shows the power spectral density (PSD) of wall pressure before and after the estimated background noise has been subtracted. It is shown later in Chapter 5 that the spectrum obtained after subtracting the estimated background noise (black line) agrees well with the literature.

It is evident in Figure 4.7 that the majority of the background noise in the present wind tunnel occurs at the lower frequencies as is expected. This highlights the importance of accounting for the background noise when investigating a low-frequency phenomenon such as the VLSMs. The PSD obtained after directly subtracting the noise field signal from the wall-pressure signal is also shown. The background noise is not fully removed in this case, thus justifying the use of the Wiener filtering technique. The MATLAB code used to estimate the background noise using the Wiener filter is provided in Appendix B.

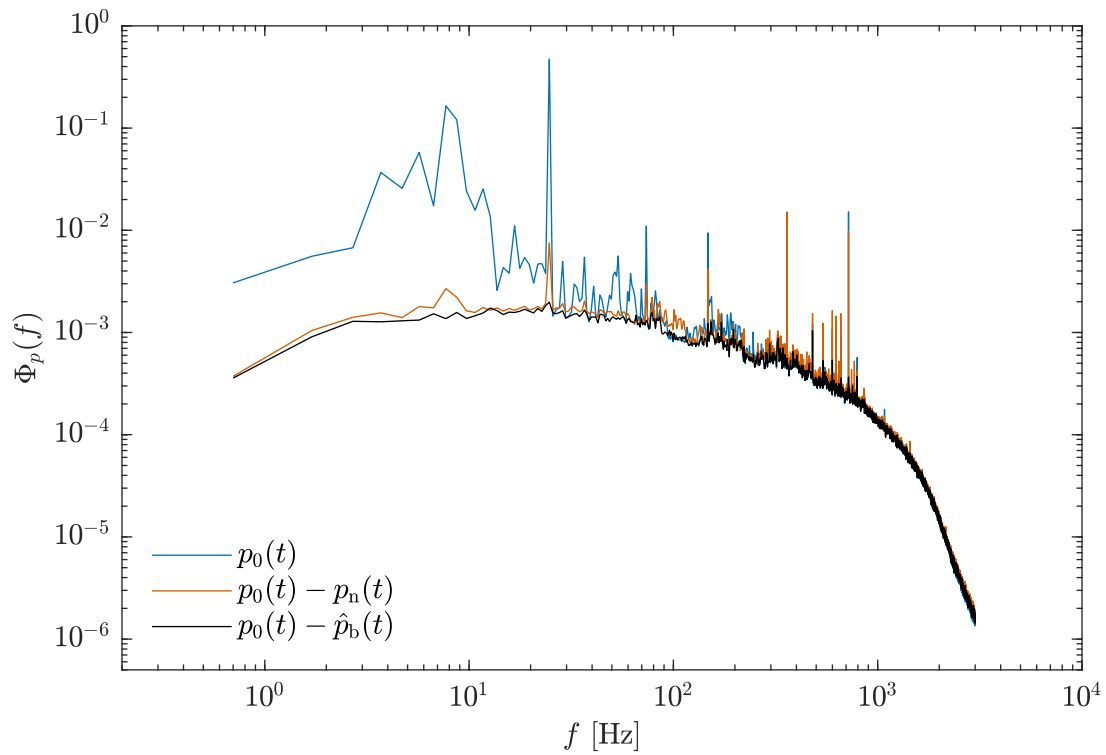


Figure 4.7: PSD of wall pressure  $\Phi_p(f)$  without background noise treatment ( $p_0(t)$ ), after subtracting the noise field signal ( $p_0(t) - p_n(t)$ ), and after subtracting the background noise estimated using the Wiener filter ( $p_0(t) - \hat{p}_b(t)$ ).

## Chapter 5

# Low-Frequency Wall-Pressure Sources in a Turbulent Boundary Layer

Following the discussion in Section 2.3.3, it is apparent that there are several open questions regarding the coupling between wall pressure and the largest motions in a TBL. First, there is some evidence that the VLSMs do in fact influence wall pressure in some way as is indicated by the elongated features observed in the wall-pressure footprints of Beresh et al. (2013) and the space-time pressure-velocity correlations of Buchmann et al. (2016) and Naka et al. (2015). However, a clear connection between wall pressure and the VLSMs has not yet been made and a mechanism governing the coupling has not been observed or proposed. Second, the large-scale motions associated with wall pressure by Naka et al. (2015) seem to be manifestations of the averaging process of the correlations because it is not straightforward to associate them with any of the instantaneous coherent motions commonly observed in TBLs. Further investigation is therefore needed to determine why the space-time pressure-velocity correlations appear as they do. Finally, the frequency information associated with the large-scale pressure-velocity coupling has been neglected in past investigations. That is, it is not known whether any features of the wall-pressure power spectrum can be attributed to hairpin packets or VLSMs or which frequency ranges that these motions affect. Each of these issues are examined in this chapter using simultaneous wall-pressure and high-speed PIV measurements in a TBL at  $Re_\tau = 2600$ . We begin by comparing the pressure and velocity statistics with those of past investigations to ensure our measurements are reliable. This includes a comparison of wall-pressure statistics, velocity statistics, and space-time pressure-velocity correlations. The normalized cross-spectra between wall pressure and velocity at a range of wall-normal locations are then investigated in the form of the magnitude-squared coherence function. Two distinct frequency bands of high coherence are found to occupy the low-frequency, mid-frequency, and overlap regions of the wall-pressure spectrum. Filters are used to isolate the wall-pressure fluctuations associated with each band, and the space-time pressure-velocity correlations are recomputed using the filtered wall-pressure signals to isolate the motions associated with each band of high coherence. We find that this analysis decomposes the correlations into simpler, more interpretable parts which can easily be associated with known coherent motions.

## 5.1 Experimental Setup

### 5.1.1 Turbulent Boundary Layer Configuration

The floor of the wind tunnel was used to generate the TBL as discussed in Section 3.1.2, resulting in the boundary layer parameters displayed in Table 5.1. A section of the floor at centre span was replaced by a flush-mounted acrylic plate with dimensions of 1.2 m  $\times$  0.6 m (streamwise-spanwise). The plate was modified to accommodate the pressure measurement system discussed in Chapter 4. This configuration placed the wall-pressure measurement location  $(x, y, z) = (0, 0, 0)$  roughly 7.75 m downstream from the boundary layer tripping device while the freestream microphone was located at  $(x, y, z) = (0, 2.1\delta, -5.4\delta)$  as depicted in Figure 5.1.

### 5.1.2 Wall-Pressure Measurements

The real-time system described in Section 3.3 was used to collect the signals from the pressure measurement system during experiments. A total of 10 minutes of microphone-only measurements were recorded for determining the single-point wall-pressure statistics. The remainder of the wall-pressure measurements were synchronized with PIV measurements using the procedure described in Section 3.3.2. The acquisition frequency of the real-time system was 20 kHz in all cases.

### 5.1.3 Particle Image Velocimetry

The PIV system described in Section 3.2.3 was used to conduct three separate PIV experiments for the purpose of capturing the velocity field of the TBL. The FOVs associated with each experiment are shown schematically in Figure 5.1 where each FOV is numbered accordingly. All collected images were pre-processed in the same way. First, the minimum of each ensemble was subtracted to reduce the background noise. Second, the images were divided by the background-subtracted ensemble average to normalize the intensity counts.

The FOV denoted as FOV1 in Figure 5.1 was used to capture the flow field from the wall to beyond the height of the TBL for determining  $\delta$ ,  $\delta^*$ ,  $\theta$ , and  $U_\infty$ . These measurements were therefore not synchronized with wall pressure. A 1-mm-thick laser sheet, formed within FOV1 using a combination of spherical and cylindrical lenses, was used to illuminate the tracer particles. A single camera and a 200-mm lens with an aperture setting of  $f_o/5.6$  resulted in a cropped FOV of  $(\Delta x, \Delta y) = 47 \text{ mm} \times 140 \text{ mm}$  with a resolution of 109.6  $\mu\text{m}/\text{pixel}$ . A total of 10000 double-frame images were collected over four sets at an acquisition rate of 25 Hz, corresponding to a total sampling time of  $5.0 \times 10^4 \delta / U_\infty$ . Following preprocessing, the images were processed using a multi-pass cross-correlation algorithm. The final pass employed  $32 \times 32$ -pixel Gaussian-weighted interrogation windows with 75% overlap.

The FOV denoted as FOV2 in Figure 5.1 was used to capture the coupling between wall pressure and velocity throughout the logarithmic and lower-wake layers of the TBL. These measurements were therefore recorded simultaneously with the wall-pressure fluctuations. The same laser sheet from FOV1 was utilized here. A single camera and a 300-mm lens with an aperture setting of

---

Reynolds numbers	$Re_\tau$	2600	
	$Re_\theta$	6000	
Freestream velocity	$U_\infty$	11.8	(m/s)
Boundary layer thickness	$\delta$	$93.8 \times 10^{-3}$	(m)
Displacement thickness	$\delta^*$	$11.5 \times 10^{-3}$	(m)
Momentum thickness	$\theta$	$8.6 \times 10^{-3}$	(m)
Friction velocity	$U_\tau$	0.46	(m/s)
Viscous lengthscale	$\lambda$	$36.5 \times 10^{-6}$	(m)
Shape factor	$H$	1.34	
Kinematic viscosity	$\nu$	$1.7 \times 10^{-5}$	(m <sup>2</sup> /s)
Density	$\rho$	1.1	(kg/m <sup>3</sup> )

Table 5.1: Boundary layer parameters at the pressure measurement location and fluid properties. The viscous lengthscale was determined by fitting the mean velocity profile to the logarithmic law of the wall with  $\kappa = 0.41$  and  $C = 5.0$ .

---

$f_o/8$  resulted in a cropped FOV of  $(\Delta x, \Delta y) = 9 \text{ mm} \times 82 \text{ mm}$  with a resolution of  $64.4 \text{ } \mu\text{m}/\text{pixel}$ . The FOV was cropped to be narrow to allow for longer sequences of images to be collected, as the high-speed camera memory is limited and longer sequences are required for convergence of the pressure-velocity cross-statistics. A total of 120000 double-frame images were collected over eight sets at an acquisition rate of 1 kHz, corresponding to a total sampling time of  $1.5 \times 10^4 \delta / U_\infty$ . The 1 kHz acquisition rate is sufficient for computing the cross-spectra between wall pressure and velocity while resolving the frequencies of the low-frequency, mid-frequency, and overlap regions of the wall-pressure power spectrum associated with the present TBL as will be shown later in Section 5.2.1. The PIV images were processed as described above for FOV1.

Stereoscopic PIV was conducted in the FOV denoted as FOV3 in Figure 5.1. The wall-pressure fluctuations were again recorded simultaneously. Two cameras each with a Scheimpflug adapter and a 300-mm lens with an aperture setting of  $f_o/11$  were used. A 2-mm-thick laser sheet was formed within FOV3 using a spherical lens and a collimator. A thicker laser sheet was used here to improve the correlation between double-frame images, as the freestream flow direction is normal to FOV3. Both cameras were placed in a forward-scattering orientation with respect to the laser sheet with  $90^\circ$  between their lines of sight. The cameras were calibrated using a two-step process which included a 3D target calibration followed by a self-calibration using a small set of particle images (Wieneke, 2005). This resulted in a FOV of  $(\Delta y, \Delta z) = 94 \text{ mm} \times 188 \text{ mm}$  with an effective resolution of  $102.8 \text{ } \mu\text{m}/\text{pixel}$ . Note that the usable wall-normal  $(\Delta y)$  portion of the FOV is roughly 47 mm due to the height of the laser sheet, which was reduced to retain laser power and obtain a sufficient intensity count in the images. A total of 21600 double-frame images were collected over

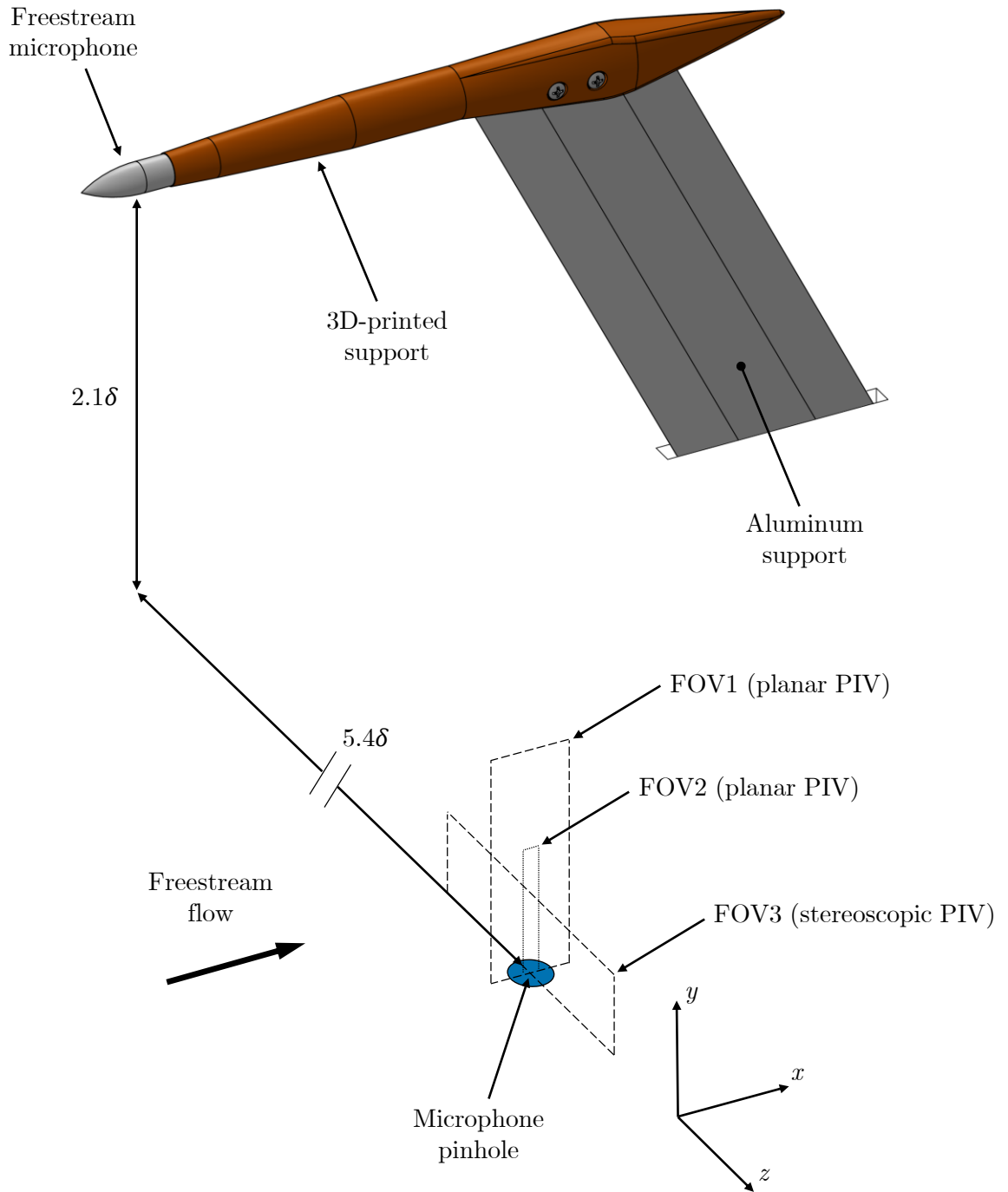


Figure 5.1: Schematic of the experimental setup. The axes origin is located at the microphone pinhole and is offset here to not interfere with the FOVs.

eight sets at an acquisition rate of 1 kHz, corresponding to a total sampling time of  $2.7 \times 10^3 \delta / U_\infty$ . A multi-pass stereoscopic cross-correlation algorithm was applied to the double-frame images using  $48 \times 48$ -pixel Gaussian-weighted interrogation windows with 75% overlap for the final pass.

## 5.2 Previously-Established Statistics

It is important to verify that the present wall-pressure and velocity measurements are reliable before moving forward with the primary analyses in Section 5.3. This is accomplished here by comparing the measurement statistics with those that have been previously established in the literature. Specifically, we will look at single-point velocity statistics (the mean profile, Reynolds stresses, and power spectra), single-point wall-pressure statistics (the power spectrum, probability density, and root-mean-square value), and space-time pressure-velocity correlations.

### 5.2.1 Single-Point Wall-Pressure and Velocity Statistics

The mean velocity profile and Reynolds stresses, evaluated using each of the three PIV measurements conducted in the present experimental campaign, are displayed on semi-logarithmic axes in Figure 5.2. The mean velocity profiles in Figure 5.2(a) are compared to the logarithmic law of the wall with  $\kappa = 0.41$  and  $C = 5.0$ . The profiles from the three PIV measurements agree well with one another and with the logarithmic law up to approximately  $y/\lambda = 400$ . It is also evident that the viscous sublayer ( $y/\lambda \lesssim 5$ ) and buffer layer ( $5 \lesssim y/\lambda \lesssim 30$ ) are not captured by the present measurements. This is not an issue for the investigation because the measurements have been optimized to capture the largest motions that occupy the logarithmic and wake layers of the TBL. The Reynolds stresses (excluding the spanwise velocity component) from all three experiments are shown in Figure 5.2(b). The streamwise normal component from the hotwire measurements of Hutchins and Marusic (2007a) at  $Re_\tau = 2630$  is also included for comparison. It can be seen in the figure that the present measurements conducted using planar PIV (FOV1 and FOV2) agree well with one another, and  $\langle u^2 \rangle / U_\tau^2$  agrees well with the measurements of Hutchins and Marusic (2007a). In contrast, some deviation is observed for the stereoscopic PIV measurements (FOV3). This is attributed to the added uncertainties associated with stereoscopic calibration, particularly with respect to the out-of-plane component (streamwise in this case). Despite this, Figure 5.2(b) reveals that the Reynolds stresses calculated from stereoscopic PIV agree reasonably well with those calculated from planar PIV. However, to remain conservative, the use of the present stereoscopic PIV measurements will be used primarily for qualitative analyses.

The PSD of streamwise velocity fluctuation as a function of wavenumber ( $\Phi_u(k_x); k_x = 2\pi f / \langle U \rangle$ ) has been computed using both sets of high-speed PIV data (FOV2 and FOV3) and is displayed in Figure 5.3 for two wall-normal locations within the logarithmic layer. The spectra have been normalized such that they can be easily compared to the work of Balakumar and Adrian (2007), who consolidated the spectra from several investigations of various wall-bounded flows with Reynolds numbers similar to that of the present TBL. The spectra of Figure 5.3 show excellent agreement with those shown in Balakumar and Adrian (2007), including the collapse of the curves in the  $k_x^{-1}$

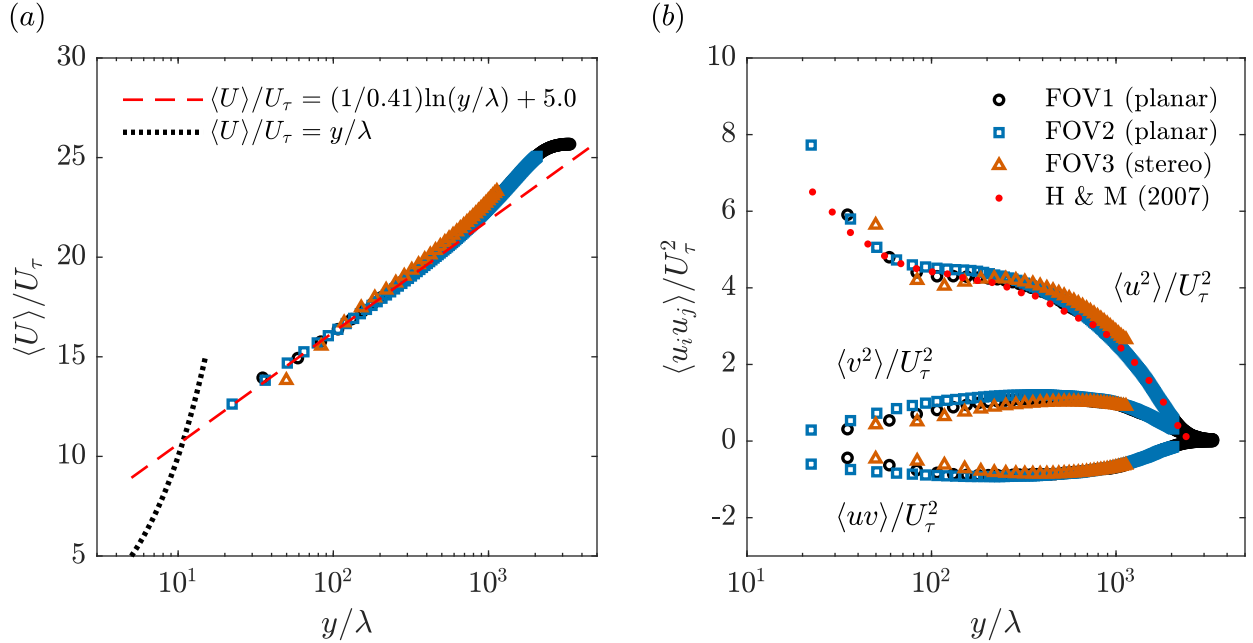


Figure 5.2: Velocity statistics at the pressure measurement location ( $x = z = 0$ ) from the three PIV experiments: (a) mean velocity profiles and (b) Reynolds stresses. H & M (2007) refers to the hotwire measurements of Hutchins and Marusic (2007a) at  $Re_\tau = 2630$ .

region (roughly  $k_x^{-1.04}$  here). We also see good agreement between the spectra from the planar (FOV2) and stereo (FOV3) data when they are compared at the same wall-normal location. Note that the increase in spectral densities at higher wavenumbers is associated with PIV noise. As we will see later, these higher wavenumbers (frequencies) are not important to the conclusions of the present chapter.

The PSD of wall pressure ( $\Phi_p(\omega)$ ) is displayed in Figure 5.4 using both inner- and outer-layer normalizations. The frequencies displayed range from 0.7 Hz to 3 kHz, which is the reliable range of measurable frequencies as discussed in Chapter 4. The divisions between the low-frequency, mid-frequency, overlap, and high-frequency regions of the spectrum as defined by Hwang et al. (2009) are included for reference, revealing that the present wall-pressure measurements capture the frequencies associated with all four regions. The upper frequency captured by the PIV measurements as dictated by the Nyquist criterion ( $\leq 500$  Hz) is also displayed, indicating that the PIV measurements resolve the frequencies of the low- and mid-frequency regions and nearly all of the overlap region. The low- and mid-frequency regions collapse over a range of Reynolds numbers when they are nondimensionalized using outer-layer variables (Farabee and Casarella, 1991; Tsuji et al., 2007; Klewicki et al., 2008), suggesting that these frequencies are caused by the motions of the outer layer. Since both the PIV and wall-pressure measurements capture the entirety of these regions, the synchronized measurements should resolve the large-scale pressure-velocity coupling relevant to this investigation.

The spectrum displayed in Figure 5.4 features the characteristics expected for the wall pressure

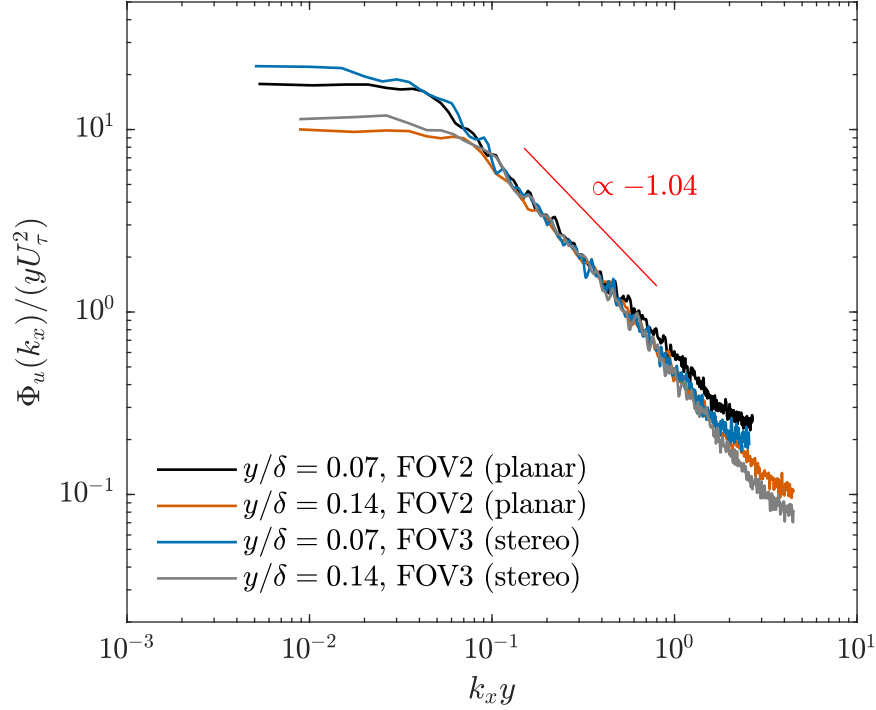


Figure 5.3: PSD of streamwise velocity fluctuation as a function of wavenumber ( $\Phi_u(k_x)$ ;  $k_x = 2\pi f/\langle U \rangle$ ) computed from the high-speed PIV measurements of FOV2 and FOV3. Note that  $y/\delta = 0.07$  and  $0.14$  coincide with roughly  $y/\lambda = 180$  and  $360$ , respectively.

beneath a TBL (Hwang et al., 2009). More specifically, the spectrum climbs in magnitude as frequency is increased until a peak is reached in the mid-frequency region. The spectrum then declines in magnitude and passes through two ranges of constant proportionality, one in the overlap region and one in the high-frequency region. The constant decay in the high-frequency region has been observed to be roughly  $\omega^{-5}$  to  $\omega^{-6}$  (McGrath and Simpson, 1987; Goody, 2004; Palumbo, 2012; Van Blitterswyk and Rocha, 2017). The presently observed decay of  $\omega^{-5.60}$  shown in Figure 5.4 is therefore in good agreement with the literature. The same can be said about the  $\omega^{-0.65}$  decay in the overlap region, which is typically observed to be around  $\omega^{-0.7}$  (McGrath and Simpson, 1987; Goody, 2004; Tsuji et al., 2007; Van Blitterswyk and Rocha, 2017). The behaviour of the low-frequency region is not well established at the moment as was discussed in Section 2.3.3. As is evident in Figure 5.4, the low-frequency region measured here grows with  $\omega^{1.07}$  and therefore shows the best agreement with the work of Panton and Linebarger (1974).

The root-mean-square wall pressure was calculated by integrating the PSD plotted in Figure 5.4 followed by taking the square root. The inner-normalized value is  $p_{\text{rms}}/\rho U_\tau^2 = 3.16$ , which represents an error of only 1.7% when compared with the empirical relation derived by Farabee and Casarella (1991) (see Equation (2.19)). The present wall-pressure fluctuations have a skewness of 0.056 and a flatness of 4.39, which agree with the values reported by Schewe (1983), Tsuji et al.

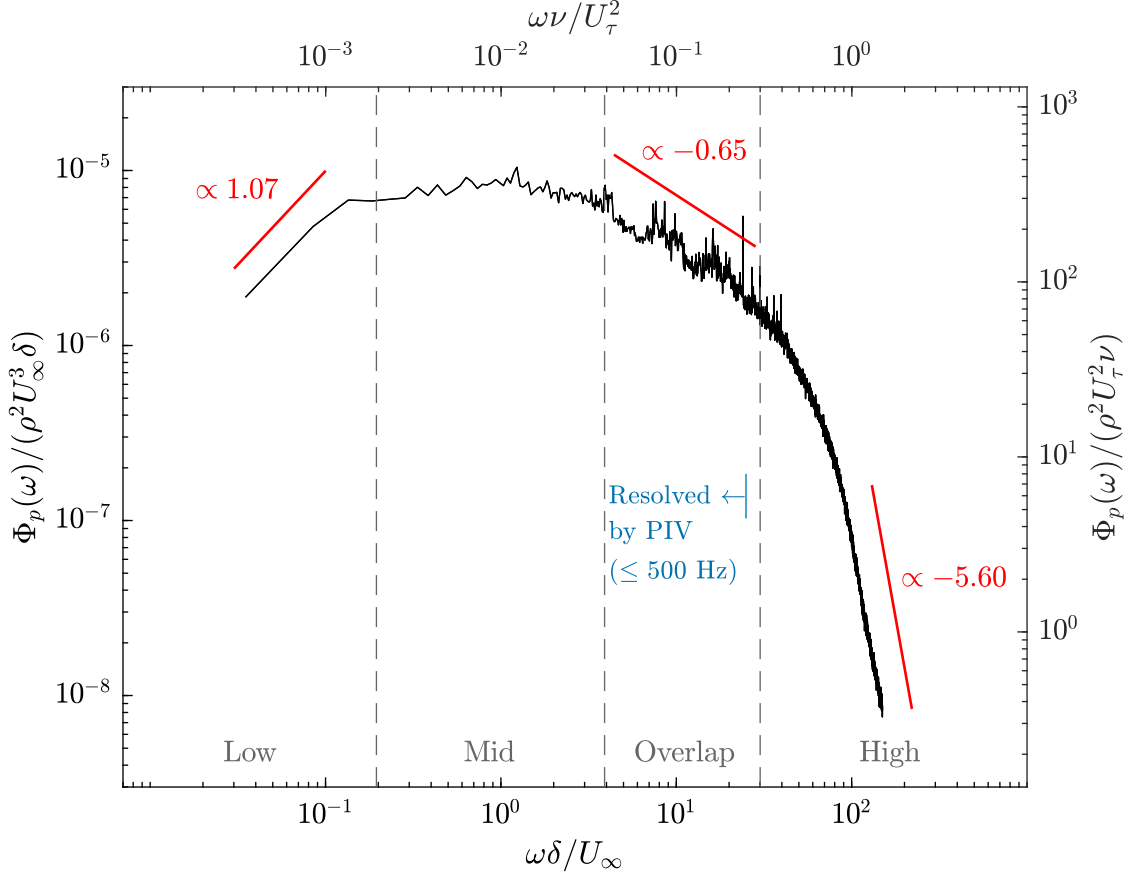


Figure 5.4: PSD of wall pressure ( $\Phi_p(\omega)$ ) normalized using both inner- and outer-layer variables. The divisions between the four regions of the spectrum are set as defined by Hwang et al. (2009). The upper frequency resolved by PIV is dictated by the Nyquist criterion.

(2007), and Naka et al. (2015). The probability density of the present wall-pressure measurements normalized by  $p_{\text{rms}}$  is plotted on linear and semi-logarithmic axes in Figures 5.5(a,b), respectively. Here, the dashed line is a Gaussian fit to the data for comparison. The approximate envelope of values reported by Tsuji et al. (2007) for  $5870 \leq Re_\theta \leq 16700$  (Figure 2.10) is also shown on the semi-logarithmic axes in Figure 5.5(b) using a grey outline. Since the extreme tails of the probability density functions in Tsuji et al. (2007) exhibit large amounts of scatter, the envelope depicts the range of values that we expect the functions to fall within. When looking at the probability density on linear axes in Figure 5.5(a), we can see that the measured density clearly deviates from the Gaussian fit at the peak and for densities ranging from roughly 0.05 to 0.2. This same deviation is visible in the results of Schewe (1983) and Tsuji et al. (2007). An even larger deviation from Gaussian behaviour is visible when looking at the semi-logarithmic axes in Figure 5.5(b). This deviation occurs at the extreme tails of the distribution and is indicative of the HAPPs in wall-pressure fluctuation that have been studied in the past (Johansson et al., 1987; Karangelen et al., 1993; Kim et al., 2002; Ghaemi and Scarano, 2013). As is evident in the figure, the tails of the

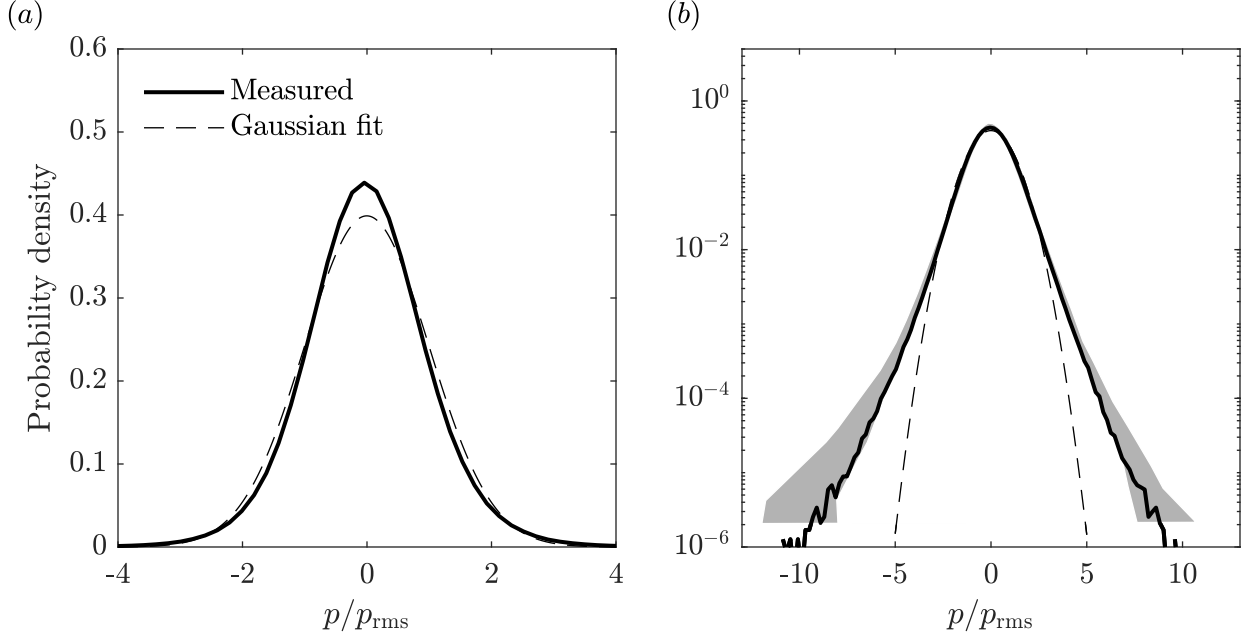


Figure 5.5: Measured probability density of wall-pressure fluctuations compared to a Gaussian fit of the same data; shown on (a) linear and (b) semi-logarithmic axes. The grey outline in (b) is the approximate envelope of values reported by Tsuji et al. (2007) for  $5870 \leq Re_\theta \leq 16700$ .

present probability density function fall within the approximate envelope of values from Tsuji et al. (2007).

### 5.2.2 Space-Time Pressure-Velocity Correlations

We now employ space-time pressure-velocity correlations along with Taylor’s hypothesis to investigate the spatial correlation between wall pressure and velocity throughout the TBL. This is done to compare the present pressure-velocity coupling with the results of Buchmann et al. (2016) and Naka et al. (2015) and to establish baselines for later comparison within the present study. Note that Dennis and Nickels (2008) evaluated the accuracy of using Taylor’s hypothesis to construct spatial fields in a TBL and showed that the majority of the large-scale errors occur for extrapolations beyond roughly  $\pm 3.5\delta$  from the measurement location. As we will see, the main features of all correlations computed in this investigation fall within this range and therefore we can apply Taylor’s hypothesis here.

We define the space-time pressure-velocity correlation as

$$\mathbf{R}_{pu_i}(\Delta t, y, z) = \frac{1}{\rho U_\infty^3} \langle p(t) u_i(t - \Delta t, 0, y, z) \rangle, \quad (5.1)$$

where the correlations have been normalized using  $\rho U_\infty^3$  to remain consistent with Naka et al. (2015). The correlations have also been computed using only  $p > 0$  and  $p < 0$  to isolate the

motions associated with positive and negative wall-pressure fluctuations. We denote these two conditional cases as  $\mathbf{R}_{pu_i}^+ = \mathbf{R}_{pu_i}|_{p>0}$  and  $\mathbf{R}_{pu_i}^- = \mathbf{R}_{pu_i}|_{p<0}$ .

Equation (5.1) was applied separately to the PIV snapshots from FOV2 and FOV3 and then Taylor’s hypothesis was used to transform  $\Delta t$  into streamwise distance using the local advection velocity  $U_c$ . Here we set  $U_c$  as the mean streamwise velocity at the corresponding wall-normal location, as the mean has been shown to closely match the advection velocity for  $y > 0.05\delta$  (Lee and Sung, 2011). This technique was employed to avoid the nonphysical streamwise stretching and compression of the correlations that can occur when a single advection velocity is chosen for use with Taylor’s hypothesis. Since each wall-normal location is associated with a different  $U_c$ , the streamwise extent of the correlation at each  $y$  is different. Interpolation has therefore been used to form a common  $\Delta t U_c$  grid for plotting. On this grid,  $\Delta t U_c < 0$  represents upstream from the pressure measurement location, while  $\Delta t U_c > 0$  represents downstream. Finally, the symmetry (and antisymmetry) of these correlations about the  $z = 0$  plane was exploited to improve the convergence of the results computed using the stereoscopic PIV measurements of FOV3. This was accomplished by flipping each component of the correlation about  $z = 0$ , adding it to the original (or subtracting in the case of antisymmetry), and then dividing the result by 2. The outcome of this procedure is that the results appear perfectly symmetric (or antisymmetric) about  $z = 0$  with the benefit of reduced noise.

Plots of  $\mathbf{R}_{pu_i}$ ,  $\mathbf{R}_{pu_i}^+$ , and  $\mathbf{R}_{pu_i}^-$  in streamwise–wall-normal planes are given in Figure 5.6. The streamwise and wall-normal components of the correlations are plotted at  $z = 0$ , while the spanwise component is at  $z/\delta = 0.2$  to match the plane location plotted by Naka et al. (2015). Note that this plane must be offset in the spanwise direction because  $\mathbf{R}_{pw}$  is antisymmetric about the  $z = 0$  plane and is therefore zero within it. In general, the shapes, sizes, and magnitudes of the correlations are in good agreement with those of Buchmann et al. (2016) and Naka et al. (2015), with a few exceptions that will be detailed shortly.

The contours of  $\mathbf{R}_{pu}$  in Figure 5.6(a) reveal that  $p$  is positively correlated with  $u$  directly above the pressure measurement location throughout nearly the whole boundary layer thickness and extending upstream to  $\Delta t U_c/\delta \approx -3$ . Two regions of weaker negative correlation between  $p$  and  $u$  extend downstream. The first region begins just past the pressure measurement location and extends at an angle from the wall to reach  $\Delta t U_c/\delta \approx 2.3$  and  $y/\delta \approx 0.7$ . The second region sits close to the wall and reaches to  $\Delta t U_c/\delta \approx 8$  (not entirely shown to keep the figure manageable). These same features are visible in the correlations of both Buchmann et al. (2016) and Naka et al. (2015), although there are some differences in the sizes of the features between all three studies. The results of Naka et al. (2015) suggest that these size differences could be Reynolds number effects. When we consider  $\mathbf{R}_{pu}^+$ , the region of positive correlation and the second region of negative correlation both become larger and more intense, while the first region of negative correlation disappears. The intensified region of positive correlation now extends across the range  $-4 \lesssim \Delta t U_c/\delta \lesssim 1$ , making its total streamwise extent  $\sim 5\delta$ . In contrast, the intensified region of negative correlation extends to roughly  $\Delta t U_c/\delta \approx 8.5$ . The contours of  $\mathbf{R}_{pu}^-$  show the opposite change to what was observed

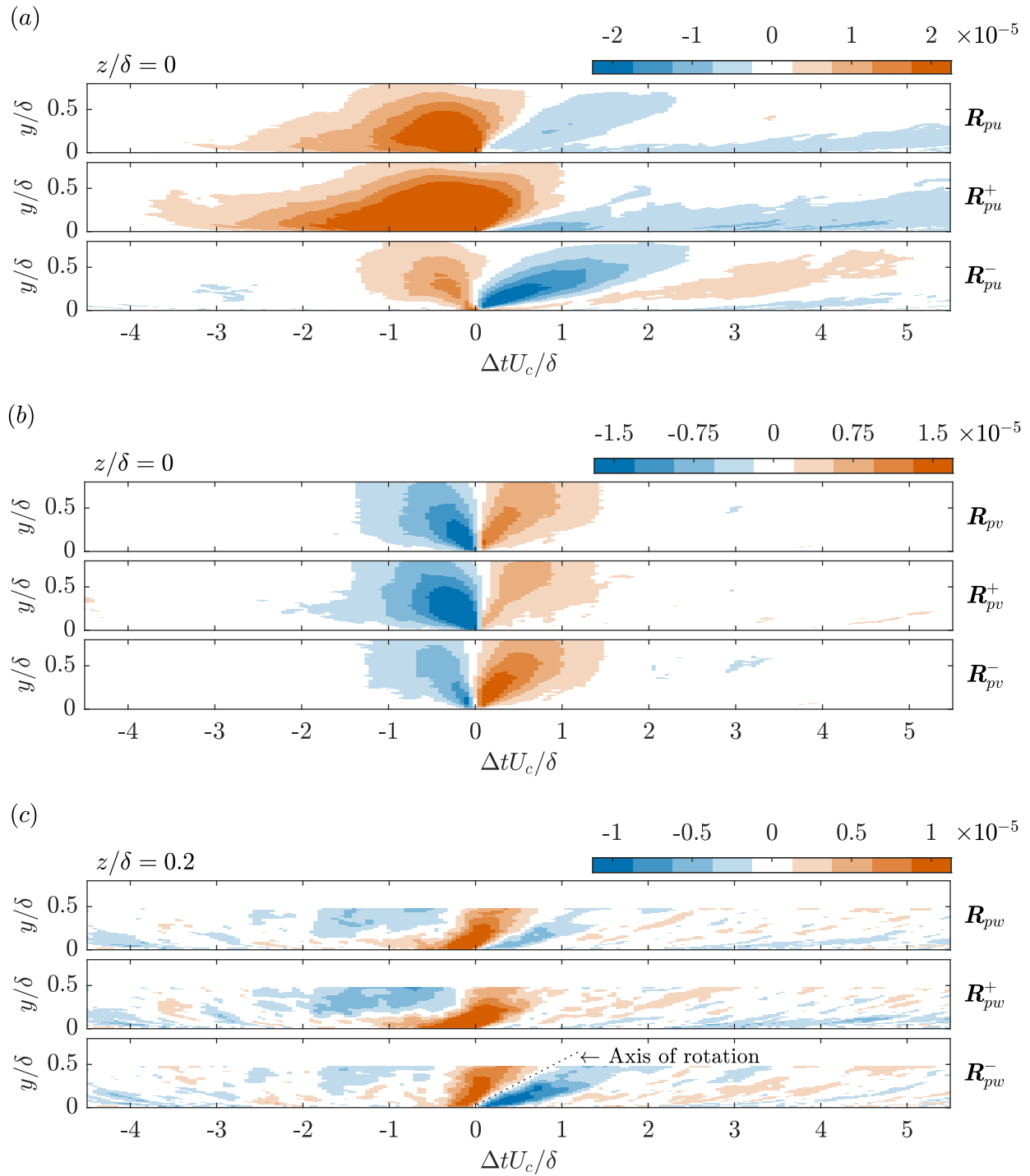


Figure 5.6: Space-time pressure-velocity correlations ( $R_{p u_i}$ ) as defined by Equation (5.1) calculated using the (a) streamwise, (b) wall-normal, and (c) spanwise velocity components. The superscripts ‘+’ and ‘-’ denote correlations computed using only  $p > 0$  or  $p < 0$ , respectively. The streamwise–wall-normal planes in (a) and (b) are located at  $z = 0$ , while those in (c) are located at  $z = 0.2\delta$ . The plots in (c) do not cover as much of the wall-normal distance due to the limitations of FOV3.

for  $\mathbf{R}_{pv}^+$ ; the first region of negative correlation has grown larger and more intense while the other two regions have become smaller and weaker. A second region of weak positive correlation has also emerged within the correlations, this time extending downstream at an angle from the wall to  $\Delta t U_c / \delta \approx 5$ .

Figure 5.6(b) reveals that the contours of  $\mathbf{R}_{pv}$  are nearly antisymmetric about  $\Delta t U_c = 0$ . The upstream region shows a negative correlation between  $p$  and  $v$ , while the downstream region shows a positive correlation which is slightly weaker than the former but comparable in size. The contours extend to  $\Delta t U_c / \delta \approx \pm 1.5$  and appear to reach the full height of the boundary layer. The same correlation in Naka et al. (2015) shows more differences between the sizes of the two lobes of correlation but are overall in good agreement with the present results. Comparison with Buchmann et al. (2016) is not possible because only the streamwise component of the correlation was reported in their study. When we consider  $\mathbf{R}_{pv}^+$ , the upstream region of correlation becomes more intense and the downstream region less intense; the opposite is true for  $\mathbf{R}_{pv}^-$ . This too is observed in the results of Naka et al. (2015). When  $\mathbf{R}_{pv}^+$  and  $\mathbf{R}_{pv}^-$  are considered together, it is evident that the motions that are most highly correlated with wall pressure generally have  $u$  and  $v$  components of opposite sign. This indicates that sweeps and ejections are an important feature of the pressure-velocity coupling.

Finally, the contours of  $\mathbf{R}_{pw}$  at  $z/\delta = 0.2$  are given in Figure 5.6(c). The contours indicate that the spanwise motions associated with wall pressure occupy up to at least  $y/\delta = 0.5$ . A region of positive correlation between  $p$  and  $w$  sits above  $\Delta t U_c / \delta = 0$  and has a total streamwise extent of  $\sim 1.5\delta$ . The region of positive correlation is attached and inclined to the wall and sits between two weaker regions of negative correlation, both of which also have streamwise extents of  $\sim 1.5\delta$ . The upstream region of negative correlation is away from the wall and extends horizontally across the mid-region of the boundary layer. The downstream region of negative correlation is narrow, inclined, and attached to the wall. When considering  $\mathbf{R}_{pw}^+$ , the region of positive correlation and the upstream region of negative correlation both become stronger, while the downstream region of negative correlation disappears. When considering  $\mathbf{R}_{pw}^-$ , the downstream region of negative correlation becomes stronger, the region of positive correlation becomes smaller, and the upstream region of negative correlation nearly disappears. These correlations are again consistent with the results of Naka et al. (2015).

The regions of positive and negative correlation in Figure 5.6(c) feature spanwise motion in opposite directions. When coupled with the wall-normal component of the correlations, it is evident that these patterns are associated with quasi-streamwise rotational motions. For example, when looking immediately downstream from the pressure measurement location,  $\mathbf{R}_{pv_i}^-$  shows spanwise motion towards  $z = 0$  near the wall, upward motion around  $z = 0$ , and motion away from  $z = 0$  farther from the wall to form a rotational pattern. The downstream interface between positive and negative correlation in  $\mathbf{R}_{pw}^-$  is therefore related to the rotational axes of an inclined vortical motion as is labelled in Figure 5.6(c). Similarly, the upstream interface between positive and negative correlation in  $\mathbf{R}_{pw}^+$  is associated with a vortical motion that is more horizontal. Because of the

symmetry of  $\mathbf{R}_{pv}$  and antisymmetry of  $\mathbf{R}_{pw}$  (about  $z = 0$ ), these vortical motions exist as counter-rotating pairs. This observation also supports the coupling between ejection/sweeping motions and wall pressure, as these motions are often induced by quasi-streamwise vortices.

All components of  $\mathbf{R}_{pu_i}^+$  and  $\mathbf{R}_{pu_i}^-$  can be used to visualize the motions and vortical structures associated with positive and negative wall-pressure fluctuations by forming vector fields from the correlations. These visualizations are presented in Figure 5.7, where the background shows the streamwise component of the correlations using the same colour scaling as Figure 5.6(a). Note that the correlations for negative wall-pressure fluctuations have been multiplied by  $-1$  so that the vector directions represent the true flow direction in the visualization. Figures 5.7(a,d) show the streamwise–wall-normal plane of the corresponding vector field at  $z = 0$ . These subfigures are marked with vertical lines which represent the locations of spanwise–wall-normal planes that are plotted directly below. The locations of these planes have been selected to show the most important features of each field. The vector density has been decimated and the vector lengths in the spanwise–wall-normal planes have been increased to improve the visualizations.

The visualization of  $\mathbf{R}_{pu_i}^+$  shown in Figures 5.7(a–c) reveals that positive wall-pressure fluctuations are associated with an elongated high-speed region with a relatively strong sweeping motion at its leading edge. This sweep is flanked by large low-speed zones and counter-rotating streamwise vortical motions, both of which can be seen in Figure 5.7(b); these vortical motions are nearly horizontal as is evident in the correlation patterns of  $\mathbf{R}_{pw}^+$  shown in Figure 5.6(c). A first-quadrant event, i.e., a motion with positive  $u$  and  $v$ , exists downstream from the large sweep as can be seen in Figures 5.7(a,c). The visualization of  $-\mathbf{R}_{pu_i}^-$  shown in Figures 5.7(d–f) indicates that negative wall-pressure fluctuations are associated with a localized upstream ejection and an elongated downstream sweep. This particular sweep sits away from the wall over most of its length. Figure 5.7(e) shows that the upstream ejection is not associated with counter-rotating vortex pairs, while Figure 5.7(f) shows that the downstream sweep is; these vortical motions are more strongly inclined with respect to the wall as is indicated in the patterns of  $\mathbf{R}_{pw}^-$  shown in Figure 5.6(c).

The motions visualized in Figure 5.7 are consistent with those discussed by Naka et al. (2015). However, they are not a satisfying description of the large-scale pressure-velocity coupling because it is difficult to find clear patterns of hairpin packets or VLSMs by inspection of these visualizations. This is because the correlations represent a superposition of many coherent structures of varying types, sizes, and locations. We therefore conclude that the flow patterns of Figure 5.7 are manifestations of the averaging process of the correlations. As we will see in the following sections, decomposing these correlations using different wall-pressure frequency bands yields simpler parts that are interpretable in terms of the large-scale coherent structures that are known to exist within TBLs.

### 5.3 Frequency-Dependent Pressure-Velocity Coupling

We now move on to the primary analyses of the present chapter. Our goal here is to scrutinize the coupling between the fluctuating wall pressure and velocity throughout the TBL as a function

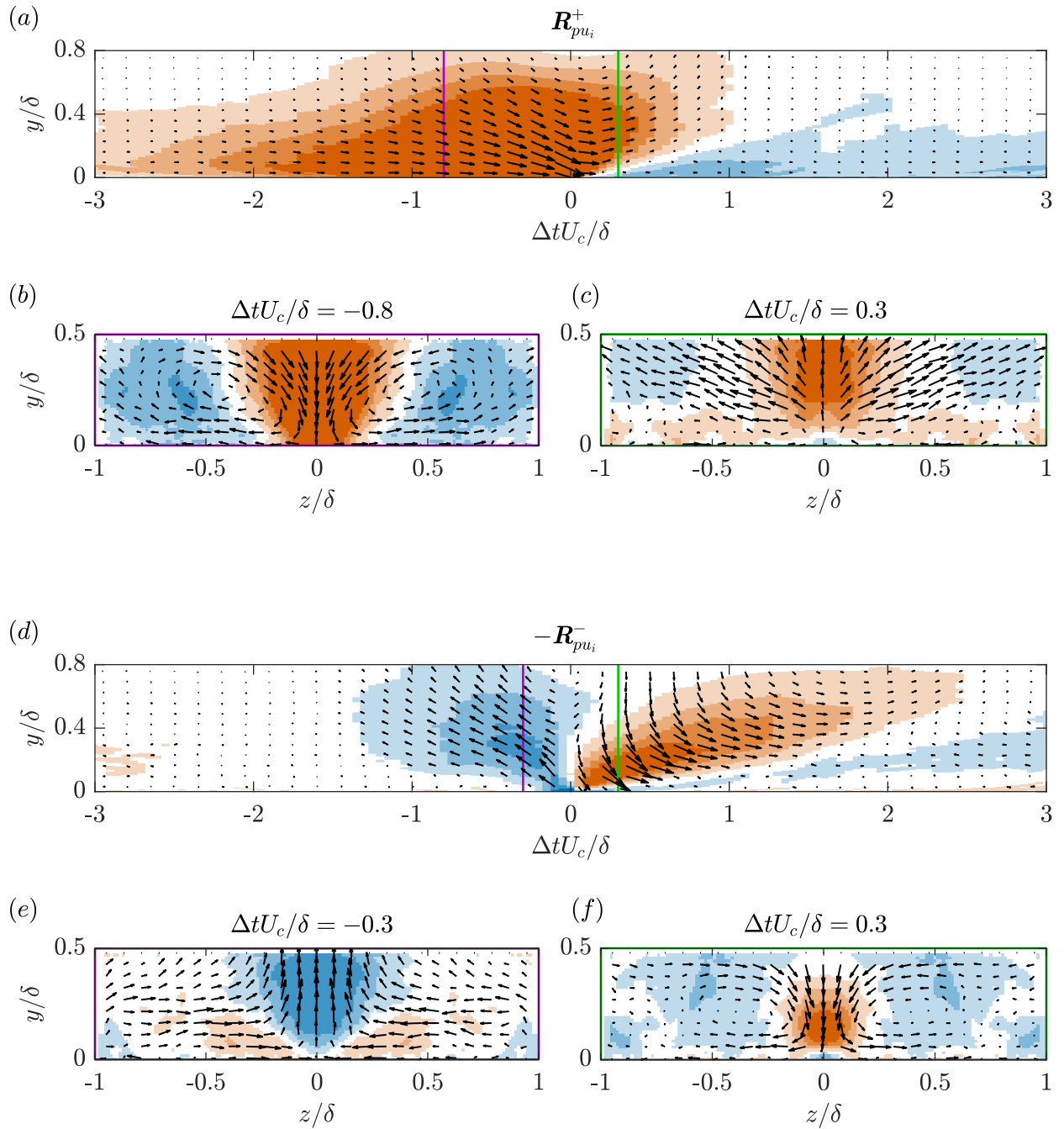


Figure 5.7: Visualizations of the vector fields associated with (a–c)  $\mathbf{R}_{pu_i}^+$  and (d–f)  $-\mathbf{R}_{pu_i}^-$ . The background colour represents the streamwise component of the correlations and has the same scaling as Figure 5.6(a). The coloured lines in (a,d) show the locations of the spanwise–wall-normal planes that are plotted directly below. The vector lengths in (b,c,e,f) have been altered relative to those in (a,d) to improve the visualizations.

of frequency. As we will see, there are two distinct coupling mechanisms at the lower frequencies that affect different frequency bands. We first identify these bands using estimates of the coherence between wall pressure and velocity. We then extract the space-time pressure-velocity correlations associated with each band to expose the underlying coherent structures responsible for the observed coupling.

### 5.3.1 Coherence Between Wall Pressure and Velocity

The cross-spectrum between wall pressure and velocity will allow us to study the pressure-velocity coupling as a function of frequency. Here we employ a normalized form of the cross-spectral density known as the magnitude-squared coherence, which will simply be referred to as the coherence moving forward. The coherence between the fluctuating wall pressure and a fluctuating velocity component is defined as

$$\mathbf{C}_{pu_i}(\omega, y) = \frac{|\Phi_{pu_i}(\omega, y)|^2}{\Phi_p(\omega)\Phi_{u_i}(\omega, y)}, \quad (5.2)$$

where  $\Phi_{pu_i}(\omega, y)$  is the cross-spectral density between  $p(t)$  and  $u_i(t, 0, y, 0)$ , and  $\Phi_{u_i}(\omega, y)$  is the PSD of  $u_i(t, 0, y, 0)$ . Equation (5.2) is estimated here using Welch's overlapping segment method. The coherence function is bounded by 0 and 1, with 0 representing no correlation between the two signals at a given frequency. A coherence of 1 occurs when the two signals are related through a single-input single-output linear, time-invariant system. The latter will never be realized for a turbulent flow due to the nonlinearity and multiple inputs of the governing equations, but the coherence will allow us to probe any coupling that may exist between wall pressure and velocity.

The estimated coherence between wall pressure and the fluctuating velocity components  $u$  and  $v$  for the wall-normal range of FOV2 are presented on logarithmic axes in Figures 5.8(a,b). The PSD of wall pressure is included in Figure 5.8(c) with the frequency axis aligned to those showing  $\mathbf{C}_{pu_i}$  for reference. When looking at Figure 5.8(a), it is immediately apparent that there are two separate regions of high coherence with distinct characteristics. We demarcate these two regions using the dotted vertical lines in the figure at  $\omega\delta/U_\infty = 0.9$  (17.5 Hz) and 8.0 (160 Hz). These demarcations were selected by visual inspection of the coherence patterns. Note that there is a slight overlap in frequencies for which the first region of high-coherence transitions to the second, and therefore the interface separating the two regions is not a straight vertical line. Despite this, we have selected the single frequency of  $\omega\delta/U_\infty = 0.9$  as the division between these two regions to simplify the analysis moving forward. The upper frequency of the second region of high coherence was selected as the point at which the coherence drops below  $\sim 0.05$  in Figure 5.8(b).

The first coherent region in Figure 5.8(a), defined by  $\omega\delta/U_\infty < 0.9$ , reveals high coherence between  $p$  and  $u$  for wall-normal locations up to roughly  $y/\lambda = 1300$  ( $\sim 0.5\delta$ ). In contrast, for the same frequencies, the coherence between  $p$  and  $v$  in Figure 5.8(b) is much weaker. This suggests that low frequency  $u$  occupying half the boundary layer thickness correlates with low-frequency

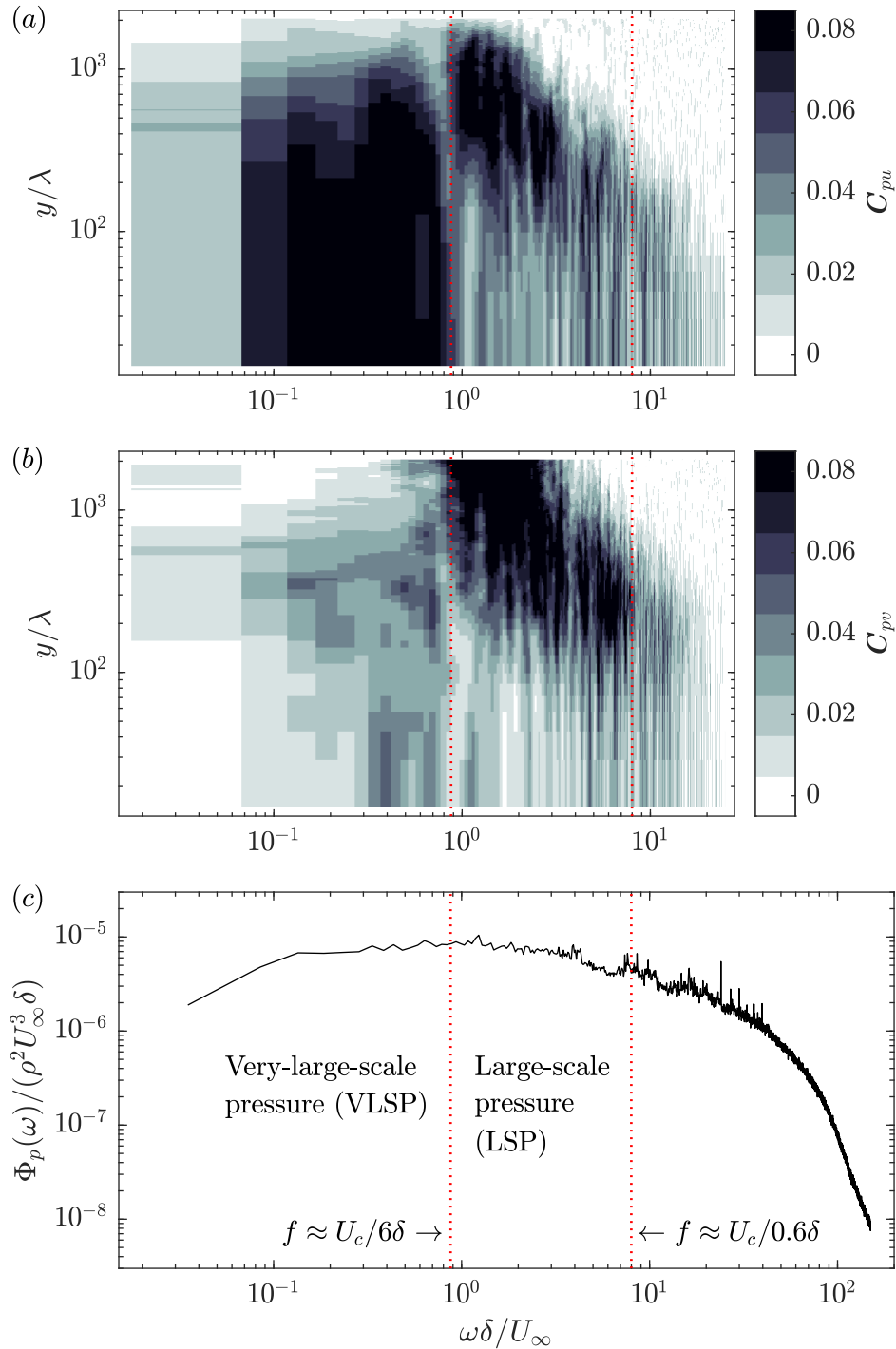


Figure 5.8: Estimated coherence between wall pressure and velocity fluctuation ( $C_{pu_i}$ ) as a function of wall-normal distance as defined by Equation (5.2) for the (a) streamwise and (b) wall-normal velocity components. Computed using the high-speed PIV measurements from FOV2. The PSD ( $\Phi_p(\omega)$ ) normalized by outer-layer variables is shown in (c) with the frequency axis aligned for reference.

wall pressure. To estimate the size of the structures associated with the first coherent region, we assume that the advection velocity of these structures is the mean velocity at the half-height of the coherent region ( $y/\lambda = 650$ ;  $y = 0.25\delta$ ), corresponding to  $U_c \approx 0.82U_\infty$ . A pressure disturbance advecting at this velocity would need to have a wavelength of  $\sim 6\delta$  to produce the upper cutoff frequency of  $\omega\delta/U_\infty = 0.9$ . Note that one full wavelength would be made up of a positive structure ( $p > 0$ ) followed by a negative structure ( $p < 0$ ) to produce a pattern similar to a sinusoid. The first coherent region therefore seems to be associated with high- and low-pressure structures occupying up to  $\sim 0.5\delta$  in height and extending more than  $3\delta$  in length. This is consistent with the VLSPs, and for this reason we will refer to the pressure fluctuations in the first coherent region as the very-large-scale pressure (VLSP) fluctuations as labelled in Figure 5.8(c).

We will now consider the second region of high coherence in Figure 5.8 defined by  $0.9 < \omega\delta/U_\infty < 8.0$ . This region is markedly different than the one associated with the VLSP fluctuations. First, a higher coherence is observed between  $p$  and  $v$  than between  $p$  and  $u$ , although the latter is still quite strong. Second, the region sits at an angle, with lower frequencies associated with locations farther from the wall. This is reminiscent of the attached-eddy hypothesis, as larger attached eddies that extend farther from the wall would be associated with lower frequencies due to the size of the pressure disturbance that they produce. Finally, the second region of high coherence between  $p$  and  $v$  extends farther from the wall than the coherence of the VLSP, surpassing the maximum captured by FOV2 ( $\sim 0.8\delta$ ). It is possible that  $C_{pv}$  reaches the full height of the boundary layer, and this is not observed for  $C_{pu}$ . This suggests that the pressure fluctuations associated with this region are stronger than the VLSP fluctuations, as they appear to influence the wall pressure from a greater wall-normal distance. To estimate the size of the structures associated with the upper cutoff frequency of the second region of high coherence ( $\omega\delta/U_\infty = 8.0$ ), we assume an advection velocity of  $U_c = 0.74U_\infty$ . This is the mean velocity at  $y/\lambda = 300$ , which is roughly the mid-point of the high-coherence region at the upper cutoff as is visible in Figure 5.8(b). A pressure disturbance advecting at this velocity would need to have a wavelength of  $\sim 0.6\delta$  to reproduce the cutoff frequency of  $\omega\delta/U_\infty = 8.0$ . We therefore conclude, using the same logic invoked for VLSP, that the second region of high coherence seems to be associated with high- and low-pressure structures with streamwise dimensions ranging from roughly  $0.3\delta$  to  $3\delta$ . We can consider this range of eddy sizes as being large scale, and therefore the wall-pressure fluctuations associated with the second region of high coherence will be referred to as the large-scale pressure (LSP) fluctuations as labelled in Figure 5.8(c).

It is interesting to note that the demarcation between VLSP and LSP coincides with the peak of the wall-pressure spectrum as is evident in Figure 5.8(c). The location of the peak, and the different proportionality behaviours on either side, may therefore be associated with a transition between wall-pressure sources, as  $C_{pui}$  indicates that different motions are responsible for the wall pressure in the frequency bands on either side of  $\omega\delta/U_\infty = 0.9$ . The nature of these two types of motions will be determined in sections 5.3.2 and 5.3.3. It should also be noted that the two frequency cutoffs do not coincide with the transition between any of the regions of the wall-pressure power spectrum

shown in Figure 5.4. It can be seen in the figure that  $\omega\delta/U_\infty = 0.9$  is roughly one-quarter of the way through the mid-frequency region, while  $\omega\delta/U_\infty = 8.0$  is roughly one-third of the way through the overlap region.

We now investigate the estimated phase between  $p$  and  $u_i$  from the cross-spectral densities, denoted as  $\angle\Phi_{pu_i}(\omega)$ . These estimates are given in Figure 5.9 for the same domain shown for the coherence estimates, and the demarcations for the LSP and VLSP bands are included for reference. Here, a positive phase indicates that  $p$  leads  $u_i$ , while a negative phase indicates that  $p$  lags  $u_i$ . The noisy region in the top right corner of both subfigures is due to the general lack of coherence between  $p$  and  $u_i$  at high frequencies and wall-normal locations as can be seen in Figure 5.8. A cursory glance at Figure 5.9 makes it clear that  $\angle\Phi_{pu}(\omega)$  is always positive in the regions of non-zero coherence, while  $\angle\Phi_{pv}(\omega)$  is always negative. This is in agreement with the space-time pressure-velocity correlations of Figure 5.6, which show that the positive peak of  $\mathbf{R}_{pu}$  always exists upstream from the wall-pressure measurement location (i.e.,  $p$  leads  $u$ ), and that the positive peak of  $\mathbf{R}_{pv}$  always exists downstream (i.e.,  $p$  lags  $v$ ). Focusing now on the region of high coherence within the LSP band of Figure 5.8, we can see that Figure 5.9(a) indicates a phase varying from roughly  $0.25\pi$  to  $0.35\pi$  between  $p$  and  $u$ , while Figure 5.9(b) indicates a phase of roughly  $-0.5\pi$  to  $-0.6\pi$  between  $p$  and  $v$ . In contrast, the region of high coherence within the VLSP band of Figure 5.8 shows different behaviour. Here, we can see a phase of roughly  $0.1\pi$  to  $0.25\pi$  between  $p$  and  $u$ , and a phase of roughly  $-0.7\pi$  to  $-0.8\pi$  between  $p$  and  $v$ . These results support the notion that different mechanisms are responsible for the observed coupling in the LSP and VLSP bands.

We have further evaluated the characteristics of the LSP and VLSP fluctuations by applying filters to isolate the associated frequencies. A lowpass filter with a cutoff frequency of  $\omega\delta/U_\infty = 0.9$  was used to isolate the VLSP fluctuations, and a bandpass filter with cutoffs of  $\omega\delta/U_\infty = 0.9$  and  $8.0$  was used to isolate the LSP fluctuations. These filters were designed as digital finite impulse response filters with the cutoff frequencies placed at  $-6$  dB attenuation. The filter slopes were made as steep as possible while keeping the filters numerically tractable, and they were applied such that the filter time delay was compensated. The filter responses are shown in Figure 5.10. We refer to the two filtered wall-pressure signals as  $p_{LS}$  and  $p_{VLS}$ .

The probability density functions of  $p_{LS}$  and  $p_{VLS}$  are compared to that of the full spectrum in Figure 5.11. The functions are displayed on linear and semi-logarithmic axes and are compared to Gaussian fits for reference. The horizontal axes are normalized using  $p_{rms}$  of the full spectrum in all cases. Figure 5.11(a) reveals that the peak probability density of  $p_{VLS}$  is more than four times that of the full spectrum, while the peak for  $p_{LS}$  is not quite double. This indicates that the wall-pressure fluctuations within these two frequency bands are lower in magnitude in general, with the  $p_{VLS}$  having the lowest magnitudes. More precisely, the root-mean-square value of  $p_{LS}$  and  $p_{VLS}$  are 53% and 20% of  $p_{rms}$ , respectively. This is consistent with the results of Beresh et al. (2013), who found that low-frequency wall-pressure fluctuations are weaker than high-frequency wall-pressure fluctuations. Figure 5.11(a) also reveals that  $p_{LS}$  deviates slightly from the Gaussian fit at the peak, while  $p_{VLS}$  does not. Figure 5.11(b) reveals some deviation from Gaussian at the

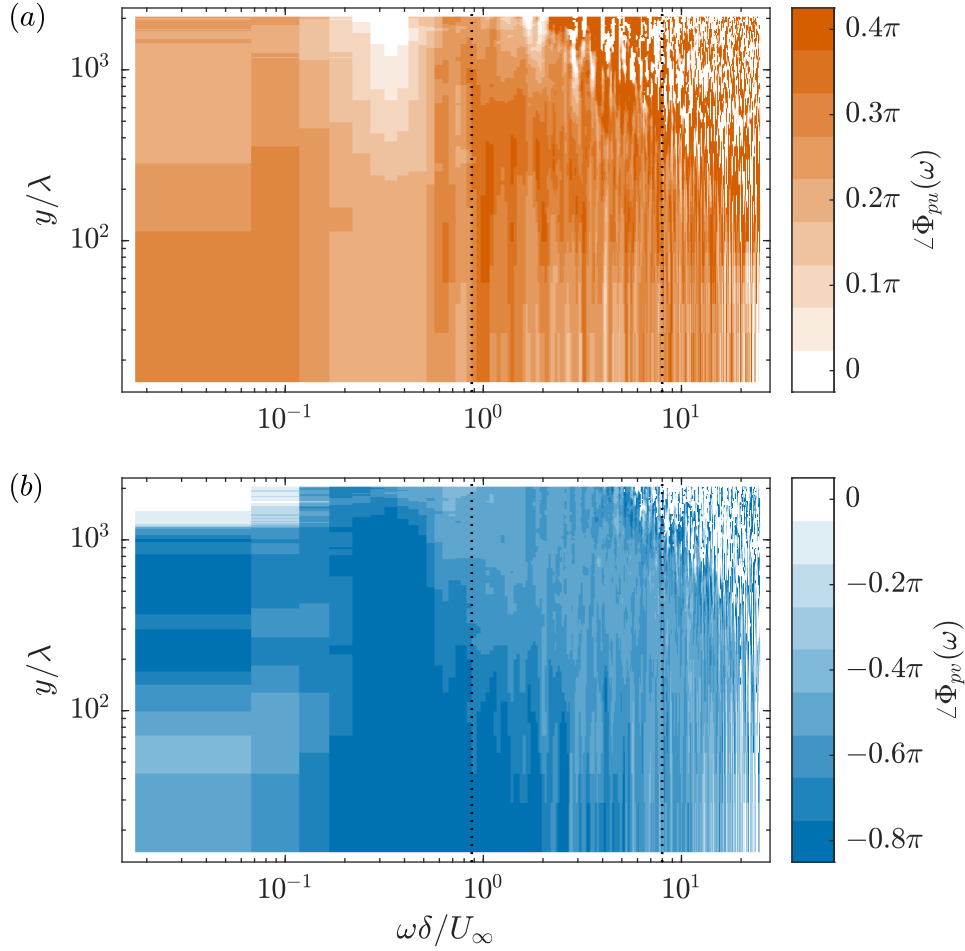


Figure 5.9: Estimated phase between wall pressure and velocity fluctuation ( $\angle\Phi(\omega)_{pu_i}$ ) as a function of wall-normal distance for the (a) streamwise and (b) wall-normal velocity components. Computed using the measurements from FOV2. A positive phase indicates that  $p$  leads  $u_i$  while a negative phase indicates that  $p$  lags  $u_i$ .

extreme tails for  $p_{LS}$ , but this is again not observed for  $p_{VLS}$ , which appears to adhere to Gaussian behaviour at all amplitudes. We therefore conclude that the VLSP fluctuations are Gaussian, while the LSP fluctuations are nearly Gaussian.

### 5.3.2 Very-Large-Scale Coupling

In the previous section, the coherence function between wall pressure and fluctuating velocity revealed two distinct frequency bands of high coherence which appear to be associated with structures with lengths ranging from roughly  $0.3\delta$  to  $3\delta$  for one band and lengths greater than  $3\delta$  for the other. We therefore refer to these bands as the LSP and VLSP fluctuations, respectively, and we denote their pressure signals as  $p_{LS}$  and  $p_{VLS}$ . Within this section, we further investigate the pressure-velocity coupling associated with the VLSP band. The coupling observed in the LSP band will be

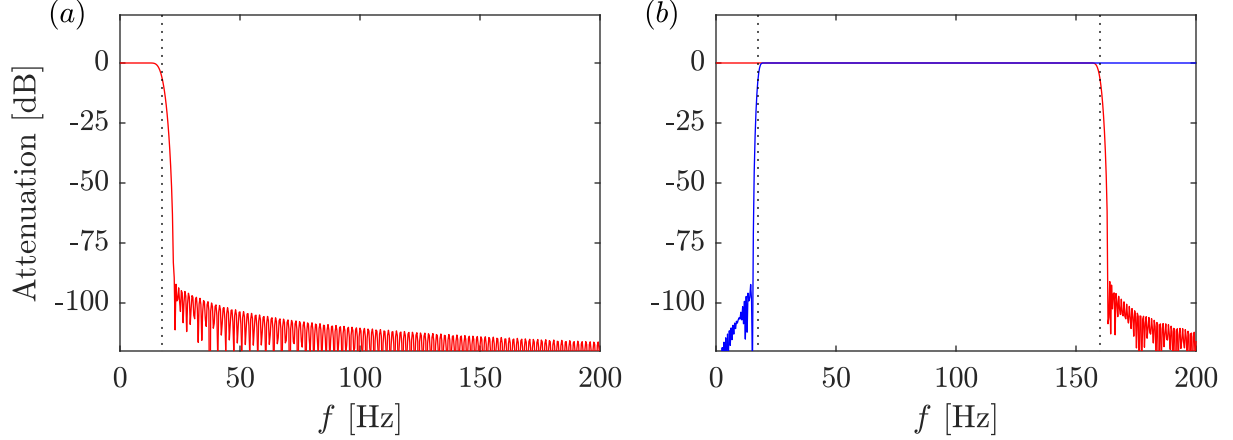


Figure 5.10: The filters used to isolate the (a) VLSP fluctuations and (b) LSP fluctuations. The red and blue filter responses denote lowpass and highpass filters, respectively. The vertical dotted lines denote the filter cutoff frequencies and coincide with the points of  $-6$  dB attenuation.

investigated in Section 5.3.3.

We revisit the space-time pressure-velocity correlations computed in Section 5.2.2, but this time using  $p_{\text{VLS}}$  in place of  $p$ . By using only  $p_{\text{VLS}}$  to compute the correlations, we are isolating the motions that cause these fluctuations and therefore we are extracting the portion of  $\mathbf{R}_{p u_i}$  associated with the VLSP band. We define the space-time pressure-velocity correlation associated with the VLSP band as  $\mathbf{R}_{p u_i}^{\text{VLS}} = \mathbf{R}_{p u_i}|_{p=p_{\text{VLS}}}$  following Equation (5.1) where  $p_{\text{VLS}}$  has been isolated using a lowpass filter as described in Section 5.3.1. We also consider the correlations computed using only  $p_{\text{VLS}} > 0$  or  $p_{\text{VLS}} < 0$  to isolate the motions associated with each sign of fluctuation. These conditional cases are denoted as  $\mathbf{R}_{p u_i}^{\text{VLS}+} = \mathbf{R}_{p u_i}^{\text{VLS}}|_{p_{\text{VLS}}>0}$  and  $\mathbf{R}_{p u_i}^{\text{VLS}-} = \mathbf{R}_{p u_i}^{\text{VLS}}|_{p_{\text{VLS}}<0}$ .

We begin by considering the streamwise-wall-normal slices of  $\mathbf{R}_{p u_i}^{\text{VLS}}$ ,  $\mathbf{R}_{p u_i}^{\text{VLS}+}$ , and  $\mathbf{R}_{p u_i}^{\text{VLS}-}$  in Figure 5.12. The streamwise and wall-normal components are plotted at  $z = 0$ , while the spanwise component is plotted at  $z/\delta = 0.2$ . Note that the colourbar scaling is reduced compared to that of  $\mathbf{R}_{p u_i}$  in Figure 5.6 because the correlation magnitudes are considerably weaker, especially for the wall-normal and spanwise components. This is likely because the wall-pressure fluctuations in the VLSP band are five times weaker than those of the full spectrum as was shown in Figure 5.11.

Figure 5.12 makes it immediately apparent that the motions most correlated with the VLSP fluctuations are unlike those captured by the correlations computed using the full wall-pressure spectrum. The contours of  $\mathbf{R}_{p u_i}^{\text{VLS}}$  displayed in Figure 5.12(a) reveal that  $p_{\text{VLS}}$  is positively correlated with  $u$  over a large streamwise extent of  $-3.8 \lesssim \Delta t U_c / \delta \lesssim 1.8$  and reaching beyond  $y/\delta = 0.8$  in height. A much smaller and weaker region of negative correlation exists upstream, and a somewhat weaker but highly elongated region of negative correlation extends far downstream from the positively correlated region. The entirety of these regions are not shown in Figure 5.12(a) to keep the figure manageable. However, we note that the upstream region of weak negative correlation exists between  $-6.6 \lesssim \Delta t U_c / \delta \lesssim -4.2$ , and the downstream region extends to upwards of  $\Delta t U_c / \delta \approx 12$ .

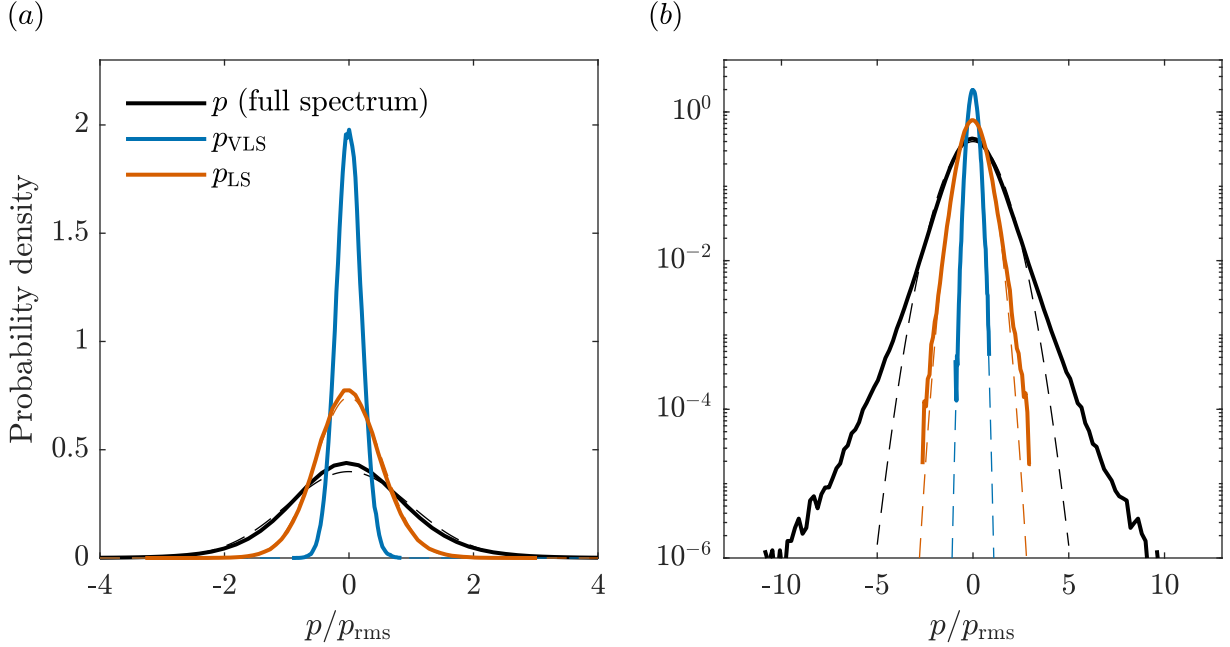


Figure 5.11: Probability density of the full spectrum of wall-pressure fluctuations compared to that of the LSP and VLSP fluctuations shown on (a) linear and (b) semi-logarithmic axes. The dashed lines represent Gaussian fits to the same data.

This latter region of correlation seems to be the source of the highly elongated, wall-attached region of negative correlation visible in the contours of  $\mathbf{R}_{pu}$  and  $\mathbf{R}_{pu}^+$  shown in Figure 5.6(a). In contrast to the correlations computed using the full wall-pressure spectrum, the contours of  $\mathbf{R}_{pu}^{\text{VLS}+}$  and  $\mathbf{R}_{pu}^{\text{VLS}-}$  remain largely unchanged relative to  $\mathbf{R}_{pu}^{\text{VLS}}$ .

Figure 5.12(b) reveals a large region of negative correlation in the contours of  $\mathbf{R}_{pv}^{\text{VLS}}$ . This region extends through the range  $-4.3 \lesssim \Delta t U_c / \delta \lesssim 1.1$ , exceeds  $y/\delta = 0.8$ , and has a different shape overall when compared to that of  $\mathbf{R}_{pu}^{\text{VLS}}$ . Regions of weaker positive correlation with similar shapes sit immediately upstream and downstream from this region of negative correlation, revealing a clear alternating pattern. The coherence estimates of Figure 5.8 showed a much higher coherence between  $p_{\text{VLS}}$  and  $u$  than between  $p_{\text{VLS}}$  and  $v$ . This is also apparent in the present correlations, as  $\mathbf{R}_{pv}^{\text{VLS}}$  is approximately four times weaker than  $\mathbf{R}_{pu}^{\text{VLS}}$ . In addition, the contours of  $\mathbf{R}_{pv}^{\text{VLS}+}$  and  $\mathbf{R}_{pv}^{\text{VLS}-}$  also appear to remain relatively unchanged compared to  $\mathbf{R}_{pv}^{\text{VLS}}$ , just as was the case for the streamwise component. The regions of high correlation that overlap between  $\mathbf{R}_{pu}^{\text{VLS}}$  and  $\mathbf{R}_{pv}^{\text{VLS}}$  reveal that the motions most correlated with  $p_{\text{VLS}}$  feature  $u$  and  $v$  of opposite sign. However, these motions are different from sweeps and ejections, which are typically more localized and intense. Instead, these motions appear to be large-scale high- and low-speed streaks with relatively weak wall-normal velocity components.

The wall-normal velocity visible in  $\mathbf{R}_{pv}^{\text{VLS}}$  is supported by the contours of  $\mathbf{R}_{pw}^{\text{VLS}}$  in Figure 5.12(c). The near-wall region of strong positive correlation within the subfigure indicates that there is fluid motion away from  $z = 0$  beneath the high-speed streaks (splating) and motion towards  $z = 0$

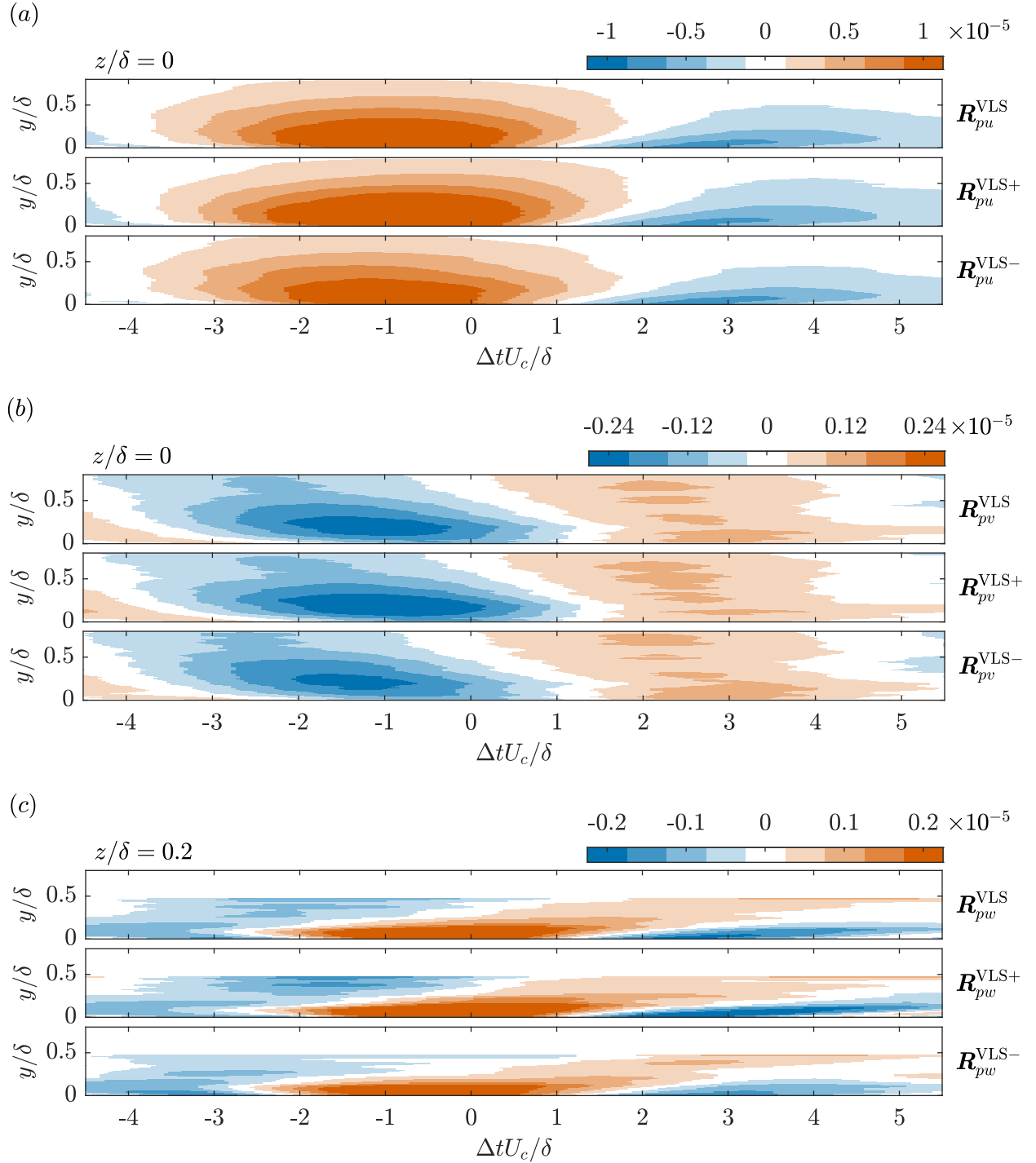


Figure 5.12: (a) Streamwise, (b) wall-normal, and (c) spanwise components of the space-time pressure-velocity correlations computed using pressure filtered to isolate the VLSP fluctuations ( $\mathbf{R}_{p u_i}^{\text{VLS}} = \mathbf{R}_{p u_i}^{\text{VLS}}|_{p=p_{\text{VLS}}}$ ) following Equation (5.1). The superscripts ‘+’ and ‘-’ denote correlations computed using only  $p_{\text{VLS}} > 0$  or  $p_{\text{VLS}} < 0$ , respectively. The streamwise–wall-normal planes in (a) and (b) are located at  $z = 0$ , while those in (c) are located at  $z = 0.2\delta$ . The plots in (c) do not cover as much of the wall-normal distance due to the limitations of FOV3.

beneath the low-speed streaks (an influx to replace the fluid being lifted). Additionally, a region of weaker negative correlation with a similar streamwise extent exists upstream from the region of positive correlation. A large portion ( $\sim 3\text{--}4\delta$ ) of these two regions of opposite correlation overlap in the streamwise direction, forming a region where the spanwise motion near the wall is opposite to the spanwise motion above it. When considered along with  $\mathbf{R}_{pv}^{\text{VLS}}$ , which has a comparable magnitude, it is straightforward to see that the large-scale streaks associated with the VLSP band are accompanied by quasi-streamwise vortex pairs that are nearly horizontal. Finally, Figure 5.12(c) reveals that the contours of  $\mathbf{R}_{pw}^{\text{VLS}}$  are also largely invariant when considering only positive or negative VLSP fluctuations, just as was the case for the other two components of the correlation. This suggests that the motions that are responsible for  $p_{\text{VLS}} > 0$  and  $p_{\text{VLS}} < 0$  are quite similar but opposite to one another.

To conclude our analysis of the pressure-velocity coupling in the VLSP band, we form visualizations of the motions responsible for  $p_{\text{VLS}} > 0$  and  $p_{\text{VLS}} < 0$ . The vector fields associated with  $\mathbf{R}_{pui}^{\text{VLS}+}$  and  $-\mathbf{R}_{pui}^{\text{VLS}-}$  are presented in Figures 5.13(a–c) and 5.13(d–f), respectively. The latter correlation has been multiplied by  $-1$  to capture the correct flow direction of the associated velocity fluctuations. Figures 5.13(a,d) show the streamwise–wall-normal plane of the corresponding vector field at  $z = 0$ . These subfigures are marked with vertical lines which represent the locations of spanwise–wall-normal planes of the same vector field that are plotted directly below. To improve the visualizations, the vector density has been decimated and the vector lengths in the spanwise–wall-normal planes have been increased. The background colour denotes the streamwise component of the correlations and has the same scaling as Figure 5.12(a).

The average motion associated with  $p_{\text{VLS}} > 0$  in Figures 5.13(a–c) is a region of positive streamwise velocity fluctuation extending  $\sim 5.6\delta$  in the streamwise direction, spanning to  $z/\delta \approx \pm 0.4$ , and reaching to at least  $y/\delta = 0.8$  in height. This motion is accompanied by a relatively weak negative wall-normal component and is flanked by similar regions of low streamwise velocity. Quasi-streamwise vortical motions with a slight angle with respect to the wall are found at the interfaces between the primary high-speed region and the adjacent low-speed regions. This inclination is apparent from the change in height of the vortical motions between Figures 5.13(b,c). The average motion associated with  $p_{\text{VLS}} < 0$  in Figures 5.13(d–f) is similar to the one for  $p_{\text{VLS}} > 0$ , but with an opposite direction of velocity fluctuation. This low-speed region is also flanked by large opposite motions and quasi-streamwise vortices. It also appears to be a bit narrower than the motion associated with  $p_{\text{VLS}} > 0$ .

The motions visualized in Figure 5.13 can clearly be associated with the VLSPs, as all visible features are consistent with the statistical appearance of the VLSPs reported in the literature to date. The observed streamwise extent of the correlations is greater than the minimum of  $3\delta$  defined for the VLSPs (Balakumar and Adrian, 2007) and also closely matches the length of the VLSPs as it appears in statistical measures ( $\sim 6\delta$ ) (Hutchins and Marusic, 2007a; Lee and Sung, 2011). Additionally, the wall-normal and spanwise extents of the correlations capture the range of heights and widths of the VLSPs measured in previous work (Dennis and Nickels, 2011a). The structure of

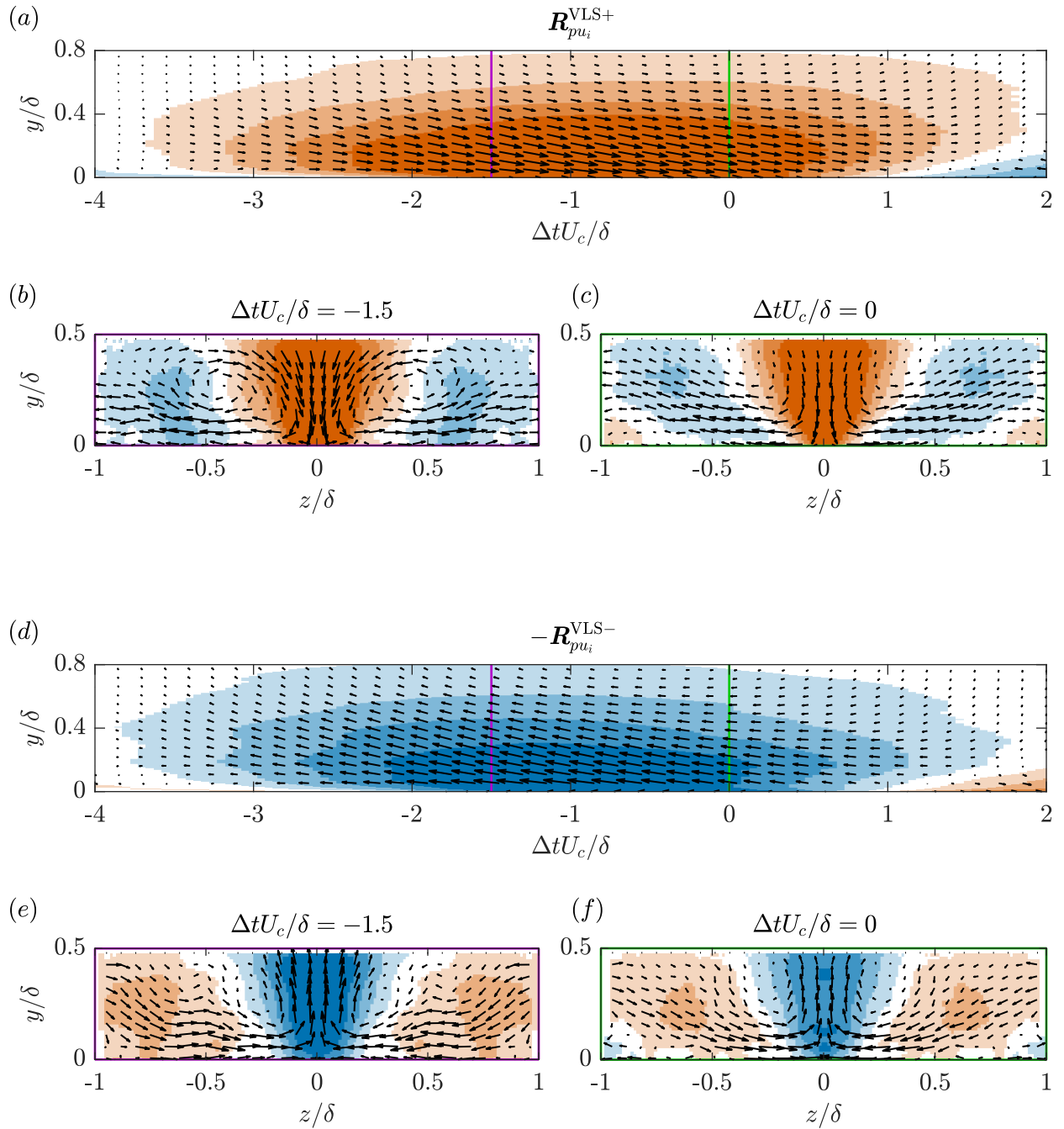


Figure 5.13: Visualizations of the vector fields associated with (a–c)  $\mathbf{R}_{pui}^{\text{VLS}+}$  and (d–f)  $-\mathbf{R}_{pui}^{\text{VLS}-}$ . The background colour represents the streamwise component of the correlations and has the same scaling as Figure 5.12(a). The coloured lines in (a,d) show the locations of the spanwise–wall-normal planes that are plotted directly below. The vector lengths in (b,c,e,f) have been altered relative to those in (a,d) to improve the visualizations.

the correlations also shows that low-speed VLSMs are flanked by high-speed VLSMs and vice versa, and that the interfaces between these opposite motions feature counter-rotating streamwise vortical motions. This exact structure has been observed in statistical representations of the VLSMs in past investigations (Hutchins and Marusic, 2007b; Marusic and Hutchins, 2008; Chung and McKeon, 2010; Hutchins et al., 2012), where the counter-rotating vortical motions are often referred to as “roll modes”. It is well accepted at this point that the low-speed VLSMs exist between the legs of large hairpins (Kim and Adrian, 1999; Elsinga et al., 2010; Lee and Sung, 2011; Dennis and Nickels, 2011b). These hairpins exist in packets which induce the elongated low-speed zones via the ejection of near-wall fluid. The same hairpins also cause the formation of elongated high-speed zones at the sides of the packets, as the outer regions of the hairpin legs sweep high-speed fluid towards the wall. This process results in the observed spanwise staggering of opposite VLSMs. It also explains the weak wall-normal components and “roll modes” in the correlations, which appear as average motions due to the continuous presence of hairpins. We can therefore conclude that the pressure-velocity coupling observed within the VLSP band of Figure 5.8 is a direct result of the VLSMs.

### 5.3.3 Large-Scale Coupling

We now move on to investigating the pressure-velocity coupling observed within the LSP band of Figure 5.8. We denote the wall-pressure fluctuations within the LSP band as  $p_{LS}$ , and we have isolated these fluctuations using a bandpass filter as described in Section 5.3.1. We compute space-time pressure-velocity correlations using  $p_{LS}$  to isolate the portion of  $\mathbf{R}_{pu_i}$  associated with the LSP fluctuations, and we define this correlation as  $\mathbf{R}_{pu_i}^{LS} = \mathbf{R}_{pu_i}|_{p=p_{LS}}$  following Equation (5.1). The correlations computed using only  $p_{LS} > 0$  or  $p_{LS} < 0$  are also considered and are denoted as  $\mathbf{R}_{pu_i}^{LS+} = \mathbf{R}_{pu_i}|_{p_{LS}>0}$  and  $\mathbf{R}_{pu_i}^{LS-} = \mathbf{R}_{pu_i}|_{p_{LS}<0}$ .

Streamwise-wall-normal planes of  $\mathbf{R}_{pu_i}^{LS}$ ,  $\mathbf{R}_{pu_i}^{LS+}$ , and  $\mathbf{R}_{pu_i}^{LS-}$  are given in Figure 5.14. To remain consistent with the previous analyses, the streamwise and wall-normal components are plotted at  $z = 0$ , while the spanwise component is plotted at  $z/\delta = 0.2$ . We note that the colourbar scaling is the same as that used to show  $\mathbf{R}_{pu_i}$  in Figure 5.6. When looking at Figure 5.14 as a whole, it is clear that the overall structure of  $\mathbf{R}_{pu_i}^{LS}$  is quite similar to that of  $\mathbf{R}_{pu_i}$ . However, one change that is immediately apparent is that the most elongated, wall-attached features of  $\mathbf{R}_{pu_i}$  are no longer present. These features can clearly be attributed to the lower frequencies of the VLSP band as was shown in Section 5.3.2.

The contours of  $\mathbf{R}_{pu}^{LS}$  in Figure 5.14(a) feature a region of positive correlation that sits above the pressure measurement location and reaches upstream to  $\Delta t U_c/\delta \approx -1.1$  and to at least  $y/\delta = 0.8$  in height. A region of negative correlation begins just downstream from the pressure measurement location, extending from the wall at an angle to reach  $\Delta t U_c/\delta \approx 2.3$  and  $y/\delta \approx 0.8$ . An alternation between positive and negative correlation in the streamwise direction is now visible, as two new regions of weak correlation have emerged farther upstream and downstream with opposite sign to the regions that are adjacent. When considering  $\mathbf{R}_{pu}^{LS+}$ , the contours closest to the pressure

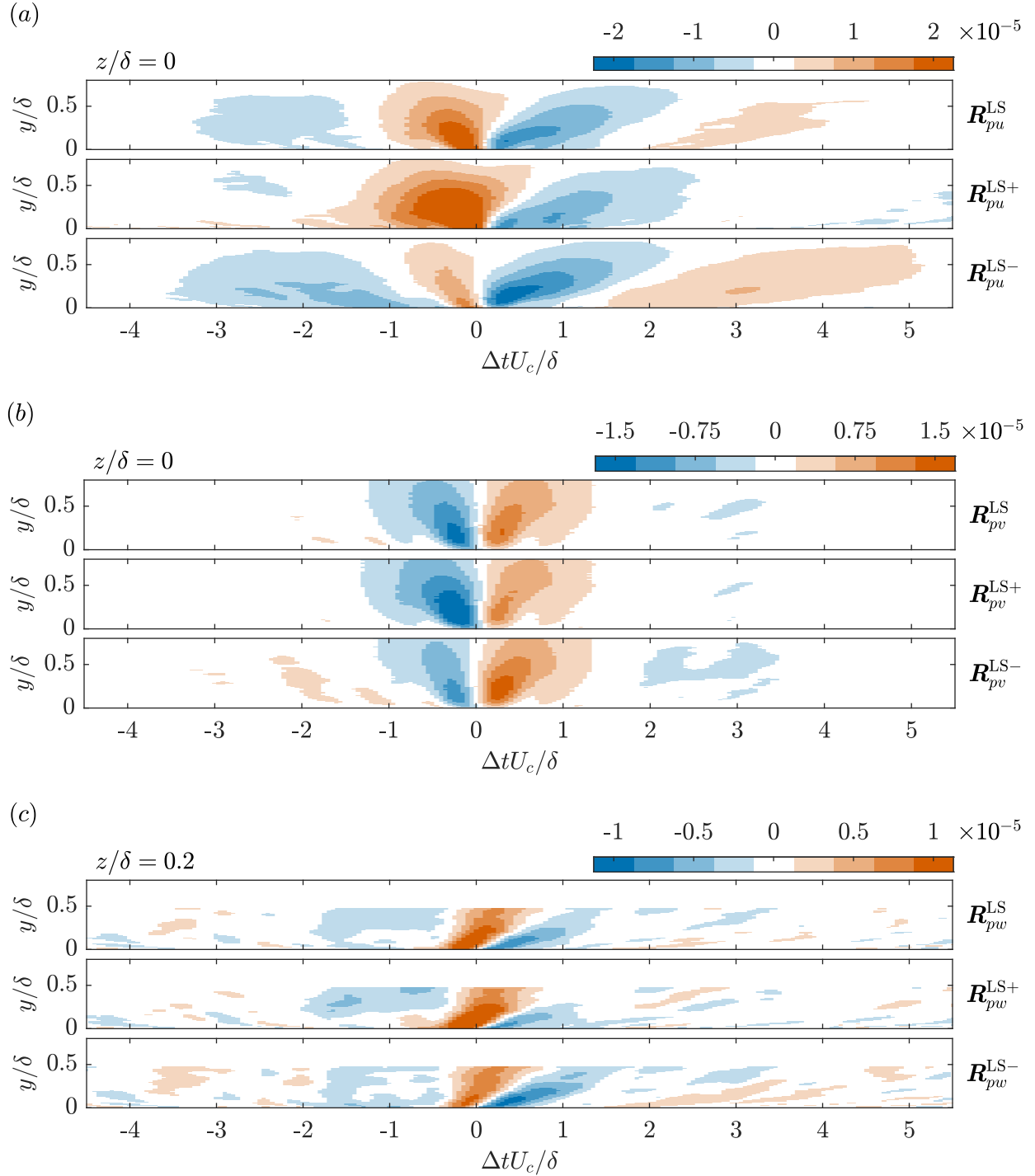


Figure 5.14: (a) Streamwise, (b) wall-normal, and (c) spanwise components of the space-time pressure-velocity correlations computed using pressure filtered to isolate the LSP fluctuations ( $\mathbf{R}_{p u_i}^{\text{LS}} = \mathbf{R}_{p u_i}^{\text{LS}}|_{p=p_{\text{LS}}}$ ) following Equation (5.1). The superscripts ‘+’ and ‘-’ denote correlations computed using only  $p_{\text{LS}} > 0$  or  $p_{\text{LS}} < 0$ , respectively. The streamwise–wall-normal planes in (a) and (b) are located at  $z = 0$ , while those in (c) are located at  $z = 0.2\delta$ . The plots in (c) do not cover as much of the wall-normal distance due to the limitations of FOV3.

measurement location enlarge, and the outer regions of weak correlation mostly disappear. For  $\mathbf{R}_{pu}^{\text{LS-}}$ , the region of positive correlation immediately upstream from the pressure measurement location becomes smaller, and the outer regions of weak correlation enlarge. These outer regions of correlation have now become quite elongated with streamwise extents of  $\sim 3\text{--}4\delta$ .

The contours of  $\mathbf{R}_{pv}^{\text{LS}}$  in Figure 5.14(b) are nearly identical to those of  $\mathbf{R}_{pv}$  in Figure 5.6(b). Some small differences are found in the magnitudes, but the shapes and sizes do not change much when only the LSP fluctuations are considered. This remains true when the correlations are computed using only the positive or negative wall-pressure fluctuations. Similarly,  $\mathbf{R}_{pw}^{\text{LS}}$ ,  $\mathbf{R}_{pw}^{\text{LS+}}$ , and  $\mathbf{R}_{pw}^{\text{LS-}}$  in Figure 5.14(c) are quite similar to their full-spectrum counterparts in Figure 5.6(c). We will therefore not describe these contours in detail for the sake of brevity. However, we note that the patterns of Figures 5.14(b,c) reveal that inclined counter-rotating vortex pairs exist downstream from the wall-pressure measurement location in all cases. These downstream vortices were only present for negative wall-pressure fluctuations in the full-spectrum correlations.

The strong similarities between  $\mathbf{R}_{pu_i}^{\text{LS}}$  and  $\mathbf{R}_{pu_i}$  indicate that the dominant pressure-velocity coupling is primarily a result of the LSP band, even when the full spectrum of wall-pressure fluctuations is considered. The differences between these two sets of correlations, which are primarily found in the streamwise component, can be clearly attributed to the influence of the VLSP band and therefore to the VLSPMs. However, the similarities between  $\mathbf{R}_{pu_i}^{\text{LS}}$  and  $\mathbf{R}_{pu_i}$  also reveal that isolating the space-time pressure-velocity correlations associated with the entire LSP band does not bring us much closer to understanding the pressure-velocity coupling, as the motions associated with  $\mathbf{R}_{pu_i}^{\text{LS+}}$  and  $\mathbf{R}_{pu_i}^{\text{LS-}}$  are almost the same as those associated with  $\mathbf{R}_{pu_i}^+$  and  $\mathbf{R}_{pu_i}^-$ . Despite this, the correlations of Figure 5.14 do provide us with a hint.  $\mathbf{R}_{pu_i}^{\text{LS+}}$  indicates that positive wall-pressure fluctuations are associated with a localized ejection followed by a localized sweep, and vice versa for  $\mathbf{R}_{pu_i}^{\text{LS-}}$ . When these motions are considered along with the inclined vortex pairs evident in Figures 5.14(b,c), we can see that  $\mathbf{R}_{pu_i}^{\text{LS}}$  provides evidence of large hairpin packets.

Hairpin packets are characterized as streamwise-aligned sequences of full or partial hairpins (canes, legs, and heads) that increase in size with downstream distance. Packets of various sizes exist, often superimposed to form a hierarchy (Adrian, 2007). The inner region of a hairpin forms ejection motions, while the outer region forms sweeping motions, and so each advecting hairpin results in a sweep followed by an ejection. It then follows that an advecting packet forms a longer series of alternating sweeps and ejections. Recall from Figure 5.8 that the region of high coherence associated with the LSP fluctuations is reminiscent of the attached-eddy hypothesis. Hairpin vortices are indeed considered attached eddies because their sizes generally increase with wall-normal distance. The region of high coherence in conjunction with  $\mathbf{R}_{pu_i}^{\text{LS}}$  therefore suggests that the pressure-velocity coupling in the LSP band may be caused by the passage of hairpin packets. To test this notion, we further decompose  $\mathbf{R}_{pu_i}^{\text{LS}}$  into smaller frequency bands in an attempt to expose the hierarchical organization of the packets.

The frequencies associated with the LSP band have been split into quartiles, with each containing exactly one quarter of the frequency range. We denote the pressure fluctuations associated with

these quartiles as  $p_{LS_q}$ , where the subscript  $q$  is used to index the  $q^{\text{th}}$  quartile of the LSP band. The frequency ranges associated with each quartile are given in Table 5.2. The quartiles are isolated with the filters shown in Figure 5.15 which were designed using the same guidelines described in Section 5.3.1, and then are used to decompose the correlations associated with the LSP band into simpler parts. We define the space-time pressure-velocity correlations associated with each quartile of the LSP band as  $\mathbf{R}_{pu_i}^{LS_q} = \mathbf{R}_{pu_i}|_{p=p_{LS_q}}$  following Equation (5.1). The resulting correlations are displayed using streamwise-wall-normal planes in Figure 5.16. The planes containing  $\mathbf{R}_{pu}^{LS_q}$  and  $\mathbf{R}_{pv}^{LS_q}$  are located at  $z = 0$ , while those of  $\mathbf{R}_{pw}^{LS_q}$  are located at different spanwise locations depending on the size of the structures captured by the correlations. These locations are  $z/\delta = 0.25, 0.2, 0.15$ , and  $0.1$  for increasing  $q$ . Finally, we note that the colourbar scaling is different than that of  $\mathbf{R}_{pu_i}^{LS}$  shown in Figure 5.14.

Figure 5.16 clearly shows that the application of Equation (5.1) to individual quartiles of the LSP band has decomposed the correlations into a hierarchy of self-similar structures. The same pattern is visible for each quartile, with the primary difference being its overall size, which decreases with increasing  $q$ . These sizes appear to span roughly one order of magnitude.  $\mathbf{R}_{pu}^{LS_q}$  and  $\mathbf{R}_{pv}^{LS_q}$  in Figures 5.16(a,b) reveal the presence of ejections and sweeps occurring immediately upstream and downstream from the pressure measurement location, just as was the case for  $\mathbf{R}_{pu_i}^{LS}$  in Figure 5.14. Specifically, we have a sweep immediately upstream from the pressure measurement location and an ejection immediately downstream for  $p_{LS_q} > 0$ , and vice versa for  $p_{LS_q} < 0$ . However, the alternating pattern now extends farther upstream and downstream to produce a longer sequence of ejections and sweeps. These motions are accompanied by inclined vortical structures as is evident from the contours of  $\mathbf{R}_{pw}^{LS_q}$  in Figure 5.16(c). Since the LSP band is associated with the self-similar flow pattern visible in Figure 5.16, it is evident that considering the entire LSP range at once averages out much of the underlying pattern that forms the correlations. It is straightforward to see by inspection how combining the correlations of each quartile would produce the patterns of  $\mathbf{R}_{pu_i}^{LS}$  shown in Figure 5.14.

We have further investigated  $\mathbf{R}_{pu_i}^{LS_q}$  by selecting one quartile of the LSP band and visualizing the motions associated with  $p_{LS_q} > 0$  and  $p_{LS_q} < 0$  using vector fields constructed from the correlations. We used the conditional correlations denoted as  $\mathbf{R}_{pu_i}^{LS_q+} = \mathbf{R}_{pu_i}^{LS_q}|_{p_{LS_q}>0}$  and  $\mathbf{R}_{pu_i}^{LS_q-} = \mathbf{R}_{pu_i}^{LS_q}|_{p_{LS_q}<0}$  for this purpose to isolate the motions associated with each sign of fluctuation, and we have selected

---

	$\omega\delta/U_\infty$	$f$ [Hz]
$q = 1$	0.9–2.7	17.5–53.1
$q = 2$	2.7–4.4	53.1–88.8
$q = 3$	4.4–6.2	88.8–124.3
$q = 4$	6.2–8.0	124.3–160.0

---

Table 5.2: Frequency ranges associated with the quartiles of the LSP band.

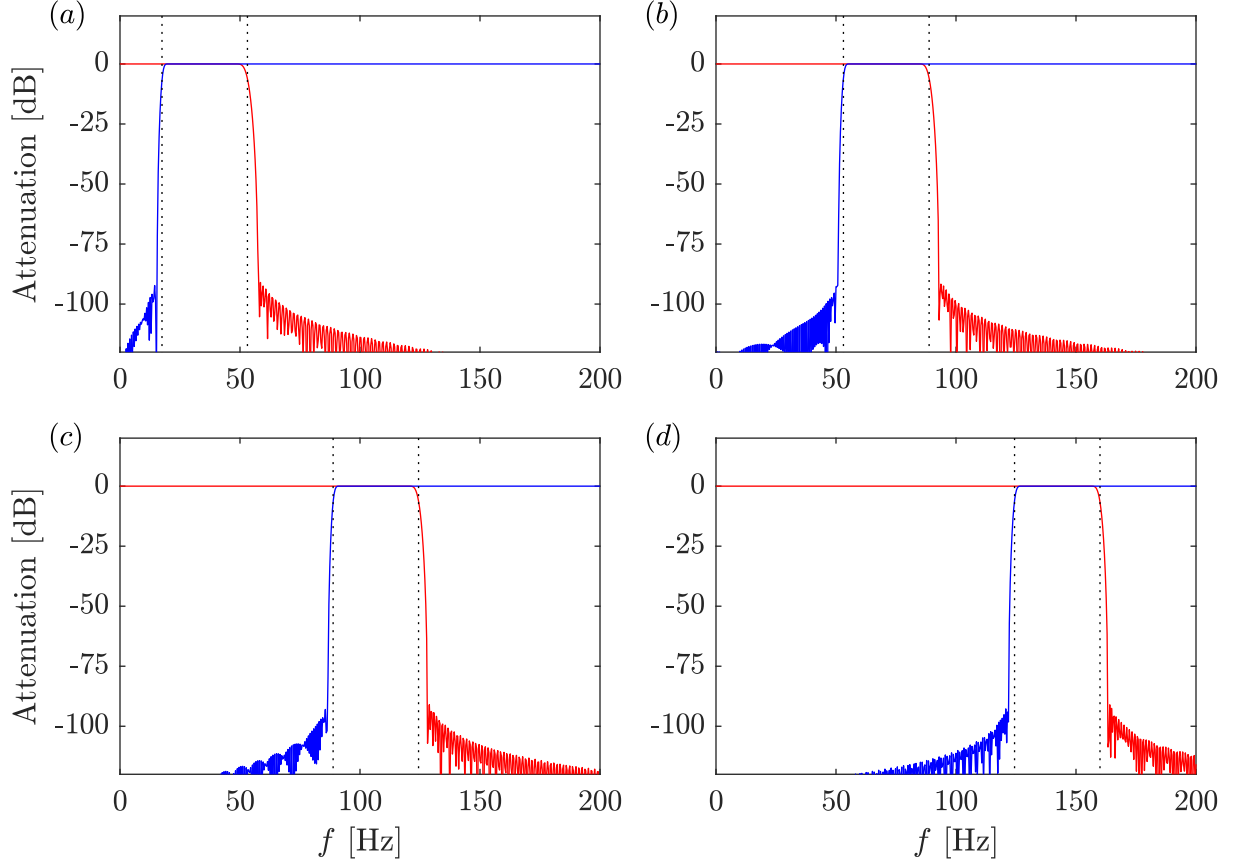


Figure 5.15: The filters used to isolate quartiles of the LSP band: (a)  $q = 1$ , (b)  $q = 2$ , (c)  $q = 3$ , and (d)  $q = 4$ . The red and blue filter responses denote lowpass and highpass filters, respectively. The vertical dotted lines denote the filter cutoff frequencies and coincide with the points of  $-6$  dB attenuation.

the quartile  $q = 3$  ( $4.4 < \omega\delta/U_\infty < 6.2$ ) for the visualization. Given that the patterns of  $\mathbf{R}_{p_{u_i}}^{\text{LS}_q}$  are self-similar, the motions visible in the correlations for  $q = 3$  represent the general behaviour of all quartiles, just on a different scale. The visualizations associated with  $\mathbf{R}_{p_{u_i}}^{\text{LS}_3^+}$  and  $-\mathbf{R}_{p_{u_i}}^{\text{LS}_3^-}$  are presented in Figures 5.17(a,b) and 5.17(c,d), respectively. The latter correlation was multiplied by  $-1$  to capture the correct flow direction of the associated velocity fluctuations. Figures 5.17(a,c) show the vector fields in the streamwise–wall-normal plane at  $z = 0$ . The horizontal lines within these subfigures show the location of the streamwise–spanwise planes plotted in Figures 5.17(b,d). The wall-normal location of these latter planes ( $y/\delta = 0.09$ ) was selected to best show patterns of the inclined vortical motions visible in the correlations of Figure 5.16.

The visualizations of  $\mathbf{R}_{p_{u_i}}^{\text{LS}_3^+}$  and  $-\mathbf{R}_{p_{u_i}}^{\text{LS}_3^-}$  in Figure 5.17 reveal a significant change within the long series of sweeps and ejections visible in the correlations. The sweeping motions are now larger and more intense, while the ejection motions are smaller and less intense. It is apparent that the contours for both  $p_{\text{LS}_3} > 0$  and  $p_{\text{LS}_3} < 0$  reveal the same pattern with only a streamwise shift between the two cases. In the streamwise–wall-normal planes of Figures 5.17(a,c), we see a series

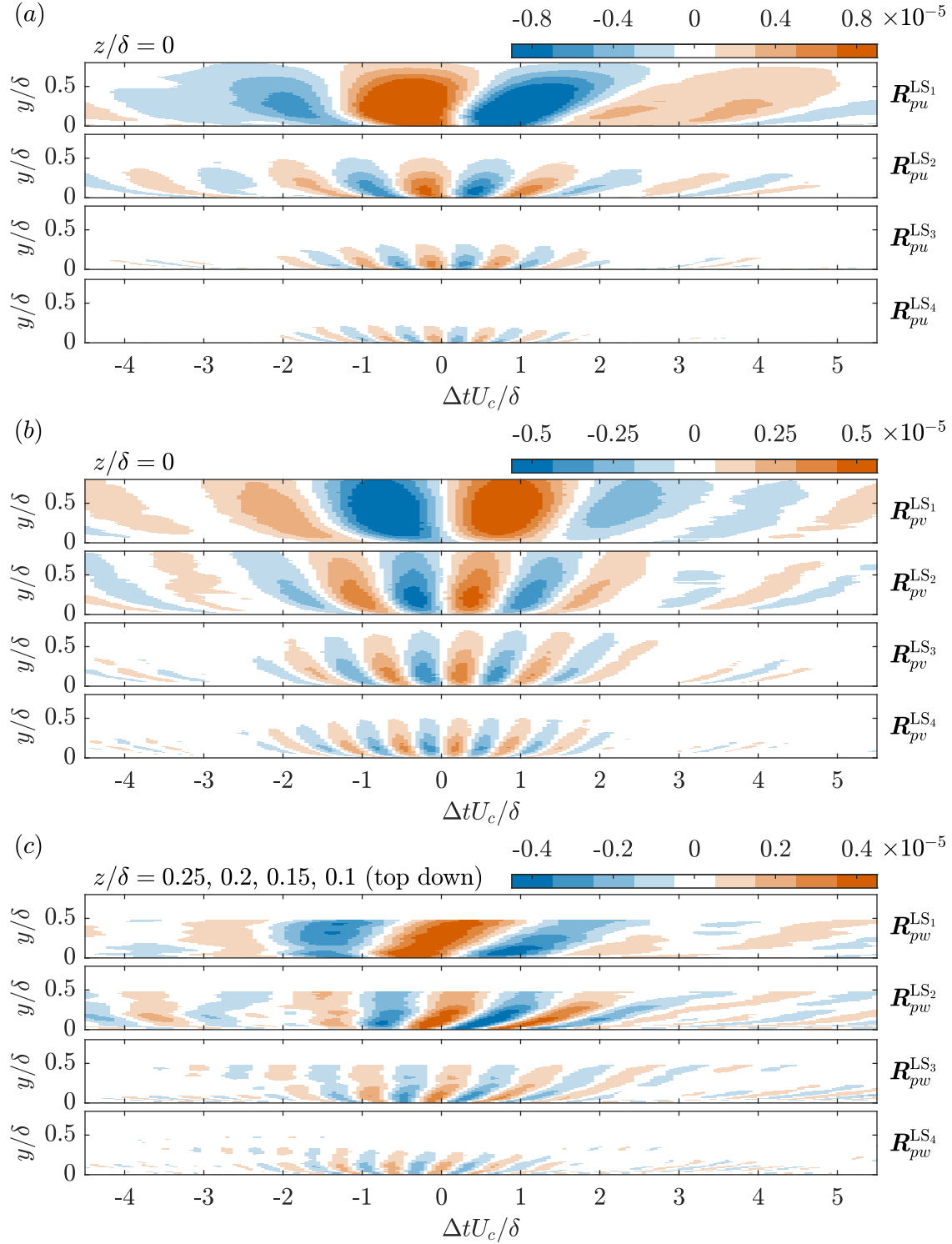


Figure 5.16: (a) Streamwise, (b) wall-normal, and (c) spanwise components of the space-time pressure-velocity correlations computed using pressure filtered to isolate quartiles of the LSP band ( $\mathbf{R}_{pu_i}^{LSq} = \mathbf{R}_{pu_i}|_{p=p_{LSq}}$ ;  $q = 1, 2, 3, 4$ ) following Equation (5.1). The frequency range associated with each quartile is given in Table 5.2.  $\mathbf{R}_{pu}^{LSq}$  and  $\mathbf{R}_{pv}^{LSq}$  are plotted at  $z = 0$ , while  $\mathbf{R}_{pw}^{LSq}$  is plotted at  $z/\delta = 0.25, 0.2, 0.15, \text{ and } 0.1$  for increasing  $q$ .

of spanwise vortices that are all rotating clockwise; the approximate locations of these vortices are marked in the figure. The size and wall-normal location of these spanwise vortices increases with downstream distance, and each is also associated with a pair of inclined vortices (also marked) that can be seen in the portion of the vector fields shown in the streamwise–spanwise planes of Figures 5.17(*b,d*). These patterns are consistent with hairpins, as each of these structures features a head (spanwise vortex) rotating clockwise and legs (inclined vortex pairs) rotating to produce an ejection between them. Since these structures align in the streamwise direction and increase in size with downstream distance, the observed pattern can clearly be attributed to hairpin packets.

The vector field associated with  $p_{LS_3} > 0$  shown in Figures 5.17(*a,b*) reveals that positive wall-pressure fluctuations occur between two hairpins where an upstream sweep opposes a downstream ejection to form an inclined shear layer structure. Such inclined shear layers are known to exist upstream from hairpins just as observed in the figure (Adrian, 2007). In contrast, the vector field associated with  $p_{LS_3} < 0$  shown in Figures 5.17(*c,d*) reveals that negative wall-pressure fluctuations occur when the head of a hairpin, which has a low-pressure core, exists directly over the pressure measurement location. Thus, the advecting series of hairpins results in the alternation between positive and negative wall-pressure fluctuation at a frequency that depends on the size and spacing of the hairpins and the advection velocity of the packet.

These observations are consistent with the findings of past studies. The earlier works of Kim (1983), Thomas and Bull (1983), and Kobashi and Ichijo (1986) associated a negative-positive-negative wall-pressure fluctuation pattern with the bursting cycle. According to the present results, two hairpins in succession would cause this negative-positive-negative pattern. Of course, we now know that the bursting process is simply a series of ejections and sweeps caused by hairpin packets (Adrian, 2007). Kim (1983) and Kobashi and Ichijo (1986) also associated the pattern with inclined vortex pairs, while Thomas and Bull (1983) associated it with shear layer and horseshoe structures, thus providing even more support for our observations. Past studies of HAPPs at the wall have also drawn conclusions that support the present results. Johansson et al. (1987) associated positive and negative HAPPs with shear layer structures and sweep-type motions, respectively. Sweeps are formed by the heads of hairpins, and so both of these conclusions match what is observed here. Ghaemi and Scarano (2013) concluded that the HAPPs can be directly tied to hairpin vortices. They found that positive HAPPs are caused when ejections formed by hairpins are opposed by upstream sweeps to form a shear layer, and their visualization of this shows remarkable agreement with the patterns of Figure 5.17. Their measurements of acceleration showed that the lower region of this shear layer contains a stagnation point, which reveals the source of the increased pressure. They also found that negative HAPPs are caused by the low-pressure cores of vortical structures, including hairpin heads. The structures that they found to cause positive and negative wall-pressure fluctuations are therefore consistent with the present observations. The excellent agreement between the present results and the literature allows us to conclude that the pressure-velocity coupling observed within the LSP band of Figure 5.8 is a direct result of advecting hairpin packets of varying sizes.

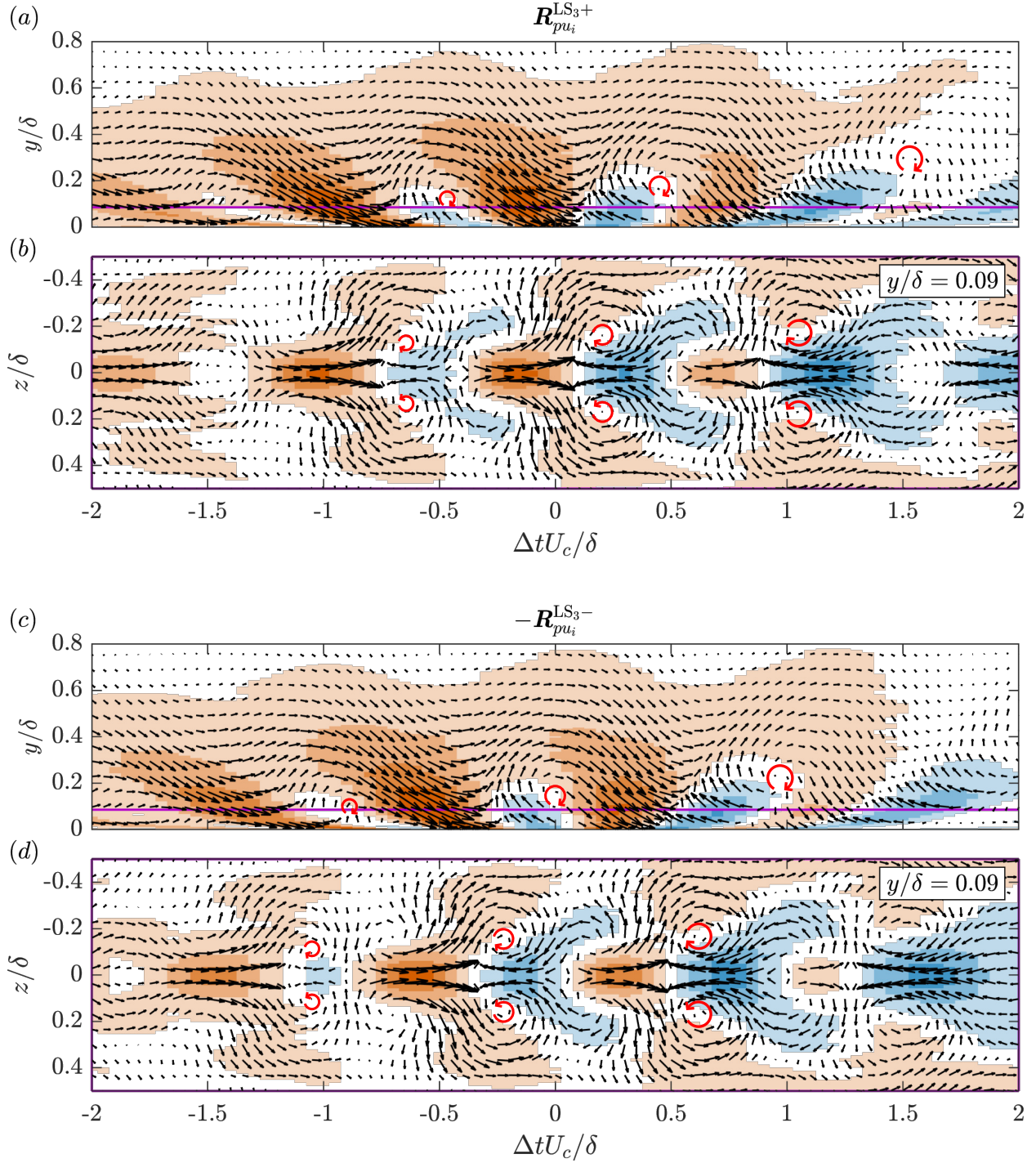


Figure 5.17: Visualizations of the vector fields associated with (a)  $\mathbf{R}_{pu_i}^{LS_3+}$  and (b)  $-\mathbf{R}_{pu_i}^{LS_3-}$ . These visualizations represent the quartile within the LSP band defined by  $4.4 < \omega\delta/U_\infty < 6.2$ . The background colour represents the streamwise component of the correlations and has the same scaling as Figure 5.16(a). The horizontal lines in (a,c) show the location of the associated streamwise-spanwise planes plotted directly below. The vector lengths in (b,d) have been altered relative to those in (a,c) to improve the visualizations. Rotational markers have been added to clearly show the locations of the vortical motions.

## 5.4 Further Discussion

### 5.4.1 Decomposition of the Pressure-Velocity Correlations

Filters were used to isolate the LSP and VLSP fluctuations, and space-time pressure-velocity correlations were computed using the filtered pressure signals. This analysis technique was found to decompose the pressure-velocity correlations into simpler parts that were easy to interpret in terms of the coherent motions that are known to exist within TBLs. This is in stark contrast to the correlations computed using the full wall-pressure spectrum, which made it difficult for past investigators to conclusively identify the sources of the wall-pressure fluctuations (Buchmann et al., 2016; Naka et al., 2015). We believe this is because the full-spectrum correlations act to smear the patterns caused by motions of varying types, sizes, and locations. This analysis was possible because of the coherence estimates, which clearly showed which frequency bands were associated with different coupling mechanisms and therefore informed the design of the filters. This technique may be useful for identifying the pressure-velocity coupling mechanisms in other turbulent flows that feature a large separation of scales and varying types of coherent motions.

### 5.4.2 Very-Large-Scale Motions and Wall Pressure

The analysis of Section 5.3.2 has shown that the pressure-velocity coupling observed within the VLSP band of Figure 5.8 is caused by the VLSMs. Our results indicate that high-speed VLSMs cause positive wall-pressure fluctuations, while low-speed VLSMs cause negative wall-pressure fluctuations. This observation is the opposite of what one would expect when considering the conservation of energy. It then seems that the wall-normal and spanwise velocity components of these elongated structures are primarily responsible for the observed low-frequency pressure modulation. This was also noted by Naka et al. (2015) for the relationship between field pressure and the VLSMs. The observed weak splatting and lifting of fluid beneath these high- and low-speed structures appears to be the mechanism by which wall pressure is affected. The downward motions associated with high-speed VLSMs transport fluid toward the wall, causing a positive pressure. Conversely, the upward motions associated with low-speed VLSMs causes a suction near the wall and therefore a negative pressure. The frequency at which this occurs then depends on the length, advection velocity, and meandering of these structures. We emphasize that the wall-pressure fluctuations associated with the VLSMs are five times weaker than those associated with the full wall-pressure spectrum in the present investigation as was discussed in Section 5.3.1. This is likely because the wall-normal component associated with the VLSMs is relatively weak. This also explains the lower coherence between wall pressure and the wall-normal velocity component observed within the VLSP band.

The correlations associated with the VLSMs indicate that their peak pressure effect is shifted towards the front of the structure. This was also observed in the VLSP band of the phase plots shown in Figure 5.9, which indicate that wall pressure leads streamwise velocity fluctuation. The reason for this phase delay is not clear at the moment, but it is interesting to discuss this point in

terms of the pressure gradients within the VLSMs. Since the peak wall pressure is shifted towards the front of the structure, the streamwise pressure gradient at the wall is of the same sign over most of the length of a VLSM. For a high-speed VLSM, there is an adverse pressure gradient at the wall over most of the length because the highest wall pressure is observed near the front of the structure. In contrast, there is a favourable pressure gradient at the wall over most of the length of a low-speed VLSM because the minimum wall pressure is observed near the front of the structure. This may explain the mechanism by which the VLSMs act to modulate the amplitude and frequency of the near-wall motions as has been shown in previous studies (Mathis et al., 2009; Ganapathisubramani et al., 2012). These works have shown that high-speed VLSMs amplify the near-wall turbulence, while low-speed VLSMs suppress it. This is consistent with the pressure gradients observed here, as adverse pressure gradients are known to increase turbulence, while favourable pressure gradients are known to reduce it. It is also interesting to note that these studies have found the opposite modulation effect farther away from the wall in the latter half of the logarithmic layer. When looking at the results of Naka et al. (2015), who associated field pressure with the VLSMs, it seems that the peak field pressure occurs near the back of the highly elongated structures visible in their correlations. This suggests that the streamwise pressure gradient within the VLSMs changes direction away from the wall, and would also explain the different modulation effects observed at the wall and farther from it.

### 5.4.3 Hairpin Packets and Wall Pressure

In Section 5.3.3, we showed that the pressure-velocity coupling of the LSP band can be attributed to advecting hairpin packets. The mechanism by which hairpin packets affect wall pressure found in our results is not new to the community. However, there are a few novel insights to note. First, we have shown that hairpin packets beyond the logarithmic layer ( $y/\delta \gtrsim 0.2$  here) affect wall pressure by the same mechanism as the smallest hairpins very close to the wall ( $y/\lambda \lesssim 60$ ) by comparison with the results of Ghaemi and Scarano (2013). However, the present results indicate that the lower-frequency wall-pressure fluctuations associated with these larger hairpins are relatively weak, while the results of Ghaemi and Scarano (2013) reveal that the smaller hairpins near the wall are capable of causing HAPPs. It then seems to be the case that the smaller hairpins cause stronger wall-pressure fluctuations, presumably because they are closer to the wall. The agreement between the present results and those of Ghaemi and Scarano (2013) also implies that the region of high coherence between wall pressure and velocity that is associated with the hairpin packets should extend to frequencies that are higher than what is observed here. This would likely be the case if the resolution of our velocity measurements was improved, as they currently limit the spatial and temporal scales that can be resolved. In fact, there is evidence to support this within the coherence plots of Figure 5.8, which show an extension of the region associated with the hairpins to higher frequencies, but with a much lower magnitude. Second, we have shown that the lowest frequency that can be associated with the hairpins in the present study coincides with the peak of the wall-pressure spectrum. This suggests that the peak is a lower limit to the frequencies that

are affected by hairpin packets, although it is likely that this is not a hard cutoff and that the hairpins may have some diminishing influence at lower frequencies. This needs to be confirmed over a range of Reynolds numbers and by other investigators. Despite this, both of these points have implications for those looking to model the wall-pressure fluctuations by taking advantage of the hairpin paradigm (eg., Ahn et al. (2010)).

#### 5.4.4 Conceptual Model of the Low- and Mid-Frequency Wall-Pressure Sources

According to the present results, the low- and mid-frequency regions of the wall-pressure spectrum shown in Figure 5.4 are captured by the VLSP band and the first two quartiles of the LSP band. This indicates that the dominant wall-pressure sources contributing to these two regions are the VLSMs and the largest hairpin packets which extend beyond the logarithmic layer. This agrees well with previous works showing that the low- and mid-frequency regions of the spectrum scale with outer-layer variables (Farabee and Casarella, 1991; Tsuji et al., 2007; Klewicki et al., 2008). It is now accepted in the literature that the largest hairpin packets generally exist around the low-speed VLSMs (Kim and Adrian, 1999; Elsinga et al., 2010; Lee and Sung, 2011; Dennis and Nickels, 2011b). We also know that the VLSMs are staggered in the spanwise direction and meander as they advect downstream. These structural consistencies allow us to formulate a conceptual model for the dominant low- and mid-frequency wall-pressure sources and their mechanisms. A schematic of this conceptual model is presented in Figure 5.18. The schematic shows the VLSMs staggered in the spanwise direction with the interfaces between adjacent structures featuring vortical motions, which are a result of the continuous presence of hairpins (full and partial) around the elongated low-speed structures. The inner ejections and outer sweeps of these hairpins induce the weak wall-normal components of the VLSMs, which cause the low-frequency modulation of wall pressure via splatting and lifting at the wall. The same hairpins feature low-pressure heads and form regions of stagnation between one another, and therefore they influence wall pressure at a higher frequency as they advect downstream. The superposition of these two mechanisms then leads to the wall-pressure fluctuations of the low- and mid-frequency regions of the spectrum. We emphasize that this conceptual model is meant to describe the predominant low- and mid-frequency wall-pressure sources that originate from coherent motions. Since we are dealing with turbulence, we expect some proportion of the fluctuations at these frequencies to originate from large motions that are less coherent.

## 5.5 Summary

Simultaneous pressure and high-speed PIV measurements were employed to investigate the wall-pressure fluctuations caused by the largest motions within a TBL at  $Re_\tau = 2600$ . The normalized cross-spectra between wall pressure and velocity throughout the TBL was studied using an estimate of the magnitude-squared coherence function. Two distinct regions of high coherence between wall pressure and velocity were identified. The first region spanned from the lowest frequencies up to the peak of the wall-pressure spectrum and reached to approximately  $y/\lambda = 1300$  ( $\sim 0.5\delta$ ) in

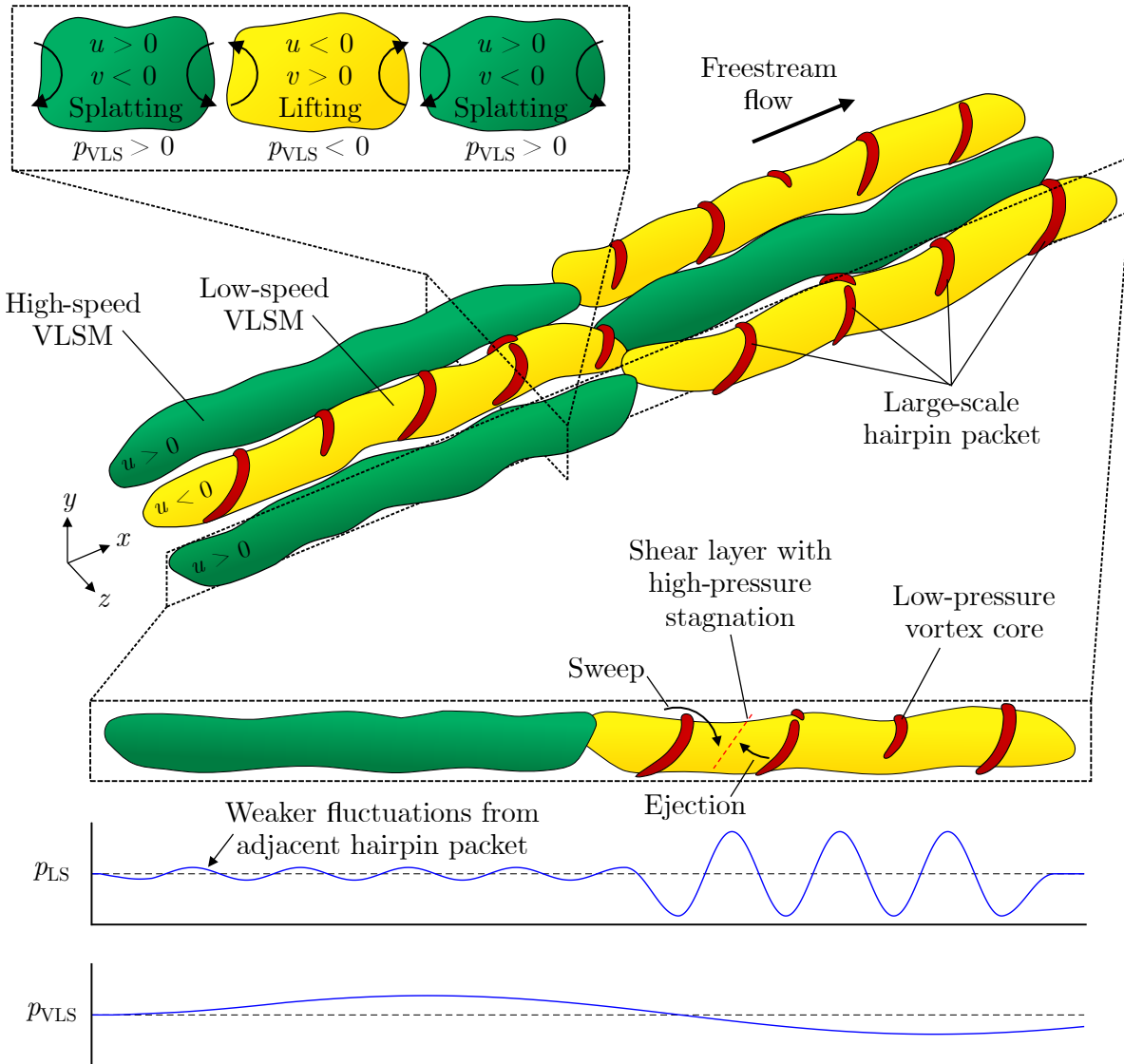


Figure 5.18: Simplified schematic showing the coherent structures that contribute to the low- and mid-frequency regions of the wall-pressure spectrum ( $\omega\delta/U_\infty \lesssim 4$  in the present work).

the wall-normal direction. A much higher coherence was observed for the streamwise component of velocity relative to the wall-normal component. The second region of high coherence spanned from the peak of the wall-pressure spectrum to approximately one-third of the way into the overlap region. A higher coherence was observed here for the wall-normal velocity component, although the streamwise component was also quite strong. The region exceeded the wall-normal extent of our measurements and was oriented at an angle, with lower frequencies being associated with distances farther from the wall, thus suggesting that attached eddies may be responsible for these wall-pressure fluctuations. We termed the frequency bands containing the first and second regions of high coherence the VLSP and LSP bands after estimating the streamwise extent of the motions associated with the fluctuations. We applied filters to isolate each of these bands, and then computed space-time pressure-velocity correlations using the filtered pressure signals to identify the motions responsible for the observed pressure-velocity coupling.

The pressure-velocity correlations computed to isolate the LSP band revealed that the observed pressure-velocity coupling is a result of advecting hairpin packets with sizes spanning at least an order of magnitude to reach well beyond the end of the logarithmic layer. Positive wall-pressure fluctuations were observed when the sweep from the head of an upstream hairpin opposes the ejection from between the legs of the downstream hairpin. This process forms an inclined shear layer and a region of stagnation, which leads to the positive pressure. Conversely, negative wall-pressure fluctuations were observed when the low-pressure head of a hairpin exists directly over the pressure measurement location. An advecting hairpin packet therefore results in the alternation between positive and negative wall-pressure fluctuation, and the frequency at which this occurs depends on the size and spacing of the hairpins and the advection velocity of the packet. The lowest frequency that could be attributed to the hairpin packets seems to coincide with the peak of the wall-pressure spectrum, although it is possible that the hairpins may have some diminishing influence at lower frequencies.

The pressure-velocity correlations associated with the VLSP band reveal patterns that can be easily attributed to the VLSMs. High-speed VLSMs were found to cause positive wall-pressure fluctuations, while low-speed VLSMs were found to cause negative wall-pressure fluctuations. Although the streamwise component of these structures is the dominant motion, it appears that the weaker wall-normal component is responsible for the observed low-frequency wall-pressure modulation. The weak downward motion of the high-speed VLSMs appears to push fluid into the wall to cause a positive pressure as is evident from the splatting that occurs beneath these structures. In contrast, the weak lifting motion of the low-speed VLSMs seems to cause a suction and therefore a negative pressure as fluid is lifted away from the wall. This is accompanied by an influx of fluid that occurs near the wall beneath these low-speed structures. The alternation between splatting and lifting that occurs beneath the VLSMs as they advect downstream therefore appears to be the mechanism by which they modulate low-frequency wall pressure. The correlations also reveal that the local extrema of wall pressure occurs near the front of the VLSMs, indicating that the streamwise pressure gradient at the wall is in the same direction over most of the structure length.

These pressure gradients at the wall are consistent with the amplitude and frequency modulation that has been observed to occur beneath the VLSMs (Mathis et al., 2009; Ganapathisubramani et al., 2012).

The demarcation between the LSP and VLSP bands observed here coincides with the peak of the wall-pressure power spectrum. It then follows that the change in behaviour of the spectrum at this extremum may be caused by the transition between pressure sources that occurs at this point in the frequency domain. Frequencies lower than that of the peak location are associated primarily with the VLSMs, while higher frequencies (up to a point) are associated primarily with hairpin packets. More experiments at various Reynolds numbers are needed to confirm whether the demarcation between LSP and VLSP always occurs at the spectral peak, but this information could be useful to those developing models for the low-frequency behaviour of the spectrum, which remains unresolved at this point. Given what we have learned in the present investigation, it seems that the roll-off of the low-frequency range of the wall-pressure spectrum could be caused by the length distribution of the VLSMs populating the TBL, as the longest motions causing the lowest frequencies would be more rare and would therefore contribute less to the PSD.

**Part III**  
**Actuation**

## Chapter 6

# Development of the Active Surface

This chapter details the development of the active surface used for boundary layer forcing. The following are covered: the actuation requirements, actuator selection, assembly design, surface deformation characteristics, and tuning of the device. Note that the height of the active surface deformation in the positive wall-normal direction is denoted as  $h$ .

### 6.1 Actuation Requirements

The primary use of the active surface is to determine whether active surface deformations can be used to target the VLSMs for control purposes. The actuation requirements are therefore dictated by the characteristics of the VLSMs in the present TBL. First, it is known that the VLSMs are a logarithmic-layer phenomenon. It follows that the active surface deformations should be capable of penetrating into this layer. The logarithmic layer of the present TBL begins at  $y/\lambda \approx 30$  and ends at  $y/\lambda \approx 400$ , which corresponds to  $1.1 \text{ mm} \lesssim y \lesssim 14.6 \text{ mm}$ . It seems reasonable to require penetration into the first 10% of the logarithmic layer, and so the active surface must be able to deform at least 2.45 mm in both wall-normal directions. Second, the active surface should be able to operate at the frequencies associated with the VLSMs. Chapter 5 revealed that the VLSMs in the present TBL occupy frequencies of up to around 17.5 Hz. The active surface must therefore be able to operate reliably at frequencies of up to at least 20 Hz. Third, the dimensions of the surface deformations should be large enough to produce an effect on the scale of the VLSMs which have widths of at most  $0.5\delta$  (Dennis and Nickels, 2011b). This corresponds to roughly 47 mm in the present TBL and so the active surface must therefore be capable of producing surface deformations that are around 47 mm wide. Finally, the active surface must be able to produce smooth surface deformations while being embedded into the surrounding surface such that it does not disturb the boundary layer flow when undeformed ( $h = 0$ ).

### 6.2 Actuator Selection

The actuator used to operate the active surface must have specifications that are commensurate with the above requirements. Piezoelectric actuators are one type of actuator commonly used to

implement moving surfaces for the purposes of active flow control (e.g., Jacobson and Reynolds (1998); Segawa et al. (2002); Gibeau et al. (2019)). However, these actuators are typically more well-suited for small displacements and high frequencies. To satisfy both the amplitude and frequency requirements described above, a linear voice coil (i.e., electromagnetic) actuator featuring an integrated position sensor was selected (BEI Kimco LAS16-23-000A-P01-4E). This linear actuator is capable of maximum displacements of  $\pm 3.04$  mm at frequencies of up to 117 Hz (sinusoidal) with a stall force of 17 N according to the manufacturer data sheet. Unfortunately, these frequencies are not achieved here due to the actuator having to work against various forces (surface tension, gravity, etc.). However, sufficient performance is achieved as will be described shortly. The actuator is powered using an external power supply (GW Instek GPS-2303) and controlled using a servo drive (Ingenia Pluto) that has been programmed using Ingenia MotionLab software. Once programmed, the displacement of the actuator can be read from the integrated position sensor and the desired displacement can be set using an external voltage signal. Both of these signals are managed using the real-time system described in Section 3.3.

### 6.3 Active Surface Assembly

The active surface assembly was developed to be a circular insert that can be fastened flush to various surfaces over which boundary layers form as is shown in the cross-sectional schematic of Figure 6.1(a). The origin of the coordinate axes is placed at the centre of the undeformed active surface as shown in the figure; the circular shape therefore produces deformations that are axisymmetric about the associated  $y$ -axis. This geometry was selected for several reasons. First, a simple geometry facilitates manufacturing. Second, the present work was concerned with local surface deformations, and the circular geometry seems ideal for producing a localized deformation. Third, a simpler geometry helps isolate the effect of the moving surface instead of, for example, the effect of a complicated protrusion or depression. And finally, the geometry was to be easily reproducible by future researchers who wish to contribute further advancements to the topic.

The primary feature of the assembly is a circular disk of smooth silicone rubber that can be deformed in the wall-normal direction using the linear actuator. The rubber features a thickness of 1.52 mm, a 50A Shore hardness, and is rated for high temperatures so that the high-speed PIV laser does not heat and damage the surface during experiments. The portion of the flexible disk that is free to deform has a diameter of  $D = 100$  mm as is shown in Figure 6.1(a); the portion of the disk beyond this diameter is attached to the insert using an adhesive while retaining some tension in the material so that it does not sag where it is unsupported. The flexible disk is driven from underneath by a smaller rigid disk with a diameter of  $d = 50$  mm (selected by rounding the required deformation width of 47 mm discussed previously). The rigid disk is attached to the linear actuator on one end using threads and is attached to the flexible disk on the other end using an adhesive. Levelling posts allow for fine adjustment of the actuator location with respect to the flexible disk to ensure the surface is flat at zero displacement. With the exception of the silicone rubber disk, all custom-made components (shown in yellow, red, and violet in Figure 6.1(a)) were

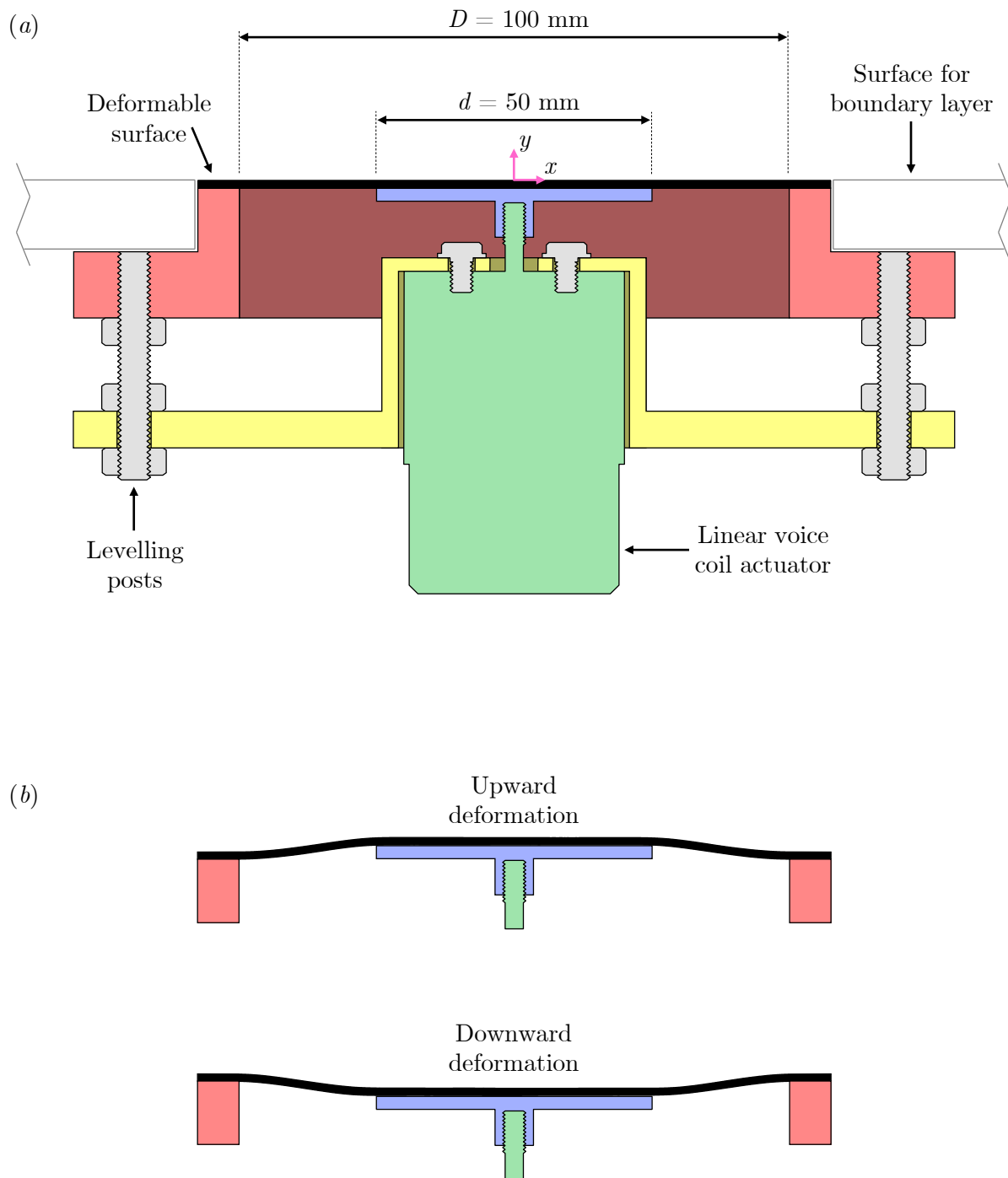


Figure 6.1: Cross-sectional schematics of (a) the active surface assembly and (b) the upward and downward surface deformation. Note that the assembly is axisymmetric and therefore the deformation is as well.

machined from aluminum. Photographs of the complete assembly are provided in Figure 6.2.

When actuated, the centre of the active surface moves up or down uniformly over an area that is set by the small rigid disk. The maximum surface displacement therefore occurs over this area, the diameter of which was selected to match the approximate width of the VLSMs. The remainder of the surface experiences a displacement that changes radially as the surface transitions from the displacement set by the small rigid disk to the fixed zero displacement of the boundary layer plate as is shown schematically in Figure 6.1(b). Note that the ratio  $d/D$  is important for determining the gradient of the radial change in displacement for radii between  $d$  and  $D$ . The ratio  $d/D = 0.5$  was selected to produce a relatively gradual surface deformation while keeping the active surface a reasonable size. Note that this also produces  $D \approx \delta$  as long as  $d$  is set to match the width of the VLSMs.

## 6.4 Shape of the Surface Deformations

The shape of the active surface when it is deformed has been measured by imaging the surface from the side. Since the deformation is axisymmetric, capturing the deformation in a plane passing through the centre of the active surface is sufficient. A thin silver line was drawn through the centre of the surface and illuminated. A camera (the same model used for PIV, see Section. 3.2.3) fitted with a 200-mm lens featuring an aperture setting of  $f_o/4$  was used to image this line for surface deformations of  $h = \pm 0.5$  mm,  $\pm 1.0$  mm,  $\pm 1.5$  mm,  $\pm 2.0$  mm, and  $\pm 2.5$  mm. An edge detection method was then used to extract the surface profiles from the images which were clearly highlighted by the silver line. Note that it was possible to capture the downward deformations using this technique due to the large aperture of the camera lens. A sample raw image of the surface deformation is shown in Figure 6.3(a). The same image with the extracted surface profile overlaid using a dotted line is shown in Figure 6.3(b) to confirm that the edge detection method does a good job of extracting the surface profile from the image. Finally, Figure 6.3(c) shows the surface profiles for all considered cases. In this subfigure the dotted lines are the same profiles as the solid lines, but they have been flipped about  $x = 0$  to highlight the symmetry of the deformation. Figure 6.3(c) reveals that the shape of the upward deformation ( $h > 0$ ) slightly differs from the shape of the downward deformation ( $h < 0$ ). More specifically, the portion of the surface that remains flat is slightly larger for  $h < 0$ . This is likely a result of how the small rigid disk interacts with the flexible disk during actuation.

## 6.5 Tuning and Performance

Tuning the active surface was accomplished by programming the servo drive using MotionLab software. This software allows for tuning many parameters. However, only the position proportional gain, position derivative gain, force proportional gain, and force integral gain were found to be necessary to operate the active surface. All other tuning parameters were therefore set to zero. A reasonable and stable starting point for these four respective gains were 4.000, 0.015, 4.000, and

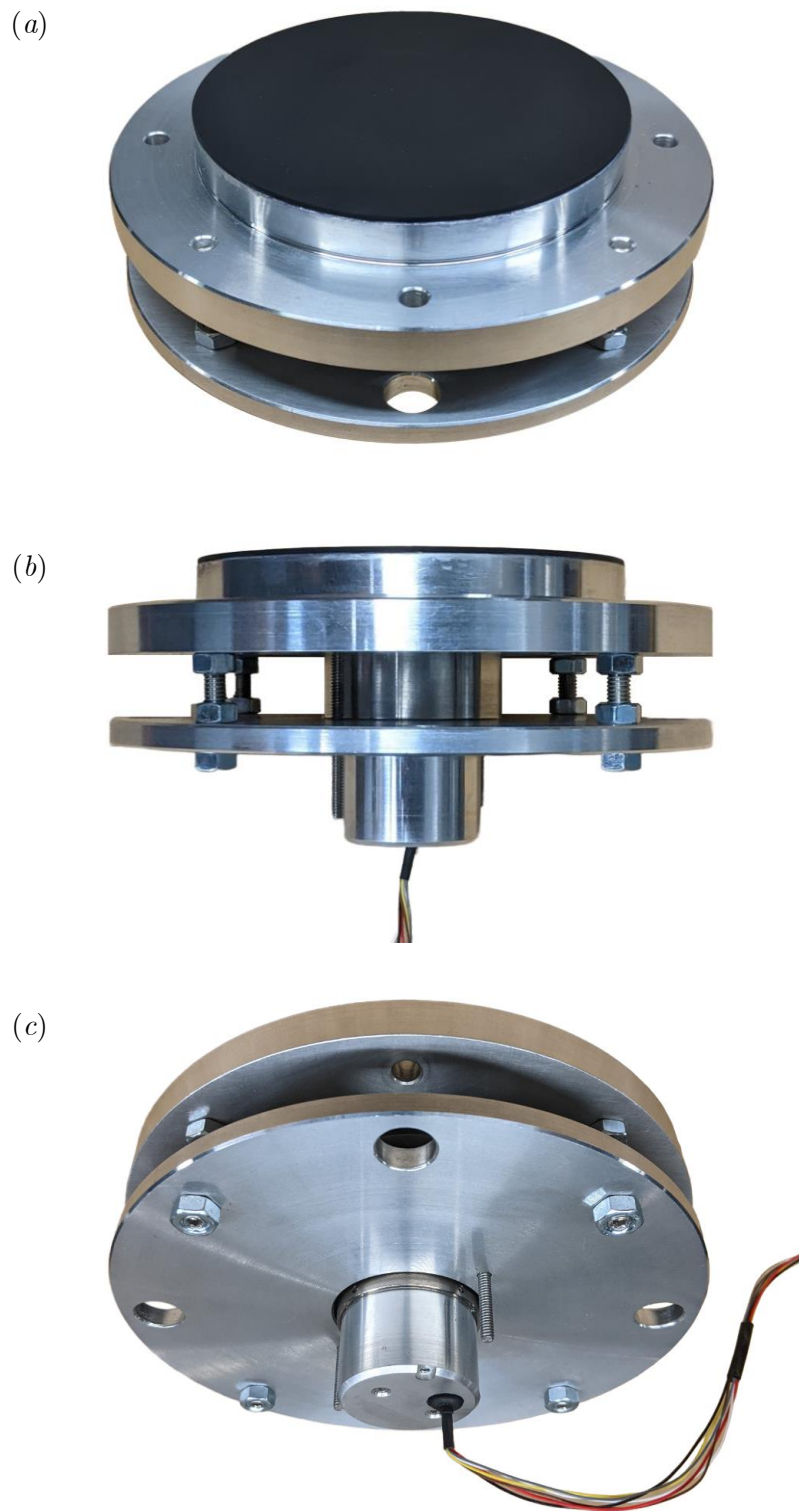


Figure 6.2: Photographs of the (a) top, (b) side, and (c) bottom of the active surface assembly. The thin threaded posts visible in (b,c) but not in the cross-sectional schematic (Figure 6.1) function only to support the surface when the device is turned off so that the silicone rubber does not stretch.

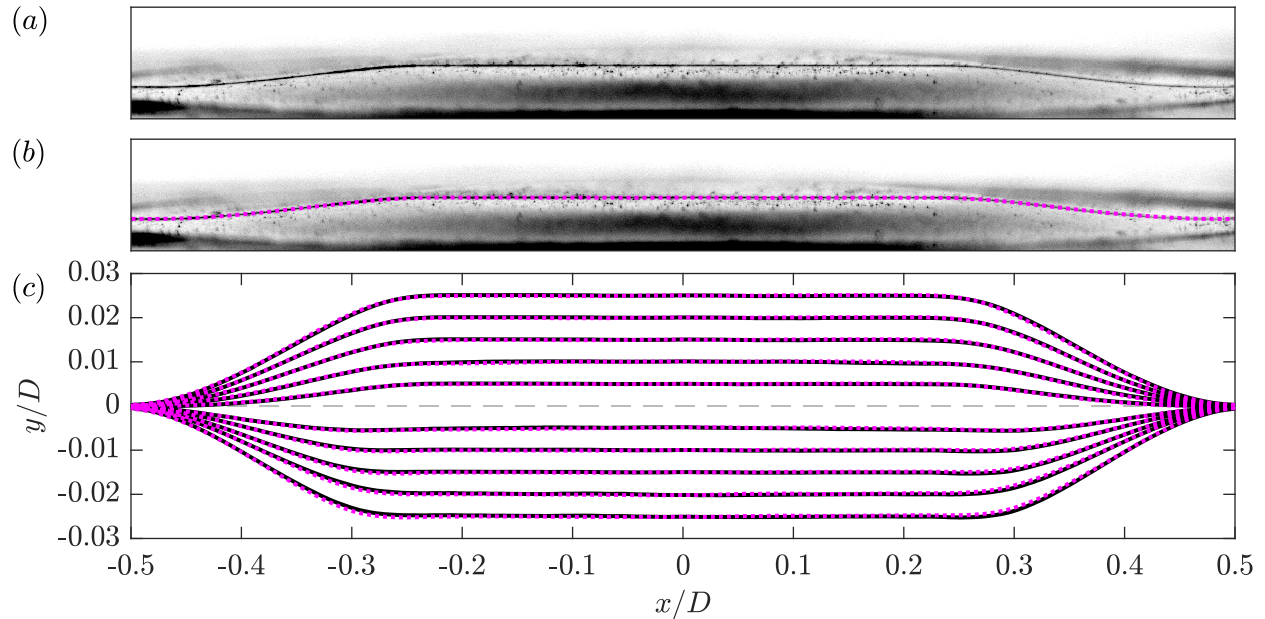


Figure 6.3: (a) Sample photograph showing the deformed surface at a displacement of 2.0 mm, (b) the same photograph with the extracted profile overlaid using a dotted line, and (c) all measured profiles of the deformed surface at displacements of  $\pm 0.5$  mm,  $\pm 1.0$  mm,  $\pm 1.5$  mm,  $\pm 2.0$  mm, and  $\pm 2.5$  mm. In (c), the vertical axis has been stretched by a factor of four to better show the profiles and the dotted lines are the same profiles flipped about  $x = 0$  to highlight the symmetry of the deformation.

0.150. These values were altered depending on the input signal being tracked to achieve optimal performance.

The displacement of the active surface was read using the voltage output from the position sensor within the voice coil actuator. This voltage was converted directly to the correct displacement in millimeters by the MotionLab software which was configured for this particular actuator. However, the conversion had to be identified if the real-time system was to be used to record the displacement of the active surface during experiments. A brief experiment was conducted to record the voltage output of the displacement sensor for various known actuator positions. A fourth-order polynomial conversion from V to mm was then fit to the data. This conversion was implemented by the real-time system to produce measurements of the active surface displacement. The uncertainty associated with this conversion is discussed in Appendix A.

A sample time series of the active surface tracking a random input signal is shown in Figure 6.4. In this case, the reference signal contains frequencies of up to 20 Hz which is the minimum frequency that the active surface should be able to handle as was discussed previously. Sufficient tracking of this signal is observed as is evident in the figure. The active surface was operated using a random input signal such as this one for the investigation documented in Chapter 7. Furthermore, periodic surface deformations at frequencies of up to 40 Hz were used for the investigations documented in Chapters 7 and 8. The actuator was tuned on a case-by-case basis to achieve adequate tracking of

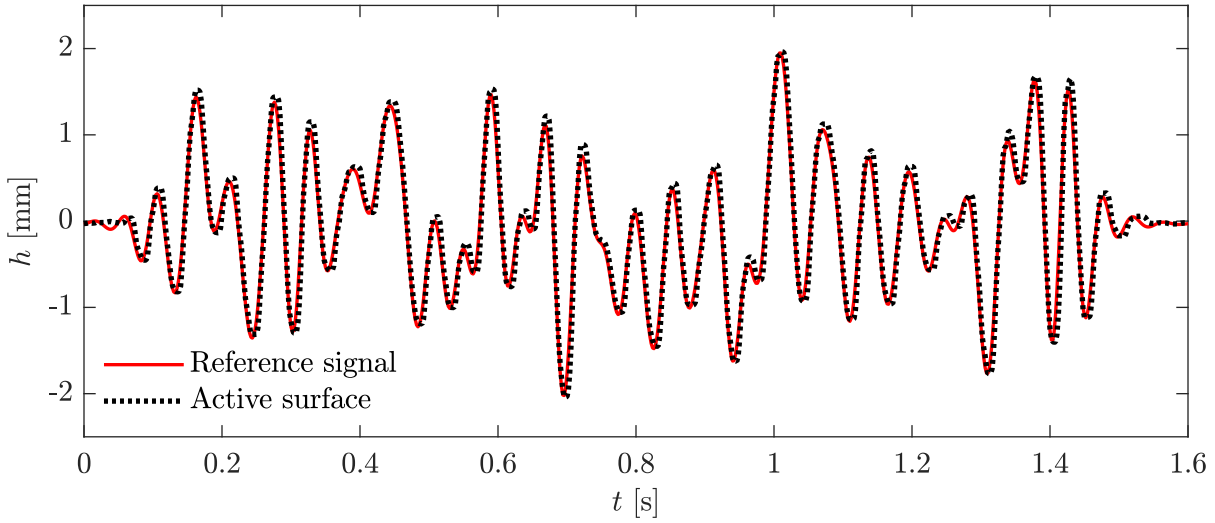


Figure 6.4: Sample time series of the active surface tracking a random input signal containing frequencies of up to 20 Hz.

some of the periodic signals, especially those at the higher frequencies.

Finally, it is important to note that the measured displacement only captures the motion of the flat portion of the deformation as set by the small rigid disk that is directly fixed to the linear actuator. The behaviour of the unsupported portion of the active surface should also be considered, as high frequencies and amplitudes could cause this portion of the surface to experience secondary oscillations depending on the properties of the material. To show that this is not a significant concern for the present investigation, high-speed videos of the active surface operating at an amplitude of 2 mm and actuation frequencies of 20 and 40 Hz have been recorded. These recordings are shown in the supplementary material of Gibeau and Ghaemi (2022) and they reveal that any secondary oscillation of the unsupported portion of the active surface is small in comparison to the primary deformations and only occurs at the highest frequencies.

## Chapter 7

# Laminar Boundary Layer Forcing with Active Surface Deformations

Section 2.4.1 made it clear that the idea of using local wall-normal surface deformations as a means of actuation for flow control has been around for a few decades. Although there is interest in the topic, the actuation concept has received far less attention when compared to more popular options such as fluidic and plasma actuation. As a result, the literature lacks the information necessary for designing a suitable surface deformation for targeting a given flow feature in a control application. More specifically, it is not clear how the frequency and amplitude of simple surface deformations affect the motions that are produced. This information is critical for determining which features of a flow can be effectively targeted using this actuation strategy. The active surface developed in Chapter 6 has therefore been deployed beneath an LBL to expand upon the sparse literature regarding how simple wall-normal surface deformations influence wall-bounded flows. The LBL was selected for two reasons: i) it is the simplest wall-bounded flow and is therefore the logical choice for an initial evaluation of a new actuator in a *clean* flow, and ii) it allows us to easily evaluate models for the input-output dynamics of the actuated flow because the unactuated flow is steady. This chapter first considers how periodic surface deformations influence the flow over a range of actuation amplitudes and frequencies with an emphasis on the spatial structure, strength, and stability of the resulting motions. Second, it is shown a simple linear model that is commonly used to design controllers is capable of capturing the input-output dynamics of the actuated flow.

## 7.1 Experimental Setup

### 7.1.1 Laminar Boundary Layer Configuration

The LBL was generated using an LBL plate as was discussed in Section 3.1.3. The active surface sat flush with the plate and the gaps between the two components were filled with a malleable polymer clay to achieve a smooth transition. The centre of the active surface was located 17.5 cm from the leading edge of the plate during experiments; the centre of the active surface is also where the origin of the coordinate system is located for the following analyses as is shown in Figure 7.1.

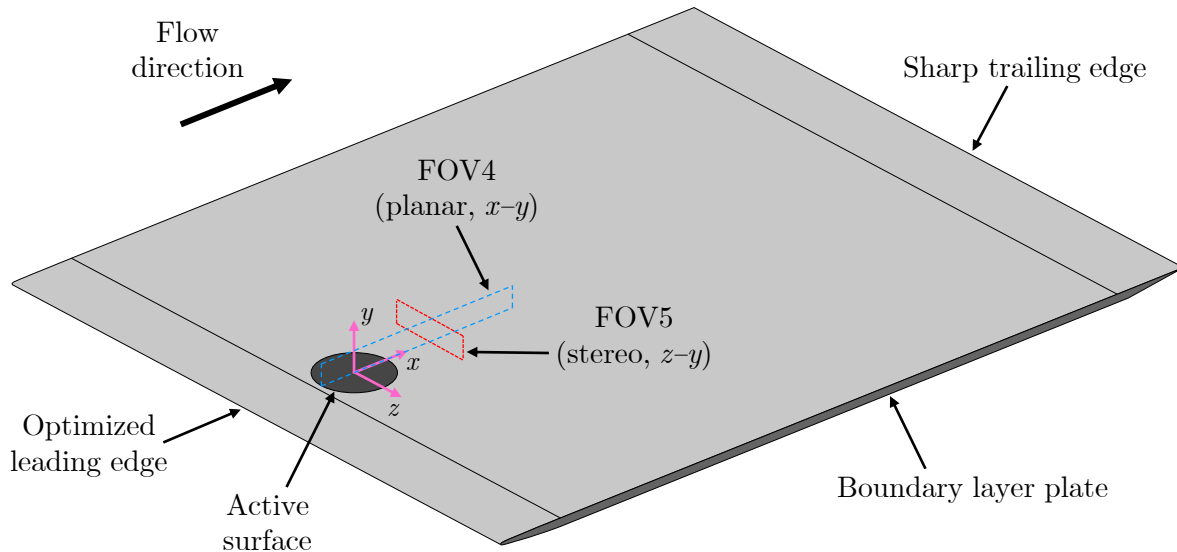


Figure 7.1: Schematic of the experiment showing the boundary layer plate, active surface, and FOVs used for PIV.

### 7.1.2 Particle Image Velocimetry

The PIV system discussed in Section 3.2.3 was used to conduct two separate high-speed PIV experiments for the purpose of capturing the performance of the active surface: a four-camera planar measurement that was stitched together into a single FOV and a stereoscopic measurement. These FOVs are numbered accordingly in Figure 7.1.

The planar PIV experiment was used to capture the flow field above and downstream from the active surface in the streamwise–wall-normal plane at centre span ( $z = 0$ ). Each camera was fitted with a  $2\times$  teleconverter and a 200-mm lens featuring an aperture setting of  $f_o/5.6$ . The combined FOV, which is denoted as FOV4 within Figure 7.1, has dimensions of  $(\Delta x, \Delta y) = 305 \text{ mm} \times 29 \text{ mm}$  and a resolution of  $64.5 \text{ }\mu\text{m}/\text{pixel}$ . FOV4 was stitched together from the sub-FOVs of four cameras to capture a larger extent of the streamwise direction while retaining sufficient resolution. However, the cameras viewing adjacent sub-FOVs could not be placed side-by-side while retaining FOV overlap for stitching because of the large size of each camera. As a result, the cameras viewing the first and third sub-FOVs were placed on one side of the test section and the cameras viewing the second and fourth sub-FOVs were placed on the other side of the test section. This arrangement required a transparent calibration target so that the cameras on opposite sides of the test section could view the same plane during the calibration process. The target was made in-house by printing a dotted grid of known dimensions onto a transparency film and adhering it to a flat piece of glass. The entirety of FOV4 was illuminated with a 1-mm-thick laser sheet formed using a combination of spherical and cylindrical lenses. The sheet was directed from downstream using a mirror that was located within the test section behind the boundary layer plate.

The parameters of the data acquisition for FOV4 were the same for all cases considered. Sets of 4000 double-frame images were collected from each of the four cameras at an acquisition rate of 500 Hz, resulting in 8 seconds of time-resolved data for each case. The images were preprocessed in two steps. The minimum of each ensemble was subtracted to reduce the background noise, and then the images were divided by the background-subtracted ensemble average to normalize the intensity counts. The preprocessed double-frame images were then cross-correlated using a multi-pass algorithm. The final pass employed  $24 \times 24$ -pixel Gaussian-weighted interrogation windows with 75% overlap. The resulting vector fields were stitched into a single FOV using the information from the target calibration, and then a post-processing round was performed. This included applying universal outlier detection (Westerweel and Scarano, 2005) to detect spurious vectors, which were then replaced using polynomial interpolation in both space and time.

The stereoscopic PIV experiment was used to capture the spanwise variation of the flow field downstream from the active surface in the spanwise-wall-normal plane. Two cameras were used, each with Scheimpflug mounts,  $2\times$  teleconverters, and 200-mm lenses with aperture settings of  $f_o/16$ . Both cameras were placed at  $45^\circ$  to the imaging plane and were arranged in a forward-scattering orientation with respect to the laser sheet. The stereoscopic FOV, which is denoted as FOV5 within Figure 7.1, was located 11 cm downstream from the centre of the active surface ( $x/D = 1.1$ ). FOV5 had dimensions of  $(\Delta z, \Delta y) = 122 \text{ mm} \times 28 \text{ mm}$  and an effective resolution of  $70.1 \text{ }\mu\text{m/pixel}$ . The stereoscopic calibration included a 3D target calibration followed by a self-calibration using a small set of particle images (Wieneke, 2005). FOV5 was illuminated with a thicker 2-mm laser sheet to improve the correlation between double-frame images since the mean flow direction was normal to the imaging plane.

The same data acquisition parameters for FOV5 were used for all cases considered. Sets of 4000 double-frame images were collected from both cameras at an acquisition rate of 1 kHz, resulting in 4 seconds of time-resolved data for each case. A higher acquisition rate was used for stereoscopic PIV compared to planar PIV to improve the temporal resolution of the measurements, as the flow structures do not remain in FOV5 for long. The same image processing steps that were applied to the planar PIV images were also applied to the stereoscopic images, with the only differences being that the multi-pass cross correlation was the stereoscopic variant of the algorithm and  $32 \times 32$ -pixel Gaussian-weighted interrogation windows were used.

Finally, trigger signals for the laser and cameras were recorded along with the actuator signals during all PIV experiments. This was done so that the resulting vector fields could be synchronized with the displacement of the active surface by using the procedure described in Section 3.3.2.

### 7.1.3 Base Flow

The mean velocity profiles at  $x/D = 0, 1, \text{ and } 2$  for the base flow (unactuated) are presented in Figure 7.2. It is evident in the figure that the velocity profiles closely match the Blasius solution at all three streamwise locations, confirming that the LBL plate produces the desired flow field. The boundary layer thickness at  $0.99U_\infty$ , displacement thickness, momentum thickness, and the

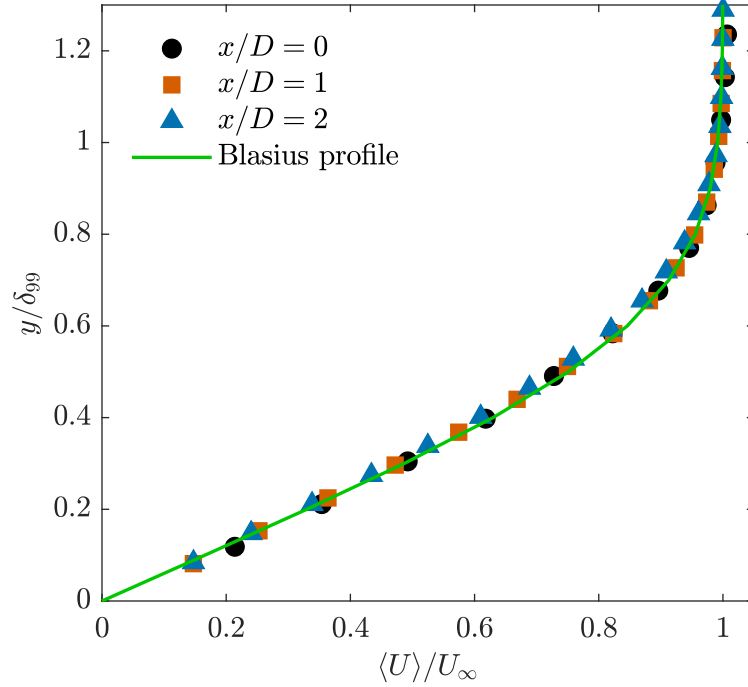


Figure 7.2: Mean boundary layer profiles for the base flow measured at three streamwise locations and compared to the Blasius solution.

Reynolds number computed using the displacement thickness at the same three streamwise locations are given in Table 7.1. Note that  $Re_{\delta^*} = 520$  at  $x/D = 2$  coincides exactly with the “indifference point” for the Blasius profile (Schlichting and Gersten, 2017). This is the largest Reynolds number that can be achieved before neutral disturbance waves, which are periodic in both space and time (Maslowe, 1986), begin to amplify within the LBL according to linear stability analysis. The present study was designed to place this point sufficiently downstream from the active surface to decrease the chance that the forcing causes an immediate transition to turbulence. However, as we will discuss later in Section 7.2.2, the periodic motions produced by the active surface can become unstable prior to this point.

The mean flow has also been evaluated for static deformations up to  $h/D = \pm 0.02$ . This was done to determine whether the active surface has an impact on the flow when the dynamic element is removed. The mean streamwise velocity of the base flow over a portion of FOV4 is shown in Figure 7.3(a) where the mean profiles (solid black lines) at several streamwise locations are overlaid along with the boundary layer thickness based on  $0.95U_\infty$  (dashed black line). This subfigure acts as the baseline for comparison of the flow fields that result from static deformation of the active surface. Consequently, the mean profiles and the boundary layer thickness of the base flow are included in the subsequent panels of Figure 7.3 with black lines to facilitate comparison. Note that the mean velocity fields of the static deformation cases are sufficient to fully characterize the behaviour of the downstream flow because no unsteadiness was observed.

---

$x/D$	$\delta_{99}$ [mm]	$\delta^*$ [mm]	$\theta$ [mm]	$Re_{\delta^*}$
0	4.1	1.4	0.5	340
1	5.3	1.9	0.7	450
2	6.0	2.2	0.8	520

---

Table 7.1: Boundary layer parameters for the base flow at three streamwise locations: boundary layer thickness at  $0.99U_\infty$ , displacement thickness, momentum thickness, and the Reynolds number computed using the displacement thickness.

Figure 7.3(b) shows the mean streamwise velocity resulting from static deformation at  $h/D = -0.02$ . The boundary layer thickness (dashed red line) can be seen to decrease slightly above the active surface when compared to that of the base flow (dashed black line), but these differences recover by  $x/D = 0.7$ . We also see a near perfect overlap between the velocity profiles (solid red and black lines) beyond this point. As was shown in Figure 7.2, the base flow adheres to the Blasius solution. We can therefore conclude that the boundary layer downstream from static deformation at  $h/D = -0.02$  quickly recovers to the Blasius solution despite the upstream depression caused by the active surface.

Figure 7.3(c) shows the mean streamwise velocity resulting from static deformation at  $h/D = 0.02$ . In contrast to the downward surface deformation, we can now see changes to the mean flow throughout FOV4. More specifically, we see a thicker boundary layer (dashed red line) compared to the base flow (dashed black line) caused by the protrusion of the active surface into the flow. This effect is strongest immediately following the active surface in the region  $0.5 < x/D < 1.0$ , but some differences persist until the end of the FOV. As can be seen by the overlaid velocity profiles (solid red lines), which are shown more clearly in the zoomed-in view of Figure 7.3(d), the profile located at  $x/D = 0.75$  no longer appears to adhere to the Blasius solution (solid black line) as the portion of the profile near the wall now features a smaller velocity gradient. This velocity profile includes a pronounced inflection point and appears similar to one near a separation point (e.g., Ma et al. (2020)). We also see a very small region of flow separation on the downstream side of the surface protrusion around  $x/D = 0.48$ . This region is only visible for  $h/D = 0.02$  and is shown in Figure 7.3(d) using the dotted red line that highlights the contour of  $\langle U \rangle = 0$ . The results from FOV5 are not shown here for brevity, but they reveal that the effect of the surface protrusion extends to roughly  $z/D = \pm 0.3$  in the spanwise direction at the location of the stereoscopic measurement ( $x/D = 1.1$ ). We can therefore consider the overall effect of static upward deformation to be an elongated streak-like region of velocity deficit. A similar effect is seen for static deformations of  $h/D = 0.015, 0.010, \text{ and } 0.005$ , but with diminishing strength as the height of the deformation is reduced.

The present results reveal that only static upward deformation of the active surface produces meaningful changes to the flow downstream from the active surface, while static downward defor-

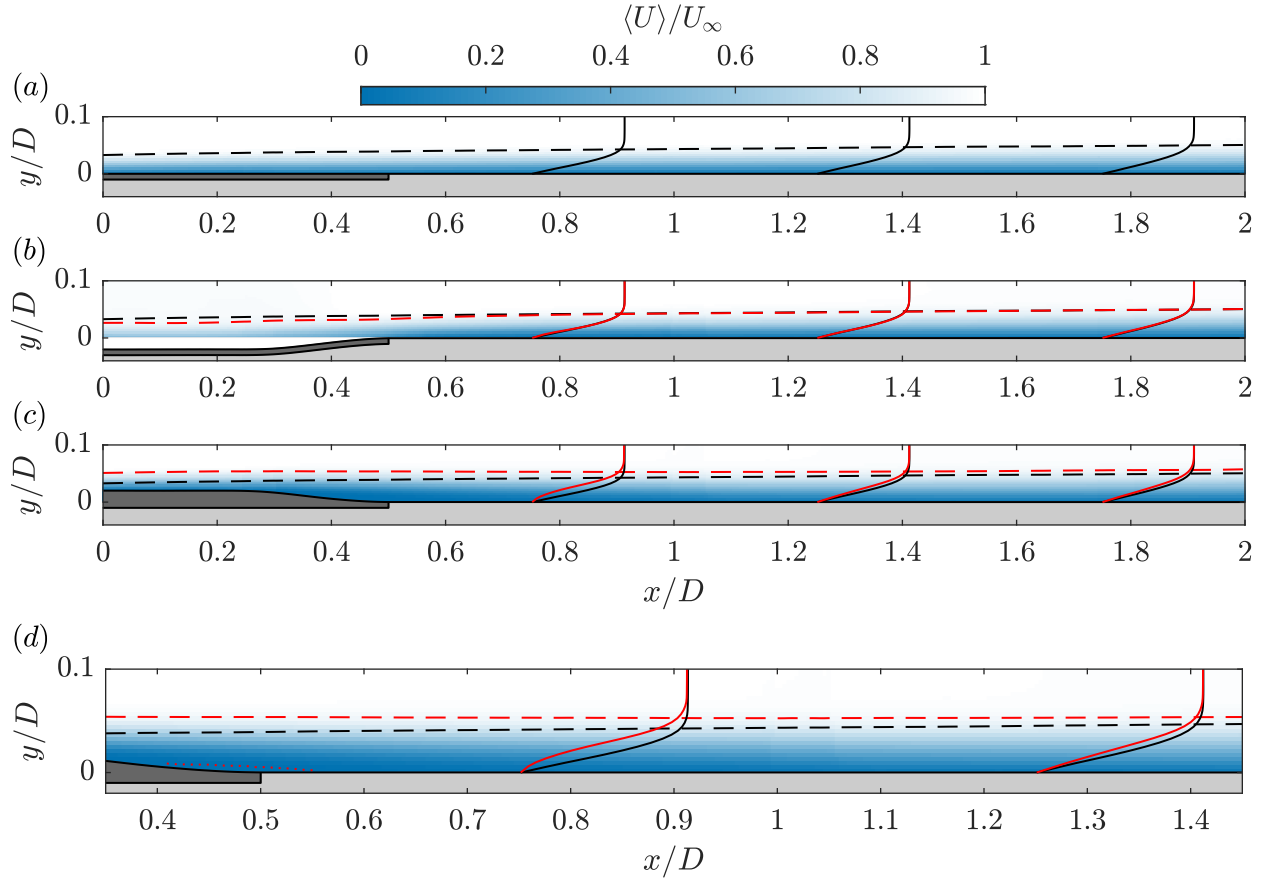


Figure 7.3: Mean streamwise velocity within FOV4 ( $z = 0$ ) for (a) the base flow, (b) static deformation at  $h/D = -0.02$ , and (c–d) static deformation at  $h/D = 0.02$ . The solid lines are mean profiles at selected streamwise locations and the dashed lines show the boundary layer thickness at  $0.95U_\infty$ . In all panels, the black lines represent the base flow while the red lines represent the static deformation cases. Note that (d) is a zoomed-in view of (c) to better show the change in velocity profiles that occurs for static deformation at  $h/D = 0.02$ . The dotted red line in (d) is a contour of  $\langle U \rangle = 0$  that highlights the small separation region on the downstream side of the active surface.

mation has a negligible impact. In contrast, periodic actuation produces both high- and low-speed motions with similar magnitudes as we will see in Section 7.2. It therefore seems to be the case that the dynamic element of the active surface is important for successful actuation, especially when producing downward deformations.

#### 7.1.4 Actuation Cases

Two types of actuation were considered in the present investigation: periodic and random deformation of the active surface. Periodic deformation was considered to investigate how the amplitude and frequency of active surface deformations affect the flow field. We operated the actuator using

the signal

$$h_r(t) = A \sin(2\pi f_a t), \quad (7.1)$$

where  $A$  is the actuation amplitude,  $f_a$  is the actuation frequency,  $t$  is time, and  $h_r$  is the reference signal in millimeters that is meant to be tracked by the actuator. We considered amplitudes of 0.5 mm, 1.0 mm, 1.5 mm, and 2.0 mm, which correspond to 12% to 49% of the local boundary layer thickness, and frequencies ranging from 4 Hz to 40 Hz in increments of 4 Hz. The actuation amplitudes and frequencies are normalized using the active surface diameter  $D = 100$  mm and the freestream velocity  $U_\infty = 4.0$  m/s throughout most of this paper. In the case of the normalized frequency this produces the Strouhal number  $St = f_a D / U_\infty$ . The normalized values therefore range from  $A/D = 0.005$  to  $0.02$  and  $St = 0.1$  to  $1.0$ . Finally, we consider a randomized  $h(t)$  signal as the second type of actuation. This was done for the purposes of system identification; more details regarding this randomized signal and its use are discussed in Section 7.3.

The results from the periodic deformation cases constitute the primary data in this chapter. The active surface was tuned on a case-by-case basis to have the amplitudes of the sinusoidal displacement patterns be within a few percent of the desired values. The phase-averaged displacement (more details on the phase-averaging process in the next section) of the active surface is shown for all actuation cases in Figure 7.4. It is clear in the figure that the phased-averaged displacement signals closely match the desired sinusoids.

### 7.1.5 Phase Averaging

A phase averaging technique was applied to the vector fields associated with the periodic deformation cases to obtain improved representations of the resulting periodic flows. We found that these phase-averaged velocity fields are an excellent representation of the instantaneous flow when the motions downstream from the active surface remain periodically organized. However, phase averages of the actuation cases that result in a transition to turbulence no longer provide a good representation of the flow beyond the point of transition. This did not pose any issues for this investigation since we are not interested in the flow downstream from a transition to turbulence. Moreover, the phase-averaged flow fields of the cases featuring transition still provide useful information. For example, they show the structure and strength of the motions leading up to transition and also the streamwise location at which transition occurs (as indicated by abrupt changes in the structure and strength). For these reasons we focus on the phase averages throughout the analysis of the periodic deformation cases.

The phase of the active surface  $\phi$  was extracted from the measurements of  $h$  using a Hilbert transform as

$$\phi = \angle(-i\mathcal{H}\{h\}) + \pi, \quad (7.2)$$

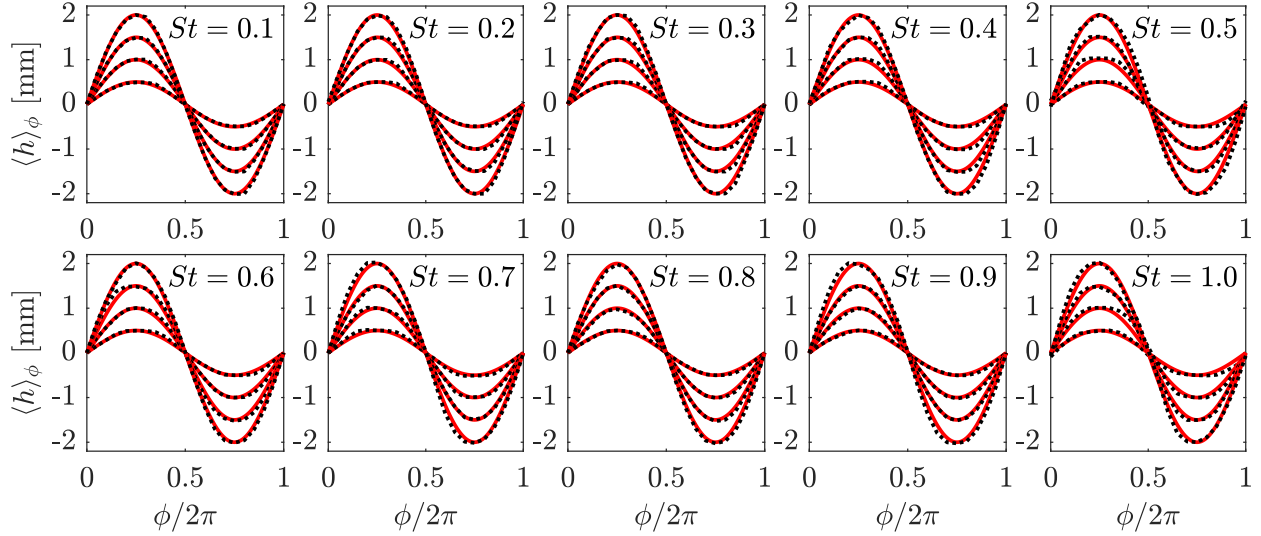


Figure 7.4: Phase averages of the active surface displacement ( $\langle h \rangle_\phi$ , dotted lines) compared to the reference sinusoids that the surface is meant to track (solid lines) for all periodic deformation cases. Note that  $\phi$  is the phase of actuation.

where  $\mathcal{H}\{h\}$  denotes the Hilbert transform of the active surface displacement. The manipulations with  $i$  and  $\pi$  were used to shift the phase such that one full cycle extends from  $\phi = 0$  to  $2\pi$  with  $\phi = 0$  representing the active surface at  $h = 0$  with a velocity in the positive wall-normal direction. The velocity fields were averaged using phase bins with widths of  $0.1\pi$  and 80% overlap. Since each set contains 4000 measurements, each average was computed using roughly 200 vector fields.

## 7.2 Motions Produced by Periodic Forcing

In this section we evaluate how the active surface influences the LBL when operated according to the periodic actuation cases discussed in Section 7.1.4. We focus on the spatial structure, strength, and stability of the periodic motions that form as a result of the active surface deformations. We consider only the streamwise velocity fluctuations, as we found that the phase averages of  $v$  are roughly five to ten times weaker than the phase averages of  $u$  (prior to instability growth).

### 7.2.1 Spatial Structure

We begin by studying the spatial structure of the motions that result from operating the active surface to produce periodic deformations. In general, the structure of the flow under these conditions can be characterized as modes featuring repeating high- and low-speed motions that form above the active surface and advect downstream. The high-speed motions form as the surface moves downwards and suction high-speed fluid towards the wall, while the low-speed motions form as the surface moves upwards and pushes low-speed fluid away from the wall. The shape, dimensions, intensity, and stability of the resulting modes depend heavily on the frequency and amplitude of

actuation. To begin investigating these modes we consider the flow formed from actuation at an amplitude of  $A/D = 0.005$ , which is the smallest amplitude considered in this chapter. The modes formed at this small actuation amplitude are generally more organized and stable than those formed using larger deformations of the active surface and therefore they allow us to more easily scrutinize how the modes vary as function of frequency. In fact, it is the only actuation amplitude considered here that produces modes that remain organized throughout the entirety of FOV4 for all actuation frequencies. As a result, the phase averages of these cases are an excellent representation of the instantaneous flow field.

Phase averages of the fluctuating streamwise velocity ( $\langle u \rangle_\phi$ ) are given in Figure 7.5 for all actuation frequencies considered at an amplitude of  $A/D = 0.005$ . A phase of  $\phi = 3\pi/2$  is shown in all cases, which corresponds to the surface being at the lowest position of the cycle with zero velocity. All panels within the figure show a series of high- and low-speed motions that alternate in the streamwise direction. The height of these motions remains relatively constant at around  $0.05D$  ( $\sim \delta_{99}$ ), but their wavelengths in the streamwise direction are a strong function of the actuation frequency. As the frequency is increased from  $St = 0.1$  to  $0.3$  (Figures 7.5(a-c)), we see a rather drastic reduction in the length of the high- and low-speed motions while the mode shape remains similar overall. When the actuation frequency reaches  $St = 0.4$  (Figure 7.5(d)) we see a break in this trend. The flow structures are now relatively weak, and the structure immediately downstream from the active surface has a positive sign of fluctuation – the opposite of what is observed for  $St = 0.1$  to  $0.3$ . We then see a return to the original mode shape as the frequency is increased through the range  $St = 0.5$  to  $0.9$  (Figures 7.5(e-i)), where the streamwise wavelengths of the modes continue to decrease as frequency is increased. Finally, we see a break in the trend once again for  $St = 1.0$  (Figure 7.5(j)), which appears to generate the same mode shape that was observed at  $St = 0.4$  but with a reduced streamwise wavelength. Overall, it appears that there are alternating transitions between two different mode types as  $St$  is increased. These mode types are maintained at the higher actuation amplitudes, although they are more intense and therefore less stable; this will be discussed in more detail in Section 7.2.2.

To further investigate the modes visible in Figure 7.5 we consider their streamwise wavelengths ( $\lambda_x$ ), i.e., the streamwise distance between motions with the same sign of fluctuation. These wavelengths were computed by applying an autocorrelation in the streamwise direction to an isolated portion of the instantaneous snapshots of streamwise velocity fluctuation that contains the periodic modes. The average of all 4000 autocorrelation curves for each case was used to extract the wavelength by locating the point at which the autocorrelation curve reaches a minimum. This point is half the wavelength because it occurs when the autocorrelation has been shifted such that adjacent structures with opposite sign of fluctuation overlap. To isolate the modes for the autocorrelation, we extracted the portion of each snapshot beyond  $x/D = 0.5$ . The height of the extracted portion was limited to  $y/D = 0.1$ , and the length was limited to  $0.75\hat{\lambda}_x$  where  $\hat{\lambda}_x$  is the streamwise wavelength estimated from the phase averages of Figure 7.5. This was done to capture the streamwise extent necessary for achieving the minimum of the autocorrelation function without including the

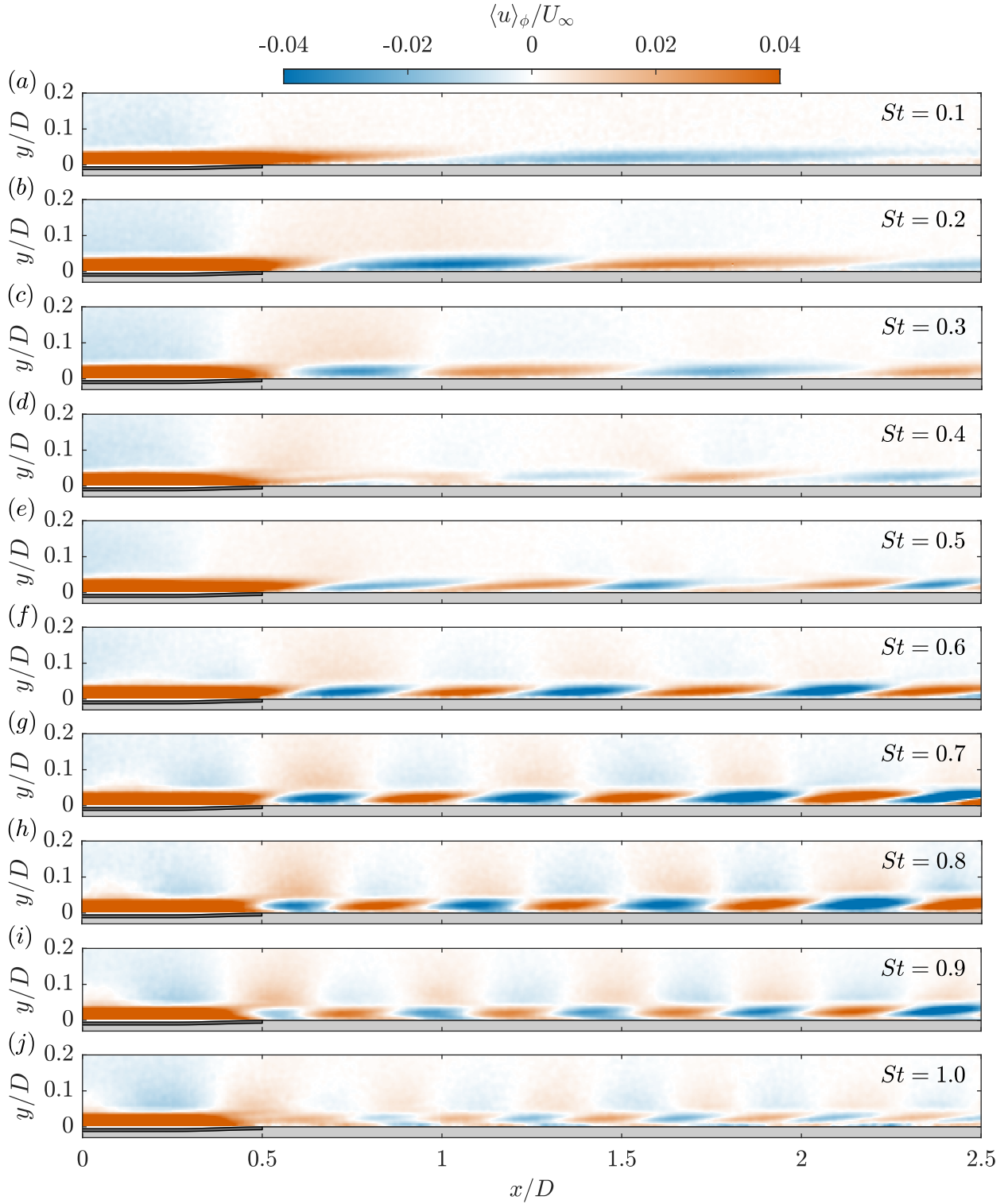


Figure 7.5: Phase averages of the fluctuating streamwise velocity ( $\langle u \rangle_\phi$ ) within FOV4 ( $z = 0$ ) resulting from periodic surface deformation at an amplitude of  $A/D = 0.005$ . The panels (a)-(j) coincide with actuation frequencies of  $St = 0.1$  through 1.0. The phase of the deformation is  $\phi = 3\pi/2$  in all cases, i.e., the surface is at the lowest position of the cycle with zero velocity.

breakdown of the modes that can occur downstream for some of the larger actuation amplitudes.

The streamwise wavelengths of the modes produced by periodic actuation are presented in Figure 7.6(a), where the values can be seen to range from roughly  $\lambda_x/D = 2.3$  at  $St = 0.1$  to  $\lambda_x/D = 0.5$  at  $St = 1.0$ . The figure reveals that the wavelength follows a power law that is proportional to  $St^{-0.7}$ , thus confirming the strong dependence on the actuation frequency that is visible in Figure 7.5. As a result of this power law, the wavelengths reduce quite quickly at the lower frequencies and then level off to a more gradual decline as frequency is increased. The actuation amplitude does not appear to have a large impact on the wavelength, with the exception being actuation at  $St = 0.4$  and  $0.5$ , which reveals wavelengths that no longer agree with the power law for a few actuation amplitudes. This seems to be associated with the emergence of the new mode type at this actuation frequency, although the same behaviour is not observed for the wavelengths at  $St = 1.0$  where the new mode type is also found.

Since the actuation frequencies are known, we can use the wavelengths shown in Figure 7.6(a) to estimate the advection velocity ( $U_c$ ) of each mode using the relation  $U_c = f_a \lambda_x$ . These advection velocities have been computed for all cases and are presented in Figure 7.6(b) along with the associated power law. The advection velocity can be seen to increase with actuation frequency, and the values range from roughly  $U_c/U_\infty = 0.2$  to  $0.45$ . Since  $U_c/U_\infty < 1$  for all cases, the modes feature a so-called “critical layer” centred upon the wall-normal location where the advection velocity of the mode matches the local mean velocity (Maslowe, 1986). The analysis of these critical layers originates from linear stability theory and will be discussed in more detail in Section 7.2.2.

The advection velocities can be used along with Taylor’s hypothesis to transform the time domain of time-resolved measurements into a spatial domain in the streamwise direction. When used with the stereoscopic measurements in the  $z$ – $y$  plane of FOV5, this allows for estimating how the motions shown in Figure 7.5 vary in the spanwise direction. This transformation has been applied to the phase-averaged measurements from FOV5 at  $A/D = 0.005$  while using the power law relation shown in Figure 7.6(b) to compute  $U_c$  (the computed values for  $U_c$  agree well with the power law for this actuation amplitude); the results are shown in Figure 7.7 for the streamwise–spanwise plane at  $y/D = 0.02$ . Note that these visualizations lose accuracy with distance from the location where the measurements were conducted. In the present case the measurements were conducted within FOV5 at  $x/D = 1.1$ , and this location is marked using a dashed line in the panels of Figure 7.7.

The visualizations of the motions in the streamwise–spanwise plane shown in Figure 7.7 reveal interesting behaviour that is not observed within the streamwise–wall-normal plane of FOV4. More specifically, we see a significant variation of the velocity fluctuations in the spanwise direction that provides insight into the true structure of the flow field downstream from the active surface for varying actuation frequencies. We can see that the different mode types really are quite distinct from one another. Some modes, for example those produced at  $St = 0.4$  and  $1.0$  (Figures 7.7(d,j)), have split down the centreline of the active surface ( $z = 0$ ) to produce two separate motions displaced in the spanwise directions. This is clearly why these modes appear to be significantly

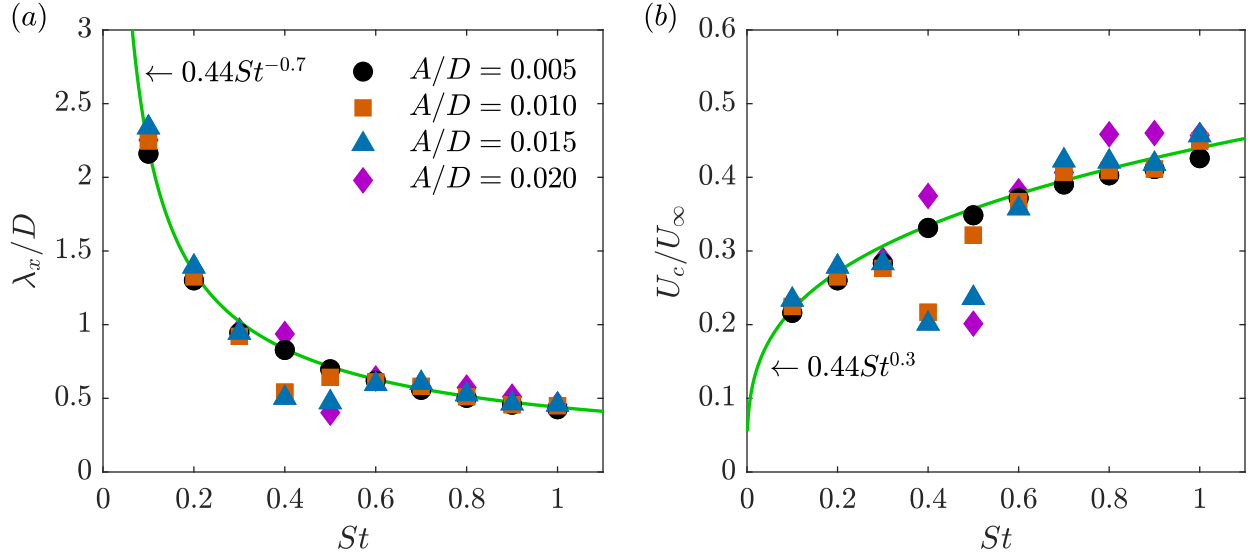


Figure 7.6: (a) The streamwise wavelength ( $\lambda_x$ ) of the modes produced by periodic deformation of the active surface and (b) the associated advection velocities of the modes computed as  $U_c = f_a \lambda_x$ .

weaker in Figures 7.5(d,j). In contrast, other actuation frequencies produce modes featuring single dominant motions concentrated along the centreline of the active surface, for example  $St = 0.1$  and  $0.6$  (Figures 7.7(a,f)). Following these observations we define the *type-1* modes as those featuring high- and low-speed motions with single maximums and minimums along  $z = 0$ . In contrast, we define the *type-2* modes as those featuring high- and low-speed motions with double maxima and minima displaced in the spanwise directions. Consequently, the mode types can be identified by plotting a velocity profile across the span near the location of maximum or minimum velocity fluctuation. Such profiles are shown in the subpanels of Figure 7.7, revealing that actuation at  $St = 0.1, 0.2, 0.6$ , and  $0.7$  produces type-1 modes while the remaining  $St$  produce type-2 modes.

A benefit of using phase-averaged velocity fields in the present investigation is that they allow for combining the results from both FOV4 and FOV5 into 3D visualizations to obtain a more complete picture of the modes produced by the active surface. Figure 7.8 shows such visualizations of the type-1 and type-2 modes and the transitions they go through with increasing  $St$ . These visualizations make use of both sets of phase averages as well as Taylor's hypothesis which was applied in the same manner as for Figure 7.7. The location of the stereoscopic measurement plane used to apply Taylor's hypothesis is shown in Figure 7.8 using a dashed black line. Note that the 3D flow field constructed from the stereoscopic measurements is most accurate close to this plane.

The visualization of the type-1 mode generated at  $St = 0.2$  is shown in Figure 7.8(a), revealing structures that can be described as flattened sheets of high- and low-speed fluid that form above the active surface and advect downstream. In contrast, Figure 7.8(b) shows the type-2 mode that is generated at  $St = 0.3$ . Here, the extrema are now displaced in the spanwise directions as per the definition of type 2. Indeed, the streamwise extent of each coherent motion in Figure 7.8(b) as represented by the isosurfaces can be seen to shrink along  $z = 0$  more drastically than it does farther

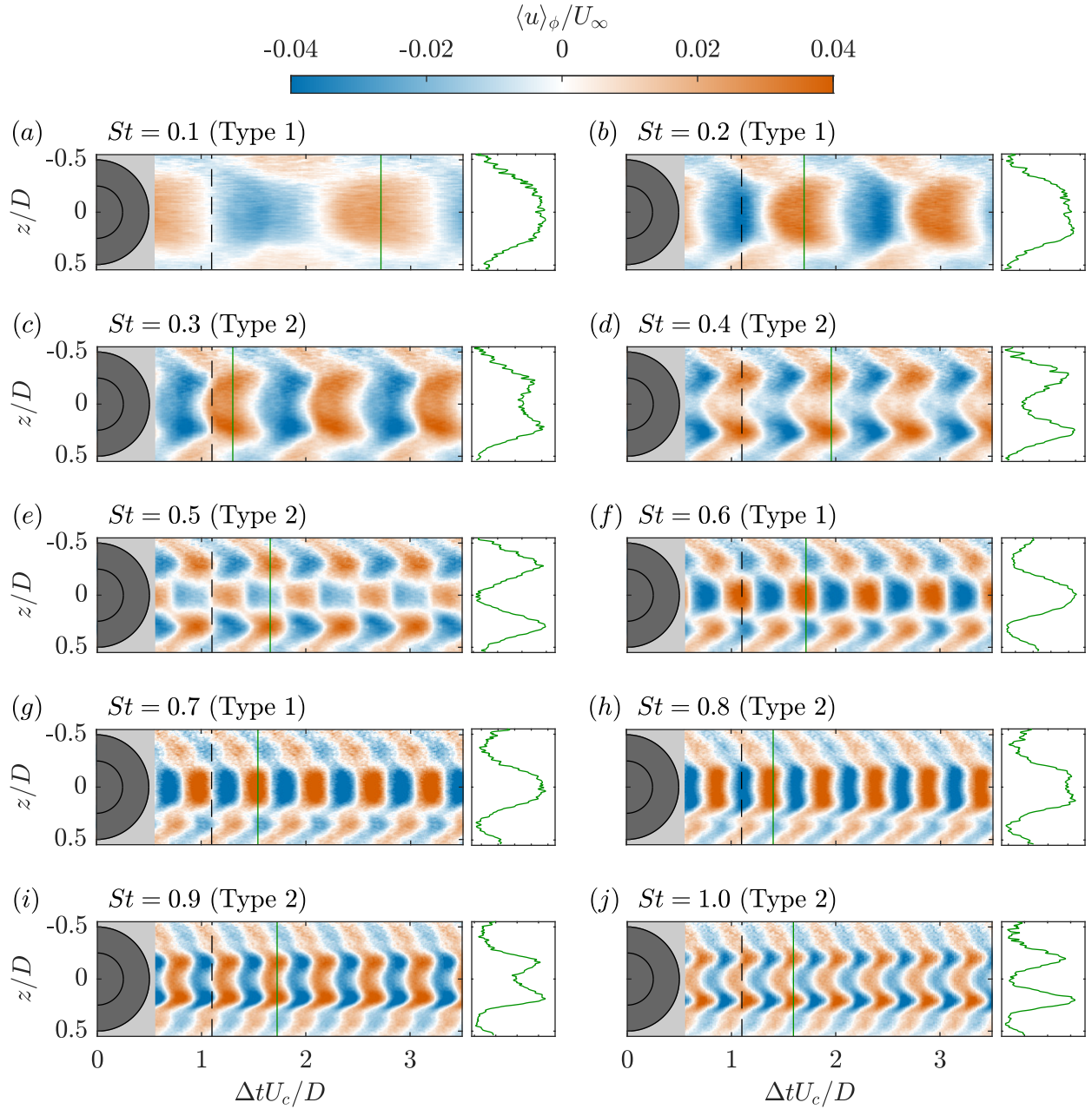


Figure 7.7: Phase averages of the fluctuating streamwise velocity ( $\langle u \rangle_\phi$ ) at a height of  $y/D = 0.02$  resulting from periodic actuation at  $A/D = 0.005$ . The panels (a) through (j) coincide with actuation frequencies of  $St = 0.1$  through  $1.0$ . The phase of actuation is  $\phi = 3\pi/2$  in all cases, which is the same phase shown in Figure 7.5. The streamwise axes have been formed by applying Taylor's hypothesis using the advection velocities computed from the power law shown in Figure 7.6(b). The dashed lines at  $x/D = 1.1$  show the location of the stereoscopic measurements (FOV5) that were used to form these visualizations. The solid green lines show the location of the extracted velocity profiles at the right of each panel.

in the spanwise directions. At  $St = 0.4$  (Figure 7.8(c)), the type-2 mode is very weak along  $z = 0$  where the isosurfaces reveal a near complete splitting of the mode along the actuator centreline. Finally, Figure 7.8(d) shows the type-2 mode that is generated at  $St = 0.5$ . The flattened sheets along  $z = 0$  are beginning to re-emerge, but the extrema of the type-2 mode still have a dominant presence farther away from  $z = 0$ .

Figure 7.8 reveals that the application of Taylor’s hypothesis to the stereoscopic measurements appears to work quite well, as there is good agreement between the isosurfaces and the contours in the  $x$ - $y$  plane obtained using planar PIV. The only exception here is the isosurface of the downstream low-speed motion in Figure 7.8(a), which does not extend as far in the streamwise direction as the contour in the  $x$ - $y$  plane. This is likely because Taylor’s hypothesis is most accurate close to the measurement location ( $x/D = 1.1$  in this case), and this particular structure extends quite far downstream. It is also interesting to note that the advection velocity was assumed to be constant across the boundary layer for the application of Taylor’s hypothesis since the power law from Figure 7.6(b) was used to compute  $U_c$  at each actuation frequency. The alternative approach would be to use the mean velocity at each wall-normal location as the advection velocity as was done in Chapter 5. However, we found that the isosurfaces no longer agreed with the measurements in the  $x$ - $y$  plane when this approach was applied. This suggests that these modes advect downstream with minimal distortion from the mean shear and with advection velocities that differ from the local mean velocity.

Considering the motions produced by periodic actuation, we can conclude that it is the type-1 modes that are most desirable for flow control applications that rely on targeting individual coherent motions. This is because these modes feature dominant motions that are concentrated along  $z = 0$ . It is typical to place sensors and actuators aligned in the streamwise direction, and so an actuator that produces its strongest effect along its own centreline is preferable. The present active surface produces type-1 modes for  $St = 0.1$  to  $0.2$  and  $St = 0.6$  to  $0.7$ . The former frequency range produces velocity fluctuations that are nearly as wide as the active surface, while the latter range produces fluctuations that are much narrower. The type-1 modes produced at low frequencies are therefore a more efficient use of the space taken up by the active surface.

### 7.2.2 Strength and Stability

In the previous section we investigated the spatial structures of the modes produced by the active surface for varying actuation frequencies. We will now explore the strength and stability of these modes as a function of both actuation frequency and amplitude. The spatial structure of a mode produced at a given actuation frequency does not change significantly as the actuation amplitude is increased (prior to the breakdown of a mode via instabilities). Instead, the velocity fluctuations become stronger, which results in the mode becoming less stable overall. To first illustrate this qualitatively we consider instantaneous visualizations of the motions produced at  $St = 0.7$  (type-1 mode) for all amplitudes considered. These visualizations are shown in Figure 7.9 where the actuation phase remains constant for all cases to facilitate comparison. Note that proper orthogonal

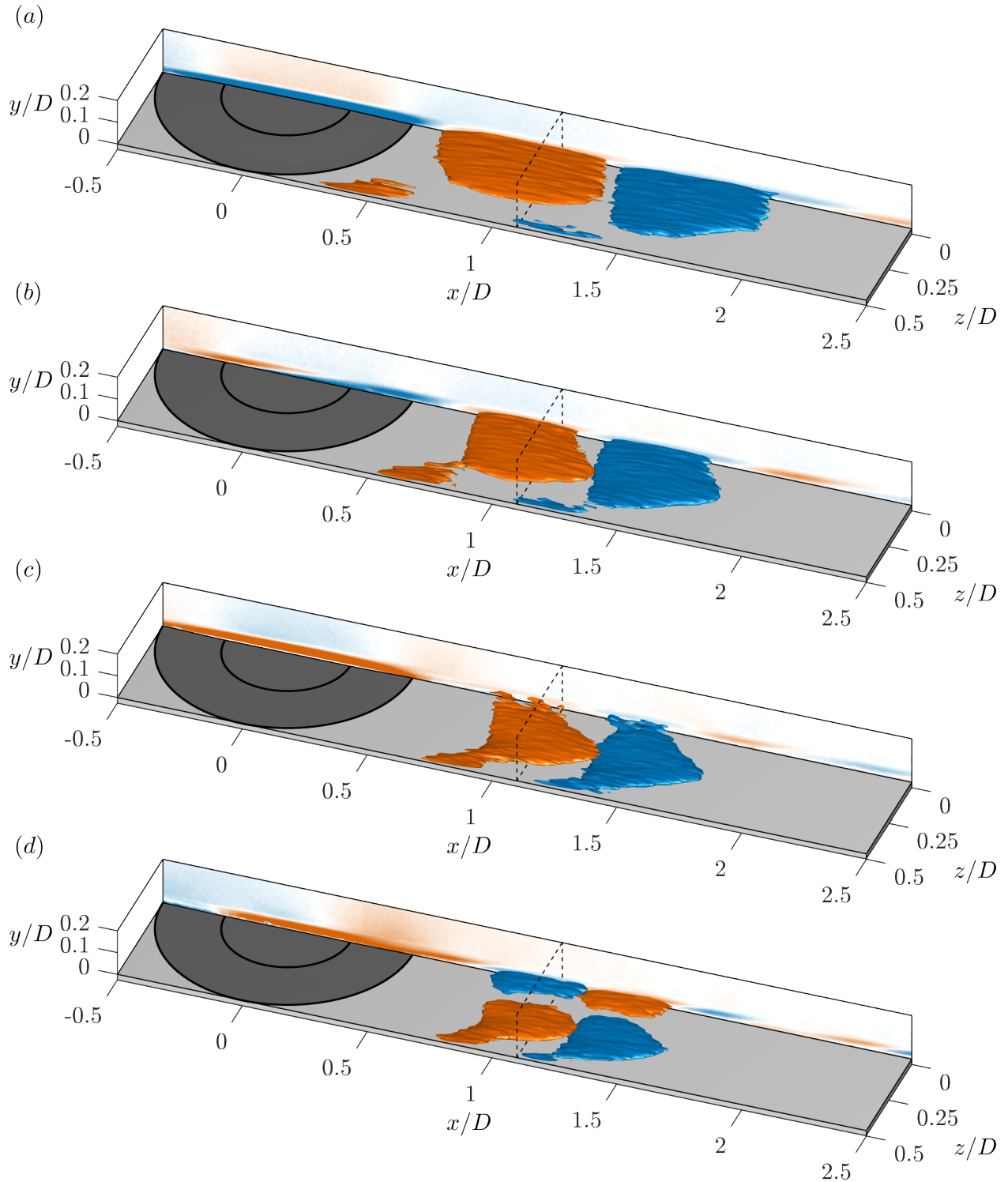


Figure 7.8: Combined phase-averaged visualizations of the motions formed by the active surface for (a)  $St = 0.2$ , (b)  $St = 0.3$ , (c)  $St = 0.4$ , and (d)  $St = 0.5$ . The isosurfaces are shown at  $\pm 0.01U_\infty$  and the contours in the  $x$ - $y$  plane have the same scaling as Figures 7.5 and 7.7. Taylor's hypothesis was used to transform the time-resolved stereoscopic measurements into three dimensions; the location of the stereoscopic plane is shown in each panel using the dashed black lines.

decomposition (POD) by the method of snapshots (Sirovich, 1987) was applied to reduce the PIV noise for the purpose of improving these visualizations. The POD reconstructions retain a minimum of 85% of the fluctuating energy.

The instantaneous visualization for  $A/D = 0.005$  (Figure 7.9(a)) is consistent with the phase averages shown in Figures 7.5(g) and 7.7(g). This is because this small actuation amplitude is not large enough to cause the mode to break down within the FOV and therefore the periodicity is retained. However, while the mode remains organized, we can see that the high- and low-speed motions are increasing in strength with downstream distance. This suggests that the mode is unstable and may grow to the point of decomposition at some point farther downstream. When the actuation amplitude is increased to  $A/D = 0.01$  (Figure 7.9(b)), we can see that the mode now begins to break down within FOV4 as is evidenced by the high- and low-speed motions overlapping with one another near  $x/D = 1.8$ . It seems that this may be the natural progression of these modes when the strength of the fluctuations surpasses some threshold since high- and low-speed motions that alternate in the streamwise direction would have a tendency to approach one another as a result of their different advection velocities. Once the actuation amplitude is further increased to  $A/D = 0.015$  or  $0.02$  (Figures 7.9(c,d)) it is clear that the coherent structures have begun to break down into smaller motions within the FOV.

All motions shown in Figure 7.9 are quite similar to one another up to roughly  $x/D = 1.3$ . Although the height of the surface deformation has increased fourfold across the cases considered, the height of the high- and low-speed motions just downstream from the active surface does not change much. Instead, increasing the amplitude of the surface deformation increases the strength of the motions. This is most obvious when looking at the low-speed motion located around  $x/D = 1$  in each panel of Figure 7.9, which can clearly be seen to increase in strength as the actuation amplitude is increased. In fact, it appears that it is these low-speed motions that initiate the breakdown of the mode, as they are observed to lift up and eventually participate in the emergence of the turbulent motions as can be seen in Figures 7.9(c,d). These low-speed motions will produce an inflection point within the instantaneous boundary layer profile; such an inflection point is well-known to be associated with instability (Schlichting and Gersten, 2017; Schmid and Henningson, 2001).

The instantaneous visualizations shown in Figure 7.9 are generally representative of what happens to all modes when the actuation amplitude is increased. More specifically, increasing the amplitude increases the strength and decreases the stability of the motions while the spatial structure of the mode at a given frequency is roughly retained until an instability begins to grow. At the point of instability the high- and low-speed structures begin to overlap, leading to an eventual breakdown into smaller turbulent motions. Despite this generally applicable observation, these visualizations are essentially qualitative and are therefore limited in their ability to capture the full extent of the present results. To better quantify the strength and stability of the motions for all periodic actuation cases, we return to the phase averages. As described in Section 7.1.5, the phase-averaged results are an excellent representation of the instantaneous motions when they re-

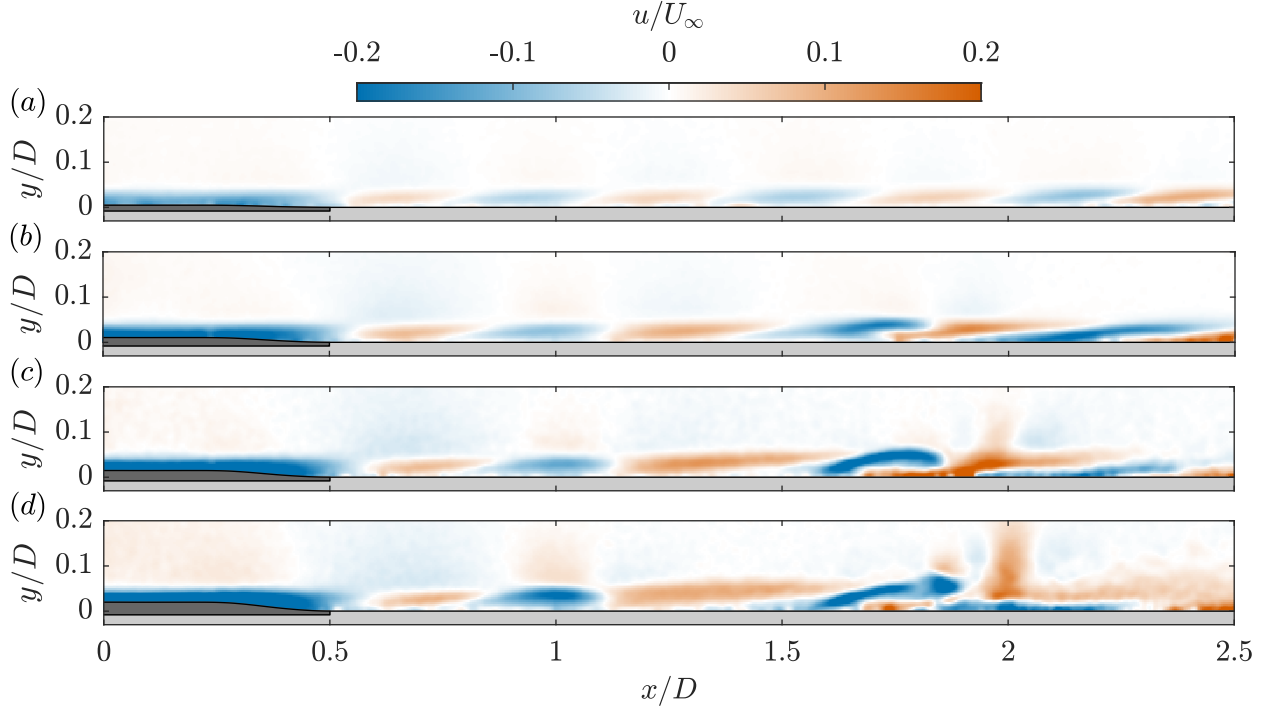


Figure 7.9: Instantaneous visualizations of streamwise velocity fluctuation ( $u$ ) produced at an actuation frequency of  $St = 0.7$  for actuation amplitudes of (a)  $A/D = 0.005$ , (b)  $A/D = 0.01$ , (c)  $A/D = 0.015$ , and (d)  $A/D = 0.02$ . The phase of the actuator is roughly  $\phi = \pi/2$  in all cases, i.e., the surface is at the highest position of the cycle with zero velocity.

main organized and periodic, but they no longer accurately represent the instantaneous flow once a mode begins to break down. This is not an issue for the present analysis because we are interested in the strength of the periodic motions while they remain organized and whether this strength decays (stable) or grows (unstable) with downstream distance. Both pieces of information can be extracted from the phase averages and therefore they provide an excellent summary of the strength and stability of the modes produced by the active surface as a function of actuation frequency and amplitude.

The maximum absolute values of the phase-averaged streamwise velocity fluctuations ( $\max(|\langle u \rangle_\phi|)$ ) are presented in Figure 7.10 as a function of streamwise distance for all periodic actuation cases. The figure includes the measurements from both FOV4 (solid lines) and FOV5 (star symbols). The results from FOV4 consider the maximum over the wall-normal and phase dimensions along  $z = 0$ , while the results from FOV5 consider the maximum over the spanwise, wall-normal, and phase dimensions at  $x/D = 1.1$ . When these two sets of results agree (the star symbol is close to the solid line) it is because the maximum occurs near  $z = 0$  (type-1 mode) and is captured by both FOVs. When a significant discrepancy is observed it is because the maximum occurs away from  $z = 0$  (type-2 mode) and is therefore only captured by the measurement in FOV5. The quantity plotted in Figure 7.10 provides a measure of the average peak strength of the fluctuations produced by the

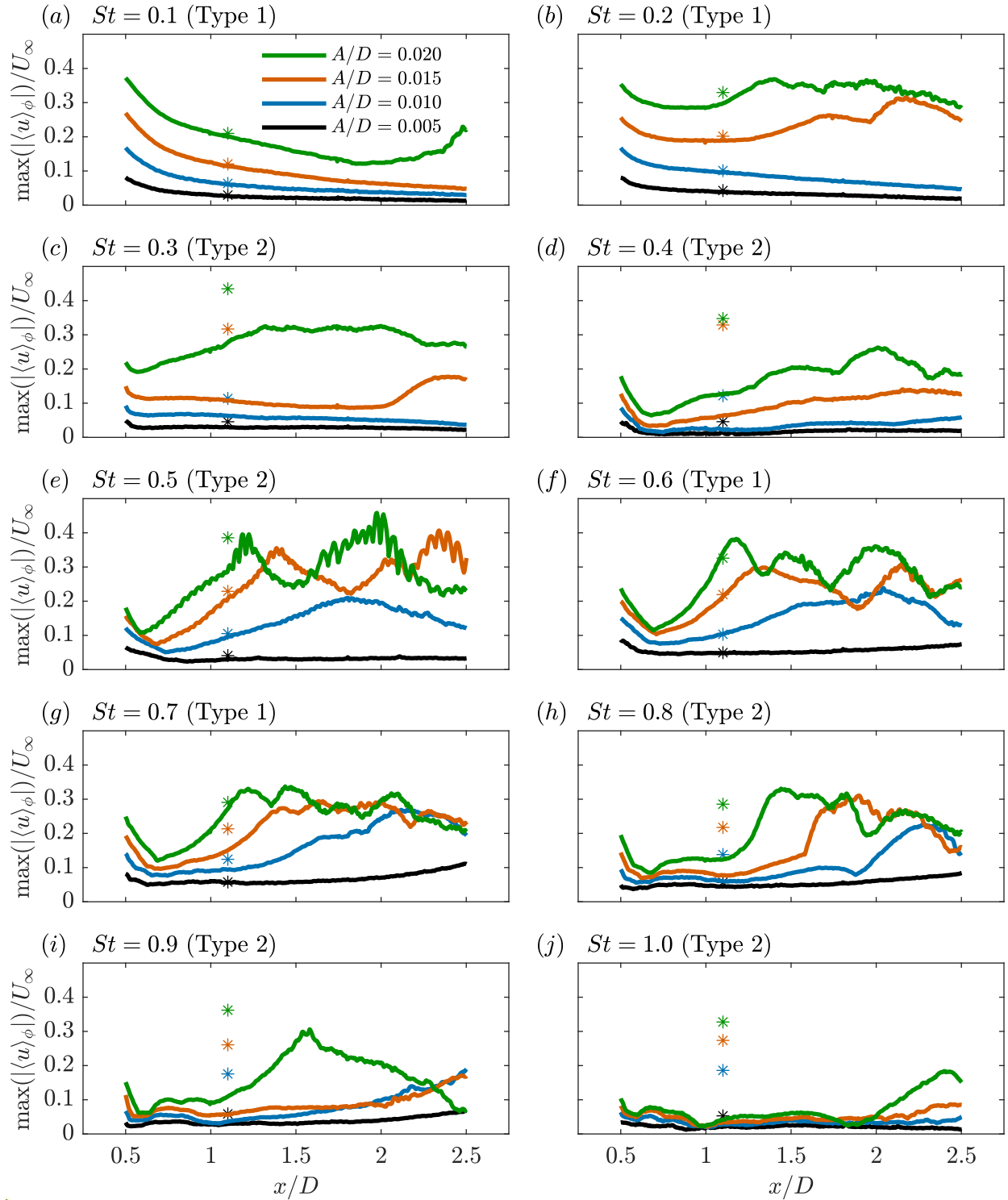


Figure 7.10: Maximum absolute values of the phase-averaged streamwise velocity fluctuations (i.e., the strength of the modes) within  $z = 0$  as a function of streamwise distance for all periodic deformation cases. The panels (a) through (j) coincide with actuation frequencies of  $St = 0.1$  though 1.0. The star symbols represent the same quantity extracted from the stereoscopic measurements at  $x/D = 1.1$ .

active surface and will simply be referred to as the *strength* of the modes to ease the discussion moving forward.

First we consider the strength and stability of the flow downstream from the active surface at the frequency and amplitude combinations that produce type-1 modes. As shown previously (Figure 7.7) this occurs for  $St = 0.1, 0.2, 0.6,$  and  $0.7$ . Since FOV4 is located at  $z = 0$ , the results shown in Figure 7.10 are well-suited for quantifying the strength and stability of these type-1 modes. The velocity fluctuations produced by periodic deformation at  $St = 0.1$  (Figure 7.10(a)) appear to remain stable for amplitudes ranging from  $A/D = 0.005$  to  $0.015$  as is indicated by the observed decay in strength with streamwise distance. In contrast, actuation at  $A/D = 0.02$  produces a mode with a strength that begins to grow substantially beyond  $x/D = 2$ , thus indicating that the associated mode has become unstable. Similar behaviour is observed for  $St = 0.2$  (Figure 7.10(b)), but at this frequency both  $A/D = 0.015$  and  $0.02$  produce an unstable mode. We can also see that the points from FOV5 agree well with the curves from FOV4 for  $St = 0.1$  and  $0.2$ , indicating that the maximum strength occurs near  $z = 0$  and confirming that these are in fact type-1 modes. This is also the case for  $St = 0.6$  and  $0.7$  (Figures 7.10(f,g)). However, these actuation frequencies appear to produce type-1 modes that are unstable for all actuation amplitudes considered. This is indicated by the strength either becoming erratic within FOV4 ( $A/D \geq 0.01$ ) or continuing to grow with downstream distance ( $A/D = 0.005$ ).

The strength of the type-1 modes produced at  $St = 0.1$  and  $0.2$  for the same actuation amplitudes are quite similar if we only consider the portion of the curves prior to instability growth. If we look at the strength at the edge of the active surface ( $x/D = 0.5$ ) we can see that both actuation frequencies produce a maximum strength that ranges from roughly  $0.1U_\infty$  to  $0.35U_\infty$  as the actuation amplitude is increased (Figures 7.10(a,b)). These values then decay at similar rates with downstream distance for the cases that remain stable. Since the actuation frequency has doubled between these two cases, so has the velocity of the surface. Despite this, the strength remains similar. The same result is visible for the type-1 modes produced at  $St = 0.6$  and  $0.7$  (Figures 7.10(f,g)), i.e., the strength of the fluctuations produced at the edge of the active surface is similar for both frequencies as long as we are considering the same actuation amplitude. However, these fluctuations are weaker overall compared to those produced at  $St = 0.1$  and  $0.2$ .

Unfortunately, the present results do not allow us to quantify the strength of the type-2 modes as well as we can quantify that of the type-1 modes. This is because the extrema have moved away from  $z = 0$  and therefore the strongest velocity fluctuations occur outside of FOV4 which is where the results shown in Figure 7.10 are concentrated. Despite this, the results in Figure 7.10 indicate that the modes produced at higher frequencies are generally unstable while the low frequencies ( $St \leq 0.2$ ) have higher stability. Moreover, these low-frequency modes are stronger and of type 1. Together, these characteristics suggest that low-frequency operation of the active surface is the best option for flow control.

We will now briefly consider the modes produced by the active surface in the framework of linear stability analysis. Such an analysis considers neutral disturbance waves superimposed on a

base flow (e.g., the Blasius profile) and their subsequent growth or decay according to a linearized version of the Navier-Stokes equations (Schlichting and Gersten, 2017). In this context, a neutral wave is one that is periodic in both space and time (Maslowe, 1986) and must have a magnitude small enough to still be considered linear. These latter two points are where the present work deviates from the requirements of the linear analysis. The motions produced by the active surface are periodic in time but not in space since the actuator is finite in the spanwise direction. Moreover, since we are concerned with flow control we are not interested in small disturbances. Instead, we are interested in producing velocity fluctuations with large magnitudes that can potentially be used to target various flow features. For these reasons we cannot expect our results to agree with those of the linear stability analysis. This is likely why we see instability prior to  $x/D = 2$  where  $Re_{\delta^*} = 520$ , i.e., the “indifference point” for the Blasius profile (Schlichting and Gersten, 2017). However, there are still a few instances where we can make comparisons with the linear theory.

One characteristic of the linear theory is existence of a “critical layer” centred upon a critical point where the advection velocity of the disturbance matches the local mean velocity. This point causes a mathematical singularity in the inviscid analysis that can only be remedied by restoring the effect of viscosity within the critical layer, thus indicating that viscous effects are important within this layer. Similarly, the Stokes layer that forms adjacent to the wall as a result of the periodically-fluctuating velocity field is a second region where viscous effects are important. Whether these two layers overlap with one another or are separated is related to the neutral stability curve for the Blasius profile (Schmid and Henningson, 2001); overlapping layers indicates a lower-branch mode while separated layers indicate an upper-branch mode. Other characteristics of these modes include the maximum  $u$  of the mode occurring somewhere within the critical layer and a 180-degree phase shift in  $u$  occurring somewhere in the outer region of the boundary layer (Jacobi and McKeon, 2011). We can consider these characteristics to determine whether the modes produced by the present active surface are consistent with the critical-layer-type modes that arise from linear stability analysis.

The type-1 modes at  $St = 0.2, 0.6$  and the type-2 modes at  $St = 0.4, 1.0$  are shown in Figure 7.11 along with the estimated size and locations of the Stokes (solid magenta lines) and critical (dotted black lines) layers. The type-1 modes (Figures 7.11(a,c)) are strongest along  $z = 0$  and have therefore been plotted using the measurements from FOV4. In contrast, the type-2 modes (Figures 7.11(b,d)) have been plotted from the measurements in FOV5 via Taylor’s hypothesis since their strongest fluctuations are displaced in the spanwise directions; these latter two subplots contain the same data as Figure 7.7 but shown in a different plane. We have estimated the thickness of the Stokes layer as  $\sqrt{\nu/\pi f_a}$  (Schlichting and Gersten, 2017). The centre of the critical layer is defined by the critical point (dashed black lines) where the advection velocity of the mode matches the local mean velocity. The maximum streamwise velocity fluctuation occurs within the critical layer and so we have used the location of the maxima to estimate the minimum thicknesses of the critical layers. The maximum is always located above the critical point for the present modes (this is typical of critical-layer-type modes (Jacobi and McKeon, 2017)), and so the upper bounds of

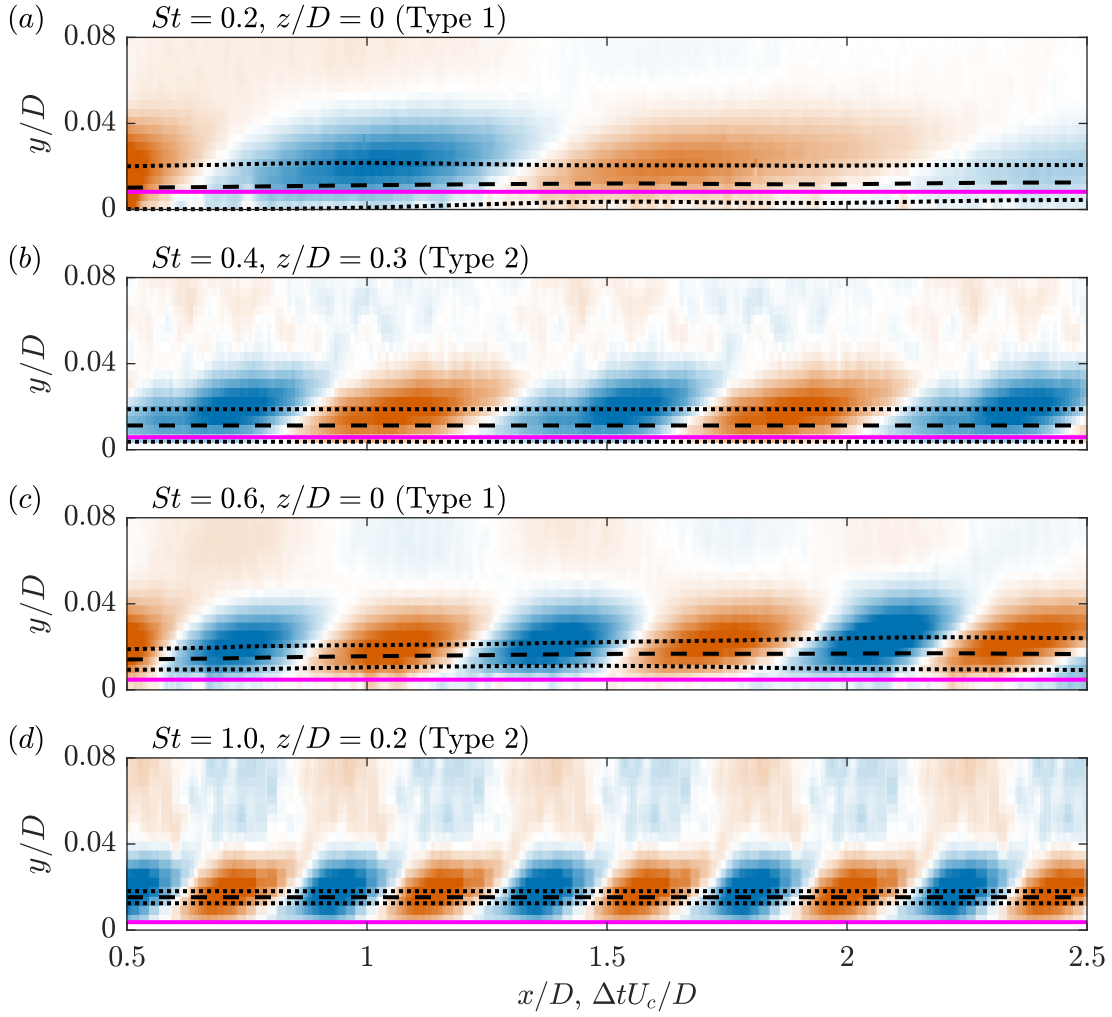


Figure 7.11: Type-1 modes at (a)  $St = 0.2$  and (c)  $St = 0.6$  from FOV4 and type-2 modes at (b)  $St = 0.4$  and (d)  $St = 1.0$  from FOV5 (via Taylor’s hypothesis) with the estimated location of the Stokes layers (solid magenta lines) and critical layers (black dotted lines) overlaid. The critical points (black dashed lines) are at the centre of the critical layer. The wall-normal dimension is stretched here to better show the Stokes and critical layers. The colorbar scaling is the same as for Figures 7.5 and 7.7.

the estimated critical layers in Figure 7.11 have been set by the maxima locations while the lower bounds are set by symmetry about the critical points.

The estimated Stokes and critical layers for  $St = 0.2$  and  $0.4$  in Figures 7.11(*a,b*) show clear overlap with one another, even with the critical layers being defined by a minimum thickness. This indicates that the type-1 and type-2 modes produced by actuation at the lower frequencies have structures in the streamwise–wall-normal plane that are consistent with lower-branch modes. In contrast, the estimated Stokes and critical layers for  $St = 0.6$  and  $1.0$  in Figures 7.11(*c,d*) are separated, which indicates that the type-1 and type-2 modes at higher frequencies have upper-branch structures. However, this particular observation is not absolute because the present critical layers were estimated using a minimum thickness, and so it remains possible that they are actually thick enough to produce overlap with the Stokes layers. Despite this, it seems likely that at least the type-2 mode at  $St = 1.0$  (Figure 7.11(*d*)) has an upper-branch structure because the estimated Stokes and critical layers are quite far apart. Finally, we can see that there is a change in the sign of streamwise velocity fluctuation somewhere in the range  $y/D = 0.04$  to  $0.05$  for all cases shown in Figure 7.11. This is characteristic of the 180-degree phase shift described earlier and is therefore another indication that the motions produced by the active surface are consistent with the critical-layer-type modes that arise from linear stability analysis.

Considered along with Figure 7.10, Figure 7.11 suggests that the type-1 modes with a lower-branch structure are more stable than the type-1 modes with an upper-branch structure. Unfortunately, it is difficult to comment on the stability of the type-2 modes in the context of their critical-layer-type structures due to the spanwise location of FOV4, which does not allow for monitoring the peak strength of the type-2 modes as a function of streamwise distance.

### 7.3 Data-Driven Modelling of the Actuated Flow

A important aspect of any active control strategy is the model that is used to develop the controller. These models can take many forms and range from simple physics-informed heuristics to complex mathematical representations of system dynamics. One model type that is commonly applied in experimental campaigns to develop controllers for wall-bounded flows is the nonparametric linear transfer function (NLTF) (e.g., the work of Rathnasingham and Breuer (2003), Juillet et al. (2014), and Brito et al. (2021)). This type of model is used to describe the input-output behaviour of a given system and can be identified using data-driven methods. In this section, we investigate how well the input-output dynamics of the present active surface can be captured using a NLTF model.

#### 7.3.1 Modelling with Nonparametric Linear Transfer Functions

The NLTF describes the input-output relationship between two variables in the frequency domain to the extent that this relationship can be captured by linear dynamics. In the present work we consider the input to our system to be the height of the active surface  $h(t)$  and the output of the system to be the streamwise velocity fluctuation  $u(t)$  at some point downstream from the active

surface. The relationship between these two variables according to the NLTF model is then

$$\tilde{u}(f) = G_{hu}(f)\tilde{h}(f), \quad (7.3)$$

where  $G_{hu}(f)$  is the NLTF between  $h(t)$  and  $u(t)$  while  $\tilde{h}(f) = \mathcal{F}\{h(t)\}$  and  $\tilde{u}(f) = \mathcal{F}\{u(t)\}$  are the Fourier transforms of the input and output, respectively. We can then employ the convolution theorem for Fourier transforms to yield

$$u(t) = g_{hu}(t) * h(t), \quad (7.4)$$

where the symbol ‘\*’ denotes a convolution and  $g_{hu}(t)$  is the impulse response of the system. The impulse response and NLTF are therefore equivalent representations of the system dynamics and are related through the Fourier transform as  $G_{hu}(f) = \mathcal{F}\{g_{hu}(t)\}$ . As a result, either of these can be identified to obtain the desired model of the system.

There are numerous ways to identify either the NLTF or the associated impulse response of a system such that they are consistent with Equations (7.3) and (7.4). For example, the impulse response can be measured directly using an impulse response experiment. This technique is not typically used in experimental studies because it is often difficult to generate a true impulse response with a physical actuator, and this is indeed the case for the present active surface. Instead, it is typical to identify the dynamics by applying statistical approaches to randomized input-output data. One common approach employs the cross spectral density between the input and output to directly estimate the NLTF (Brito et al., 2021). Another approach utilizes Wiener filtering to estimate the impulse response (Rathnasingham and Breuer, 2003) which can then be used to obtain the NLTF via the Fourier transform. We have elected to use the Wiener filtering method because we found that it outperforms the spectral estimation method when applied to the present system. The application of the Wiener filter as outlined by Hayes (1996) has been implemented in the present work and will be briefly detailed below.

The Wiener filter is used as an estimator whose coefficients represent the (finite) impulse response of the associated system. When this impulse response is convolved with the input to the system, it produces an optimal estimate of the output according to the minimum mean-square criterion. Since the Wiener filter is a digital filter with discrete coefficients, it is applied using sampled measurements. It should therefore be understood that  $h(t)$  and  $u(t)$  are considered discrete signals for the implementation of the Wiener filter moving forward. Equations (7.3) and (7.4) are still valid in discrete time and are related through the discrete Fourier transform.

The impulse response associated with the Wiener estimator is identified by solving the Wiener-Hopf equations, which are expressed using the present nomenclature as

$$\mathbf{R}_h \mathbf{c} = \mathbf{r}_{hu}, \quad (7.5)$$

where  $\mathbf{R}_h$  is a Toeplitz matrix containing the autocorrelations of  $h(t)$ ,  $\mathbf{c}$  is a vector containing the

filter coefficients, and  $\mathbf{r}_{hu}$  is a vector containing the cross-correlations between  $h(t)$  and  $u(t)$ . The compact notation of Equation (7.5) can be expanded to yield

$$\begin{bmatrix} r_h(0) & r_h(1) & \dots & r_h(m-1) \\ r_h(1) & r_h(0) & \dots & r_h(m-2) \\ r_h(2) & r_h(1) & \dots & r_h(m-3) \\ \vdots & \vdots & & \vdots \\ r_h(m-1) & r_h(m-2) & \dots & r_h(0) \end{bmatrix} \begin{bmatrix} c(0) \\ c(1) \\ c(2) \\ \vdots \\ c(m-1) \end{bmatrix} = \begin{bmatrix} r_{hu}(0) \\ r_{hu}(1) \\ r_{hu}(2) \\ \vdots \\ r_{hu}(m-1) \end{bmatrix}, \quad (7.6)$$

where  $m$  is the selected order of the Wiener filter and therefore also the length of the identified impulse response. Once a system identification experiment has been performed to obtain  $h(t)$  and  $u(t)$ , the above Wiener-Hopf equations can be solved to obtain the identified impulse response as  $\hat{g}_{hu}(t) = \mathbf{c}$  and therefore also the associated NLTF as  $\hat{G}_{hu}(f) = \mathcal{F}\{\hat{g}_{hu}(t)\}$  (the hat accents have been added to denote that these are estimates). Note that an order of  $m = 250$  has been used to solve Equation (7.6) in all cases presented here. The MATLAB code used to perform the Wiener system identification is provided in Appendix B.

The characteristics of the input signal used in the system identification experiment are critical for achieving good results. The amplitude of the input must be large enough to elicit a response from the system, and the frequency spectrum of the input must cover the range of frequencies relevant to the application. The results from Section 7.2 indicate that large deformations of the present active surface result in the production of highly unstable motions. They also indicate that the lower range of the frequencies considered here seems most promising for flow control applications. We have therefore performed our system identification experiment using an input signal that halves both the frequency range and maximum deformation considered in Section 7.2. More specifically, we have used an input signal that produces maximum surface deformations of  $h/D = \pm 0.01$  and covers frequencies up to  $St = 0.5$ . Note that this frequency range contains both the type-1 and type-2 modes identified in Section 7.2.

Two sets of data were collected using two different input signals: one for the purpose of system identification (i.e., model training) and one for model evaluation. These two input signals were completely uncorrelated but featured nearly identical statistics. The PSD of these input signals ( $\Phi_h$ ) and samples of the corresponding time series are shown in Figure 7.12. Figure 7.12(a) reveals that the PSD of both signals have almost perfect overlap. The frequency response is flat for frequencies up to  $St = 0.5$ , at which point a significant drop in the spectral power is observed. Figure 7.12(b) shows the random nature of the input signals in the time domain and confirms that the magnitudes do not exceed  $h/D = \pm 0.01$  (note that only 25% of the total input signals are shown).

The velocity fluctuations farther downstream from the active surface that are generated at lower actuation amplitudes have magnitudes on the order of a few percent of  $U_\infty$ , which is similar to the PIV noise in the present data sets. Although the system identification process discussed

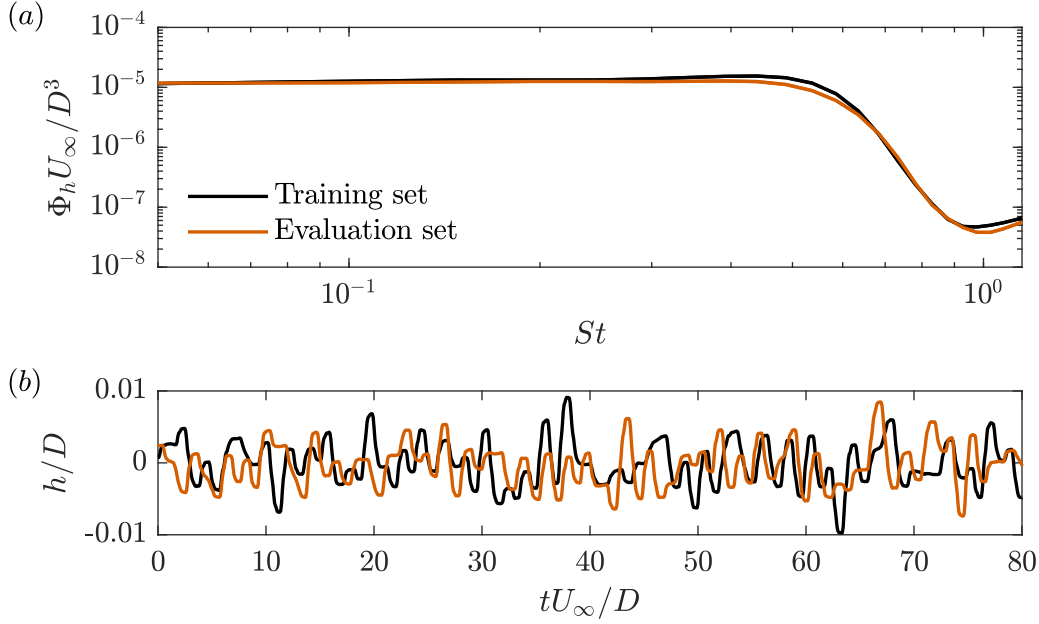


Figure 7.12: (a) The PSD of the input used for system identification and model evaluation ( $\Phi_h$ ) and (b) samples of the corresponding time series.

above ignores the uncorrelated PIV noise, this noise can still pose a problem for evaluating the performance of the NLTF model using the PIV measurements. We have therefore employed POD to produce noise-reduced versions of the instantaneous velocity fields. The method of snapshots (Sirovich, 1987) was applied to an isolated region within FOV4 defined by  $0.5 \leq x/D \leq 2.5$  and  $0 \leq y/D \leq 0.2$ . This region was isolated because it reduces the computations required for POD while retaining the entirety of the fluctuating velocity field downstream from the active surface. These data were then reconstructed using varying numbers of POD modes to identify the point at which the basis should be truncated to reduce the PIV noise. Figures 7.13(a,b) show the PSD of the fluctuating velocity signals extracted from the evaluation data set at  $x/D = 1$  and 2 ( $y/D = 0.03$ ) after being reconstructed using varying numbers of POD modes. The PSD of the random forcing input is also shown (scaled) for reference to highlight the frequency at which a large drop in the PSD of the velocity signal is expected. The frequencies up to this drop-off will be referred to as the relevant frequency range.

The PSD of the raw signals at both  $x/D = 1$  and 2 show a large spectral density at frequencies beyond those of the forcing input. This noise floor is a result of the high-frequency PIV noise and is therefore not physical. Figures 7.13(a,b) reveal that the noise floor drops significantly when fewer POD modes are used to reconstruct the data. However, if the number of modes used for reconstruction is too small, the spectral density reduces substantially in the relevant frequency range as well, indicating that some physical variation within the data set is not being captured. We must therefore reconstruct the data using a number of POD modes that maximizes the reduction of the noise floor while minimizing the loss of spectral density in the relevant frequency range. This

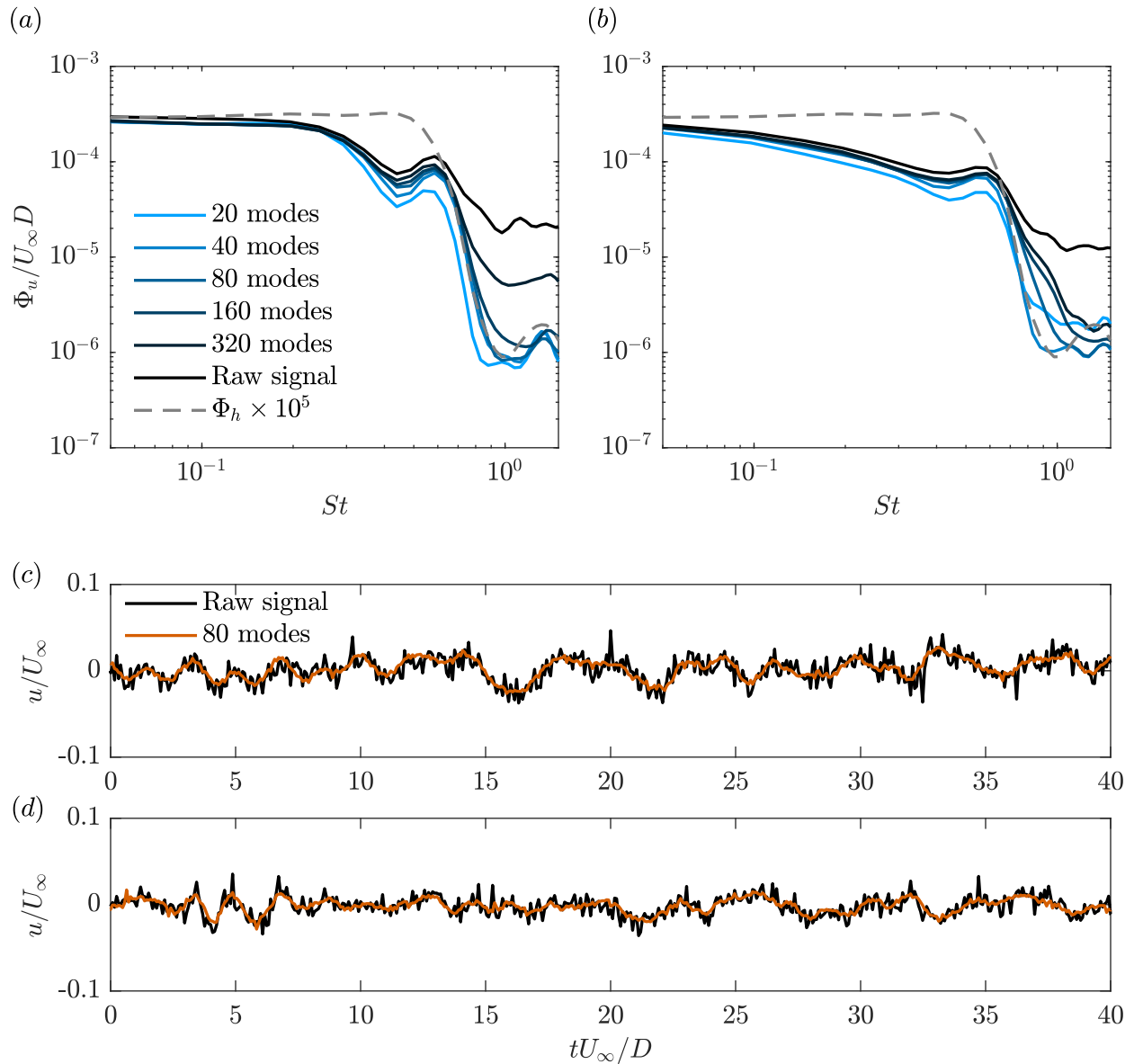


Figure 7.13: PSD and instantaneous samples of the streamwise velocity fluctuations from the evaluation data set reconstructed using varying numbers of POD modes. The results are plotted for (a,c)  $x/D = 1, y/D = 0.03$  and (b,d)  $x/D = 2, y/D = 0.03$ . The PSD of the forcing input ( $\Phi_h$ ) is shown (scaled) for reference.

will result in a noise-reduced data set that still captures the physical variations within the velocity field.

By inspection of Figures 7.13(*a,b*), we have elected to reconstruct the system identification data sets using the first 80 POD modes. As can be seen in the figure, this balances the two requirements of noise reduction in the high-frequency range and spectral density retention in the relevant frequency range. Instantaneous samples of the reconstructed streamwise velocity fluctuation compared to the raw signal at  $x/D = 1$  and  $2$  are shown in Figures 7.13(*c,d*). These results reveal that the reconstructed data do a good job of capturing the variation of the velocity field while greatly reducing the high-frequency PIV noise. This noise-reduced data has been used to both identify and evaluate the NLTFs in the present work. The streamwise velocity fluctuations have been extracted from the noise-reduced velocity fields at  $y/D = 0.03$  for all cases, which is roughly the half-height of the high- and low-speed structures generated by the active surface (see Figure 7.5).

The magnitude of the identified NLTFs that relate  $h$  with  $u$  at streamwise locations of  $x/D = 1$  and  $2$  are presented in Figure 7.14(*a*). The training input from Figure 7.12(*a*) has been overlaid using a grey dashed line to highlight the frequency range that received significant forcing during the system identification experiment; the portions of the NLTFs that fall outside of this range will be less reliable because these frequencies were not forced adequately. Both NLTFs are relatively flat up to  $St = 0.3$ , at which point the magnitude begins to drop. The magnitude then starts to recover around  $St = 0.5$ , peaks near  $St = 0.7$ , and then begins to drop once again. This observed modulation of the magnitudes can be attributed to the switching between type-1 and type-2 modes that occurs with increasing actuation frequency as was discussed in Section 7.2. The frequencies at which the reductions in magnitude occur are consistent with the emergence of the type-2 modes visible in Figure 7.7.

The Wiener filter coefficients that represent the impulse responses associated with the NLTFs in Figure 7.14(*a*) are shown in Figure 7.14(*b*), where all  $m = 250$  coefficients are displayed. Neither of the two impulse responses look much like those that are typical of simple linear systems, which usually oscillate and eventually damp out. Some low-frequency oscillatory behaviour is observed prior to  $tU_\infty/D = 5$  for both cases, but the remainder of the identified impulse responses appear quite erratic. In general, these impulse responses are difficult to interpret in a meaningful way. However, we must keep in mind that they are sets of filter coefficients meant to describe the dynamics of a nonlinear system of high dimension.

### 7.3.2 Model Evaluation

We now move on to evaluating the estimates produced by the NLTF model. These estimates have been obtained by convolving the identified impulse responses with the input to the evaluation data set as

$$\hat{u}(t) = \hat{g}_{hu}(t) * h(t), \quad (7.7)$$

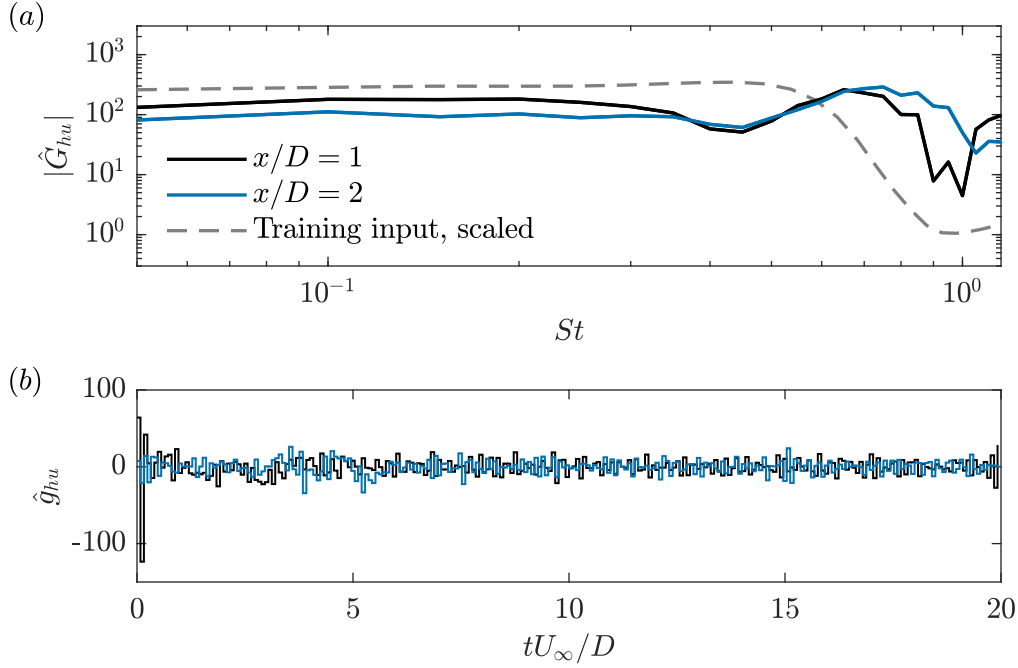


Figure 7.14: (a) The magnitude of the NLTFs relating  $h$  with  $u$  at two downstream locations (extracted at  $y/D = 0.03$ ) and (b) the associated Wiener filter coefficients which represent the impulse responses. The grey dashed line in (a) is the training input from Figure 7.12(a) and is shown here (scaled) to highlight the frequency range of the NLTFs that received adequate forcing during the system identification experiment.

where  $\hat{u}(t)$  is the estimated streamwise velocity fluctuation downstream from the active surface. We then compare these estimates to the velocity fluctuations measured using the POD-filtered PIV within FOV4 to determine how well the NLTF model captures the input-output dynamics of the present system.

The comparison is first made using the correlation coefficient between  $u(t)$  and  $\hat{u}(t)$  at all locations downstream from the active surface. This coefficient is denoted as  $r_{u\hat{u}}$  and is presented in Figure 7.15. The results show that the correlation coefficient is  $r_{u\hat{u}} = 0.95$  at  $x/D = 0.5$ , indicating that the NLTF model does a great job of estimating the streamwise velocity fluctuations immediately downstream from the active surface. The coefficient then begins to decline with increasing distance from the active surface, most likely due to the nonlinearity of the system. The two streamwise locations for which the NLTF models are presented in Figure 7.14 are highlighted in Figure 7.15, revealing correlation coefficients of  $r_{u\hat{u}} = 0.86$  and  $0.71$  for  $x/D = 1$  and  $2$ , respectively. Finally, the coefficient reaches a value of  $r_{u\hat{u}} = 0.70$  at the end of FOV4 ( $x/D = 2.5$ ). The decline in  $r_{u\hat{u}}$  can be seen to slow beyond  $x/D = 2$ . However, it is unlikely that this trend is sustained beyond the end of FOV4 because it only becomes more difficult for the NLTF model to capture the input-output behaviour as nonlinearities grow with downstream distance. It is therefore more likely that the correlation coefficient begins to drop drastically at some point beyond  $x/D = 2.5$ .

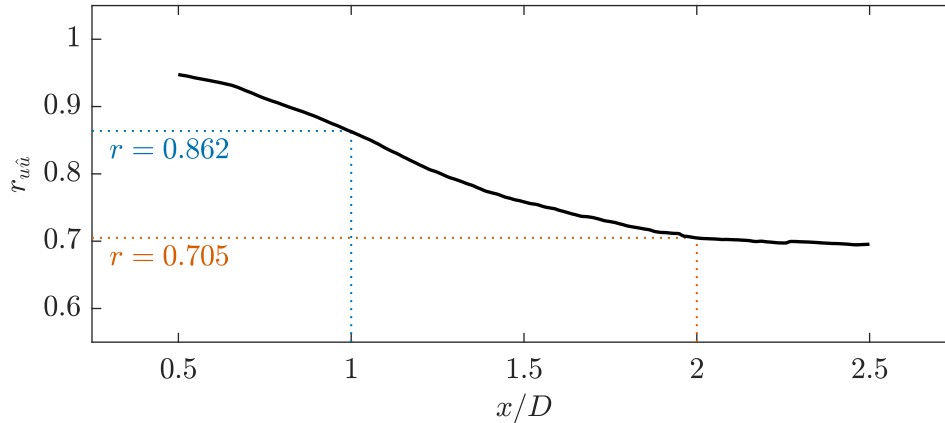


Figure 7.15: The correlation coefficient between the measured ( $u$ ) and estimated ( $\hat{u}$ ) streamwise velocity fluctuations as a function of streamwise location. The two streamwise locations that are highlighted are the same locations for which the NLTFs and impulse responses are plotted in Figure 7.14.

The PSD and instantaneous signals of  $u$  and  $\hat{u}$  at  $x/D = 1$  and  $2$  are presented in Figure 7.16 to further compare the characteristics of the estimated and measured streamwise velocity fluctuations. The PSD of  $u$  and  $\hat{u}$  at  $x/D = 1$  in Figure 7.16(a) show excellent agreement over the majority of the targeted frequency range, with the exception of some small differences at the lowest frequencies ( $St < 0.1$ ). Larger differences are observed at the highest frequencies ( $St > 0.8$ ), but this range did not receive adequate forcing during the system identification experiment and therefore falls outside of the range of frequencies that was meant to be captured by the NLTF model. In addition, the observation that  $St = 0.2$  to  $0.6$  is well-captured indicates that the model is capable of accounting for the emergence of the type-2 mode since this frequency range contains the transition from type 1 to type 2 and then back to type 1 (see Figure 7.7). The instantaneous signals of  $u$  and  $\hat{u}$  at  $x/D = 1$  in Figure 7.16(b) also show good agreement. While there are some instances where  $\hat{u}$  shows larger differences from  $u$  (e.g., near  $tU_\infty/D = 2$ ), the general behaviour of the output signal is well-captured by the NLTF model at  $x/D = 1$ . There is also no clear phase shift between  $u$  and  $\hat{u}$ , indicating that the phase information is well-captured by the model. Instead, we can see that the discrepancies lie mainly in the amplitude of the estimated fluctuations. The PSD of  $u$  and  $\hat{u}$  at  $x/D = 2$  in Figure 7.16(c) reveals that the frequency content is not as well captured by the NLTF model when it is applied to the velocity fluctuations farther downstream. We see similar differences at the higher frequencies, but the discrepancy at the lowest frequencies is much larger and now extends up to roughly  $St = 0.3$ . Despite this, the instantaneous signals of  $u$  and  $\hat{u}$  at  $x/D = 2$  in Figure 7.16(d) reveal that the behaviour of the signal is still captured relatively well by the NLTF model, although it is clear that there are instances where the discrepancy between  $u$  and  $\hat{u}$  becomes somewhat large (e.g., near  $tU_\infty/D = 65$ ). Once again, there is no clear phase shift between  $u$  and  $\hat{u}$ ; the discrepancies appear to be associated with the amplitudes.

A control strategy applied in a wall-bounded flow would typically aim at manipulating the

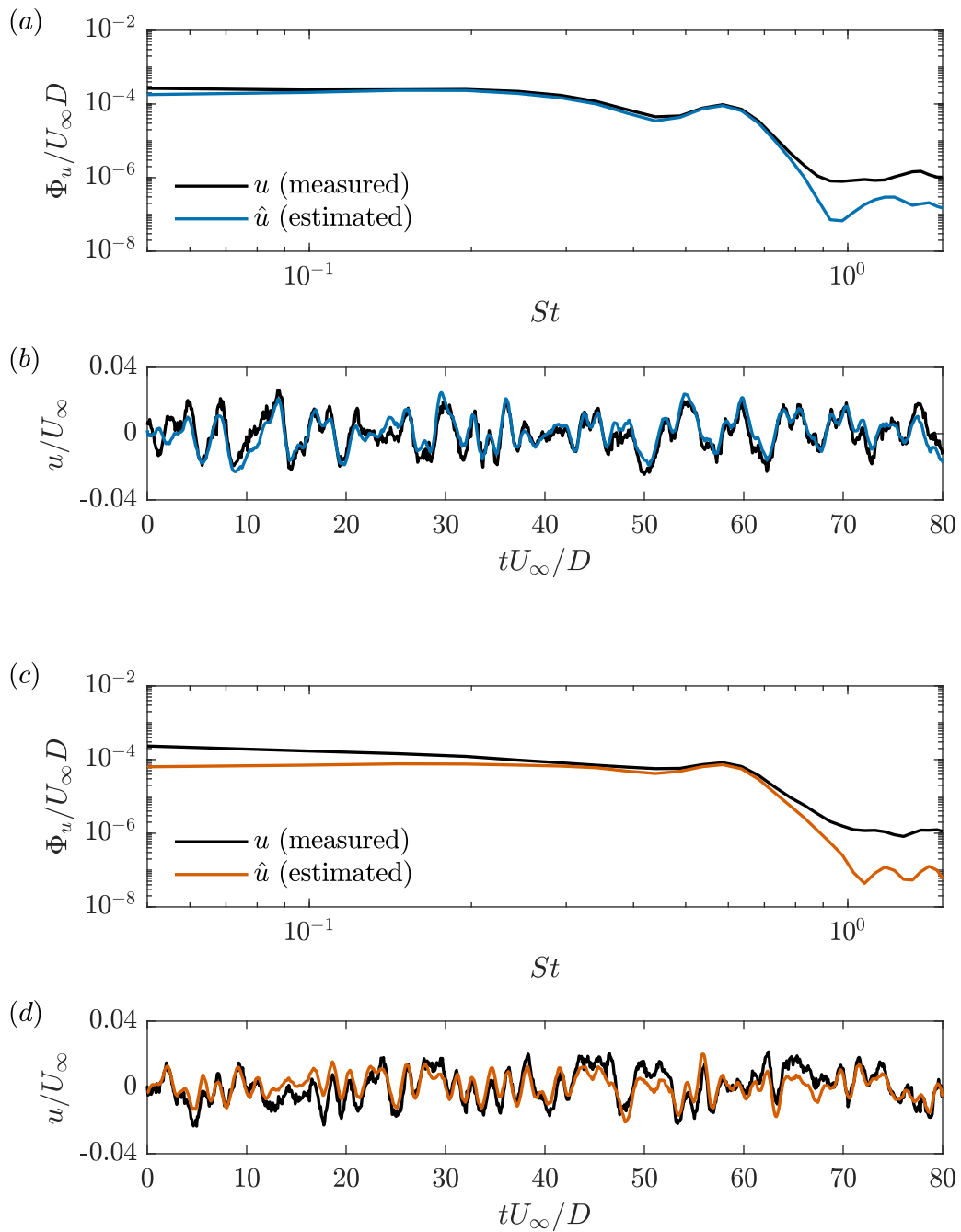


Figure 7.16: The PSD and instantaneous samples of the streamwise velocity fluctuations that were measured ( $u$ ) and estimated by the NLTF model ( $\hat{u}$ ) at (a,b)  $x/D = 1$  and (c,d)  $x/D = 2$ .

flow field just downstream from the actuator. The results discussed above suggest that the NLTF model is quite capable of capturing the dynamics of the present actuated flow for the purpose of developing such a control strategy. Although the performance of the present NLTF model reduces when it is used to estimate the velocity fluctuations farther downstream, we have seen that the estimates are reasonable even at  $x/D = 2$ . Moreover, this has been accomplished using a simple linear model. It is likely that more complicated models would perform even better.

## 7.4 Further Discussion

### 7.4.1 Comparison with Past Results

Only a few other studies have considered how active axisymmetric surface deformations influence wall-bounded flows locally, namely the work of Carlson and Lumley (1996), Kim et al. (2003), and Dearing et al. (2007). By simulating a minimal flow unit, Carlson and Lumley (1996) showed that an upward surface deformation that is Gaussian in shape can be used to target streaky structures by pushing them away from the wall. The observed mechanism allowed for decreasing and increasing drag by targeting the high- and low-speed streaks, respectively. The present results are partially consistent with this mechanism in that an upward deformation of the active surface would produce a low-speed motion that could potentially be used to weaken a high-speed streak and produce drag reduction. However, it is not clear whether this same low-speed motion would produce a drag increase if introduced below a low-speed streak.

Kim et al. (2003) studied actuation in a TBL using axisymmetric deformations that produced a concave/convex geometry. They considered  $A/D = 0.1$ , which is five times the maximum amplitude investigated here, and  $St = 0.1, 0.2, 0.3$ , and  $1.0$ , with the latter frequency only being used for a flow visualization. Considering the limited actuation cases investigated, they could only determine the performance of their actuator as a function of a few frequencies and not at all as a function of amplitude. Moreover, their measurements were made using a hotwire rake, which is quite limited when compared to the high-speed PIV utilized here. Despite these drawbacks, their results show similarities with ours that should be mentioned. More specifically, they found that upward deformations produce low-speed motions while downward deformations produce high-speed motions. These motions were concentrated along the centreline of the actuator for  $St = 0.1$ , but produced what the authors referred to as an “M-shaped” velocity profile across the span at  $St = 0.3$ . This observation is consistent with the type-2 mode that occurs at the same frequency in the present results. Additionally, the motions produced by their actuator exhibited stability characteristics that were similar to what was found here in two ways. First, the motions produced at low frequencies persisted for longer distances downstream. Second, the overlap between high- and low-speed motions, i.e., the break down of the mode, was found to occur more quickly at high actuation frequencies. Both observations therefore suggest that actuation at low frequencies produces motions that are more stable overall.

The flow visualization employed by Kim et al. (2003) at  $St = 1.0$  was used to show that their

active surface deformations can be used to produce streamwise vortices. These vortices are similar to those observed by Dearing et al. (2007), who also employed concave/convex deformations at  $A/D = 0.1$  but at much higher frequencies of  $St = 6$  to  $58$  (note that these  $St$  are different than those reported by Dearing et al. (2007) because they employed a different definition of the Strouhal number). While these vortices were not the focus of the present work, our results from FOV5 reveal that streamwise vortices can indeed form at the higher actuation amplitudes and frequencies. However, it is not clear whether they form at the active surface due to its motion or if they form via instability of the modes downstream. This distinction cannot be known using the present data since FOV5 was located at  $x/D = 1.1$ .

#### 7.4.2 Linearity of the Actuated Flow

Linear systems theory forms the backbone of the available modern control techniques. As a result, the ability to obtain an accurate linear model of a system is critical for designing a controller. Of particular importance is the state-space representation of a linear system. If this type of model can be obtained, and it accurately represents the dynamics of the system, then it becomes relatively straightforward to implement Kalman filters, linear quadratic regulators, model predictive controllers, and other powerful tools from the modern control systems arsenal. As was shown in Section 7.3, the NLTF model was capable of capturing the input-output behaviour of the present actuated flow with reasonable accuracy. This model provides access to the impulse response of the system, the components of which are often referred to as the Markov parameters. The Markov parameters can be used along with the eigensystem realization algorithm (Brunton and Kutz, 2019) to obtain a linear state-space representation of the system dynamics, thus opening the door to the tools discussed above. Since the dynamics of the present system are relatively well-captured by a simple linear model, it seems likely that the use of wall-normal surface deformations as a form of actuation is amenable to the powerful tools of modern control theory. Combining these tools with active surfaces may therefore yield control systems that are capable of producing more desirable outcomes in many fluid-dynamical systems.

### 7.5 Summary

The present chapter considered actuation of an LBL using the active surface developed in Chapter 6. The investigation was conducted using an LBL to provide insight into how surface deformations influence wall-bounded flows in general and to allow for the exploration of a linear modelling technique, the performance of which cannot be easily evaluated in a turbulent flow. We considered periodic and random operation of the active surface, with the latter being used for the purpose of system identification. The resulting motions were captured using high-speed PIV.

Operating the active surface to produce periodic (sinusoidal) surface deformations allowed for studying the resulting motions as a function of the frequency and amplitude of actuation. In general, periodic actuation produces modes featuring a repeating series of high- and low-speed motions with similar magnitudes. The high-speed motions form as the surface moves downwards

and suction high-speed fluid towards the wall, while the low-speed motions form as the surface moves upwards and pushes low-speed fluid away from the wall. We found that the frequency of actuation determines the spatial structure of the resulting modes, while the amplitude of actuation determines their strength.

The spatial structures of the modes undergo two primary changes as the actuation frequency is increased. First, the streamwise wavelength decreases proportionally to  $St^{-0.7}$ . Second, the modes experience an alternating series of transitions between two distinct mode types. We define the type-1 modes as those featuring high- and low-speed motions with single maximums and minimums along  $z = 0$ . In contrast, the type-2 modes are those featuring high- and low-speed motions with double maxima and minima displaced in the spanwise directions. Type-1 modes were found for  $St = 0.1, 0.2, 0.6,$  and  $0.7$ , while type-2 modes were found for the remaining  $St$  investigated here.

The spatial structure of the modes produced at a given frequency does not change much as the amplitude of the periodic deformation is increased. Interestingly, this is also true when considering the height of the resulting motions, which appears to remain similar despite the fourfold increase in the magnitude of the surface deformations considered here. Instead, increasing the amplitude increases the strength of the resulting velocity fluctuations, and this often leads to highly unstable motions that eventually break down. The present results indicate that small amplitudes and low frequencies generally produce modes that are more stable. Moreover, we found that the lowest frequencies of  $St = 0.1$  and  $0.2$  produce the strongest type-1 velocity fluctuations. Considering the strength, stability, and type-1 structure of the motions produced at  $St = 0.1$  and  $0.2$ , we can conclude that it is these low frequencies that offer the best performance for flow control purposes.

Finally, we employed a data-driven technique to identify a simple linear model for the input-output dynamics of the actuated flow. A nonparametric linear transfer function was obtained using a Wiener filter applied to a training data set with a randomized input. The characteristics of this transfer function agree well with the previous results obtained using periodic forcing. Comparison to the results from an evaluation data set indicates that the simple linear model is capable of capturing the input-output dynamics of the actuated flow, especially in the region immediately downstream from the active surface. This type of linear model provides access to many of the tools from modern control theory, and so this result is promising for the future use of active surface deformations as an actuation strategy for flow control applications.

## Chapter 8

# Turbulent Boundary Layer Forcing with Active Surface Deformations

Chapter 7 demonstrated that active surface deformations at  $St \leq 0.2$  are the most well-suited for flow control in an LBL because, at these low frequencies, the resulting motions are stronger, more stable, and concentrated along the centreline of the actuator. This is promising for the targeting of VLSMs because the VLSMs occupy the lowest frequencies of the turbulence spectrum. However, it is not clear how well the results of Chapter 7 obtained using an LBL will translate to a TBL at a much higher Reynolds number. The primary objective of the present chapter is therefore to evaluate the impact of active surface deformations applied locally beneath a TBL at  $Re_\tau = 2600$ , i.e., the same TBL investigated in Chapter 5. The active surface is operated to generate surface deformations sinusoidally at frequencies of  $St \leq 0.2$ , which also covers the range of frequencies occupied by the VLSMs. High-speed PIV is used to capture the velocity field, and phase averaging is used to extract the periodic motions produced by the active surface. The analysis then focuses on the characteristics of these periodic motions and the impact that they have on the surrounding turbulence, with the latter being accomplished using a triple decomposition. Finally, an attempt to implement feed-forward control using the upstream wall-pressure signal is discussed.

## 8.1 Experimental Setup

### 8.1.1 Turbulent Boundary Layer Configuration

The floor of the wind tunnel was again used to generate the TBL as discussed in Section 3.1.2. A section of the floor at centre span was replaced by a flush-mounted acrylic plate with dimensions of  $1.2 \text{ m} \times 0.6 \text{ m}$  (streamwise-spanwise). The plate was modified to accommodate the wall-pressure measurement system developed in Chapter 4 and the active surface developed in Chapter 6; any gaps between these components and the plate were filled using a malleable polymer clay to ensure a smooth surface for the TBL. The origin of the coordinate system  $(x, y, z) = (0, 0, 0)$  is at the centre of the undeformed active surface which was located 7.6 m downstream from the boundary layer tripping device. A schematic of the overall experimental setup is provided in Figure 8.1.

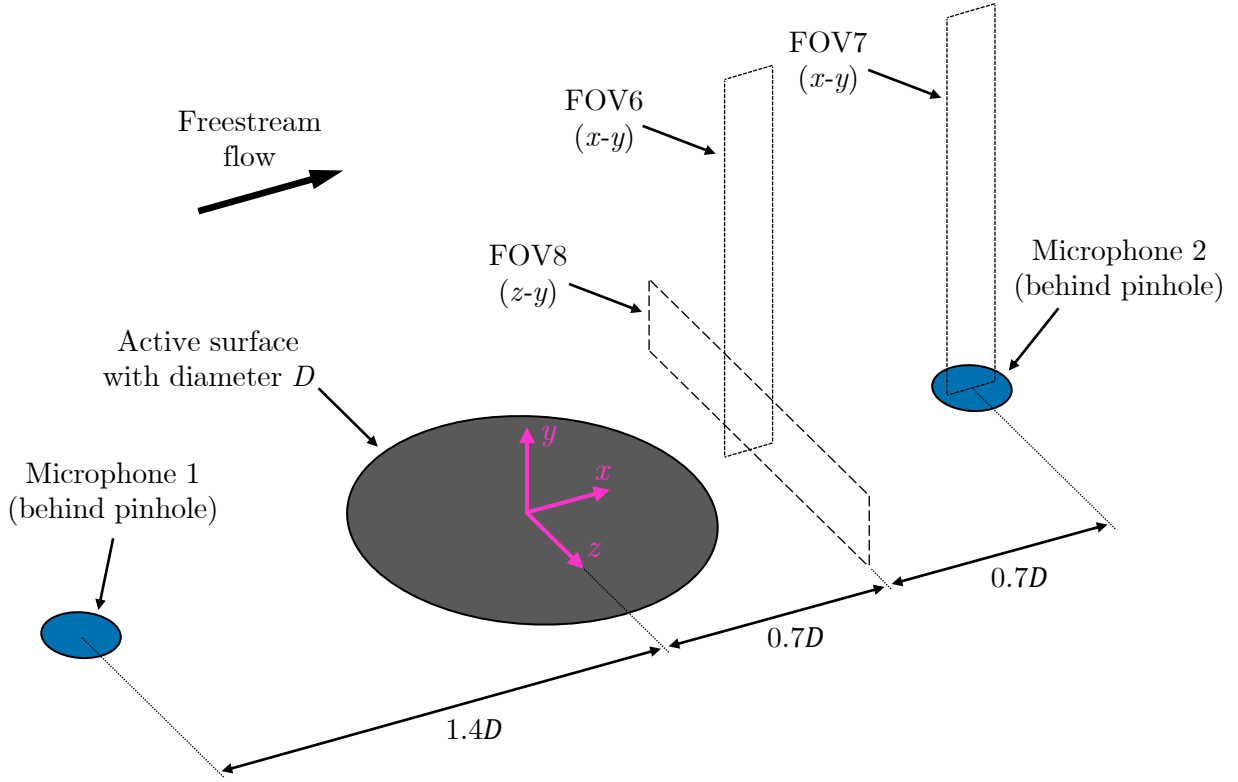


Figure 8.1: Schematic of the experimental setup showing the active surface, wall-pressure measurement locations, and FOVs used for PIV. Planar PIV was conducted within FOV6 and FOV7; stereoscopic PIV was conducted within FOV8.

### 8.1.2 Wall-Pressure Measurements

Measurements of wall pressure were conducted at  $x/D = \pm 1.4$  as is shown schematically in Figure 8.1. The real-time system described in Section 3.3 was used to collect these measurements at an acquisition frequency of 20 kHz in all cases. The wall-pressure measurements were used only for the design and implementation of the feed-forward control strategy. More details regarding these measurements are provided later in Section 8.3.3.

### 8.1.3 Particle Image Velocimetry

Three high-speed PIV experiments were used to measure the flow downstream from the active surface as is shown schematically in Figure 8.1 where the FOVs are numbered accordingly. The PIV system discussed in Section 3.2.3 was used in all cases. Once again, the trigger signals for the laser and cameras were recorded along with the actuator signals during all PIV experiments to allow data synchronization via the procedure outlined in Section 3.3.2.

The FOVs denoted as FOV6 and FOV7 in Figure 8.1 were used to capture the velocity field in the streamwise-wall-normal ( $x$ - $y$ ) plane along the centreline of the active surface ( $z = 0$ ) using planar

PIV. The high-speed cameras have limited onboard memory, and so these FOVs were cropped to be tall and narrow to capture longer sequences of images for the purpose of statistical convergence. This allowed for extracting high-speed measurements across the entire boundary layer thickness at locations of  $x/D = 0.7$  and  $1.4$ . A 200-mm lens with an aperture setting of  $f_o/5.6$  was used for imaging, resulting in FOV dimensions of  $(\Delta x, \Delta y) = 13 \text{ mm} \times 114 \text{ mm}$  at a resolution of  $93.4 \text{ }\mu\text{m}/\text{pixel}$ . Illumination for the measurements was provided by a 1-mm-thick laser sheet formed by a series of spherical and cylindrical lenses. Sets of 15000 double-frame images were recorded at 1 kHz within both FOVs (asynchronously). Four sets were recorded when capturing the base flow (no actuation), resulting in 60000 measurement instances over a total sampling time of 60 seconds ( $7.50 \times 10^3 \delta/U_\infty$ ). Twelve sets were recorded for each actuation case to improve the convergence of the phase-averaged statistics, resulting in 180000 measurement instances over a total sampling time of 180 seconds ( $2.25 \times 10^4 \delta/U_\infty$ ). Ten sets were recorded for feed-forward operation of the active surface, resulting in 150000 measurement instances over a total sampling time of 150 seconds ( $1.88 \times 10^4 \delta/U_\infty$ ). All images were preprocessed by subtracting the minimum of the respective ensemble to reduce background noise followed by dividing the images by the background-subtracted ensemble average to normalize the intensity counts. A multi-pass cross-correlation algorithm was used to compute the vector fields from the PIV images. The final pass employed  $32 \times 32$ -pixel Gaussian-weighted interrogation windows with 75% overlap.

The stereoscopic FOV denoted as FOV8 in Figure 8.1 was used to capture the velocity field in the spanwise-wall-normal ( $z$ - $y$ ) plane at  $x/D = 0.7$ . Two cameras featuring Scheimpflug mounts and 200-mm lenses with aperture settings of  $f_o/16$  were placed at  $45^\circ$  to the imaging plane and were arranged in a forward-scattering orientation with respect to the 2-mm-thick laser sheet used to illuminate the FOV. FOV8 captured an area of  $(\Delta z, \Delta y) = 120 \text{ mm} \times 31 \text{ mm}$  and had an effective resolution of  $70.5 \text{ }\mu\text{m}/\text{pixel}$ . The calibration processes included a 3D target calibration followed by a self-calibration using a set of particle images (Wieneke, 2005). Sets of 4000 double-frame images were collected at a frequency of 250 Hz. Four sets were recorded for the base flow, resulting in 16000 measurement instances over 64 seconds ( $8.00 \times 10^3 \delta/U_\infty$ ). Eight sets were recorded for each actuation case to improve the convergence of the phase averages, resulting in 32000 measurement instances over 128 seconds ( $16.0 \times 10^3 \delta/U_\infty$ ). The same preprocessing steps that were applied to the planar PIV images were also applied to the stereoscopic PIV images. A multi-pass stereoscopic cross-correlation algorithm was then used to compute the vector fields. The final pass employed  $48 \times 48$ -pixel Gaussian-weighted interrogation windows with 75% overlap.

#### 8.1.4 Base Flow

Here we present the statistical characteristics of the TBL used to investigate the performance of the active surface. This is done to provide the various parameters used for data normalization and to confirm that the desired TBL has been reproduced properly. The basic fluid properties and boundary layer parameters computed from FOV6 at  $x/D = 0.7$  are presented in Table 8.1. The friction Reynolds number, freestream velocity, boundary layer thickness, and viscous lengthscale

---

Kinematic viscosity	$\nu$	$1.7 \times 10^{-5}$	(m <sup>2</sup> /s)
Density	$\rho$	1.1	(kg/m <sup>3</sup> )
Reynolds numbers	$Re_\tau$	2600	
	$Re_\theta$	6000	
Freestream velocity	$U_\infty$	11.8	(m/s)
Boundary layer thickness	$\delta$	$94.4 \times 10^{-3}$	(m)
Displacement thickness	$\delta^*$	$12.2 \times 10^{-3}$	(m)
Momentum thickness	$\theta$	$9.0 \times 10^{-3}$	(m)
Friction velocity	$U_\tau$	0.46	(m/s)
Viscous lengthscale	$\lambda$	$36.8 \times 10^{-6}$	(m)
Shape factor	$H$	1.36	

Table 8.1: Fluid properties and boundary layer parameters at  $x/D = 0.7$ . The viscous lengthscale was determined by fitting the mean velocity profile to the logarithmic law of the wall with  $\kappa = 0.41$  and  $C = 5.0$ .

---

are all within 1% of what was presented Chapter 5, confirming that the desired TBL has been successfully reproduced.

The mean velocity and Reynolds stresses computed from each FOV and compared to the data of Chapter 5 are presented in Figure 8.2. The mean velocity profiles in Figure 8.2(a) agree well with one another with the exception of the points nearest to the wall from FOV8. The small deviations observed can likely be attributed to reflections at the wall within the PIV images and the uncertainties associated with the stereoscopic calibration process. The logarithmic law of the wall with  $\kappa = 0.41$  and  $C = 5.0$  is also shown in the figure, which confirms the expected behaviour of the profile and indicates that the logarithmic region extends to roughly  $y/\lambda = 400$  in the wall-normal direction. The Reynolds stresses presented in Figure 8.2(b) reveal a similar story: excellent agreement between the data from FOV6, FOV7, and Chapter 5 (FOV2), and some deviations observed for the data from FOV8. These deviations are mostly observed for  $\langle u^2 \rangle$ , which makes sense considering that the streamwise component of the stereoscopic measurements is the out-of-plane component and therefore contains the largest measurement uncertainty. However, the data from FOV8 is used qualitatively in the present work and therefore these small statistical discrepancies do not pose an issue for our investigation. Overall, Figure 8.2 reveals that the mean velocity and Reynolds stresses of the present TBL agree well with those of Chapter 5.

Finally, Figure 8.3 shows the pre-multiplied spectra of  $u$  computed at  $x/D = 0.7$  where  $\Phi_u$  is the PSD of  $u$ ,  $k_x = 2\pi f/\langle U \rangle$  is the streamwise wavenumber, and  $\Lambda_x = \langle U \rangle/f$  is the streamwise wavelength. The blue lines in the figure represent the actuation frequencies which will be discussed in Section 8.1.5. The pre-multiplied spectra are shown here to highlight the expected behaviour of the TBL that has been documented in a previous work at the same Reynolds number (Hutchins

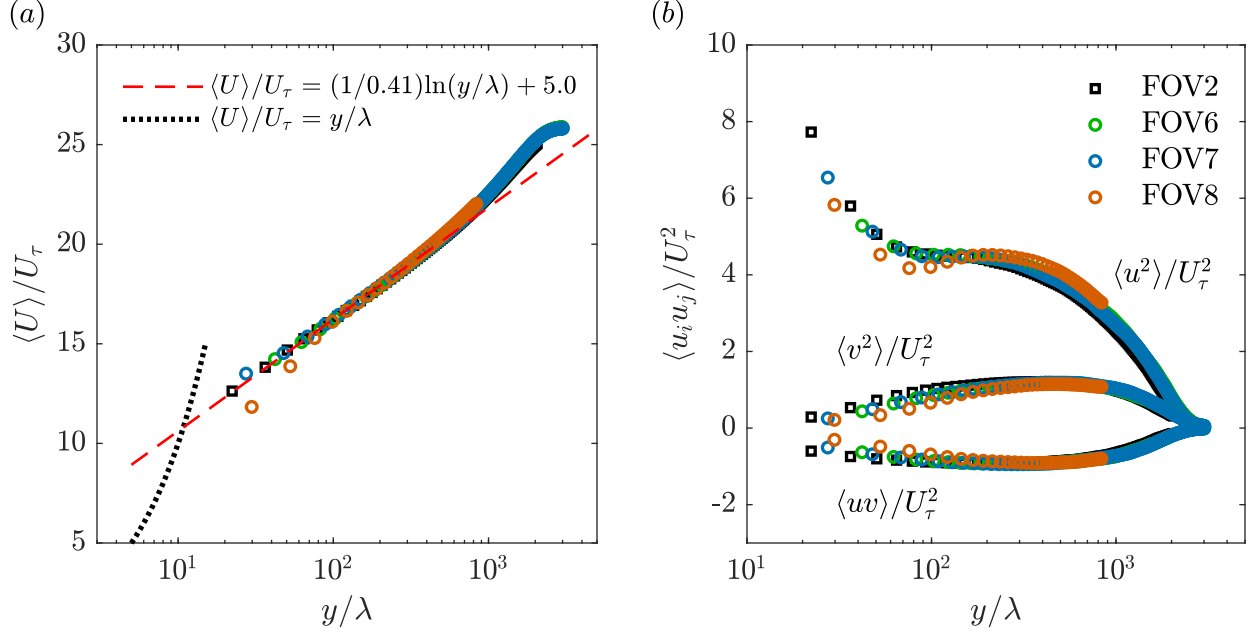


Figure 8.2: The (a) mean velocity profiles and (b) Reynolds stresses for the base flow from all three PIV FOVs and compared to the data of Chapter 5 (FOV2).

and Marusic, 2007a): a high-energy “inner site” near the wall at  $y/\lambda \approx 15$  (not entirely captured by the present measurements) and  $\Lambda_x/\lambda \approx 1000$  ( $\Lambda_x/\delta \approx 0.4$ ) and a high-energy “outer site” in the logarithmic region near  $\Lambda_x/\delta \approx 6$  (marked using the white oval in Figure 8.3). The inner site is attributable to the near-wall cycle that produces the large peak in  $\langle u^2 \rangle$  while the outer site is attributable to the VLSMs. The presence of the outer site in Figure 8.3 therefore confirms that VLSMs occupy the present TBL.

### 8.1.5 Actuation Cases

We consider periodic operation of the active surface to determine how actuation affects the present TBL as a function of frequency. The active surface was again operated using the signal

$$h_r(t) = A \sin(2\pi f_a t). \quad (8.1)$$

We consider a constant actuation amplitude of  $A = 2.7$  mm ( $= 73\lambda$ ,  $0.03\delta$ ) and four actuation frequencies of  $f_a = 6, 12, 18,$  and  $24$  Hz which correspond to Strouhal numbers of  $St = f_a D / U_\infty = 0.05, 0.10, 0.15,$  and  $0.20$ , therefore covering the range of normalized frequencies that appear suitable for flow control according to the results from Chapter 7. These four  $St$  are laid over the pre-multiplied spectra in Figure 8.3, revealing that  $St = 0.10$  coincides with the center of the outer site associated with the VLSMs. Moreover, Chapter 5 revealed that the VLSMs exist at frequencies up to roughly 18 Hz in the present TBL, which coincides with actuation at  $St = 0.15$ .

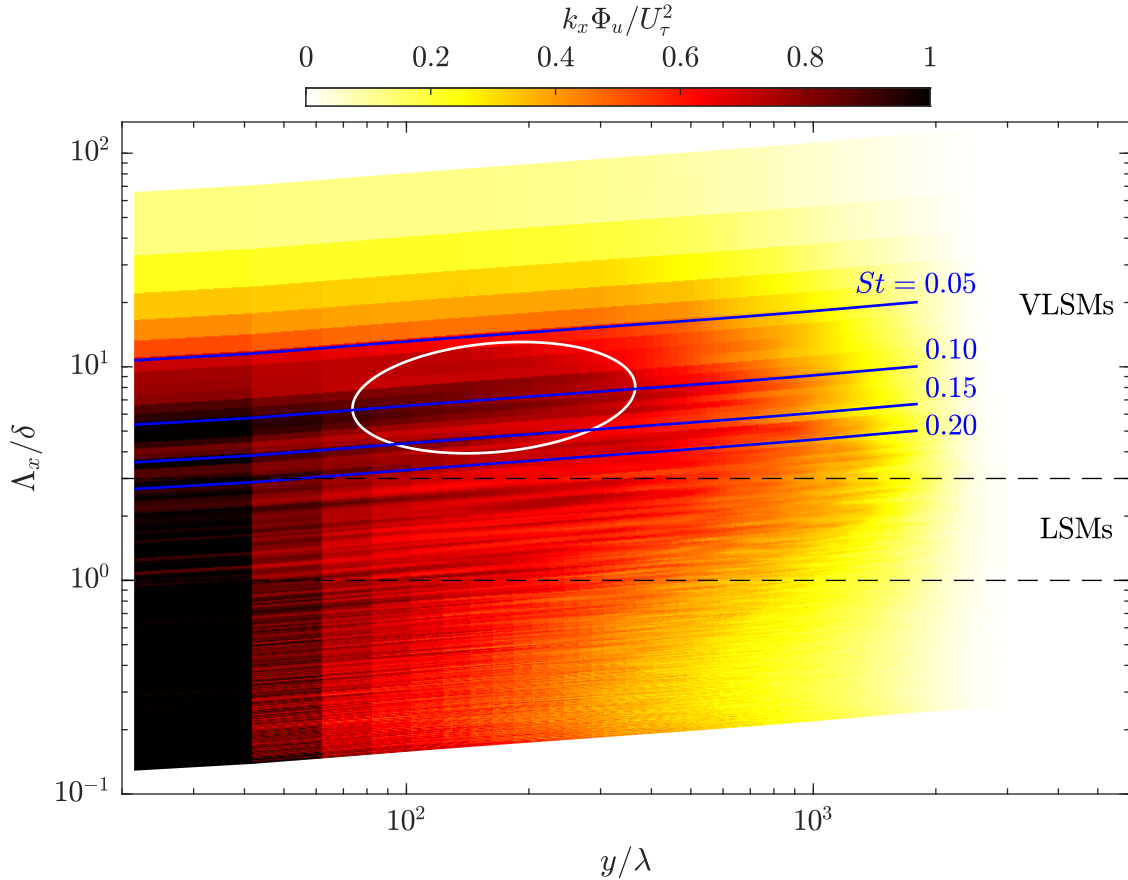


Figure 8.3: Pre-multiplied spectra of the streamwise velocity fluctuation computed using the data from FOV6 ( $x/D = 0.7$ ). The streamwise wavenumbers and wavelengths of  $u$  were computed as  $k_x = 2\pi f / \langle U \rangle$  and  $\Lambda_x = \langle U \rangle / f$ , respectively. The blue lines represent the four actuation frequencies of  $St = 0.05, 0.10, 0.15,$  and  $0.20$  considered in the present investigation. The wavelength ranges of the LSMs ( $1-3\delta$ ) and the VLSMs ( $> 3\delta$ ) are also shown, as is the approximate location of the outer site (white oval).

We can therefore say that  $St = 0.05$  and  $0.10$  represent actuation within the frequency range of the VLSMs,  $St = 0.20$  represents actuation within the range of the LSMs ( $1-3\delta$  in length), and  $St = 0.15$  represents actuation at the transition between LSMs and VLSMs.

The active surface was once again tuned on a case-by-case basis to have the amplitudes of the sinusoidal displacement patterns be within a few percent of the desired values. The phase-averaged displacement of the active surface is shown for all actuation cases in Figure 8.4, where it is evident that the phased-averaged displacement signals closely match the desired sinusoids.

### 8.1.6 Phase Averaging and Triple Decomposition

A phase averaging technique has been used to extract the periodic motions produced by the active surface and to determine how the Reynolds stresses vary across the actuation cycles. The phase of

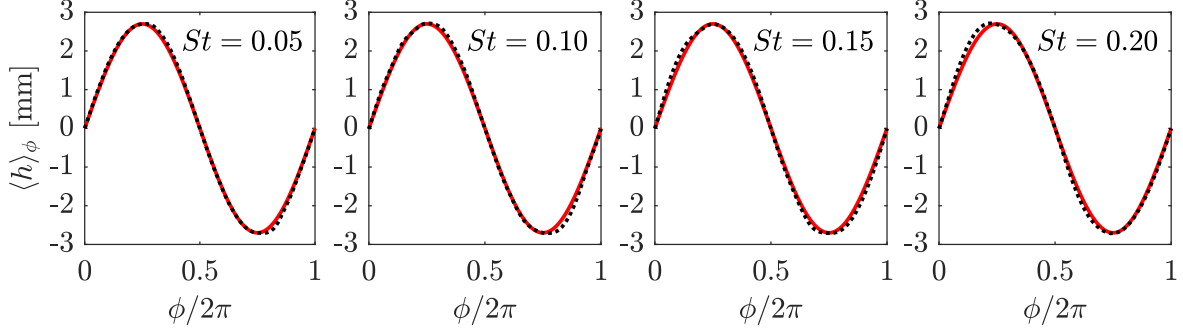


Figure 8.4: Phase averages of the active surface displacement ( $\langle h \rangle_\phi$ , dotted lines) compared to the reference sinusoids that the surface is meant to track (solid lines) for all periodic deformation cases.

the active surface was again computed using a Hilbert transform as

$$\phi = \angle(-i\mathcal{H}\{h\}) + \pi, \quad (8.2)$$

where the manipulations with  $i$  and  $\pi$  were used to shift the phase such that one full cycle extends from  $\phi = 0$  to  $2\pi$  with  $\phi = 0$  representing the active surface at  $h = 0$  with a velocity in the positive wall-normal direction. The velocity measurements were averaged using two different protocols depending on what the result would be used for. When computing phase averages for a quantitative analysis, the velocity fields were averaged using phase bins with widths of  $0.1\pi$  and 80% overlap, resulting in 100 bins with 9000 measurement instances per bin for FOV6 and FOV7. When computing phase averages for a qualitative analysis, the velocity fields were averaged using phase bins with widths of  $0.4\pi$  and 99.5% overlap, resulting in 1000 bins with 36000 measurement instances per bin for FOV6/FOV7 and 6400 measurement instances per bin for FOV8. The latter protocol produced smoother results for visualizations. However, the wider bins reduce the peak values of the phase averages which is why a different phase averaging protocol was used for quantitative analyses.

Following computation of the phase averages, a triple decomposition (Hussain and Reynolds, 1970) was conducted as

$$U_i = \langle U_i \rangle + \langle u_i \rangle_\phi + u'_i, \quad (8.3)$$

where  $u'_i$  is what remains of the turbulent fluctuations. This decomposition allows for studying the motions produced by actuation using  $\langle u_i \rangle_\phi$  and studying the impact that these motions have on the surrounding turbulence using  $u'_i$ . The latter component was computed as  $u'_i(t) = u_i(t) - \langle u_i \rangle_\phi(t)$  where  $\langle u_i \rangle_\phi(t)$  was interpolated from  $\langle u_i \rangle_\phi$  using  $\phi(t)$ .

## 8.2 Periodic Motions Produced by Actuation

This section focuses on characterizing the motions produced by the active surface when operated beneath the TBL. We consider the spatial structure, advection velocity, and strength of the motions, and we investigate normalizing the results to compare between the present TBL and the LBL of Chapter 7. We then use what we have learned to create visualizations that show what the motions produced by the active surface are likely to look like in 3D space. Note that the active surface diameter  $D$  is used as a lengthscale for normalization of the spatial domain. This is done to retain the lengthscale used by the present definition of the Strouhal number and to show the results relative to the dimensions of the active surface. However,  $D$  is only 6% larger than  $\delta$  in the present TBL, and so  $D$  can be thought of as a proxy for  $\delta$  when interpreting the normalized results.

### 8.2.1 Phase Averages

We begin by considering the raw phase averages since they form the core of the analyses performed in this section. Phase averages of the fluctuating streamwise velocity ( $\langle u \rangle_\phi$ ) in the  $\phi$ - $y$  plane computed using the data from FOV6 and FOV7 are presented in Figure 8.5. The left (Figures 8.5(a-d)) and right (Figures 8.5(e-h)) columns in the figure contain the phase averages at  $x/D = 0.7$  and 1.4, respectively, for all actuation frequencies. The phase axis (or time axis) has been flipped in all cases to display the motions as if they were moving from left to right to facilitate visualization in a manner similar to that of Taylor’s hypothesis. The solid and dashed lines are outlines of the high- and low-speed motions, respectively, while the dotted lines show the constant amplitude of the active surface deformations.

The phase averages in the  $\phi$ - $y$  plane at  $x/D = 0.7$  (Figure 8.5(a-d)) are shown with the overlaid outlines representing  $\langle u \rangle_\phi / U_\infty = \pm 0.02$ , which is roughly 40% of the peak strength. The strongest fluctuations are contained within these outlines, but some weaker influence on the boundary layer can be seen to extend well beyond the end of the logarithmic layer ( $y/\lambda \approx 400$ ). In all cases the phase averages reveal high- and low-speed structures, with the latter occurring mostly within the first half of the phase cycle ( $0 < \phi < \pi$ ). FOV6 is located just downstream from the edge of the active surface, and the phase cycle begins with an upward motion. It therefore appears that the low-speed motions form from upward surface deformations and the high-speed motions form from downward surface deformations. This is consistent with the results of Kim et al. (2003) and Chapter 7. It is also evident that the magnitudes of the high- and low-speed motions are similar to one another, and that these magnitudes do not change much as  $St$  is increased. Instead, we see a change in the shape of the motions that are produced. At  $St = 0.05$  and 0.10 (Figure 8.5(a,b)) the motions are relatively flat (i.e., they have negligible inclination) and extend to around  $y/D \approx 0.05$  ( $y/\lambda \approx 150$ ) in the wall-normal direction according to the solid and dashed outlines, which is roughly twice that of the surface deformation amplitude (dotted line). When the actuation frequency is increased to  $St = 0.15$  (Figure 8.5(c)), the motions begin to lift up at their fronts to form an inclined structure, with the low-speed motion lifting up more than the high-speed motion. This occurs to an even larger extent for  $St = 0.20$  (Figure 8.5(d)), which produces a low-speed motion that extends to

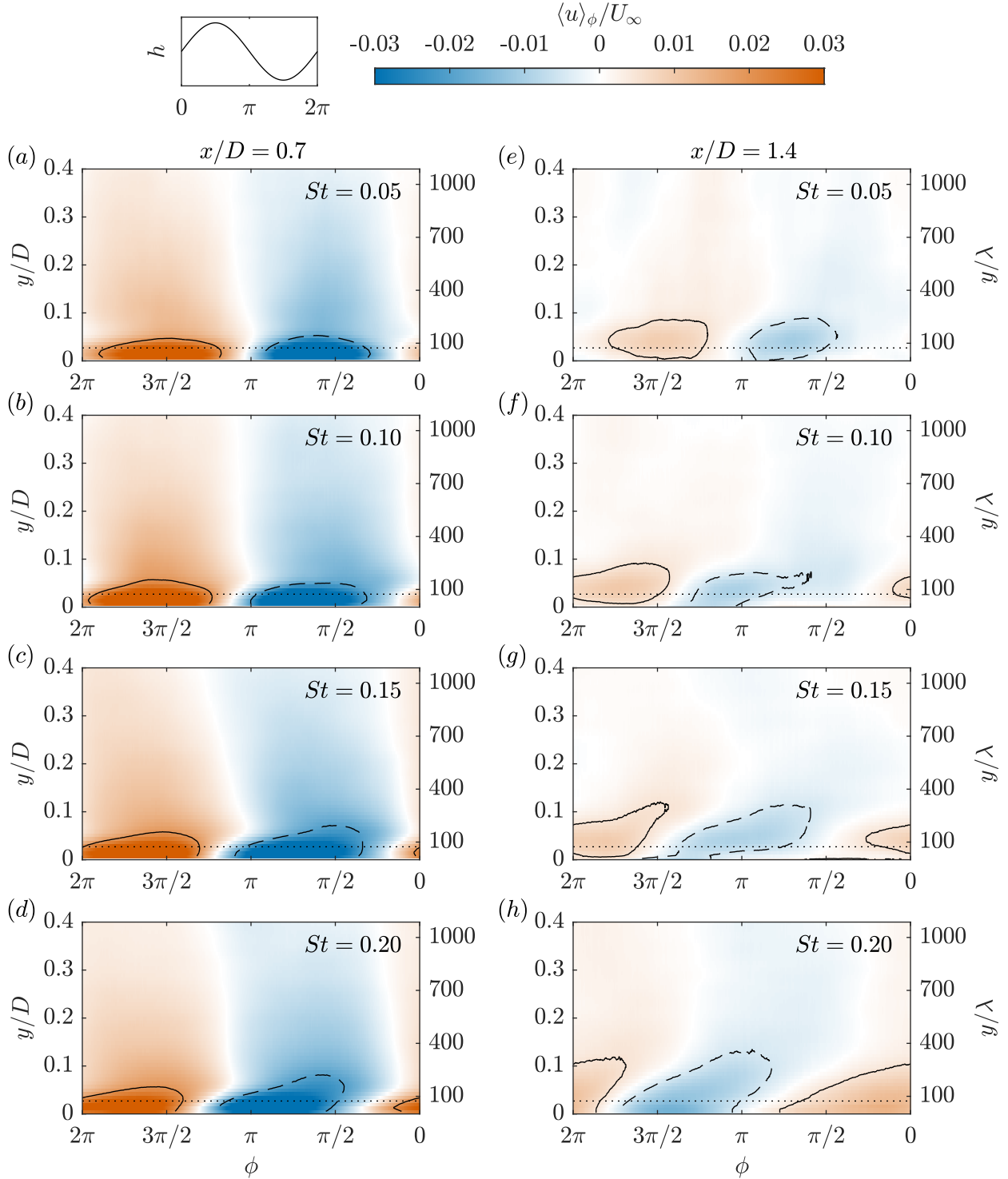


Figure 8.5: Phase averages of the streamwise velocity component ( $\langle u \rangle_\phi$ ) in the  $\phi$ - $y$  plane for all actuation frequencies computed using (a–d) the data from FOV6 at  $x/D = 0.7$  and (e–h) the data from FOV7 at  $x/D = 1.4$ . The phase axis has been flipped to display the motions as if they were moving from left to right. The solid and dashed lines represent positive and negative values of (a–d)  $\langle u \rangle_\phi / U_\infty = \pm 0.02$  and (e–h)  $\langle u \rangle_\phi / U_\infty = \pm 0.005$ . The dotted lines show the constant amplitude of the active surface deformations.

$y/D \approx 0.09$  ( $y/\lambda \approx 250$ ) according to the dashed outline in the subfigure. It is worth noting that the flat motions are produced at  $St = 0.05$  and  $0.10$ , which correspond to frequencies associated with the VLSMs in the present TBL as was discussed in Section 8.1.5. Similarly, the most inclined motion is produced at  $St = 0.20$ , which corresponds to the frequency range of the LSMs.

The phase averages in the  $\phi$ - $y$  plane at  $x/D = 1.4$  (Figure 8.5(e-h)) represent the same motions discussed above after they have advected  $0.7D$  downstream; this advection produces a phase shift between the motions at  $x/D = 0.7$  and  $1.4$  which is visible in the figure. The motions at  $x/D = 1.4$  are now roughly five times weaker than they were at  $x/D = 0.7$  and are therefore shown with the overlaid outlines at  $\langle u \rangle_\phi / U_\infty = \pm 0.005$ . This allows for a fairer comparison of the shapes of the phase averages between  $x/D = 0.7$  and  $1.4$  as represented by these outlines. In addition to becoming weaker, the motions produced at  $St = 0.05$  (Figure 8.5(e)) have lifted away from the wall and increased in height to reach  $y/D \approx 0.09$  ( $y/\lambda \approx 250$ ). The high-speed motion (solid outline) remains relatively flat while the low-speed motion (dashed outline) appears to now have some inclination. Similar changes are observed for the motions produced at  $St = 0.10$  (Figure 8.5(f)), but with the low-speed motion appearing as a thinner wall-attached structure. At  $St = 0.15$  and  $0.20$  (Figure 8.5(g,h)) the stronger inclination is once again evident for both the high- and low-speed motions. The motions produced at  $St = 0.20$  in particular are quite organized, inclined, and relatively large, extending up to the end of the logarithmic region at  $y/D \approx 0.14$  ( $y/\lambda \approx 390$ ). Overall, the motions produced by the active surface appear to reduce in strength and diffuse away from the wall as they advect downstream.

The same phase averages at  $x/D = 0.7$  from Figure 8.5(a-d) have been computed at  $y/D = 0.02$  in the  $\phi$ - $z$  plane using the data from FOV8 and are shown in Figure 8.6 to reveal how the motions produced by the active surface vary in the spanwise direction. The phase axis has once again been flipped to show the motions as if they were advecting from left to right, and the dotted lines represent the inner diameter of the active surface (see Figure 6.1) to show the region that experiences the maximum surface deformation. The regions of maximum fluctuation and the interfaces between high- and low-speed motions along  $z = 0$  in Figure 8.6 occur at the same phase when compared to Figure 8.5(a-d), confirming that the phase averages computed from FOV6 and FOV8 are in good agreement with one another. All four phase averages in the  $\phi$ - $z$  plane show that the maximum velocity fluctuations are concentrated along  $z = 0$ . This indicates that the active surface is producing type-1 modes for  $St \leq 0.2$ , which is what was observed within the LBL of Chapter 7 at the same  $St$ . We also see that the strongest of the streamwise velocity fluctuations are bounded by the dotted lines ( $z/D = \pm 0.25$ ), which makes sense because this region experiences the largest surface deformations. These dotted lines represent a width that is roughly equal to the maximum width of the VLSMs. The strongest regions of the high- and low-speed motions therefore cover widths that are similar to those of the VLSMs. Finally, we note that the patterns in the  $\phi$ - $z$  plane observed for  $St = 0.05$ ,  $0.10$ , and  $0.15$  (Figure 8.6(a-c)) are quite similar. For these three  $St$  we see that the interface between the high- and low-speed motions that is closest to  $\phi = 0$  is curved while the interface that is closer to  $\phi = \pi$  is relatively straight. The opposite is true for  $St = 0.20$

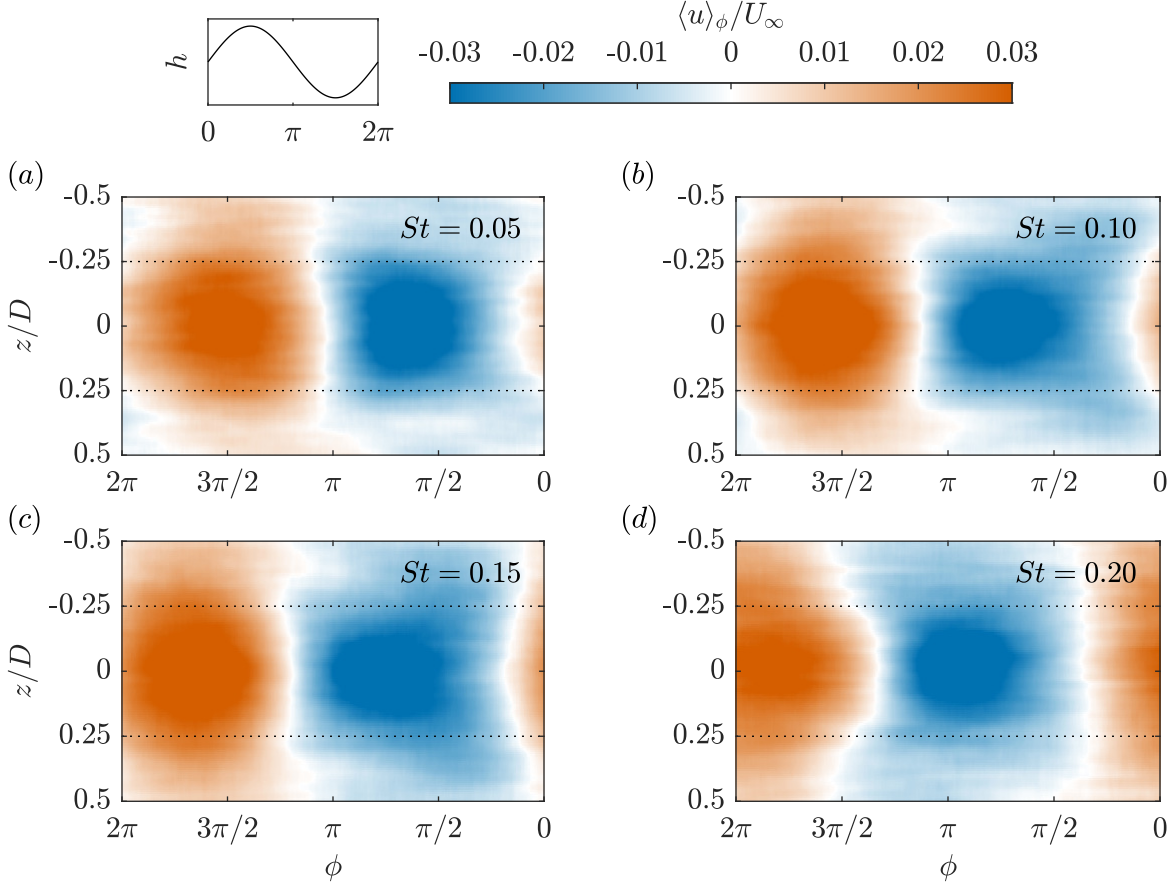


Figure 8.6: Phase averages of the streamwise velocity component ( $\langle u \rangle_\phi$ ) in the  $\phi$ - $z$  plane at  $x/D = 0.7$  and  $y/D = 0.02$  computed using the data from FOV8 for (a)  $St = 0.05$ , (b)  $St = 0.10$ , (c)  $St = 0.15$ , and (d)  $St = 0.20$ . The phase axis has been flipped to display the motions as if they were moving from left to right. The dotted lines represent the inner diameter of the active surface, i.e., the region that experiences the maximum surface deformation.

(Figure 8.6(d)) as we can see that the interface closest to  $\phi = 0$  is straight while the interface that is closer to  $\phi = \pi$  is curved.

The above discussion has considered only the phase averages of the streamwise velocity for two reasons. First, the present investigation focuses on targeting the VLSMs which are a phenomenon characterized primarily as long, meandering regions of streamwise velocity fluctuation. It therefore makes sense to focus on producing streamwise velocity fluctuations that can be used to oppose the VLSMs. Second, we have found that  $\langle v \rangle_\phi$  is an order of magnitude weaker than  $\langle u \rangle_\phi$  for all cases. This was also observed in the LBL of Chapter 7.

## 8.2.2 Structure and Strength

We now work to further understand the structure and strength of the motions produced by the active surface within the TBL. We begin by considering two important structural characteristics: the advection velocity and streamwise wavelength, which are related through the actuation frequency

as

$$U_c = f_a \lambda_x. \quad (8.4)$$

The actuation frequencies are known, and so we only need to know one of these parameters to have access to the other. Following a procedure similar to that of Hussain and Reynolds (1970), the advection velocity of the motions produced at each actuation frequency has been estimated as

$$U_c = \omega_a \frac{\Delta x}{\Delta \phi}, \quad (8.5)$$

where  $\omega_a = 2\pi f_a$  is the angular actuation frequency while  $\Delta x$  and  $\Delta \phi$  are the streamwise distance and phase shift, respectively, between  $x/D = 0.7$  and  $1.4$ . We have estimated  $\Delta \phi$  by cross-correlating  $\langle u \rangle_\phi$  obtained at  $x/D = 0.7$  and  $1.4$ . These cross-correlations were computed using only the portion of the phase averages up to  $y/D = 0.08$  to isolate the region that contains the dominant structures produced by the active surface. Note that such cross-correlations are unable to identify whether there are multiple wavelengths between  $x/D = 0.7$  and  $1.4$ . However, adding  $2\pi$  to the denominator of Equation (8.5) produces values of  $U_c$  that are roughly one order of magnitude smaller than the local mean velocity. It therefore seems unlikely that there are multiple wavelengths present between  $x/D = 0.7$  and  $1.4$ .

The advection velocities estimated in the present work are plotted in Figure 8.7(a). The results from the LBL of Chapter 7 at varying actuation amplitudes are also shown. The advection velocities of Chapter 7 follow a single curve with the exception of a few points at  $St = 0.4$  and  $0.5$  which seem to be affected by the emergence of the type-2 modes; this collapse of the data is observed despite the fourfold increase in actuation amplitude considered. Figure 8.7(a) indicates that the motions produced by the active surface in the present TBL advect at velocities of around  $U_c/U_\infty = 0.5$  to  $0.6$ , which is slightly slower than the mean velocity of  $0.64U_\infty$  across the portion of the TBL that was cross-correlated to obtain  $\Delta \phi$ . These velocities are higher than those found in the LBL ( $U_c/U_\infty = 0.2$  to  $0.3$  at the same  $St$ ) but are not as high as those associated with the VLSMs, which were estimated in Chapter 5 to advect at velocities closer to  $0.8U_\infty$  in the present TBL. Note that this faster advection could be due to the VLSMs extending farther from the wall where they experience a higher mean velocity.

It is reasonable to assume that the freestream velocity is an important parameter for determining the advection velocity because the freestream velocity is the primary source of momentum. Similarly, the shape of the mean velocity profile should be an important contributor to the advection velocity as there is far more momentum close to the wall in the present TBL compared to its laminar counterpart. Indeed, normalization with  $U_\infty$  alone does not collapse the present results with those of Chapter 7 as is clearly shown in Figure 8.7(a). We therefore consider the shape factor  $H = \delta^*/\theta$ , which is a measure of this near-wall momentum. The advection velocities normalized by both  $H$  and  $U_\infty$  are shown in Figure 8.7(b). It is evident in the figure that the present results

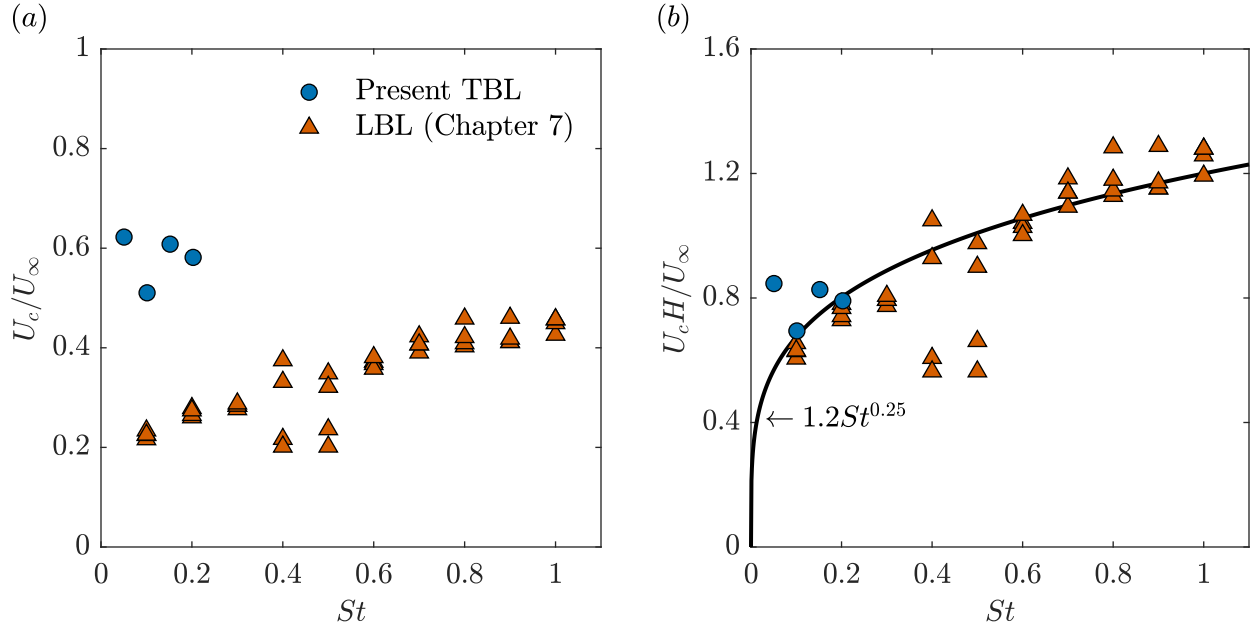


Figure 8.7: Advection velocities ( $U_c$ ) of the motions produced by the active surface normalized by (a) the freestream velocity and (b) the freestream velocity and shape factor. Comparison is made between the motions produced in the present TBL and those produced in the LBL of Chapter 7.

and those of Chapter 7 collapse on the same power-law curve under this normalization, confirming that the shape of the boundary layer profile is part of what determines the advection velocity of the motions produced by the active surface. Note that the shape factor was extracted at  $x/D = 0$  when considering the LBL data of Chapter 7.

The wavelengths of the motions produced by the active surface have been computed using Equation (8.4) and are shown normalized by the actuator diameter in Figure 8.8(a) along with the results of Chapter 7. These wavelengths aid in determining how long the motions would be if they persisted downstream. Figure 8.8(a) shows a significant increase in the wavelength of the motions produced in the present TBL as  $St$  is reduced. More specifically, we see  $\lambda_x/D$  increase from roughly 3 to 12 as  $St$  is reduced from 0.2 to 0.05. The VLSMs are considered to be motions, either high- or low-speed, that are  $3\delta$  or more in length (Balakumar and Adrian, 2007). Since the active surface produces high- and low-speed motions in series, the smallest wavelength that occurs at the scale of the VLSMs is  $6\delta$ . This cutoff is highlighted in Figure 8.8(a), revealing that the active surface only produces motions at the scale of the VLSMs at the lowest actuation frequency of  $St = 0.05$  in the present TBL, although the wavelength produced at  $St = 0.10$  is nearly at the cutoff.

Figure 8.8(a) shows that the wavelengths produced in the LBL of Chapter 7 are shorter than those produced here for a given  $St$ . This is a result of the different advection velocities shown in Figure 8.7(a), which were shown to agree once the shape factor of the boundary layer profile was employed in the normalization of Figure 8.7(b). It then follows that the shape factor should also be used in the normalization of wavelength. Indeed, Figure 8.8(b) shows that the wavelengths

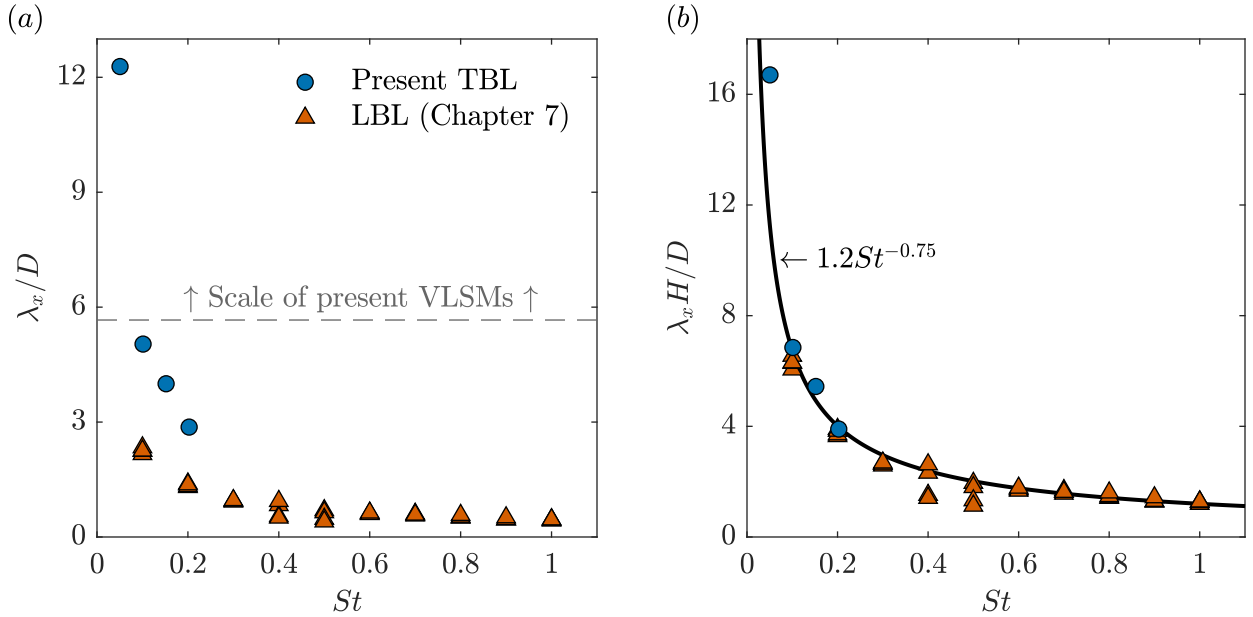


Figure 8.8: Wavelengths ( $\lambda_x$ ) of the motions produced by the active surface normalized by (a) the actuator diameter and (b) the actuator diameter and shape factor. Comparison is made between the motions produced in the present TBL and those produced in the LBL of Chapter 7.

normalized using both  $D$  and  $H$  collapse along a single power-law curve. Together, Figures 8.7(b) and 8.8(b) indicate that the advection velocity and wavelength of the motions produced by the active surface are functions of  $U_\infty$ ,  $f_a$ ,  $D$ , and  $H$ .

We now consider the strength of the high- and low-speed motions which we define as  $S^+ = \max(\langle u \rangle_\phi)$  and  $S^- = -\min(\langle u \rangle_\phi)$ , respectively, along  $z = 0$ . We only have access to the strength values at two streamwise locations, and so we cannot fully characterize the decay in strength as a function of streamwise distance. We have therefore modelled the spatial decay as exponential following Hussain and Reynolds (1970), who also considered the periodic forcing of a turbulent wall-bounded flow. The resulting curves have been extrapolated over  $0.5 \leq x/D \leq 3.0$  and are plotted in Figures 8.9(a,b) along with the values extracted from the phase averages.

The extrapolated exponential fits allow for estimating the peak strength of the motions at the edge of the active surface ( $x/D = 0.5$ ), which can easily be read using the dashed lines in Figures 8.9(a,b). The uncertainty associated with the peak strength values is roughly  $0.007U_\infty$ ; this value was obtained by considering the maximum variation of the exponential fits at  $x/D = 0.5$  when accounting for the uncertainty values estimated in Appendix A. We estimate that the high-speed motions (Figure 8.9(a)) produced at  $St = 0.05, 0.10$ , and  $0.15$  reach a peak strength of roughly  $0.07U_\infty$  while the high-speed motion produced at  $St = 0.20$  only reaches  $0.05U_\infty$ . However, the high-speed motion produced at  $St = 0.20$  appears to decay more slowly, resulting in a higher strength than the other three actuation frequencies for  $x/D > 1$ . Despite this, it seems that the strength of all high-speed motions decays to less than 1% of  $U_\infty$  before reaching  $x/D = 2$ . The

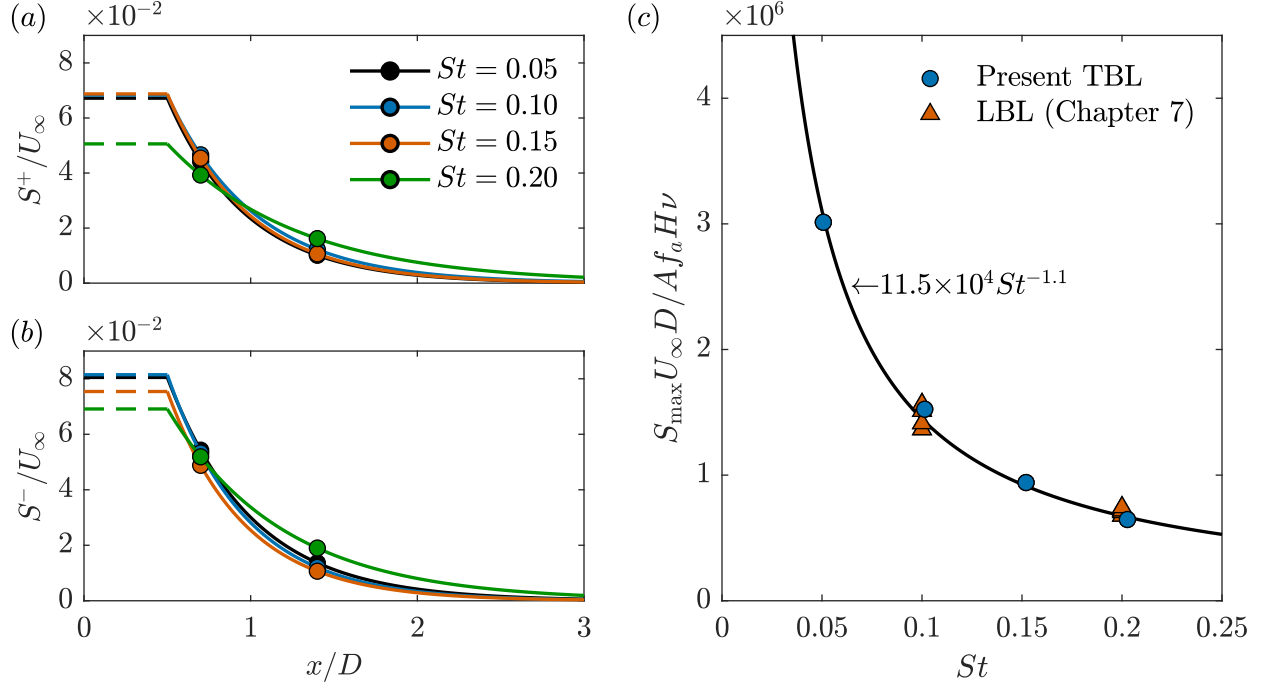


Figure 8.9: Strength of the (a) high- and (b) low-speed motions produced by the active surface in the present TBL as a function of streamwise distance. The markers represent the values extracted from  $\langle u \rangle_\phi$ . The solid lines represent a fit to the extracted data assuming exponential spatial decay. (c) The peak strength of the motions produced by the active surface in the present TBL compared to the LBL results of Chapter 7.

peak strengths of the low-speed motions (Figure 8.9(b)) are estimated to be larger than those of the high-speed motions, reaching  $0.08U_\infty$  for  $St = 0.05$  and  $0.10$ ,  $0.075U_\infty$  for  $St = 0.15$ , and  $0.07U_\infty$  for  $St = 0.20$ . Despite the stronger motions, we still estimate a reduction to less than 1% of  $U_\infty$  before reaching  $x/D = 2$ . Moreover, just like the high-speed motions, the low-speed motion produced at  $St = 0.20$  appears to decay more slowly than those produced at the other three actuation frequencies.

The motions produced by active surface deformations in the present TBL are much weaker in terms of  $U_\infty$  and decay more quickly with downstream distance when compared to the LBL results of Chapter 7 at the same  $St$ . In Chapter 7, we found that the strength of the motions produced by the active surface depends primarily on the amplitude of the surface deformation. The amplitude considered here is larger than all amplitudes considered in Chapter 7, but the LBL utilized is quite different than the present TBL in terms of thickness, velocity gradients, etc. We have therefore formulated a new normalization for the strength values by considering that they depend on both the active surface and the boundary layer. We assume that the parameters relevant to the operation of the active surface are  $D$ ,  $f_a$ , and  $A$ , while the parameters relevant to the boundary layer are  $U_\infty$ ,  $H$ , and  $\nu$ . The inclusion of the shape factor, despite it being dimensionless, was inspired by the normalization of the advection velocity and wavelength used in Figures 8.7 and 8.8. Various combinations of these parameters were considered and tested in a trial-and-error manner. Only

one normalization was found to collapse the data onto a single curve. The resulting normalization is presented in Figure 8.9(c) along with the results from Chapter 7 for  $St \leq 0.2$ , where  $S_{\max}$  is the estimated peak strength produced by the active surface ( $= \max(|\langle u \rangle_\phi|)$  at  $x/D = 0.5$ ). It is clear in the figure that the peak strength values collapse along the same power-law curve over this low- $St$  range. This suggests that the strength of the motions produced by the active surface at  $St \leq 0.2$  depends on far more parameters in comparison to the advection velocity and wavelength.

### 8.2.3 Visualization of the Induced Motions

The phase averages used throughout the previous sections capture the motions produced by the active surface in the wall-normal, spanwise, and phase dimensions. However, it is difficult to know what the motions produced by the active surface look like in 3D space when only considering the raw phase averages because the phase axis represents a different time scale at each actuation frequency. We have therefore constructed a model for visualizing what the average motions are likely to look like in the three spatial dimensions. The model employs Taylor's hypothesis to extend the phase averages  $\langle u \rangle_\phi = f(\phi, y, z)$  in the streamwise direction. The exponential curves of Figure 8.9(b) are then applied to account for the spatial decay in strength. These strength curves have been applied as shown in the subfigure including the constant portion marked by the dashed lines. That is, the exponential was applied for  $x/D > 0.5$  such that the magnitude of the phase averages at the measurement location is unchanged while a constant multiplier was used for the region  $x/D \leq 0.5$ . The model  $\langle u \rangle_\phi^m$  was formed using the phase averages measured at  $x/D = 0.7$  (FOV6 and FOV8) and is expressed for  $x/D \geq 0$  as

$$\langle u \rangle_\phi^m(\phi, x, y, z) = \begin{cases} e^{b(0.5D-x_m)} \langle u \rangle_\phi(\phi', y, z) & 0 \leq x/D \leq 0.5 \\ e^{b(x-x_m)} \langle u \rangle_\phi(\phi', y, z) & 0.5 < x/D, \end{cases} \quad (8.6)$$

$$\phi'(\phi, x) = \phi + \frac{\omega_a}{U_c}(x_m - x), \quad (8.7)$$

where  $b < 0$  captures the exponential decay according to the curves of Figure 8.9(b),  $x_m$  is the measurement location, and  $\phi'$  is the phase modified to account for both  $\phi$  and  $x$  in the application of Taylor's hypothesis. Equation (8.6) perfectly represents the phase-averaged motions at the measurement location  $x_m$  but loses accuracy as we move farther from this streamwise location. Nevertheless, it provides an estimate what the motions produced by the active surface look like in the three spatial dimensions of the present TBL.

The models for all  $St$  are shown in the streamwise-wall-normal plane at  $z = 0$  in Figure 8.10 where the dashed lines mark the measurement location of the phase averages (FOV6). The phase of the active surface in the figure is  $\phi = 4\pi/5$ , which corresponds to the surface having a downward velocity just after having reached its peak deformation. This phase was selected to highlight the low-

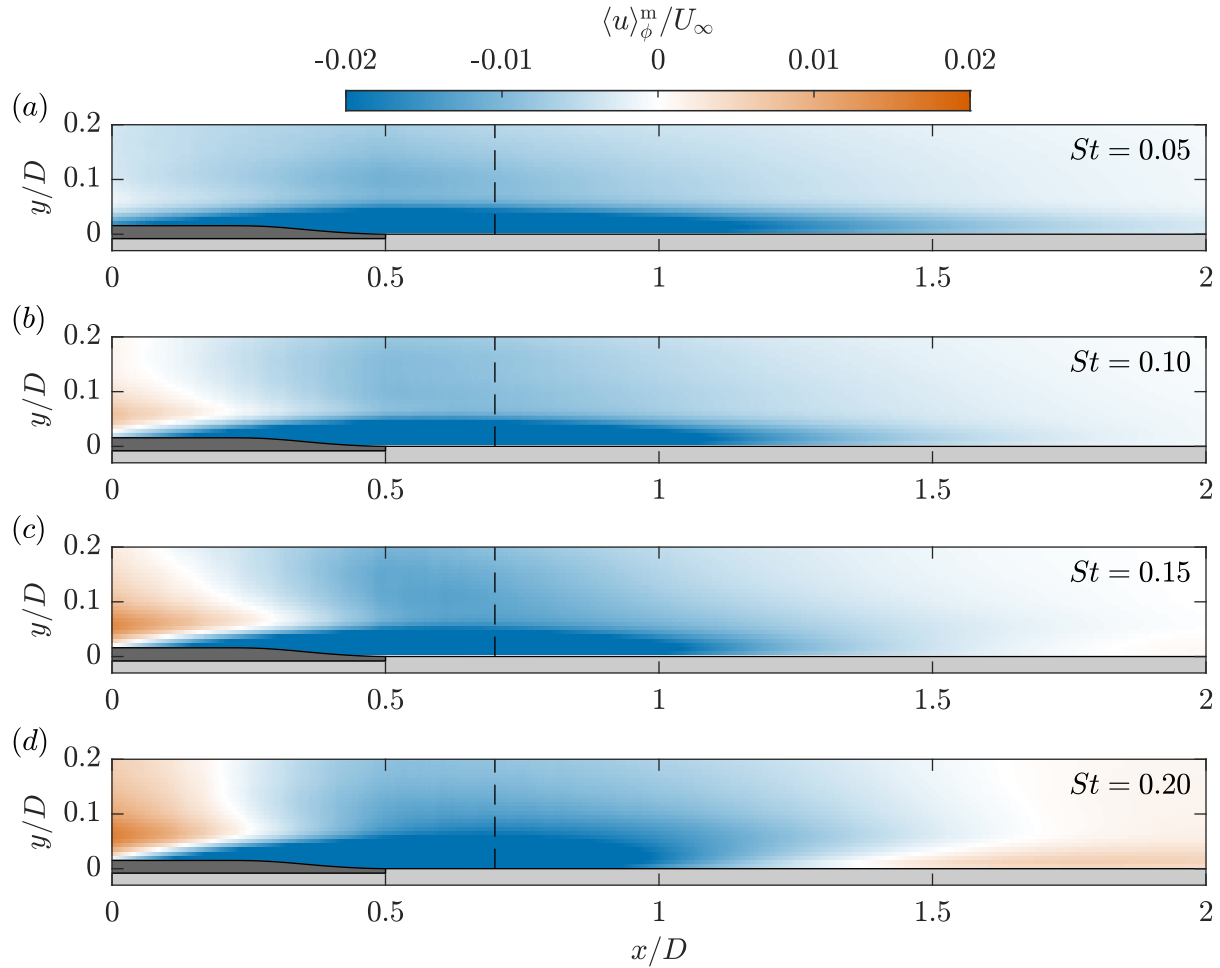


Figure 8.10: The model  $\langle u \rangle_\phi^m$  shown at  $z = 0$  and  $\phi = 4\pi/5$  for actuation frequencies of (a)  $St = 0.05$ , (b)  $St = 0.10$ , (c)  $St = 0.15$ , and (d)  $St = 0.20$ . The dashed lines show the measurement location used to form the models (FOV6). The position of the active surface is displayed accurately.

speed motions formed by an upward motion of the active surface. Increasing the phase by  $\pi$  shows very similar high-speed motions formed by a downward motion of the surface. The model for  $St = 0.05$  in Figure 8.10(a) shows the long wavelength associated with the lowest actuation frequency as the low-speed motion can be seen to extend to the end of the displayed FOV. The shrinking of these wavelengths with increasing actuation frequency is clear throughout Figures 8.10(b–d), with the latter even showing the adjacent high-speed motion downstream. It is interesting to note that the low-speed motions appear quite similar for all  $St$  considered within the region  $x/D \leq 1.0$ .

Figure 8.11 shows the models for all  $St$  in the streamwise–spanwise plane at  $y/D = 0.02$  and  $\phi = 4\pi/5$ , which is the same phase shown in Figure 8.10. Once again, the dashed lines mark the measurement location of the phase averages (FOV8). Just as before, the large change in wavelength with  $St$  is clear. However, in contrast to the streamwise–wall-normal plane, visualizing the motions in the streamwise–spanwise plane highlights the spanwise extent of the region that is most affected by

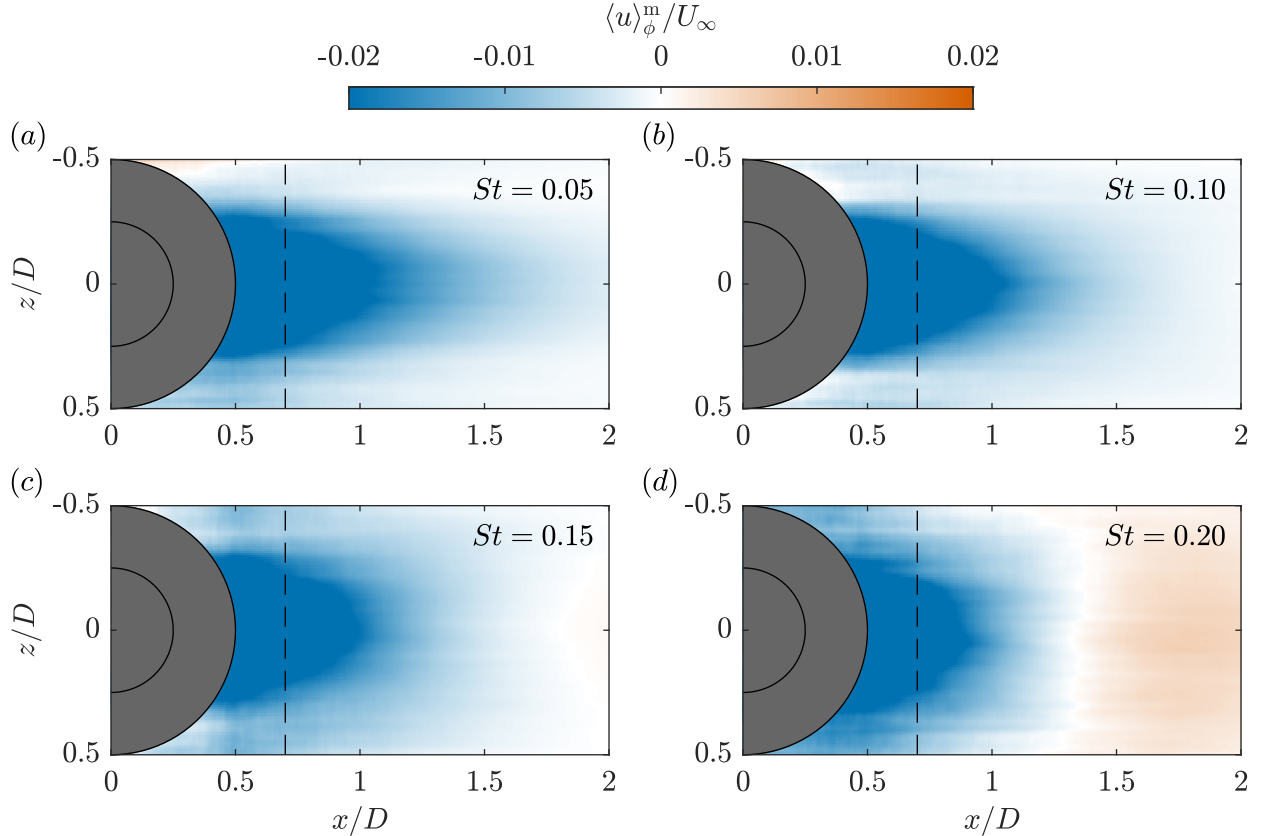


Figure 8.11: The model  $\langle u \rangle_\phi^m$  shown at  $y/D = 0.02$  and  $\phi = 4\pi/5$  for actuation frequencies of (a)  $St = 0.05$ , (b)  $St = 0.10$ , (c)  $St = 0.15$ , and (d)  $St = 0.20$ . The dashed lines show the measurement location used to form the models (FOV8).

the active surface. More specifically, we see a semi-elliptical region roughly occupying  $0.5 \leq x/D \leq 1.0$  and  $-0.25 \leq z/D \leq 0.25$  where the motions produced by the active surface are strongest. This region is slightly shorter for  $St = 0.2$  (Figure 8.11(d)), but is approximately invariant for  $St \leq 0.15$  (Figures 8.11(a–c)). These results indicate that the active surface can produce high- and low-speed motions within this region over the range of frequencies associated with the VLSMs.

### 8.3 Manipulation of Turbulence

The previous section focused on characterizing the periodic motions produced by the active surface. We will now investigate how these motions affect the mean flow and the surrounding turbulence. The latter will be accomplished by considering the Reynolds stresses using the quantity  $u'_i = u_i - \langle u_i \rangle_\phi$  introduced in Section 8.1.6. Lastly, an attempt to implement feed-forward control will be discussed.

### 8.3.1 Mean Velocity and Reynolds Stresses

The mean velocity profiles at  $x/D = 0.7$  and  $1.4$  for all  $St$  are shown in Figures 8.12(a,b). The profiles for the actuated cases at  $x/D = 0.7$  (Figure 8.12(a)) show almost no difference compared to the base flow. The only exception is closer to the wall ( $y/\lambda \lesssim 200$ ) where a slight deficit on the order of 2% is observed for all actuated cases (the uncertainty is estimated to be 0.2%). This appears to be because the low-speed motions produced by the active surface are stronger than the high-speed motions (see Figure 8.9) and so the average effect is a slight deficit. Indeed, the phase averages of Figure 8.5 show that the strongest motions occupy the same wall-normal extent as the affected region of the mean profiles. Conversely, we see no differences between the actuated cases and base flow at  $x/D = 1.4$  (Figure 8.12(b)). This is likely because of the large decay in the strength of the high- and low-speed motions by this downstream location. Overall, it appears that sinusoidal operation of the active surface does not significantly affect the mean velocity profile in the present TBL. This is in contrast to oscillatory actuation with dynamic roughness (Jacobi and McKeon, 2011; Gildersleeve et al., 2017) and piezoelectric cantilevers (Jeon and Blackwelder, 2000; Bai et al., 2014; Tang et al., 2019) which produce stronger effects on the mean flow.

The Reynolds stresses computed using both  $u_i$  and  $u'_i$  at  $x/D = 0.7$  and  $1.4$  for all  $St$  are presented in Figures 8.12(c,d). At  $x/D = 0.7$  (Figure 8.12(c)), there is a roughly 15% increase in  $\langle u^2 \rangle$  over  $y/\lambda \lesssim 200$ , which is the same region where differences in the mean profiles are visible (Figure 8.12(a)); this increase is several times larger than the uncertainty associated with these quantities. No differences are observed in  $\langle v^2 \rangle$ , confirming that the wall-normal velocity fluctuations produced by the active surface are negligible. There are also no differences in  $\langle uv \rangle$  despite the clear increase in streamwise velocity fluctuations associated with the active surface deformations. When considering  $\langle u'_i u'_j \rangle$ , which capture the structure of the turbulence less the average actuated motions, it is clear that all three components show no clear differences when compared to the base flow. Similarly, at  $x/D = 1.4$  (Figure 8.12(d)), both  $\langle u_i u_j \rangle$  and  $\langle u'_i u'_j \rangle$  show no differences with the base flow. The lack of a change in  $\langle u^2 \rangle$  at  $x/D = 1.4$  is again likely a result of the decay in strength of the motions produced by the active surface.

In total, it appears that  $\langle u'_i u'_j \rangle$  are unaffected by the active surface. However, we will show in the next section that this is only true on average, as there is actually a strong phase-dependent modulation of the turbulence statistics resulting from the motions produced by the active surface.

### 8.3.2 Phase-Averaged Reynolds Stresses

Computing  $\langle u'_i u'_j \rangle$  using actuation phase bins reveals a phase-dependent modulation of the turbulence statistics. This modulation has therefore been investigated using phase averaging applied in the same way as for  $\langle u_i \rangle_\phi$  (see Section 8.1.6). We define the phase-averaged Reynolds stresses as  $\langle u'_i u'_j \rangle_\phi$  and we facilitate their visualization using the difference

$$\Delta \langle u'_i u'_j \rangle_\phi = \langle u'_i u'_j \rangle_\phi - \langle u'_i u'_j \rangle, \quad (8.8)$$

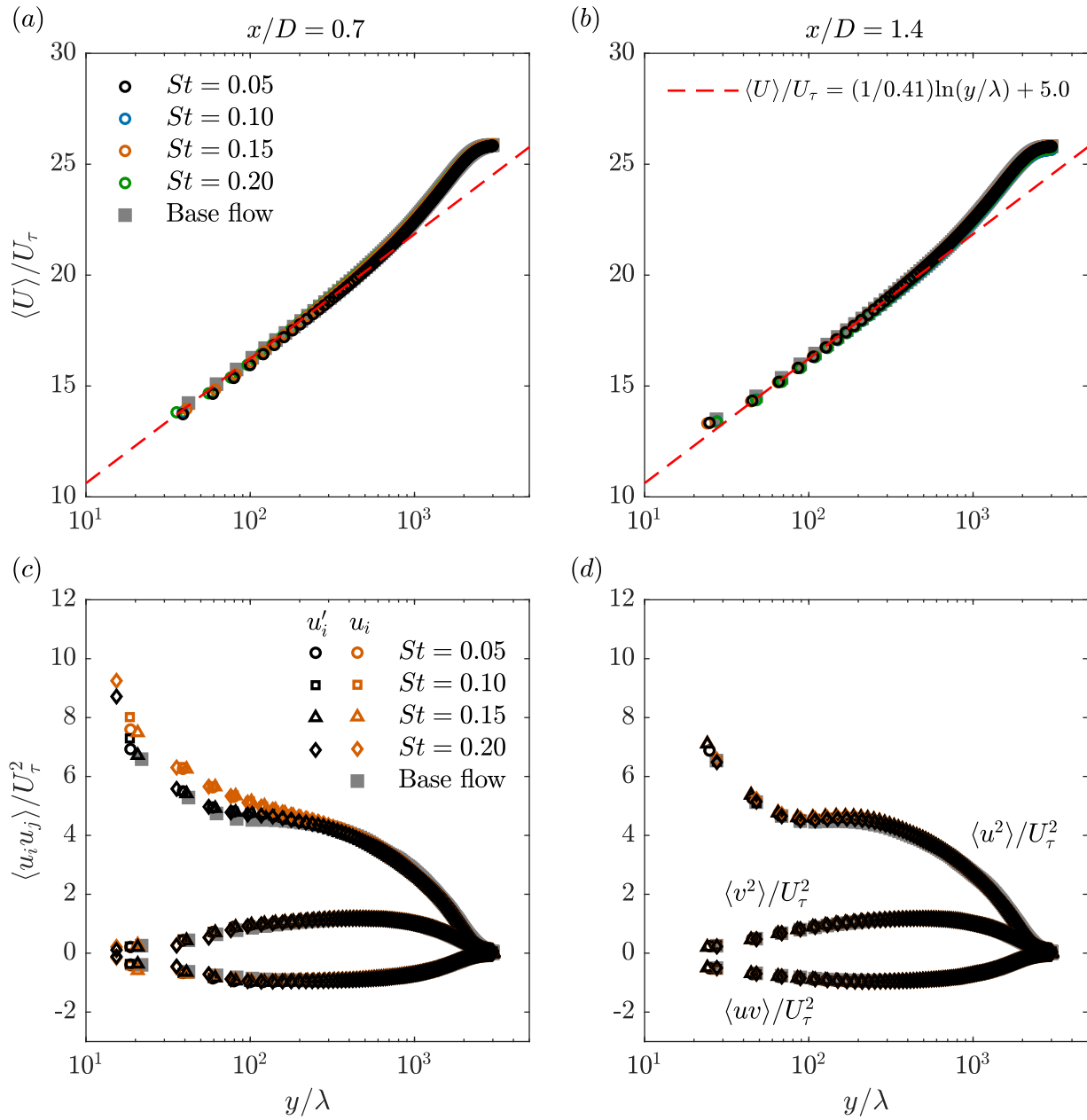


Figure 8.12: Mean velocity profiles and Reynolds stresses computed using both  $u_i$  and  $u'_i$  at all  $St$  compared to the base flow at (a,c)  $x/D = 0.7$  and (b,d)  $x/D = 1.4$ . The overlaid logarithmic law in (a,b) is the same as in Figure 8.2(a).

which shows the extent to which the Reynolds stresses are amplified or suppressed as a function of  $\phi$ . More precisely, Equation (8.8) is the difference between the phase-averaged and time-averaged Reynolds stress curves, and it represents the change in the Reynolds stresses as a function of phase with respect to the time-averaged Reynolds stresses. The resulting  $\Delta\langle u'_i u'_j \rangle_\phi$  computed in the  $\phi$ - $y$  plane using the data from FOV6 and FOV7 are shown in Figures 8.13 through 8.15. The left (panels (a-d)) and right (panels (e-h)) columns in each figure show the results at  $x/D = 0.7$  and 1.4, respectively. The solid and dashed outlines show the locations of the high- and low-speed motions, respectively, from Figure 8.5. The phase axis has been flipped to display the motions as if they were moving from left to right.

The streamwise component  $\Delta\langle u'^2 \rangle_\phi$  is shown in Figure 8.13. A strong modulation pattern that is associated with the high- and low-speed motions is visible at  $x/D = 0.7$  (Figures 8.13(a-d)). The high-speed motions (solid outlines) produce an amplification of  $\langle u'^2 \rangle$  near the wall and a suppression away from the wall. The opposite modulation pattern is visible for the low-speed motions (dashed outlines), which suppress  $\langle u'^2 \rangle$  near the wall and produce amplification away from the wall. These amplitude modulation patterns appear similar to those that are imparted on the small-scale turbulence by the VLSMs (Mathis et al., 2009; Ganapathisubramani et al., 2012). For  $St = 0.05$ , the modulated regions are roughly centered with respect to the high- and low-speed motions and are relatively flat. As  $St$  is increased, the modulated regions that are farthest from the wall become more inclined and shift upstream with respect to the associated coherent motions. Similar behaviour is visible at  $x/D = 1.4$  (Figures 8.13(e-h)), but the regions of modulation are weaker, more diffuse, and more inclined. This is likely because the associated high- and low-speed motions are also weaker, more diffuse, and more inclined at  $x/D = 1.4$  (Figure 8.5).

The modulation of the streamwise Reynolds stress visible in Figure 8.13 is quite strong. It also does not change much as a function of  $St$ . The following values are therefore reported as averages over the four  $St$  considered. The region of amplification associated with the high-speed motions at  $x/D = 0.7$  produces  $\langle u'^2 \rangle_\phi$  values that are up to 11% larger than the local  $\langle u'^2 \rangle$ . Similarly, the region of suppression associated with the high-speed motions produces values that are up to 14% smaller than the local  $\langle u'^2 \rangle$ . The amplification caused by the low-speed motions is even stronger, producing values that are up to 22% larger than the local  $\langle u'^2 \rangle$ . The suppression caused by the low-speed motions is similar to that produced by the high-speed motions, resulting in values that are up to 15% smaller than the local  $\langle u'^2 \rangle$ . These extrema are 2 to 3 times weaker and are located farther from the wall at  $x/D = 1.4$ .

The wall-normal component  $\Delta\langle v'^2 \rangle_\phi$  is shown in Figure 8.14. A strong modulation pattern associated with the high- and low-speed motions at  $x/D = 0.7$  (Figures 8.14(a-d)) is again visible. The high-speed motions (solid outlines) produce a suppression of  $\langle v'^2 \rangle$  across the entire length of the coherent motion and a weaker amplification above the motion ( $y/\lambda \gtrsim 120$ ). This weaker region of modulation shifts upstream with respect to the associated coherent motion as  $St$  is increased. A similar but opposite pattern is visible for the low-speed motions (dashed outlines), which amplify  $\langle v'^2 \rangle$  within the coherent motion and cause a weaker suppression above it. Both the high- and

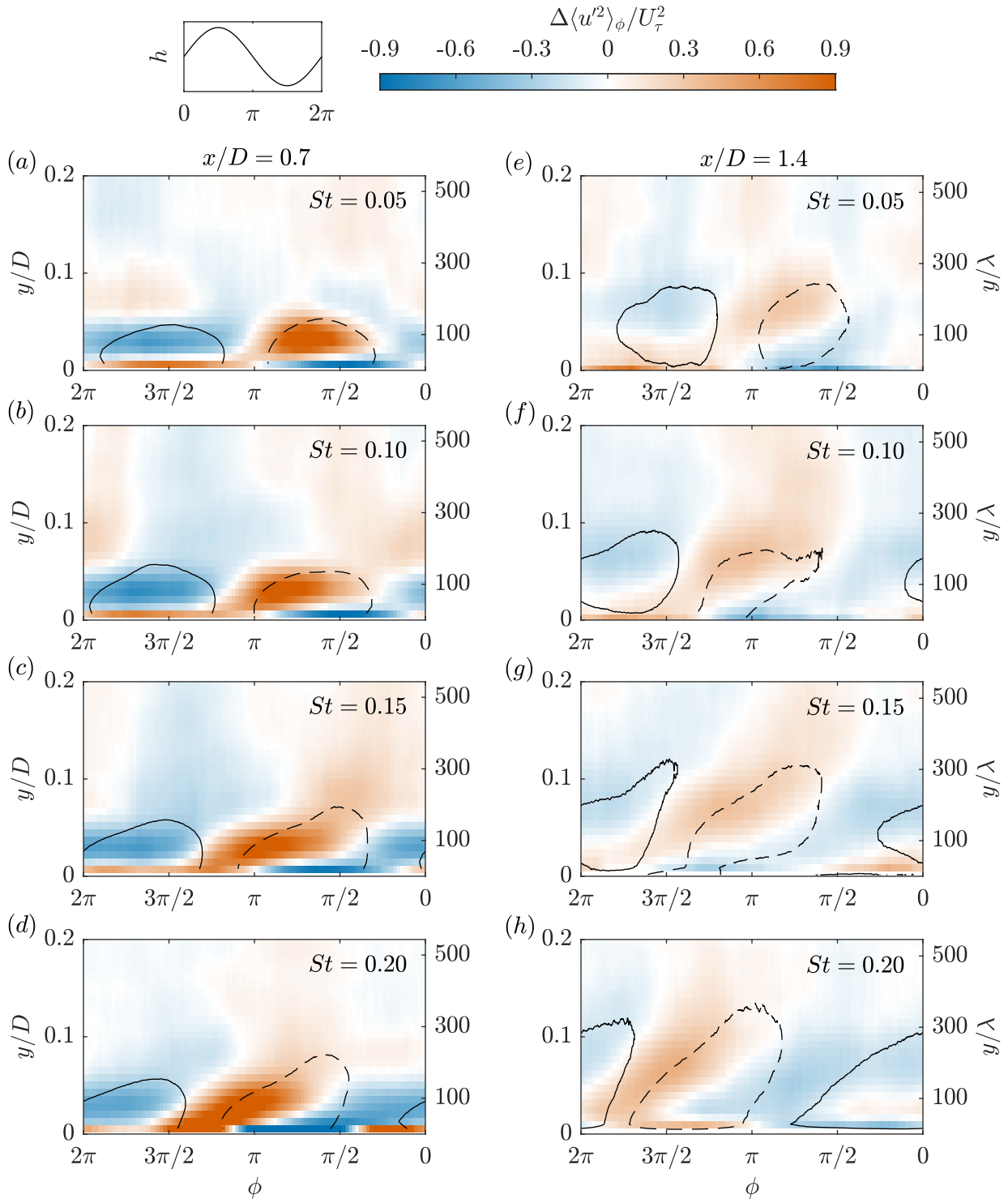


Figure 8.13: Modulation of the phase-averaged streamwise Reynolds stress ( $\Delta\langle u'^2 \rangle_\phi$ ) in the  $\phi$ - $y$  plane for all actuation frequencies computed using (a-d) the data from FOV6 at  $x/D = 0.7$  and (e-h) the data from FOV7 at  $x/D = 1.4$ . The solid and dashed outlines show the high- and low-speed motions, respectively, from Figure 8.5. The phase axis has been flipped to display the motions as if they were moving from left to right.

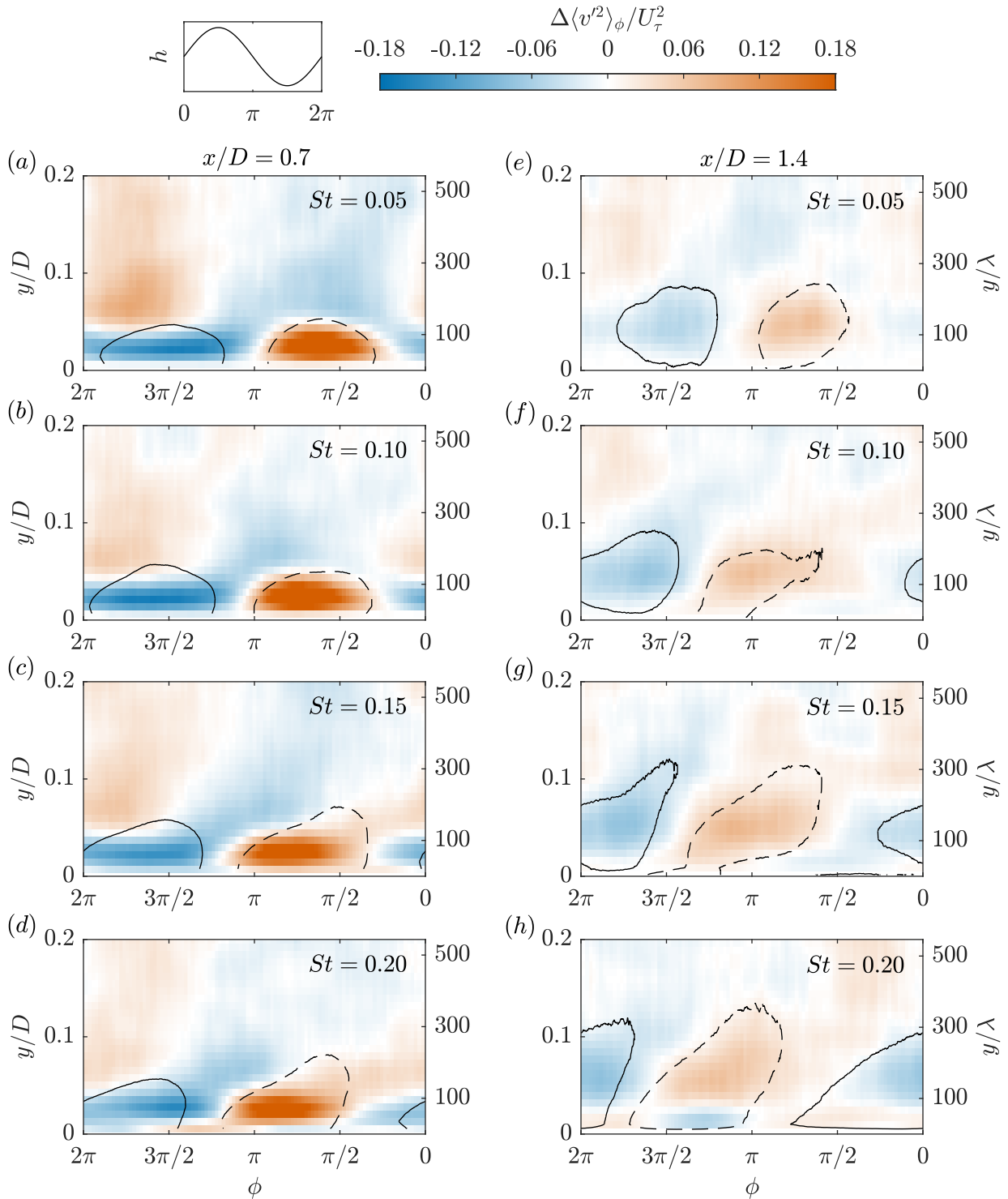


Figure 8.14: Modulation of the phase-averaged wall-normal Reynolds stress ( $\Delta \langle v'^2 \rangle_\phi$ ) in the  $\phi$ - $y$  plane for all actuation frequencies computed using (a-d) the data from FOV6 at  $x/D = 0.7$  and (e-h) the data from FOV7 at  $x/D = 1.4$ . The solid and dashed outlines show the high- and low-speed motions, respectively, from Figure 8.5. The phase axis has been flipped to display the motions as if they were moving from left to right.

low-speed motions appear to produce some weaker modulation very close to the wall opposite in sign to that of the region above for  $St = 0.20$ ; this is not visible for  $St = 0.05$  to  $0.15$ , again showing that the motions produced at the frequencies of the LSMs are a bit different than those produced at the frequencies of the VLSMs. The same patterns are visible at  $x/D = 1.4$  (Figures 8.14(e-h)) but are again weaker and more diffuse in comparison to those at  $x/D = 0.7$ .

The percent modulation of the wall-normal Reynolds stress at  $x/D = 0.7$  is even stronger than what was observed for the streamwise component. The region of suppression associated with the high-speed motions produces  $\langle v'^2 \rangle_\phi$  values that are up to 25% smaller than the local  $\langle v'^2 \rangle$ , while the region of amplification associated with the low-speed motions produces values that are up to 39% larger than the local  $\langle v'^2 \rangle$ . These values are again averages over all four  $St$ . At  $x/D = 1.4$ , the amplification is roughly 5 times weaker with respect to what was observed at  $x/D = 0.7$ . Similarly, the suppression is nearly 4 times weaker. The modulation of  $\langle v'^2 \rangle$  therefore shows a sharper decay between  $x/D = 0.7$  and  $1.4$  when compared to the modulation of  $\langle u'^2 \rangle$ .

Finally, the shear component  $-\Delta\langle u'v' \rangle_\phi$  is shown in Figure 8.15 where the negative sign has been added to have positive and negative values correspond to amplification and suppression of the Reynolds shear stress, respectively. This also allows for interpreting these results in terms of the phase-averaged turbulence production  $-\langle u'v' \rangle_\phi \partial\langle U \rangle / \partial y$ . Since  $\langle U \rangle$  and  $\langle u'v' \rangle$  are practically the same between the base and actuated flows (Figure 8.12), the modulation captured by  $-\Delta\langle u'v' \rangle_\phi$  can be thought of as the modulation of turbulence production with respect to that of the base flow.

The modulation pattern of  $-\Delta\langle u'v' \rangle_\phi$  at  $x/D = 0.7$  (Figure 8.15(a-d)) looks similar to that of  $\Delta\langle v'^2 \rangle_\phi$  at the same streamwise location. The whole area of each high-speed motion (solid outlines) experiences a suppression, resulting in  $-\langle u'v' \rangle_\phi$  values that are up to 30% smaller than the local  $-\langle u'v' \rangle$ . Similarly, the whole area of each low-speed motion (dashed outlines) experiences an amplification, resulting in values that are up to 43% larger than the local  $-\langle u'v' \rangle$ . These extrema occur around  $y/\lambda \approx 35$  to  $60$  for both suppression and amplification. At  $x/D = 1.4$  (Figure 8.15(e-h)), the maximum amplification and suppression are 11% and 9% of the local  $-\langle u'v' \rangle$ , respectively, and occur around  $y/\lambda \approx 150$  to  $190$ . These modulations of  $-\langle u'v' \rangle$  are quite strong, especially when we consider that the motions at  $x/D = 0.7$  and  $1.4$  have peak strengths of around 5% and 1% of  $U_\infty$ , respectively (Figure 8.9(a,b)).

### 8.3.3 Feed-Forward of the Wall-Pressure Signal

Motivated by the pressure-driven compliant surfaces of Luhar et al. (2015), an attempt was made to implement feed-forward control using the wall-pressure signal upstream from the active surface ( $x/D = -1.4$ ). This signal was filtered in real time to isolate the frequencies of the VLSMs. The filtered signal was then fed forward to determine the motion of the active surface. Since the low-frequency wall-pressure fluctuations were associated with the VLSMs in Chapter 5, the idea was that this strategy could potentially allow for targeting the VLSMs with the active surface. This attempt was largely unsuccessful but is documented here to highlight the lessons it reveals. The real-time system described in Section 3.3 was used to implement the elements of the feed-forward

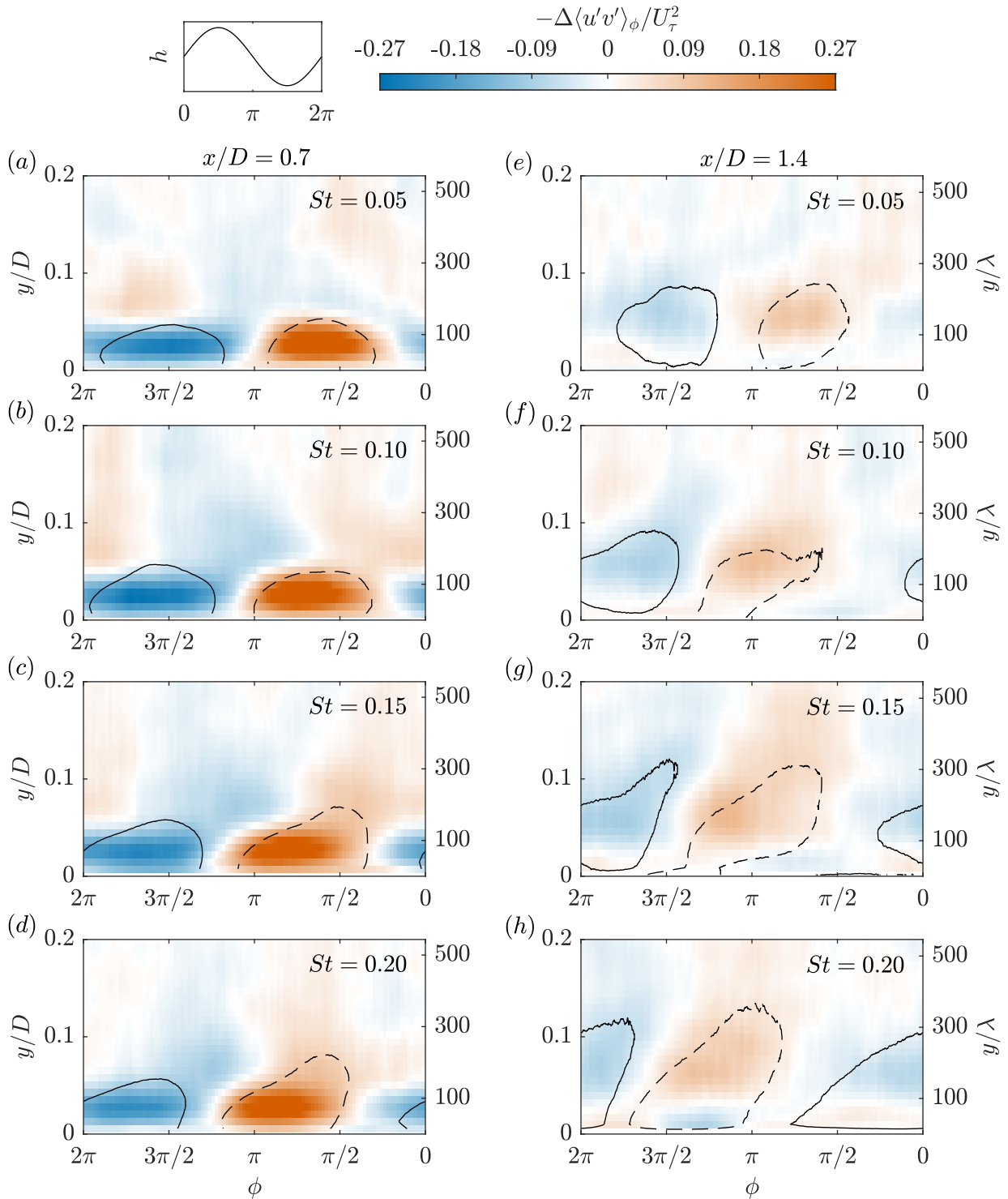


Figure 8.15: Modulation of the phase-averaged Reynolds shear stress ( $-\Delta\langle u'v' \rangle_\phi$ ) in the  $\phi$ - $y$  plane for all actuation frequencies computed using (a-d) the data from FOV6 at  $x/D = 0.7$  and (e-h) the data from FOV7 at  $x/D = 1.4$ . The solid and dashed outlines show the high- and low-speed motions, respectively, from Figure 8.5. The phase axis has been flipped to display the motions as if they were moving from left to right.

controller which are described next.

It was first necessary to have the capability to remove the wind tunnel background noise from the wall-pressure signal in real time so that the noise does not drive the motion of the active surface. A Wiener filter is used for removing background noise in the present thesis as was discussed in Section 4.5. This filter was applied in post-processing to remove the noise from the wall-pressure measurements used in the analyses of Chapter 5. However, it can also be applied in real time if the filter coefficients are identified ahead of time and the noise statistics do not change between the identification experiment and real-time implementation. An identification experiment was therefore conducted immediately before each real-time application of the Wiener filter. The necessary signals were recorded for 30 seconds and then used to identify the filter coefficients. These coefficients were applied in real time via Equation 4.9 to estimate the background noise signal so that it could be subtracted from the wall-pressure signal in real time.

Figure 8.16 shows the PSD of wall pressure beneath the present TBL compared to that of Chapter 5 and that obtained using the Wiener noise-removal filter in real time. It is clear in the figure that the wall-pressure fluctuations of the present TBL match those of the TBL studied in Chapter 5. This confirms once again that the desired TBL has been reproduced and that the conclusions of Chapter 5 regarding the pressure-velocity coupling can be used here. Similarly, the PSD obtained during real-time background noise removal also closely matches, with the exception of a portion of the high-frequency range. The deviation at the high frequencies is due to the Helmholtz resonance produced by the microphone pinhole cavity, which is not corrected for in real time. These high frequencies are filtered out of the wall-pressure signal during feed-forward operation of the active surface and therefore are not an issue here.

The active surface is similar to a speaker in its construction and therefore it produces acoustic noise when operated. This acoustic noise is also considered part of the background noise, and it too must be removed from the wall-pressure signal so that the active surface does not drive itself through acoustic feedback. The active surface was therefore operated using a pre-recorded input signal during the experiments used to identify the Wiener filter coefficients for feed-forward control. This pre-recorded signal had the same statistical characteristics as the signal being fed to the active surface during feed-forward operation and therefore the noise produced by the active surface during the identification experiments closely matched the noise produced in feed-forward operation. This was meant to eliminate the acoustic feedback of the active surface. However, the Wiener filter is not perfect; some actuator-generated noise influenced the movement of the active surface during feed-forward operation, resulting in the actuation becoming unstable for some cases. This instability was heavily dependent on the tuning parameters of the active surface, and so these parameters were selected carefully to achieve sufficient tracking of the feed-forward signal without the active surface becoming unstable.

After removal of the background noise, the wall-pressure signal was lowpass-filtered to isolate the frequencies of the VLSMs. Such a lowpass filter applied in real time introduces a “group delay” to the signal outputted by the filter, i.e., a frequency-dependent time delay (the Wiener filter does

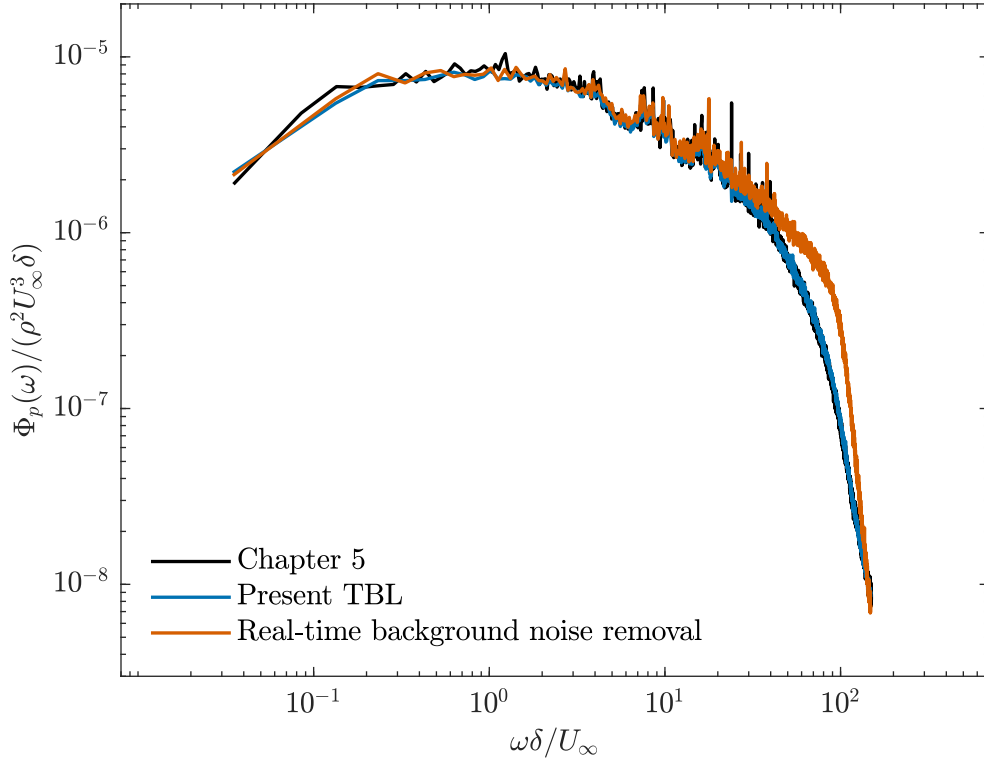


Figure 8.16: The PSD of wall pressure ( $\Phi_p$ ) beneath the present TBL at  $x/D = 1.4$  compared to that of Chapter 5 and that obtained using the Wiener noise-removal filter in real time. The PSD of the present TBL was computed using 5 minutes of wall-pressure data while the PSD from real-time background noise removal was computed using 4 minutes of wall-pressure data.

not introduce a time delay, despite it being named as a filter). Additionally, feed-forward operation of the active surface requires a time delay because it takes time for the motions sensed upstream to advect to the active surface. The lowpass filter used to isolate the low frequencies was therefore designed to have a constant group delay that is less than the time delay required for feed-forward operation of the active surface. A constant group delay is achieved using a filter with a linear phase response.

The time delay was determined by cross-correlating the wall-pressure signals at  $x/D = \pm 1.4$  after these signals had been filtered to isolate the low frequencies of interest. This produced an estimated time delay of 30 ms between the two pressure measurement locations. This is equivalent to an advection velocity of  $0.78U_\infty$  which closely matches the advection velocity estimated for the VLSMs in Chapter 5. Assuming frozen advection of the pressure fluctuations (i.e., Taylor’s hypothesis), a feed-forward time delay of 15 ms would have the active surface responding to the pressure fluctuations at  $x/D = 0$  if perfect tracking of the feed-forward signal was achieved. In reality, there is an additional time delay added to the system due to imperfect tracking of the active surface. This additional time delay could not be removed without tuning the active surface to be more aggressive in its tracking, but this produced instability through acoustic feedback. This

time delay could therefore not be removed. Nevertheless, a balance was struck which allowed for reasonable tracking with an effective total time delay of 17.7 ms (equal to the filter group delay plus the estimated tracking delay). More precisely, there is a time delay of around 17.7 ms between the wall-pressure measurement at  $x/D = -1.4$  and the response of the active surface to this measurement. Considering the advection velocity of the pressure fluctuations along with Taylor's hypothesis, actuation with this time delay is as if the active surface was responding to the low-frequency wall-pressure fluctuations at  $x/D = 0.24$ , which is still within the inner diameter of the active surface that experiences the maximum surface deformations (see Figure 6.1).

The magnitude response of the real-time lowpass filter is shown in Figure 8.17 where the frequency cutoff of the VLSMs (17.5 Hz) determined in Chapter 5 is also shown for reference. This filter is not ideal. The roll-off is quite gradual and the attenuation is only -20 dB. However, improving the filter performance would make the group delay too large, resulting in the active surface responding to pressure fluctuations that had already advected far downstream. Since the attenuation is only -20 dB, the output of the filter is quite noisy as it still contains some signal from the wall-pressure fluctuations at higher frequencies. This does not end up being an issue because the active surface is incapable of tracking these high frequencies and therefore they are filtered out mechanically by the limitations of the device.

After real-time background noise removal, the wall-pressure signal at  $x/D = -1.4$  is passed through the filter shown in Figure 8.17, a gain of +10 mm/Pa is applied, and then the resulting signal is used to operate the active surface. A sample of this reference signal and the resulting active surface displacement are shown in Figure 8.18. The reference signal (grey line) is shown with the total estimated time delay of 17.7 ms applied. This reference can be seen in the figure to saturate at  $h = \pm 2.5$  mm. This saturation was added to stop the active surface from contacting its displacement limits at  $\pm 3.04$  mm (dashed lines). As is evident in Figure 8.18, the active surface displacement (red line) still sometimes contacts both the upper and lower displacement limits of the actuator. Regardless, reasonable tracking of the reference signal, which represents the low-frequency wall-pressure fluctuations above the active surface, is observed.

The gain of +10 mm/Pa has the active surface responding to a positive wall-pressure fluctuation with an upward motion. Similarly, a negative wall-pressure fluctuation is met with a downward motion of the surface. This is an attempt to counter the VLSMs. In Chapter 5, the high- and low-speed VLSMs were associated with positive and negative wall-pressure fluctuations, respectively. In Chapter 7 and the present chapter, the active surface has been shown to produce high- and low-speed motions with downward and upward surface deformations, respectively. The present feed-forward configuration therefore has the active surface producing motions in opposition of the VLSMs assuming that the low-frequency wall-pressure signal accurately represents the VLSMs in real time.

The Reynolds stresses at  $x/D = 0.7$  resulting from feed-forward operation of the active surface are shown in comparison to those of the base flow in Figure 8.19(a). It is clear in the figure that  $\langle v^2 \rangle$  and  $\langle uv \rangle$  remain unchanged relative to the base flow. In contrast,  $\langle u^2 \rangle$  increases over the wall-

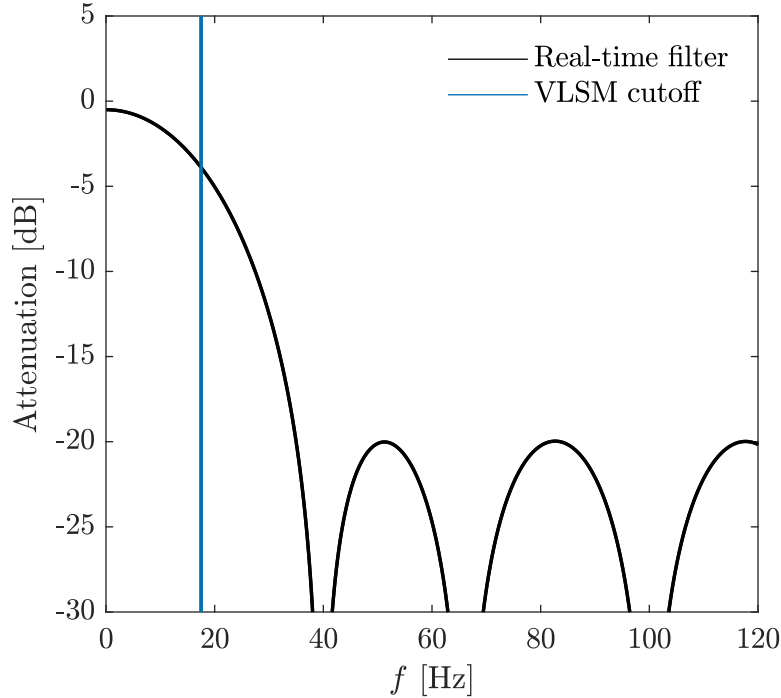


Figure 8.17: The magnitude response of the real-time filter used to isolate low-frequency wall-pressure for feed-forward operation of the active surface.

normal range  $y/\lambda \lesssim 200$ . This increase is similar to what was observed in Figure 8.12 for periodic operation of the active surface. These results indicate that the present implementation of feed-forward control is similar to open-loop operation of the active surface. However, the feed-forward scheme was designed to target the VLSMs. The lowpass filter of Figure 5.10(a) was therefore applied to isolate the very-large scales of the velocity field which are denoted using the subscript VLS. The lowpass-filtered measurements were then used to re-compute the Reynolds stresses which are shown in Figure 8.19(b). Once again, it is evident that  $\langle v^2 \rangle_{\text{VLS}}$  and  $\langle uv \rangle_{\text{VLS}}$  remain unchanged relative to the base flow. The values of  $\langle u^2 \rangle_{\text{VLS}}$  increase over  $y/\lambda \lesssim 100$  and decrease slightly over the remainder of the logarithmic layer. The slight decrease in  $\langle u^2 \rangle_{\text{VLS}}$  is within the measurement uncertainty, which is much larger when dealing with the low-frequency component of a time-resolved signal, and therefore may not be physical.

If the active surface was working to oppose the VLSMs as was desired, a reduction in  $\langle u^2 \rangle_{\text{VLS}}$  would have been observed for  $y/\lambda \lesssim 200$  which is where the active surface is most effective. There are at least two reasons why the desired result was not achieved. First, it is possible that the instantaneous, low-frequency wall-pressure signal at a single point is not a good identifier of the VLSMs in real time. The filtered space-time pressure-velocity correlations of Chapter 5 revealed a relationship between the low-frequency wall-pressure signal and the VLSMs. However, this was a statistical relationship since it was revealed through correlations. It may be the case that more sophistication is required to identify the VLSMs in real time using the low-frequency wall-pressure

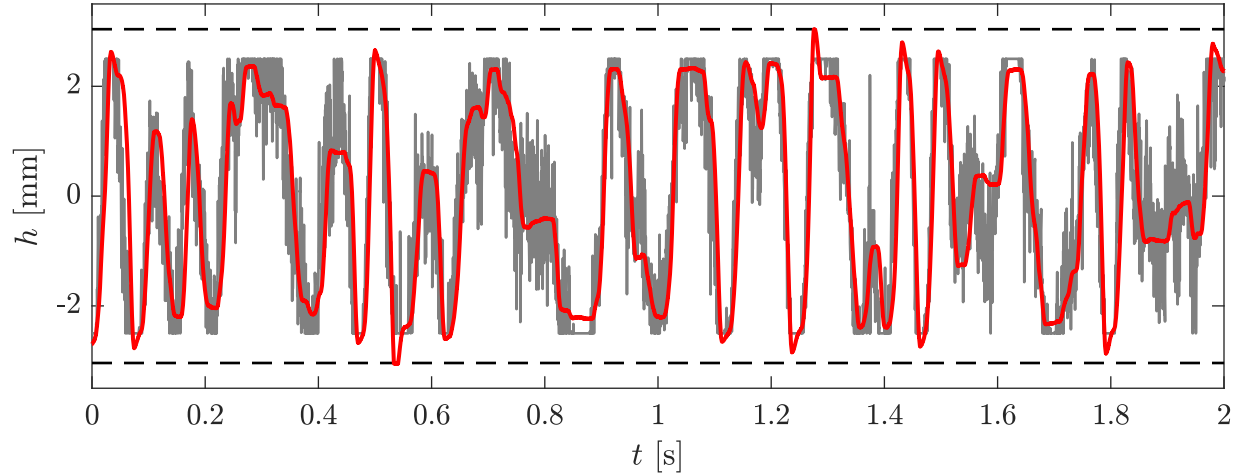


Figure 8.18: Sample tracking of the feed-forward signal: the active surface displacement (red) compared to the reference signal (grey) representing the low-frequency wall-pressure signal with a gain of +10 mm/Pa applied. The dashed lines represent the maximum possible displacement of the active surface.

signal. For example, an array of wall-pressure sensors may be necessary. Second, the acoustic feedback of the active surface could have dominated the actuation. The active surface was tuned to be stable, but it is still possible that most of the movement of the active surface during feed-forward operation was due to acoustic feedback and not due to the pressure fluctuations of the TBL. This could be why the present results for feed-forward control appear similar to open-loop actuation. Both possibilities discussed above are related to the sensing mechanism of the controller, thus highlighting the need to further investigate the use of wall-pressure signals for active flow control.

## 8.4 Further Discussion

### 8.4.1 Potential for Flow Control

The primary objective of this chapter was to determine whether active surface deformations are a feasible actuation strategy for targeting VLSMs. This targeting could potentially be implemented by producing motions with the same characteristics as the VLSMs with the goal of achieving a cancellation effect via a control scheme. Sections 8.2 and 8.3 revealed that the motions produced by the active surface do in fact have characteristics that align with those of the naturally-occurring VLSMs within the present TBL.

First, the high- and low-speed motions produced by the active surface are truly high and low speed with respect to the base flow. That is, the active surface does not simply impose a velocity deficit and then produce oscillations between the deficit state and base state; this is clear when viewing the mean velocity profiles in Figures 8.12(a,b). The ability to produce motions that are both high and low speed with respect to the base flow is due to the formation mechanism of these

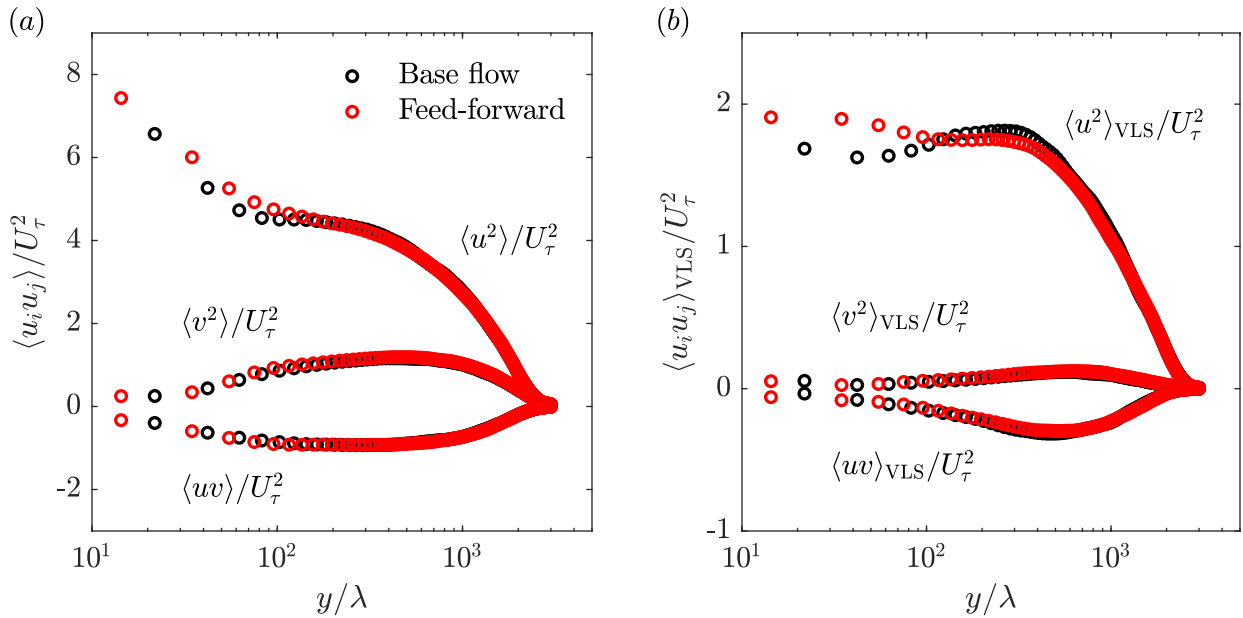


Figure 8.19: Reynolds stresses at  $x/D = 0.7$  with and without feed-forward actuation applied for (a) the full spectrum of velocity fluctuations and (b) the velocity fluctuations lowpass-filtered to isolate the very-large scales.

motions, which appears to be the movement of existing streamwise momentum, or lack thereof, in the wall-normal direction. Second, these motions can be produced within the frequency range of the present VLSMs and with widths and lengths that match those of the VLSMs. However, the motions are concentrated within  $y/\delta \lesssim 0.1$ , while the VLSMs can exist up to roughly  $y/\delta = 0.5$  (Dennis and Nickels, 2011a). They are therefore similar in structure to flattened VLSMs. Finally, the modulation of the streamwise Reynolds stress produced by the high- and low-speed motions matches the amplitude modulation produced by VLSMs (Mathis et al., 2009; Ganapathisubramani et al., 2012). More specifically, the high-speed motions produce a turbulence amplification effect near the wall and a suppression effect away from the wall. Similarly, the low-speed motions produce a suppression of turbulent fluctuations near the wall and an amplification away from it.

Considering the above, it is reasonable to use the terminology of Jacobi and McKeon (2017) and label the longest motions produced by the active surface in the present TBL as synthetic VLSMs. However, unlike the synthetic VLSMs of Jacobi and McKeon (2017), the present motions decay rapidly with downstream distance and are therefore more of a local actuation. This is clear in the visualizations of Figures 8.10 and 8.11, which show that the strongest fluctuations produced by the active surface exist in the region immediately downstream from the device. It follows that it may be possible to target the VLSMs locally within the region immediately downstream from the active surface by employing the device in a feed-forward control scheme. This was attempted in Section 8.3.3 but was ultimately unsuccessful, likely due to the sensing mechanism. The effects of suppressing the VLSMs within this region, and whether these effects persist downstream, should

therefore be the topic of future work.

Alternatively, the active surface could potentially be used for flow control by leveraging the turbulence-modulating effects displayed in Figures 8.13 through 8.15. The strong modulation of  $-\langle u'v' \rangle$  is particularly interesting due to its link to the turbulence production term. The present results show that the high-speed motions produced by downward deformations of the active surface suppress the turbulence production in the logarithmic layer by up to 30% of the local value in the base flow. Moreover, the motion that causes this effect is roughly  $0.05U_\infty$  in strength at the streamwise location where the effect was measured. This suggests that relatively weak motions produced by active surface deformations could be used to significantly manipulate the turbulence production in TBLs. However, the same high-speed motion was also found to amplify  $\langle u'^2 \rangle$  in the near-wall region, and this may cause other unwanted effects such as extreme wall-shear events. Additionally, returning the surface to zero displacement after generating a high-speed motion could produce a low-speed motion, which would amplify turbulence production in the logarithmic layer. Reducing turbulence production would therefore rely on operating the active surface in such a way as to predominantly produce high-speed motions, which may be possible with asymmetric input signals. Regardless, more work should be done to explore the turbulence-modulating effects associated with active surface deformations and their potential for turbulence control.

#### 8.4.2 Scaling Between Different Boundary Layers

The same active surface employed in the LBL of Chapter 7 has been used in the present TBL, allowing for comparing how active surface deformations affect two very different boundary layers ( $Re_\theta \approx 100$  vs.  $Re_\theta \approx 6000$ ). Both sets of results for  $St \leq 0.2$  show that the active surface can produce high- and low-speed motions with similar widths and heights. However, the advection velocity, wavelength, and strength of the motions produced are quite different between the LBL and TBL. More specifically, active surface deformations in the LBL produce motions that are shorter in the streamwise direction, advect slower, and are stronger relative to  $U_\infty$  when compared to the motions produced in the present TBL. This indicates that the boundary layer properties are important for determining the nature of the motions that can be produced using active surface deformations. It is therefore important to determine how the various characteristics of the actuated motions depend on the boundary layer properties so that active surfaces can be designed for a given flow control application.

In Section 8.2, we explored normalizations for the advection velocity, wavelength, and strength of the motions produced by the active surface. It was shown that the advection velocity in the LBL and TBL collapse along a power-law curve when the freestream velocity and shape factor are used in the normalization. The freestream velocity is the primary source of momentum, and the shape factor is inversely proportional to the amount of momentum near the wall. It therefore makes sense intuitively that these parameters would dictate the advection velocity of motions produced at the wall. By extension, the wavelengths measured in the LBL and TBL were also found to collapse on a single power-law curve when the shape factor was used in the normalization. Since the power-

law curves are functions of  $St = f_a D/U_\infty$ , we can see that the advection velocity and wavelength appear to depend on the boundary layer parameters  $U_\infty$  and  $H$  and the actuation parameters  $f_a$  and  $D$ . Normalization with these parameters appears to work well when using the present data and that of Chapter 7. However, it is necessary to consider a wider variety of boundary layers and active surfaces to make a more concrete conclusion regarding how the advection velocity and wavelength of the motions produced by active surface deformations depend on the boundary layer and actuation parameters.

The use of the shape factor for normalization was extended to the strength of the motions produced by the active surface for  $St \leq 0.2$ , resulting in the nondimensional relationship

$$\frac{S_{\max} U_\infty D}{A f_a H \nu} = c_1 St^{-1.1}, \quad (8.9)$$

where  $c_1$  is the constant shown in Figure 8.9(c); this constant is likely unique to the present active surface. If we divide Equation (8.9) by  $U_\infty$ , employ the approximation  $St^{-1.1} \approx St^{-1}$ , and rearrange, we arrive at

$$\frac{S_{\max}}{U_\infty} \approx \frac{c_1 A H}{Re_D D}. \quad (8.10)$$

This simplified relationship indicates that the peak strength as a percentage of  $U_\infty$  and at actuation frequencies of  $St \leq 0.2$  can be approximated as a function of the nondimensional parameters  $Re_D = U_\infty D/\nu$ ,  $H = \delta^*/\theta$ , and  $A/D$ . Once again, this approximate relationship holds for the presently considered data but should be verified in the future using a wider variety of boundary layers and active surfaces. Despite this caveat, Equation (8.10) provides insight regarding the situations in which active surface deformations may have superior authority for flow control applications. First,  $S_{\max}/U_\infty$  is inversely proportional to  $Re_D$ . This is in direct conflict with the idea of using active surface deformations to target VLSMs, which are a high-Reynolds-number phenomenon, but supports the use of active surface deformation for flow control at lower Reynolds numbers. Second,  $S_{\max}/U_\infty$  is proportional to  $H$ . This is again in conflict with the idea of targeting VLSMs since  $H$  reduces with Reynolds number. However, it suggests that stronger motions can be generated in situations with larger  $H$ , for example a TBL approaching trailing-edge separation over an airfoil (Ma et al., 2020). Finally,  $S_{\max}/U_\infty$  is proportional to  $A/D$ . This particular observation clearly has limits because it implies that  $A/D$  can be increased arbitrarily to obtain sufficient authority over the flow. In reality, increasing  $A/D$  too much would result in cavity flows ( $h < 0$ ) or blockages and flow separation ( $h > 0$ ). In the present TBL,  $A/D = 0.027$  ( $\sim 3\%$  of  $\delta$ ) has resulted in  $S_{\max}/U_\infty \approx 0.08$  at the  $St$  necessary for targeting VLSMs. By linear extrapolation, it follows that active surface deformations at around 7% of  $\delta$  (or roughly 9% of  $\delta$  according to Equation (8.10)) would produce high- and low-speed motions with  $S_{\max}/U_\infty \approx 0.2$  in the present TBL. This deformation amplitude is not so large as to be impractical and would likely provide sufficient authority over the flow for directly targeting the VLSMs.

## 8.5 Summary

This chapter considers the use of active wall-normal surface deformations for controlling a TBL at  $Re_\tau = 2600$ . We focus specifically on whether it is feasible to target the VLSMs locally with this actuation strategy. We employ the active surface developed in Chapter 6, which has a diameter roughly equal to the present boundary layer thickness. We operate the device periodically at a constant amplitude of  $0.03\delta$  and frequencies of  $St = f_a D/U_\infty = 0.05$  to  $0.20$ ; this range contains the frequencies associated with the naturally-occurring VLSMs. The resulting motions were captured using high-speed PIV and evaluated using a triple decomposition.

Periodic operation of the active surface produces a series of high- and low-speed streamwise velocity fluctuations concentrated within  $y/\delta \lesssim 0.1$  and  $-0.25 \lesssim z/\delta \lesssim 0.25$ . These motions are truly high and low speed with respect to the unactuated base flow since the mean velocity profile is essentially unchanged between the actuated and unactuated cases. The high- and low-speed motions form from downward and upward surface deformations, respectively, and so the formation mechanism appears to be the movement of streamwise momentum in the wall-normal direction. The extrema of these motions are concentrated along  $z = 0$ , which indicates that the active surface is generating type-1 modes according to the definition introduced in Chapter 7.

The length of the motions produced by the active surface is a function of the actuation frequency. We found that  $St \lesssim 0.1$  produce motions with lengths comparable to the VLSMs in the present TBL ( $\geq 3\delta$ ). We also found that these motions modulate turbulence in a manner similar to that of the VLSMs. The high-speed motions were found to amplify the streamwise Reynolds stress near the wall and suppress it away from the wall while the opposite pattern was observed for the low-speed motions. Additionally, the high-speed motions produced a suppression of the wall-normal Reynolds stress and turbulence production while the low-speed motions amplified these quantities. Most notably, the high-speed motions with a strength of around  $0.05U_\infty$  suppress the turbulence production in the logarithmic layer by up to 30% of the local value in the base flow.

Considering the dimensions and turbulence-modulating behaviour of the motions produced by the active surface, it is reasonable to use the terminology of Jacobi and McKeon (2017) and label these motions as synthetic VLSMs. However, unlike those of Jacobi and McKeon (2017), the synthetic VLSMs generated here decay in strength rapidly with downstream distance and act like a local actuation as a result. Moreover, the strength of this local actuation is largely invariant over the frequency range of the VLSMs. These actuated motions therefore appear to be well-suited for targeting the VLSMs locally via feed-forward control to produce a cancellation (or suppression) of the naturally-occurring VLSMs. Feed-forward control was attempted here using the upstream wall-pressure signal filtered to isolate the frequencies of the VLSMs. This attempt was ultimately unsuccessful, likely because of issues related to the sensing mechanism. Alternatively, a flow control strategy based around the turbulence-modulating characteristics of the synthetic VLSMs could also prove effective.

Finally, we compared our results to those obtained using the LBL of Chapter 7. We find that the motions produced by the active surface in the present TBL advect faster and are weaker

when compared to the motions produced in the LBL at the same  $St$  if the advection velocity and strength are normalized by  $U_\infty$ . Our results indicate that the shape factor of the boundary layer may be part of what dictates the observed differences in advection velocity (and by extension the wavelength). Similarly, the shape factor and Reynolds number may be part of what dictate the observed differences in strength.

## Part IV

# Closing

## Chapter 9

# Conclusions

The primary results chapters contain discussions and summaries of the more technical aspects of the present work. However, those discussions are not thorough in their consideration of the overarching goal of this thesis: to help enable the targeted control of VLSMs through the development of sensing and actuation capabilities. Accordingly, this chapter synthesizes the present contributions in the context of the overarching goal, discusses the limitations of the results, and provides recommendations for future work on the topic.

### 9.1 Sensing with Wall Pressure

The targeted control of VLSMs requires the ability to sense these motions in real time so that the controller can then decide how to act. Pressure sensors were selected for this purpose in the present work because they are the most practical for implementation into physical systems. In fact, even velocity measurements are conducted via pressure sensors using pitot tubes in many industrial applications. Despite their practicality, it is challenging to use pressure sensors to identify coherent motions within TBLs. As will be described next, some of the associated challenges were tackled in the present work while other challenges were highlighted by an attempt to implement feed-forward control using the wall-pressure signal in Section 8.3.3.

First, it is not straightforward to obtain reliable pressure measurements in turbulent flows. Before the pressure measurement system can be designed, it is necessary to acquire an initial understanding of the flow of interest through estimations or preliminary measurements of some kind. The measurement system must then be designed to be sensitive to the frequencies of interest, avoid spatial filtering, remove acoustic background noise, and correct for Helmholtz resonance. The latter two requirements are particularly important and are not well-explained in the fluid mechanics literature, if at all. Consequently, the first major contribution of the present thesis was to fully document the development of the pressure measurement system in Chapter 4. To the author's knowledge, the method used to correct for Helmholtz resonance is novel.

The background noise of the wind tunnel was removed from the pressure measurements using a Wiener noise cancelling filter. This technique was found to be effective in the unactuated TBL and was also shown to work when applied in real time. Nevertheless, there are problems when actuator

noise is present as was highlighted by the attempt to implement feed-forward control. Despite the actuator noise being accounted for in the identification of the Wiener filter coefficients, the removal of the actuator noise from the wall-pressure signal was imperfect. This led to acoustic feedback between the sensor and actuator, resulting in instability of the feed-forward system. Additionally, the Wiener noise cancelling filter will act to remove all parts of the wall-pressure signal that are correlated with the noise field signal. This is not an issue if the sensor is placed upstream of the actuator. However, a sensor that is downstream from the actuator will measure pressure fluctuations that are a result of the actuator noise but also a result of the actuation itself. The latter pressure fluctuations will be correlated with the actuator noise and will therefore be unintentionally removed from the pressure signal by the Wiener filter.

Another challenge is understanding the pressure-velocity relationship associated with the target motions. This was tackled in Chapter 5 where the relationship between the VLSMs and wall pressure was identified for the first time. The investigation revealed that low-frequency wall-pressure fluctuations are caused by the wall-normal velocity component of the VLSMs. More specifically, the downward motions of high-speed VLSMs cause a splatting at the wall, resulting in high pressure. Conversely, the upward motions of low-speed VLSMs cause a suction at the wall to produce a low pressure. The alternation between splatting and suction that occurs beneath the VLSMs as they meander and advect downstream therefore appears to be the mechanism by which they modulate wall pressure at the lowest frequencies of the turbulence spectrum. This result suggests that it is possible to identify the VLSMs in real time by employing the low-frequency wall-pressure signal in some way. However, the low coherence between wall pressure and the VLSMs indicates that simple thresholding of a single wall-pressure signal is likely insufficient for this identification task.

Finally, a filter was used here to isolate the low-frequency pressure signal associated with the VLSMs. The phase distortion associated with the filter has the potential to add additional challenges when identifying VLSMs in real time because it imposes a time delay on the filter output which can be quite large depending on the characteristics of the filter. If this time delay is too large, then the VLSMs that are to be identified will have advected far downstream before the filter has outputted its result. Why this is an issue for real-time identification of the VLSMs is obvious. The time delay can be reduced by relaxing the filter performance, but this may produce a result that is no longer capable of representing the VLSMs. Once again, more sophistication may be necessary to accomplish this task.

## 9.2 Actuation with Active Surface Deformations

In addition to adequate sensing, targeted control of the VLSMs requires an actuator that is capable of effectively manipulating these motions from the wall. Active surface deformations have been largely overlooked as a viable actuation strategy in the flow control literature. However, the available work on the topic suggests that it has potential. This actuation strategy was therefore selected for further exploration in this thesis. The contributions described next are believed to have advanced our understanding of actuation with active surface deformations more than any previous

study on the topic, although the previous investigations were brief, few, and far between.

It should first be mentioned that there are endless surface deformation geometries to consider when designing this type of actuator. The active surface developed in Chapter 6 produces one of the simplest possible geometries, and the device was designed this way for a few reasons. First, a simple geometry facilitates manufacturing. Second, the present work was concerned with local surface deformations, and the circular geometry seems ideal for producing a localized deformation. Third, a simpler geometry helps isolate the effect of the moving surface instead of, for example, the effect of a complicated protrusion or depression. And finally, the geometry was to be easily reproducible by future researchers who wish to contribute further advancements to the topic.

The active surface was first deployed beneath an LBL in Chapter 7. This was done to form a baseline understanding of the actuation strategy in a steady flow and to allow for later comparison with actuation in the TBL. The results indicate that the active surface is capable of producing high- and low-speed streamwise velocity fluctuations with similar magnitudes which reach up to roughly one-third of the freestream velocity. This is a fantastic result for an actuator given that the objective is to be able to generate velocity fluctuations that can be used to influence the flow. It is also remarkable that the active surface can produce both high- and low-speed motions, as many actuator types are asymmetric in their impact. That being said, the spatial structure of the actuated motions is highly dependent on the actuation frequency. Increasing the actuation frequency produced alternating transitions between type-1 and type-2 modes, with the latter type being undesirable for targeting coherent motions. It therefore may be the case that the active surface is only viable for flow control within a narrow frequency band of a given application. The LBL results indicate that it is the lowest frequencies that are the most suitable for flow control. It then follows that active surface deformations may only be suitable for flow control in situations where it is the low frequencies that are of interest.

Chapter 7 also included an application of a data-driven, linear modelling technique which was shown to successfully capture the input-output dynamics of the actuated flow. This model was identified using the LBL because the flow is steady and therefore evaluating the performance of the model is straightforward. It is not known whether the success of the technique will extend to actuation in the TBL. Nevertheless, this result is promising for the development of control strategies that utilize active surface deformations because it suggests that the actuation strategy is compatible with the tools of modern control theory which are largely limited to linear systems. More specifically, the state-space model form of a linear system is required to implement these tools, and such a model can be extracted via the eigensystem realization algorithm from the type of linear model considered here. The resulting state-space model could then be used to design an effective controller using theory and simulation.

The active surface was then deployed beneath a TBL in Chapter 8 where it was operated at the frequencies associated with the VLSMs; these low frequencies happen to occupy the (normalized) frequency range that was found to be most suitable for flow control in the LBL of Chapter 7. Once again, the device was found to be capable of producing both high- and low-speed streamwise

velocity fluctuations of type 1, i.e., the extrema of these fluctuations occur along the centreline of the active surface. These actuated motions were similar to the VLSMs in terms of their dimensions and ability to modulate the surrounding turbulence. However, their strength decays quickly with streamwise distance and therefore they are more of a local actuation. These characteristics indicate that active surface deformations are suitable for targeting VLSMs locally, although it is not known whether any manipulation of the VLSMs would persist downstream. Alternatively, the turbulence-modulating properties of the actuated motions may be suitable for turbulence control. In particular, the suppression of turbulence production caused by the high-speed actuated motions is likely worth further exploration.

Finally, the motions produced by the active surface at low frequencies were compared between the LBL and TBL. These motions are quite similar overall but with two primary differences. First, the motions produced in the TBL advect faster as a percentage of the freestream velocity compared to those produced in the LBL. Second, the motions produced in the TBL are weaker as a percentage of the freestream velocity compared to those produced in the LBL. These differences prompted the consideration of normalizations that would collapse the data onto single curves. The resulting normalizations suggest that the shape factor of the boundary layer is part of what determines the advection velocity of the motions produced by the active surface. This makes sense intuitively because the shape factor is inversely proportional to the amount of momentum near the wall where the motions are being formed. Similarly, the shape factor and Reynolds number may both determine the strength of the motions produced by the active surface. More specifically, high shape factors and low Reynolds numbers appear to be associated with stronger actuation. This does not bode well for the targeted control of VLSMs in high-Reynolds-number applications. However, there are many applications at lower Reynolds numbers where active surface deformations may be a suitable form of actuation for flow control.

### 9.3 Recommendations for Future Work

There are many directions that could be taken by those looking to extend the work done here. A few recommendations are described below.

#### **Real-Time Removal of Actuator Noise from Pressure Measurements**

The use of pressure measurements in many flow control applications relies on the ability to distinguish between acoustic noise and hydrodynamic pressure fluctuations. The attempt to implement feed-forward control revealed that the Wiener filter is not sufficient for removing acoustic actuator noise from the wall-pressure measurements in real time. It would therefore be worthwhile to develop this ability.

## **Real-Time Identification of Very-Large-Scale Motions Using Wall Pressure**

The relationship between wall pressure and the VLSMs was identified for the first time in Chapter 5. Unfortunately, the low associated coherence suggests that simple thresholding of a single wall-pressure signal is insufficient for identifying VLSMs in real time. It is recommended that this identification task be explored to determine the number of sensors and the types of algorithms that are necessary to successfully identify VLSMs using wall pressure alone.

## **Scaling and Prediction of the Motions Produced by Active Surface Deformations**

The normalizations of the advection velocity, wavelength, and strength of the motions produced by the active surface were formed using the results from two boundary layers. Further work should be done to validate or improve these normalizations using the results from a variety of boundary layers. This would enable the ability to predict how active surface deformations affect a variety of flows for the purpose of control system design.

## **Linear Modelling of Active Surface Deformations in a Variety of Boundary Layers**

The linear modelling efforts explored here should be extended to consider different boundary layers, active surfaces, frequency ranges, deformation amplitudes, etc., to determine the extent to which linear models can adequately capture the actuation dynamics. This should include the use of the eigensystem realization algorithm for identifying a state-space model.

## **Effect of Active Surface Deformation Geometry on Actuation**

The active surface deformation geometry considered here was made simple on purpose. However, different geometries may offer better performance in terms of the strength or dimensions of the motions produced by actuation. A study that considers the impact of deformation geometry on the motions that are produced by actuation is therefore recommended.

## **Proper Implementation of Feed-Forward Control with Active Surface Deformations**

Feed-forward control of the VLSMs using active surface deformations appears to have been thwarted by the inadequacy of the sensing system used here. It is recommended that the issues be resolved, either by using velocity sensors or by further developing the ability to use pressure sensors for flow control, so that proper feed-forward control of the VLSMs using active surface deformations can be explored.

# Bibliography

- M. R. Abbassi, W. J. Baars, N. Hutchins, and I. Marusic. Skin-friction drag reduction in a high-Reynolds-number turbulent boundary layer via real-time control of large-scale structures. *Int. J. Heat Fluid Flow*, 67:30–41, 2017.
- W. Abu Rowin, J. Hou, and S. Ghaemi. Turbulent channel flow over riblets with superhydrophobic coating. *Exp. Therm. Fluid Sci.*, 94:192–204, 2018.
- R. J. Adrian. Hairpin vortex organization in wall turbulence. *Phys. Fluids*, 041301, 2007.
- R. J. Adrian and Z. C. Liu. Observation of vortex packets in direct numerical simulation of fully turbulent channel flow. *J. Vis.*, 5(1):9–19, 2002.
- R. J. Adrian, C. D. Meinhart, and C. D. Tomkins. Vortex organization in the outer region of the turbulent boundary layer. *J. Fluid Mech.*, 422:1–54, 2000.
- B. K. Ahn, W. R. Graham, and S. A. Rizzi. A structure-based model for turbulent-boundary-layer wall pressures. *J. Fluid Mech.*, 650:443–478, 2010.
- M. Albers, P. S. Meysonnat, and W. Schröder. Actively reduced airfoil drag by transversal surface waves. *Flow Turbul. Combust.*, 102:865–886, 2019.
- M. Albers, P. S. Meysonnat, D. Fernex, R. Semaan, B. R. Noack, and W. Schröder. Drag reduction and energy saving by spanwise traveling transversal surface waves for flat plate flow. *Flow Turbul. Combust.*, 105:125–157, 2020.
- M. Amitay and S. Gildersleeve. Virtual and physical surface modifications as means of flow control. *AIAA J.*, 57(1):53–71, 2019.
- M. Amitay, B. A. Tuna, and H. Dell’Orso. Identification and mitigation of T-S waves using localized dynamic surface modification. *Phys. Fluids*, 28:064103, 2016.
- G. G. Arthur, B. J. McKeon, S. S. Dearing, J. F. Morrison, and Z. Cui. Manufacture of micro-sensors and actuators for flow control. *Microelectron. Eng.*, 83:1205–1208, 2006.
- F. Auteri, A. Baron, M. Belan, G. Campanardi, and M. Quadrio. Experimental assessment of drag reduction by traveling waves in a turbulent pipe flow. *Phys. Fluids*, 22:115103, 2010.
- H. L. Bai, Y. Zhou, W. G. Zhang, S. J. Xu, Y. Wang, and R. A. Antonia. Active control of a turbulent boundary layer based on local surface perturbation. *J. Fluid Mech.*, 750:316–364, 2014.
- B. J. Balakumar and R. J. Adrian. Large- and very-large-scale motions in channel and boundary-layer flows. *Phil. Trans. R. Soc. A*, 365:665–681, 2007.
- T. Barth, P. Scholz, and P. Wierach. Flow control by dynamic vane vortex generators based on piezoceramic actuators. *AIAA J.*, 49(5):921–931, 2011.
- S. J. Beresh, J. F. Henfling, and R. W. Spillers. Very-large-scale coherent structures in the wall pressure field beneath a supersonic turbulent boundary layer. *Phys. Fluids*, 25:095104, 2013.

- J. Bird, M. Santer, and J. F. Morrison. Experimental control of turbulent boundary layers with in-plane travelling waves. *Flow Turbul. Combust.*, 100:1015–1035, 2018.
- R. F. Blackwelder and H. Eckelmann. Streamwise vortices associated with the bursting phenomenon. *J. Fluid Mech.*, 94(3):577–594, 1979.
- K. S. Breuer, J. H. Haritonidis, and M. T. Landahl. The control of transient disturbances in a flat plate boundary layer through active wall motion. *Phys. Fluids A*, 1:574, 1989.
- P. P. C. Brito, P. Morra, A. V. G. Cavaliere, T. B. Araújo, D. S. Henningson, and A. Hanifi. Experimental control of Tollmien-Schlichting waves using pressure sensors and plasma actuators. *Exp. Fluids*, 62:32, 2021.
- S. L. Brunton and J. N. Kutz. *Data Driven Science and Engineering: Machine Learning, Dynamical Systems, and Control*. Cambridge University Press, 2019.
- S. L. Brunton and B. R. Noack. Closed-loop turbulence control: progress and challenges. *Appl. Mech. Rev.*, 67:050801, 2015.
- N. A. Buchmann, Y. C. Küçükosman, K. Ehrenfried, and C. J. Kähler. Wall pressure signature in compressible turbulent boundary layers. In: *Progress in Wall Turbulence 2*. ERCOFTAC Series 23, 2016.
- M. K. Bull. Wall-pressure fluctuations associated with subsonic turbulent boundary layer flow. *J. Fluid Mech.*, 28(4):719–754, 1967.
- M. K. Bull. Wall-pressure fluctuations beneath turbulent boundary layers: some reflections on forty years of research. *J. Sound Vib.*, 190(3):299–315, 1996.
- M. H. Buschmann, T. Indinger, and M. Gad-el Hak. Near-wall behaviour of turbulent wall-bounded flows. *Int. J. Heat Fluid Flow*, 30:993–1006, 2009.
- H. A. Carlson and J. L. Lumley. Active control in the turbulent wall layer of a minimal flow unit. *J. Fluid Mech.*, 329:341–371, 1996.
- L. N. Cattafesta and M. Sheplak. Actuators for active flow control. *Annu. Rev. Fluid Mech.*, 43:247–272, 2011.
- C. T. Chen. *Linear Systems Theory and Design*. Oxford University Press, 1999.
- H. Choi, P. Moin, and J. Kim. Active turbulence control for drag reduction in wall-bounded flows. *J. Fluid Mech.*, 262:75–110, 1994.
- K. S. Choi. Near-wall structure of turbulent boundary layer with spanwise-wall oscillation. *Phys. Fluids*, 14:2530, 2002.
- K. S. Choi and B. R. Clayton. The mechanism of turbulent drag reduction with wall oscillation. *Int. J. Heat Fluid Flow*, 22:1–9, 2001.
- D. Chung and B. J. McKeon. Large-eddy simulation of large-scale structures in long channel flow. *J. Fluid Mech.*, 661:341–364, 2010.
- D. Coles. The law of the wake in the turbulent boundary layer. *J. Fluid Mech.*, 1(2):191–226, 1956.
- G. M. Corcos. The structure of the turbulent pressure field in boundary-layer flows. *J. Fluid Mech.*, 18(3):353–378, 1964.
- E. R. Corino and R. S. Brodkey. A visual investigation of the wall region in turbulent flow. *J. Fluid Mech.*, 37(1):1–30, 1969.
- S. Dearing, S. Lambert, and J. Morrison. Flow control with active dimples. *Aeronaut. J.*, 111(1125):705–714, 2007.

- S. S. Dearing, J. F. Morrison, and L. Iannucci. Electro-active polymer (EAP) “dimple” actuators for flow control: design and characterization. *Sens. Actuators A*, 157:210–218, 2010.
- E. P. DeMauro, H. Dell’Orso, S. Zaremski, C. M. Leong, and M. Amitay. Control of laminar separation bubble on NACA 0009 airfoil using electroactive polymers. *AIAA J.*, 53(8):2270–2279, 2015.
- D. J. C. Dennis and T. B. Nickels. On the limitations of Taylor’s hypothesis in constructing long structures in a turbulent boundary layer. *J. Fluid Mech.*, 614:197–206, 2008.
- D. J. C. Dennis and T. B. Nickels. Experimental measurement of large-scale three-dimensional structures in a turbulent boundary layer. Part 1. Vortex packets. *J. Fluid Mech.*, 673:180–217, 2011a.
- D. J. C. Dennis and T. B. Nickels. Experimental measurement of large-scale three-dimensional structures in a turbulent boundary layer. Part 1. Long structures. *J. Fluid Mech.*, 673:218–244, 2011b.
- G. M. Di Cicca, G. Iuso, P. G. Spazzini, and M. Onorato. Particle image velocimetry investigation of a turbulent boundary layer manipulated by spanwise wall oscillations. *J. Fluid Mech.*, 467:41–56, 2002.
- S. Duvvuri and B. McKeon. Phase relations in a force turbulent boundary layer: implications for modelling of high Reynolds number wall turbulence. *Phil. Trans. R. Soc. A*, 375:20160080, 2017.
- G. E. Elsinga and J. Westerweel. Tomographic-PIV measurement of the flow around a zigzag boundary layer trip. *Exp. Fluids*, 61:28, 2012.
- G. E. Elsinga, R. J. Adrian, B. W. van Oudheusden, and F. Scarano. Three-dimensional vortex organization in a high-Reynolds-number supersonic turbulent boundary layer. *J. Fluid Mech.*, 644:35–60, 2010.
- T. Endo, N. Kasagi, and Y. Suzuki. Feedback control of wall turbulence with wall deformation. *Int. J. Heat Fluid Flow*, 21:568–575, 2000.
- T. M. Farabee and M. J. Casarella. Spectral features of wall pressure fluctuations beneath turbulent boundary layers. *Phys. Fluids A*, 3:2410, 1991.
- D. Fernex, R. Semaan, M. Albers, P. S. Meysonnat, W. Schröder, and B. R. Noack. Actuation response model from sparse data for wall turbulence drag reduction. *Phys. Rev. Fluids*, 5:073901, 2020.
- M. Gad-el-Hak. *Flow Control: Passive, Active, and Reactive Flow Management*. Cambridge University Press, 2000.
- M. Gad-el-Hak, A. Pollard, and J. Bonnet. *Flow Control: Fundamentals and Practices*. Springer Verlag, 1998.
- B. Ganapathisubramani, E. K. Longmire, and I. Marusic. Characteristics of vortex packets in turbulent boundary layers. *J. Fluid Mech.*, 478:35–46, 2003.
- B. Ganapathisubramani, E. K. Longmire, and I. Marusic. Experimental investigation of vortex properties in a turbulent boundary layer. *Phys. Fluids*, 18:055105, 2006.
- B. Ganapathisubramani, N. Hutchins, J. P. Monty, D. Chung, and I. Marusic. Amplitude and frequency modulation in wall turbulence. *J. Fluid Mech.*, 712:61–91, 2012.
- M. G. C. Garland, M. S. Santer, and J. F. Morrison. Control of cellular separation using adaptive surfaces. *J. Fluids Struct.*, 91:102609, 2019.
- M. W. Ge, L. Fang, and Y. Q. Liu. Drag reduction of wall bounded incompressible turbulent flow based on active dimples/pimples. *J. Hydrodyn.*, 29(2):261–271, 2017.

- S. Ghaemi and F. Scarano. Counter-hairpin vortices in the turbulent wake of a sharp trailing edge. *J. Fluid Mech.*, 689:317–356, 2011.
- S. Ghaemi and F. Scarano. Turbulent structure of high-amplitude pressure peaks within the turbulent boundary layer. *J. Fluid Mech.*, 735:381–426, 2013.
- B. Gibeau. Analysis and control of vortex shedding from a blunt trailing edge. Master’s thesis, *University of Alberta Libraries*, 2018.
- B. Gibeau and S. Ghaemi. A modular, 3D-printed helium-filled soap bubble generator for large-scale volumetric flow measurements. *Exp. Fluids*, 59:1–11, 2018.
- B. Gibeau and S. Ghaemi. The mode B structure of streamwise vortices in the wake of a two-dimensional blunt trailing edge. *J. Fluid Mech.*, 884:A12, 2020.
- B. Gibeau and S. Ghaemi. Low- and mid-frequency wall-pressure sources in a turbulent boundary layer. *J. Fluid Mech.*, 918:A18, 2021.
- B. Gibeau and S. Ghaemi. Laminar boundary layer forcing with active surface deformations. *Phys. Rev. Fluids*, 7:114101, 2022.
- B. Gibeau, C. R. Koch, and S. Ghaemi. Active control of vortex shedding from a blunt trailing edge using oscillating piezoelectric flaps. *Phys. Rev. Fluids*, 4:054704, 2019.
- B. Gibeau, D. Gingras, and S. Ghaemi. Evaluation of a full-scale helium-filled soap bubble generator. *Exp. Fluids*, 61:28, 2020.
- S. Gildersleeve, B. A. Tuna, and M. Amitay. Interactions of a low-aspect-ratio cantilevered dynamic pin with a boundary layer. *AIAA J.*, 55(7):2142–2157, 2017.
- M. Goldhammer. The next decade in commercial aircraft aerodynamics: a Boeing perspective. In *The KATnet II Conference: Key Aerodynamic Technologies*, Bremen, Germany, 2009.
- N. Goldin, R. King, A. Pätzold, W. Nitsche, D. Haller, and P. Woias. Laminar flow control with distributed surface actuation: damping Tollmien-Schlichting waves with active surface displacement. *Exp. Fluids*, 54:1478, 2013.
- M. Goody. Empirical spectral model of surface pressure fluctuations. *AIAA J.*, 42(9):1788–1794, 2004.
- K. Gouder, M. Potter, and J. F. Morrison. Turbulent friction drag reduction using electroactive polymer and electromagnetically driven surfaces. *Exp. Fluids*, 54:1441, 2013.
- S. P. Gravante, A. M. Naguib, C. E. Wark, and H. M. Nagib. Characterization of the pressure fluctuations under a fully developed turbulent boundary layer. *AIAA J.*, 36(10):1808–1816, 1998.
- J. Hamelin and A. E. Alving. A low-shear turbulent boundary layer. *Phys. Fluids*, 8:789, 1996.
- R. E. Hanson, H. P. Buckley, and P. Lavoie. Aerodynamic optimization of the flat-plate leading edge for experimental studies of laminar and transitional boundary layers. *Exp. Fluids*, 53:863–871, 2012.
- M. H. Hayes. *Statistical Digital Signal Processing and Modeling*. John Wiley & Sons, 1996.
- M. R. Head and P. Bandyopadhyay. New aspects of turbulent boundary-layer structure. *J. Fluid Mech.*, 107:297–338, 1981.
- L. M. Hofmann and T. Herbert. Disturbances produced by motion of an actuator. *Phys. Fluids*, 9:3727, 1997.
- W. W. Huebsch. Two-dimensional simulation of dynamic surface roughness for aerodynamic flow control. *J. Aircraft*, 43(2):353–362, 2006.

- W. W. Huebsch, P. D. Gall, S. D. Hamburg, and A. P. Rothmayer. Dynamic roughness as a means of leading-edge separation flow control. *J. Aircraft*, 49(1):108–115, 2012.
- A. K. M. F. Hussain and W. C. Reynolds. The mechanics of an organized wave in turbulent shear flow. *J. Fluid Mech.*, 41:241–258, 1970.
- N. Hutchins and I. Marusic. Evidence of very long meandering features in the logarithmic region of turbulent boundary layers. *J. Fluid Mech.*, 579:1–28, 2007a.
- N. Hutchins and I. Marusic. Large-scale influences in near-wall turbulence. *Phil. Trans. R. Soc. A*, 365:647–664, 2007b.
- N. Hutchins, J. P. Monty, B. Ganapathisubramani, H. C. H. Ng, and I. Marusic. Three-dimensional conditional structure of a high-Reynolds-number turbulent boundary layer. *J. Fluid Mech.*, 673:155–285, 2011.
- N. Hutchins, K. Chauhan, I. Marusic, J. Monty, and J. Klewicki. Towards reconciling the large-scale structure of turbulent boundary layers in the atmosphere and laboratory. *Boundary-Layer Meteorol.*, 145:273–306, 2012.
- D. Huynh and B. McKeon. Characterization of the spatio-temporal response of a turbulent boundary layer to dynamic roughness. *Flow Turbul. Combust.*, 104:293–316, 2020a.
- D. Huynh and B. McKeon. Measurements of a turbulent boundary layer-compliant surface system in response to targeted, dynamic roughness forcing. *Exp. Fluids*, 61:94, 2020b.
- D. P. Huynh, Y. Huang, and B. J. McKeon. Experiments and modeling of a compliant wall response to a turbulent boundary layer with dynamic roughness forcing. *Fluids*, 6:173, 2021.
- J. Hwang and H. J. Sung. Influence of large-scale motions on the frictional drag in a turbulent boundary layer. *J. Fluid Mech.*, 829:751–779, 2017.
- Y. F. Hwang, W. K. Bonness, and S. A. Hambric. Comparison of semi-empirical models for turbulent boundary layer wall pressure spectra. *J. Sound Vib.*, 319:199–217, 2009.
- M. Itoh, S. Tamano, K. Yokota, and S. Taniguchi. Drag reduction in a turbulent boundary layer on a flexible sheet undergoing a spanwise traveling wave motion. *J. Turb.*, 7:N27, 2006.
- G. Iuso, G. M. Di Cicca, M. Onorato, P. G. Spazzini, and M. R. Velocity streak structure modifications induced by flow manipulation. *Phys. Fluids*, 15:2602, 2003.
- I. Jacobi and B. J. McKeon. Dynamic roughness perturbations of a turbulent boundary layer. *J. Fluid Mech.*, 688:258–296, 2011.
- I. Jacobi and B. J. McKeon. Phase-relationships between scales in the perturbed turbulent boundary layer. *J. Turb.*, 18(12):1120–1143, 2017.
- S. A. Jacobson and W. C. Reynolds. Active control of streamwise vortices and streaks in boundary layers. *J. Fluid Mech.*, 360:179–211, 1998.
- W. P. Jeon and R. F. Blackwelder. Perturbations in the wall region using flush mounted piezoceramic actuators. *Exp. Fluids*, 28:485–496, 2000.
- J. Jeong and F. Hussain. On the identification of a vortex. *J. Fluid Mech.*, 285:69–94, 1995.
- A. V. Johansson, J. Y. Her, and J. H. Haritonidis. On the generation of high-amplitude wall-pressure peaks in turbulent boundary layers and spots. *J. Fluid Mech.*, 175:119–142, 1987.
- M. R. Johnson and L. W. Kostiuk. Efficiencies of low-momentum jet diffusion flames in crosswinds. *Combust. Flame*, 123:189–200, 2000.
- G. Jones, M. Santer, M. Debiasi, and G. Papadakis. Control of flow separation around an airfoil at low Reynolds numbers using periodic surface morphing. *J. Fluids Struct.*, 76:536–557, 2018.

- G. Joubert, A. Le Pape, B. Heine, and S. Huberson. Vortical interactions behind deployable vortex generator for airfoil static stall control. *AIAA. J.*, 51(1):240–252, 2013.
- T. I. Józsa, E. Balarus, M. Kashtalyan, A. G. L. Borthwick, and I. M. Viola. Active and passive in-plane wall fluctuations in turbulent channel flows. *J. Fluid Mech.*, 866:689–720, 2019.
- T. I. Józsa, E. Balarus, M. Kashtalyan, A. G. L. Borthwick, and I. M. Viola. On the friction drag reduction mechanism of streamwise wall fluctuations. *Int. J. Heat Fluid Flow*, 86:108686, 2020.
- F. Juillet, B. J. McKeon, and P. J. Schmid. Experimental control of natural perturbations in channel flow. *J. Fluid Mech.*, 752:296–309, 2014.
- S. Kang and S. Choi. Active wall motions for skin-friction drag reduction. *Phys. Fluids*, 12:3301, 2000.
- C. C. Karangelen, V. Wilczynski, and M. J. Casarella. Large amplitude wall pressure events beneath a turbulent boundary layer. *J. Fluids Eng.*, 115(4):653–659, 1993.
- W. L. Keith, D. A. Hurdis, and B. M. Abraham. A comparison of turbulent boundary layer wall-pressure spectra. *J. Fluids Eng.*, 114(3):338–347, 1992.
- K. U. Kempaiah, F. Scarano, G. E. Elsinga, B. W. van Oudheusden, and L. Bermel. 3-dimensional particle image velocimetry based evaluation of turbulent skin-friction reduction by spanwise wall oscillation. *Phys. Fluids*, 32:085111, 2020.
- K. Kevin, J. Monty, and N. Hutchins. The meandering behaviour of large-scale structures in turbulent boundary layers. *J. Fluid Mech.*, 865:R1, 2019.
- R. O. Kiesow and M. W. Plesniak. Near-wall physics of a shear-driven three-dimensional turbulent boundary layer with varying crossflow. *J. Fluid Mech.*, 484:1–39, 2003.
- C. Kim, W. P. Jeon, J. Park, and H. Choi. Effect of a localized time-periodic wall motion on a turbulent boundary layer flow. *Phys. Fluids*, 15:265, 2003.
- D. H. Kim, J. W. Chang, and J. S. Cho. Flow disturbances depending on excitation frequency on a flat plate by a piezoceramic actuator. *J. Vis.*, 16:111–121, 2013.
- J. Kim. On the structure of wall-bounded turbulent flows. *Phys. Fluids*, 26:2088, 1983.
- J. Kim, J. I. Choi, and H. J. Sung. Relationship between wall pressure fluctuations and streamwise vortices in a turbulent boundary layer. *Phys. Fluids*, 14:898, 2002.
- K. C. Kim and R. J. Adrian. Very large-scale motion in the outer layer. *Phys. Fluids*, 11(2):417, 1999.
- J. C. Klewicki and R. B. Hill. Laminar boundary layer response to rotation of a finite diameter surface patch. *Phys. Fluids*, 15:101, 2003.
- J. C. Klewicki, P. J. A. Priyadarshana, and M. M. Metzger. Statistical structure of the fluctuating wall pressure and its in-plane gradients at high Reynolds number. *J. Fluid Mech.*, 609:195–220, 2008.
- S. Klumpp, M. Meinke, and W. Schröder. Drag reduction by spanwise transversal surface waves. *J. Turb.*, 11:N22, 2010.
- S. Klumpp, M. Meinke, and W. Schröder. Friction drag variation via spanwise transversal surface waves. *Flow Turbul. Combust.*, 87:33–53, 2011.
- Y. Kobashi and M. Ichijo. Wall pressure and its relation to turbulent structure of a boundary layer. *Exp. Fluids*, 4:49–55, 1986.
- S. R. Koh, P. Meysonnat, M. Meinke, and W. Schröder. Drag reduction via spanwise transversal surface waves at high Reynolds numbers. *Flow Turbul. Combust.*, 95:169–190, 2015.

- G. J. Kunkel and I. Marusic. Study of the near-wall-turbulent region of the high-Reynolds-number boundary layer using an atmospheric flow. *J. Fluid Mech.*, 548:375–402, 2006.
- F. Laadhari, L. Skandaji, and R. Morel. Turbulence reduction in a boundary layer by a local spanwise oscillating surface. *Phys. Fluids*, 6:3218, 1994.
- A. Le Pape, M. Costes, F. Richez, G. Joubert, F. David, and J. M. Deluc. Dynamic stall control using deployable leading-edge vortex generators. *AIAA J.*, 50(10):2135–2145, 2012.
- J. Lee, J. H. Lee, J. I. Choi, and H. J. Sung. Spatial organization of large- and very-large-scale motions in a turbulent channel flow. *J. Fluid Mech.*, 749:818–840, 2014.
- J. H. Lee and H. J. Sung. Very-large-scale motions in a turbulent boundary layer. *J. Fluid Mech.*, 673:80–120, 2011.
- M. A. Leschziner, H. Choi, and K. S. Choi. Flow-control approaches to drag reduction in aerodynamics: progress and prospects. *Phil. Trans. R. Soc. A*, 369:1349–1351, 2011.
- W. Li, D. Roggenkamp, V. Paakkari, M. Klaas, J. Soria, and W. Schröder. Analysis of a drag reduced flat plate turbulent boundary layer via uniform momentum zones. *Aerosp. Sci. Technol.*, 96:105552, 2020.
- J. Lin, J. P. Laval, and J. M. Foucaut. Quantitative characterization of coherent structures in the buffer layer of near-wall turbulence. Part 1: streaks. *Exp. Fluids*, 45:999–1013, 2008.
- R. M. Lueptow. Transducer resolution and the turbulent wall pressure spectrum. *J. Acoust. Soc. Am.*, 97:370–378, 1995.
- M. Luhar, A. S. Sharma, and B. J. McKeon. A framework for studying the effect of compliant surfaces on wall turbulence. *J. Fluid Mech.*, 768:415–441, 2015.
- K. M. Lynch and F. C. Park. *Modern Robotics: Mechanics, Planning, and Control*. Cambridge University Press, 2017.
- A. Ma, B. Gibeau, and S. Ghaemi. Time-resolved topology of turbulent boundary layer separation over the trailing edge of an airfoil. *J. Fluid Mech.*, 891:A1, 2020.
- I. Marusic. On the role of large-scale structures in wall turbulence. *Phys. Fluids*, 13(3):735–743, 2001.
- I. Marusic and N. Hutchins. Study of the log-layer structure in wall turbulence over a very large range of Reynolds number. *Flow Turbul. Combust.*, 81:115–130, 2008.
- I. Marusic, D. Chandran, A. Rouhi, M. K. Fu, D. Wine, B. Holloway, D. Chung, and A. J. Smits. An energy-efficient pathway to turbulent drag reduction. *Nat. Commun.*, 12:5805, 2021.
- S. A. Maslowe. Critical layers in shear flows. *Annu. Rev. Fluid Mech.*, 18:405–432, 1986.
- R. Mathis, N. Hutchins, and I. Marusic. Large-scale amplitude modulation of the small-scale structures in turbulent boundary layers. *J. Fluid Mech.*, 628:311–337, 2009.
- B. E. McGrath and R. L. Simpson. Some features of surface pressure fluctuations in turbulent boundary layers with zero and favorable pressure gradients. NASA Contractor Report 4051, 1987.
- B. J. McKeon, I. Jacobi, and S. Duvvuri. Dynamic roughness for manipulation and control of turbulent boundary layers: an overview. *AIAA J.*, 56(6):2178–2193, 2018.
- E. Menu and S. Tavoularis. Boundary layer on a moving wall. *AIAA J.*, 45(1):313–316, 2007.
- P. S. Meysonnat, D. Roggenkamp, W. Li, B. Roidl, and W. Schröder. Experimental and numerical investigation of transversal traveling surface waves for drag reduction. *Eur. J. Mech. B Fluids*, 55:313–323, 2016.

- Y. Mito and N. Kasagi. DNS study of turbulence modification with streamwise-uniform sinusoidal wall-oscillation. *Int. J. Heat Fluid Flow*, 19:470–481, 1998.
- D. Munday and J. Jacob. Active control of separation on a wing with oscillating camber. *J. Aircraft*, 39(1):187–189, 2002.
- Y. Naka. Simultaneous measurement of fluctuating velocity and pressure in turbulent free shear flows. Doctoral thesis, *Keio University Libraries*, 2009.
- Y. Naka, M. Stanislas, J. M. Foucaut, S. Coudert, J. P. Laval, and S. Obi. Space-time pressure-velocity correlations in a turbulent boundary layer. *J. Fluid Mech.*, 771:624–675, 2015.
- S. F. Oehler and S. J. Illingworth. Linear control of coherent structures in wall-bounded turbulence at  $Re_\tau = 2000$ . *Int. J. Heat Fluid Flow*, 87:108735, 2021.
- R. F. Osborn, S. Kota, J. A. Hetrick, D. E. Geister, C. P. Tilmann, and J. Joo. Active flow control using high-frequency compliant structures. *J. Aircraft*, 41(3):603–609, 2004.
- D. Palumbo. Determining correlation and coherence lengths in turbulent boundary layer flight data. *J. Sound Vib.*, 331:3721–3737, 2012.
- M. Pamiès, E. Garnier, A. Merlen, and P. Sagaut. Opposition control with arrayed actuators in the near-wall region of a spatially developing turbulent boundary layer. *Int. J. Heat Fluid Flow*, 32:621–630, 2011.
- C. Pan and Y. Kwon. Extremely high wall-shear stress events in a turbulent boundary layer. *J. Phys.: Conf. Ser.*, 1001:012004, 2018.
- R. L. Panton and J. H. Linebarger. Wall pressure spectra calculations for equilibrium boundary layers. *J. Fluid Mech.*, 65(2):261–287, 1974.
- R. L. Panton, A. L. Goldman, R. L. Lowery, and M. M. Reischman. Low-frequency pressure fluctuations in axisymmetric turbulent boundary layers. *J. Fluid Mech.*, 97(2):299–319, 1980.
- A. Perry, I. Marusic, and M. Jones. On the streamwise evolution of turbulent boundary layers in arbitrary pressure gradients. *J. Fluid Mech.*, 461:61–91, 2002.
- S. Pirozzoli and M. Bernardini. Turbulence in supersonic boundary layers at moderate Reynolds number. *J. Fluid Mech.*, 688:120–168, 2011.
- S. B. Pope. *Turbulent Flows*. Cambridge University Press, 2000.
- A. K. Prasad and K. Jensen. Scheimpflug stereocamera for particle image velocimetry in liquid flows. *Appl. Optics*, 34:7092–7099, 1995.
- Z. X. Qiao, Y. Zhou, and Z. Wu. Turbulent boundary layer under the control of different schemes. *Proc. R. Soc. A*, 473:20170038, 2017.
- Z. X. Qiao, Z. Wu, and Y. Zhou. Turbulent boundary layer manipulation under a proportional-derivative closed-loop scheme. *Phys. Fluids*, 30:115101, 2018.
- M. Raffel, C. E. Willert, F. Scarano, C. Kähler, S. T. Wereley, and J. Kompenhans. *Particle Image Velocimetry: A Practical Guide*. Springer Berlin, 2018.
- D. Ragni, F. Schrijer, B. W. van Oudheusden, and F. Scarano. Particle tracer response across shocks measured by PIV. *Exp. Fluids*, 50:53–64, 2011.
- R. Rathnasingham and K. S. Breuer. Active control of turbulent boundary layers. *J. Fluid Mech.*, 495:209–233, 2003.
- P. Ricco. Modification of near-wall turbulence due to spanwise wall oscillations. *J. Turb.*, 5:N24, 2004.

- P. Ricco and S. Hahn. Turbulent drag reduction through rotating discs. *J. Fluid Mech.*, 722: 267–290, 2013.
- P. Ricco, M. Skote, and M. A. Leschziner. A review of turbulent skin-friction drag reduction by near-wall transverse forcing. *Prog. Aerosp. Sci.*, 123:100713, 2021.
- S. K. Robinson. Coherent motions in the turbulent boundary layer. *Annu. Rev. Fluid Mech.*, 23: 601–639, 1991.
- D. Roggenkamp, W. Jessen, W. Li, M. Klaas, and W. Schröder. Experimental investigation of turbulent boundary layers over transversal moving surfaces. *CEAS Aeronaut. J.*, 6:471–484, 2015.
- D. Roggenkamp, W. Li, M. Klaas, and W. Schröder. Influence of spanwise transversal surface wave on coherent structures in turbulent boundary layers. *Aerosp. Sci. Technol.*, 86:387–400, 2019.
- F. Scarano, S. Ghaemi, G. C. A. Caridi, J. Bosbach, U. Dierksheide, and A. Sciacchitano. On the use of helium-filled soap bubbles for large-scale tomographic piv in wind tunnel experiments. *Exp. Fluids*, 56:42, 2015.
- G. Schewe. On the structure and resolution of wall-pressure fluctuations associated with turbulent boundary-layer flow. *J. Fluid Mech.*, 134:311–328, 1983.
- H. Schlichting and K. Gersten. *Boundary-Layer Theory*. Springer Berlin, Heidelberg, 2017.
- P. J. Schmid and D. S. Henningson. *Stability and Transition in Shear Flows*. Springer-Verlag New York, 2001.
- A. Sciacchitano. Uncertainty quantification in particle image velocimetry. *Meas. Sci. Technol.*, 30: 092001, 2019.
- A. Sciacchitano and B. Wieneke. PIV uncertainty propagation. *Meas. Sci. Technol.*, 27:084006, 2016.
- T. Segawa, Y. Kawaguchi, Y. Kikushima, , and H. Yoshida. Active control of streak structures in wall turbulence using an actuator array producing inclined wavy disturbances. *J. Turb.*, 3:N15, 2002.
- A. Seshagiri, E. Cooper, and L. W. Traub. Effects of vortex generators on an airfoil at low Reynolds numbers. *J. Aircraft*, 46(1):116–122, 2009.
- R. Shaw. The influence of hole dimensions on static pressure measurements. *J. Fluid Mech.*, 7: 550–564, 1960.
- L. Sirovich. Turbulence and the dynamics of coherent structures, parts I-III. *Q. Appl. Math.*, 45: 561–590, 1987.
- C. R. Smith and S. P. Metzler. The characteristics of low-speed streaks in the near-wall region of a turbulent boundary layer. *J. Fluid Mech.*, 129:27–54, 1983.
- A. J. Smits, B. J. McKeon, and I. Marusic. High-Reynolds number wall turbulence. *Annu. Rev. Fluid Mech.*, 43:353–375, 2011.
- S. Tamano and M. Itoh. Drag reduction in turbulent boundary layers by spanwise traveling waves with wall deformation. *J. Turb.*, 13:N9, 2012.
- Z. Tang and N. Jiang. The effect of a synthetic input on small-scale intermittent bursting events in near-wall turbulence. *Phys. Fluids*, 32:015110, 2020.
- Z. Tang, N. Jiang, X. Zheng, and Y. Wu. Local dynamic perturbation effects on amplitude modulation in turbulent boundary layer flow based on triple decomposition. *Phys. Fluids*, 31:025120, 2019.

- Z. Tang, Z. Fan, X. Ma, N. Jiang, B. Wang, Y. Huang, Q. X., Q. Zhou, Z. Lu, and Y. Liu. Tomographic particle image velocimetry flow structures downstream of a dynamic cylindrical element in a turbulent boundary layer by multi-scale proper orthogonal decomposition. *Phys. Fluids*, 32:125109, 2020.
- Z. Tang, X. Ma, N. Jiang, X. Cui, and X. Zheng. Local dynamic perturbation effects on the scale interactions in wall turbulence. *J. Turb.*, 22(3):208–230, 2021.
- C. Thill, J. Etches, I. Bond, K. Potter, and P. Weaver. Morphing skins. *Aeronaut. J.*, 112(1129):117–139, 2008.
- A. S. W. Thomas and M. K. Bull. On the role of wall-pressure fluctuations in deterministic motions in the turbulent boundary layer. *J. Fluid Mech.*, 128:283–322, 1983.
- C. D. Tomkins and R. J. Adrian. Spanwise structure and scale growth in turbulent boundary layers. *J. Fluid Mech.*, 490:37–74, 2003.
- C. Tropea, A. L. Yarin, and J. Foss. *Handbook of Experimental Fluid Mechanics*. Springer Berlin, 2007.
- Y. Tsuji, J. H. M. Fransson, P. H. Alfredsson, and A. V. Johansson. Pressure statistics and their scaling in high-Reynolds-number turbulent boundary layers. *J. Fluid Mech.*, 585:1–40, 2007.
- Y. Tsuji, S. Imayama, P. Schlatter, P. H. Alfredsson, A. V. Johansson, I. Marusic, N. Hutchins, and J. Monty. Pressure fluctuations in high-Reynolds-number turbulent boundary layer: results from experiments and DNS. *J. Turb.*, 13(50):1–19, 2012.
- J. Van Blitterswyk and J. Rocha. An experimental study of the wall-pressure fluctuations beneath low Reynolds number turbulent boundary layers. *J. Acoust. Soc. Am.*, 141:1257, 2017.
- J. M. Wallace, H. Eckelmann, and R. S. Brodkey. The wall region in turbulent shear flow. *J. Fluid Mech.*, 54(1):39–48, 1972.
- L. Warwaruk and S. Ghaemi. A direct comparison of turbulence in drag-reduced flows of polymers and surfactants. *J. Fluid Mech.*, 917:A7, 2021.
- J. Westerweel and F. Scarano. Universal outlier detection for PIV data. *Exp. Fluids*, 39(6):1096–110, 2005.
- B. Wieneke. Stereo-PIV using self-calibration on particle images. *Exp. Fluids*, 39(2):267–280, 2005.
- W. W. Willmarth. Pressure fluctuations beneath turbulent boundary layers. *Annu. Rev. Fluid Mech.*, 7:13–36, 1975.
- W. W. Willmarth and C. E. Wooldridge. Measurements of the fluctuating pressure at the wall beneath a thick turbulent boundary layer. *J. Fluid Mech.*, 14(2):187–210, 1962.
- D. J. Wise and P. Ricco. Turbulent drag reduction through oscillating discs. *J. Fluid Mech.*, 746:536–564, 2014.
- D. J. Wise, C. Alvarenga, and P. Ricco. Spinning out of control: wall turbulence over rotating discs. *Phys. Fluids*, 26:125107, 2014.
- W. Y. Zhang, W. X. Huang, C. X. Xu, and G. X. Cui. Suboptimal control of wall turbulence with arrayed dimple actuators for drag reduction. *J. Turb.*, 17(4):379–399, 2016.
- J. Zhou, R. J. Adrian, and S. Balachandar. Autogeneration of near-wall vortical structures in channel flow. *Phys. Fluids*, 8:288, 1996.
- J. Zhou, R. J. Adrian, S. Balachandar, and T. M. Kendall. Mechanisms for generating coherent packets of hairpin vortices in channel flow. *J. Fluid Mech.*, 387:353–396, 1999.

# Appendices

## A Uncertainty Analysis

The uncertainties associated with quantities presented throughout this thesis are estimated in this appendix. These quantities include instantaneous measurements, means, standard deviations, variances, and covariances. Attempts to estimate the uncertainty of measures that are more complicated, for example spectra or quantities extracted through the application of a tunable algorithm, are not included. This is because these uncertainty estimations would require so much assumption and error propagation that the results would be rendered essentially meaningless.

### Approach

The total uncertainty of a quantity ( $\mathcal{E}$ ) is estimated by considering the percent bias uncertainty ( $\epsilon$ ), random error ( $E_r$ ), and convergence uncertainty ( $E_c$ ) resulting from computing statistics using a finite number of samples. The former two propagate through the statistics to produce the propagation uncertainty ( $E_p$ ). The latter is estimated using the methods outlined by Sciacchitano and Wieneke (2016), which take into account the effective number of independent samples which is defined as

$$N_{\text{eff}} = \frac{N}{\sum_{n=-\infty}^{\infty} r(n\Delta t)}, \quad (\text{A.1})$$

where  $N$  is the total number of samples collected and  $r(n\Delta t)$  is the autocorrelation function of the measurements normalized such that  $r(0) = 1$ . When the measurements are uncorrelated, the denominator of Equation (A.1) is 1 and so  $N_{\text{eff}} = N$ . Otherwise, the correlation between measurements reduces  $N_{\text{eff}}$ . Note that the denominator of Equation (A.1) is only evaluated between the first crossing of zero on either side of  $r(0) = 1$ , and  $N_{\text{eff}}$  is only used when computing the statistics of one variable (mean, standard deviation, and variance).

Consider as an example a set of measurements of the streamwise velocity  $U$ . Any given instantaneous measurement will have the form

$$\hat{U} = U(1 + \epsilon) + E_r, \quad (\text{A.2})$$

where the hat notation indicates that the measurement  $\hat{U}$  is an estimate of the true value  $U$ . The total uncertainty of this instantaneous measurement is found by subtracting  $U$  from  $\hat{U}$  while considering the absolute value of the measurement:

$$\mathcal{E}_{\hat{U}} = \epsilon|U| + E_r \approx \epsilon|\hat{U}| + E_r. \quad (\text{A.3})$$

The random errors have zero mean by definition, and so taking the mean of Equation A.2 yields

$$\langle \hat{U} \rangle = \langle U \rangle (1 + \epsilon). \quad (\text{A.4})$$

The uncertainty propagated through the mean is then

$$E_{p, \langle \hat{U} \rangle} = \epsilon |\langle U \rangle| \approx \epsilon |\langle \hat{U} \rangle|. \quad (\text{A.5})$$

The convergence uncertainty of the mean is (Sciacchitano and Wieneke, 2016)

$$E_{c, \langle \hat{U} \rangle} = \frac{\sigma_{\hat{U}}}{\sqrt{N_{\text{eff}}}}, \quad (\text{A.6})$$

where  $\sigma_{\hat{U}}$  is the standard deviation of the measurement ensemble. The estimated total uncertainty of the mean is the sum of the propagated and convergence uncertainties:

$$\mathcal{E}_{\langle \hat{U} \rangle} = \epsilon |\langle \hat{U} \rangle| + \frac{\sigma_{\hat{U}}}{\sqrt{N_{\text{eff}}}}. \quad (\text{A.7})$$

Now consider the fluctuating component of the same set of streamwise velocity measurements:

$$\hat{u} = u(1 + \epsilon) + E_r, \quad (\text{A.8})$$

where the error associated with subtracting the estimated mean value is neglected for simplicity. Assuming that the measurements and random error are uncorrelated, taking the variance of  $\hat{u}$  yields

$$\langle \hat{u}^2 \rangle = \langle u^2 \rangle (1 + 2\epsilon + \epsilon^2) + E_r^2. \quad (\text{A.9})$$

The uncertainty propagated through the variance is then

$$E_{p, \langle \hat{u}^2 \rangle} = (2\epsilon + \epsilon^2) \langle u^2 \rangle + E_r^2 \approx (2\epsilon + \epsilon^2) \langle \hat{u}^2 \rangle + E_r^2. \quad (\text{A.10})$$

The convergence uncertainty of the variance is (Sciacchitano and Wieneke, 2016)

$$E_{c, \langle \hat{u}^2 \rangle} = \langle \hat{u}^2 \rangle \sqrt{\frac{2}{N_{\text{eff}}}}, \quad (\text{A.11})$$

and so the estimated total uncertainty of the variance is

$$\mathcal{E}_{\langle \hat{u}^2 \rangle} = \left( \sqrt{\frac{2}{N_{\text{eff}}}} + 2\epsilon + \epsilon^2 \right) \langle \hat{u}^2 \rangle + E_r^2. \quad (\text{A.12})$$

Given the relationship between the variance and standard deviation, the square root of Equation (A.9) can be taken to obtain the standard deviation of  $\hat{u}$  in terms of  $\epsilon$  and  $E_r$ :

$$\sigma_{\hat{u}} = \sigma_u \sqrt{(1 + \epsilon)^2 + \epsilon'}, \quad (\text{A.13})$$

where  $\epsilon' = E_r^2 / \langle u^2 \rangle \approx E_r^2 / \langle \hat{u}^2 \rangle$ . The propagated uncertainty is then the difference between  $\sigma_{\hat{u}}$  and  $\sigma_u$ :

$$E_{p, \sigma_{\hat{u}}} = \sigma_u \sqrt{(1 + \epsilon)^2 + \epsilon'} - \sigma_u \approx \sigma_{\hat{u}} (\sqrt{(1 + \epsilon)^2 + \epsilon'} - 1). \quad (\text{A.14})$$

The convergence uncertainty of the standard deviation is (Sciacchitano and Wieneke, 2016)

$$E_{c, \sigma_{\hat{u}}} = \frac{\sigma_{\hat{u}}}{\sqrt{2(N_{\text{eff}} - 1)}}, \quad (\text{A.15})$$

and so the estimated total uncertainty of the standard deviation is

$$\mathcal{E}_{\sigma_{\hat{u}}} = \sigma_{\hat{u}} \left( \frac{1}{\sqrt{2(N_{\text{eff}} - 1)}} + \sqrt{(1 + \epsilon)^2 + \epsilon'} - 1 \right). \quad (\text{A.16})$$

Finally, the uncertainty of a covariance can be estimated by considering a second measurement, for example the fluctuating pressure:

$$\hat{p} = p(1 + \epsilon_2) + E_{r,2}, \quad (\text{A.17})$$

where  $\epsilon_2$  and  $E_{r,2}$  are the bias uncertainty and random error, respectively, of  $\hat{p}$ . Assuming that the random errors are uncorrelated with one another and with the measurements, the covariance between  $\hat{p}$  and  $\hat{u}$  can be taken to yield

$$\langle \hat{p}\hat{u} \rangle = \langle pu \rangle (1 + \epsilon + \epsilon_2 + \epsilon\epsilon_2). \quad (\text{A.18})$$

The uncertainty propagated through the covariance is then

$$E_{p, \langle \hat{p}\hat{u} \rangle} = |\langle pu \rangle| (\epsilon + \epsilon_2 + \epsilon\epsilon_2) \approx |\langle \hat{p}\hat{u} \rangle| (\epsilon + \epsilon_2 + \epsilon\epsilon_2). \quad (\text{A.19})$$

The convergence uncertainty of the covariance is (Sciacchitano and Wieneke, 2016)

$$E_{c,(\hat{p}\hat{u})} = \sigma_{\hat{p}}\sigma_{\hat{u}}\sqrt{\frac{1+r_{\hat{p}\hat{u}}^2}{N-1}}, \quad (\text{A.20})$$

where  $r_{\hat{p}\hat{u}}$  is the cross-correlation coefficient between  $\hat{p}$  and  $\hat{u}$ , i.e., a normalized form of the covariance. The estimated total uncertainty of the covariance is

$$\mathcal{E}_{\langle\hat{p}\hat{u}\rangle} = |\langle\hat{p}\hat{u}\rangle|(\epsilon + \epsilon_2 + \epsilon\epsilon_2) + \sigma_{\hat{p}}\sigma_{\hat{u}}\sqrt{\frac{1+r_{\hat{p}\hat{u}}^2}{N-1}}. \quad (\text{A.21})$$

The above estimated uncertainties of instantaneous measurements, means, standard deviations, variances, and covariances were shown using  $\hat{U}$ ,  $\hat{u}$ , and  $\hat{p}$  as examples. However, all estimated uncertainties presented here were computed in the same way.

### Estimating the Random Error and Bias Uncertainty

The random error and bias uncertainty for the measurements of velocity, pressure, and active surface displacement need to be known to employ the above equations. How these values have been estimated is described below.

It is common to estimate the uncertainty associated with an instantaneous PIV measurement as being a displacement of 0.1 pixels. As discussed by Sciacchitano (2019), this “universal constant” for PIV uncertainty is likely overly simplistic, as uncertainty depends heavily on the characteristics of each experiment. However, analyses dedicated to evaluating PIV uncertainty typically return uncertainties of around 0.1 pixels (Raffel et al., 2018), and so this value has been used here for the random error associated with the PIV processing algorithm. The 0.1 pixels has been propagated through to the computation of velocity, resulting in the values for  $E_r$  shown in Table A.1.

The bias uncertainties associated with particle time response and laser pulse timing have been ignored because they are negligible at the flow speed considered in this thesis. The bias uncertainty associated with planar calibration has been estimated as 1 pixel across the total calibration distance. In contrast, the bias uncertainty associated with stereoscopic calibration is larger due to the complexity of the calibration process. All stereoscopic measurements conducted for this work were used to capture spanwise–wall-normal planes, and so the associated calibration uncertainties

---

	FOV1	FOV2	FOV3	FOV4	FOV5	FOV6	FOV7	FOV8
$\epsilon$ [%]	0.11	0.09	2.80	0.10	2.63	0.09	0.09	1.77
$E_r$ [m/s]	0.13	0.05	0.10	0.02	0.06	0.08	0.08	0.12

---

Table A.1: Estimated bias uncertainty ( $\epsilon$ ) and random error ( $E_r$ ) associated with the PIV measurements conducted in the various FOVs.

were estimated by evaluating the change in the mean velocity profile across the span in comparison to the more reliable planar PIV measurements. The estimated values of  $\epsilon$  for the various PIV measurements are shown in Table A.1.

To estimate the uncertainty of the instantaneous wall-pressure measurements, it was assumed that the error in instantaneous pressure was due only to the calibration, as the random noise associated with the hardware chain is negligible in comparison. According to the manufacturer data, the uncertainty associated with the calibrator is  $\pm 0.2$  dB. When considered with the nominal calibration pressure of 94 dB, this leads to a calibration uncertainty of 2.3% for instantaneous pressure. Similarly, the random error associated with the hardware chain for the active surface was assumed to be negligible. The calibration uncertainty for the measured active surface displacements was estimated to be 1% by comparing the displacement values read from MotionLab to those generated by the real-time system via the polynomial conversion from V to mm (more details in Chapter 6).

### Estimated Uncertainties for Select Results Presented in Chapter 5

The estimated total uncertainty of  $p_{\text{rms}}$  was found to be 2.4% using Equation A.16. The estimated total uncertainties associated with the mean velocity and Reynolds stresses of Figure 5.2 are shown in Table A.2 as a percentage of the statistical quantity in question. Since the convergence uncertainty depends on individual statistics, the estimated total uncertainties are a function of wall-normal distance. Therefore, to arrive at the values displayed in Table A.2, the total uncertainty values were averaged across a wall-normal range extending from  $y/\delta = 0.02$  to 0.5 (roughly  $y/\lambda = 50$  to 1300). The estimated total uncertainties associated with the pressure-velocity correlations of Figures 5.6, 5.12, and 5.14 are presented in Table A.3. The values in the table represent the average uncertainty across the entire FOV used to show each correlation and are given as a percentage of the upper colourbar value used to display each correlation. For example,  $\mathbf{R}_{pu}$  in Figure 5.6(a) is displayed using a colourbar range of  $-2 \times 10^{-5}$  to  $2 \times 10^{-5}$ . Table A.3 indicates that the average uncertainty of the correlations displayed in this contour plot is 4.7% of  $2 \times 10^{-5}$ . The values are reported in this way because the correlations are zero in many places and would therefore produce infinite error if computed as a percentage of the local correlation value.

---

	$\langle U \rangle$	$\langle u^2 \rangle$	$\langle v^2 \rangle$	$\langle uv \rangle$
FOV1	0.2%	4.2%	9.8%	2.8%
FOV2	0.2%	2.2%	2.0%	0.9%
FOV3	3.1%	11.2%	12.9%	7.5%

---

Table A.2: Estimated total uncertainties associated with the mean velocity and Reynolds stresses shown in Figure 5.2.

---

---

	$R_{pu}$	$R_{pv}$	$R_{pw}$	$R_{pu}^{\text{LS}}$	$R_{pv}^{\text{LS}}$	$R_{pw}^{\text{LS}}$	$R_{pu}^{\text{VLS}}$	$R_{pv}^{\text{VLS}}$	$R_{pw}^{\text{VLS}}$
All $p$	4.7%	3.6%	16.4%	2.6%	2.1%	9.2%	2.5%	4.9%	17.7%
$p > 0$	4.7%	3.4%	15.4%	2.5%	1.9%	8.4%	2.4%	4.4%	16.0%
$p < 0$	4.1%	3.2%	14.8%	2.4%	1.8%	8.0%	2.2%	4.3%	14.9%

---

Table A.3: Estimated total uncertainties associated with the pressure-velocity correlations shown in Figures 5.6, 5.12, and 5.14. These uncertainties are given as a percentage of the upper colourbar value used to display each respective correlation.

### Estimated Uncertainties for Select Results Presented in Chapter 7

Following Equation A.3, the estimated total uncertainty of the instantaneous streamwise velocity fluctuation is  $0.001|u| + 0.02$  m/s (FOV4). Similarly, the estimated total uncertainty of the instantaneous active surface displacement is  $0.01|h|$ . The estimated total uncertainty of the mean velocities presented in Figures 7.2 and 7.3 is 0.2%. This is an average across all of FOV4, although the first vectors above the wall have uncertainties closer to 1%. The uncertainties associated with the phase averages used in Figures 7.5, 7.7, 7.8, and 7.11 cannot easily be given as a percentage because there are many places where the phase average is zero and therefore the percentage would be infinite. However, the convergence uncertainty was found to be effectively constant across all actuation frequencies and amplitudes because of the binning process of the phase averages. More precisely, the standard deviation of the measurements, which dictates the convergence uncertainty of a mean, is largely due to the bin width and measurement noise instead of the variance of the fluctuating velocity over a full actuation cycle. The total uncertainty of the phase averages is therefore most easily reported as a percentage (from the bias) plus the convergence uncertainty (averaged over the FOV). The total uncertainty of the phase averages computed from FOV4 is then estimated as  $0.001\langle u \rangle_\phi + 0.005$  m/s. Similarly, the total uncertainty of the phase averages computed from FOV5 is estimated as  $0.026\langle u \rangle_\phi + 0.01$  m/s. Note that these uncertainties extend to the strength values shown in Figure 7.10, which were extracted from the phase averages.

### Estimated Uncertainties for Select Results Presented in Chapter 8

The estimated total uncertainties associated with the mean velocity and Reynolds stresses of Figures 8.2, 8.12, and 8.19 are shown in Tables A.4, A.5, and A.6, respectively, as a percentage of the statistical quantity in question. Just as was done for the velocity statistics of Chapter 5, these total uncertainty values were averaged across a wall-normal range extending from  $y/\delta = 0.02$  to 0.5 (except for FOV8 which only extends to  $y/\delta \approx 0.3$ ). The total uncertainty of the phase averages in Figure 8.5 is estimated as  $0.001\langle u \rangle_\phi + 0.02$  m/s. Similarly, the total uncertainty of the phase averages in Figure 8.6 is estimated as  $0.018\langle u \rangle_\phi + 0.02$  m/s. Finally, the estimated total uncertainties of the phase-averaged Reynolds stresses are given in Table A.7; these values were averaged across  $y/\delta = 0.02$  to 0.5 and all actuation frequencies.

---

	$\langle U \rangle$	$\langle u^2 \rangle$	$\langle v^2 \rangle$	$\langle uv \rangle$
FOV6	0.3%	3.4%	4.0%	1.2%
FOV7	0.2%	3.3%	3.9%	1.2%
FOV8	1.8%	5.7%	10.7%	3.7%

---

Table A.4: Estimated total uncertainties associated with the mean velocity and Reynolds stresses shown in Figure 8.2.

---

	$\langle U \rangle$	$\langle u^2 \rangle$	$\langle v^2 \rangle$	$\langle uv \rangle$	$\langle u'^2 \rangle$	$\langle v'^2 \rangle$	$\langle u'v' \rangle$
$x/D = 0.7$	0.2%	2.4%	3.5%	0.8%	2.4%	3.5%	0.8%
$x/D = 1.4$	0.2%	2.4%	3.5%	0.8%	2.4%	3.5%	0.8%

---

Table A.5: Estimated total uncertainties associated with the mean velocity and Reynolds stresses shown in Figure 8.12. These values were averaged over the four actuation frequencies considered.

---

	$\langle u^2 \rangle$	$\langle v^2 \rangle$	$\langle uv \rangle$	$\langle u^2 \rangle_{\text{VLS}}$	$\langle v^2 \rangle_{\text{VLS}}$	$\langle uv \rangle_{\text{VLS}}$
Base flow	3.4%	4.0%	1.2%	6.1%	37.0%	0.9%
Feed-forward	2.5%	3.6%	0.8%	4.8%	33.1%	0.7%

---

Table A.6: Estimated total uncertainties associated with the Reynolds stresses shown in Figure 8.19.

---

	$\langle u'^2 \rangle_{\phi}$	$\langle v'^2 \rangle_{\phi}$	$\langle u'v' \rangle_{\phi}$
$x/D = 0.7$	3.7%	4.9%	2.9%
$x/D = 1.4$	3.7%	5.1%	2.9%

---

Table A.7: Estimated total uncertainties associated with the phase-averaged Reynolds stresses used to form Figures 8.13, 8.14, and 8.15.

## B MATLAB Code

### Helmholtz Resonance Correction

```
1 % This function corrects Helmholtz resonance using a second-order model
2 %
3 % resonantFrequency: resonant frequency of the second-order model
4 %     dampingRatio: damping ratio of the second-order model
5 %     acqFrequency: signal acquisition frequency
6 %     P: input pressure signal
7 %
8 %     Pc: corrected pressure signal
9
10 function [Pc] = correctHelmholtz(P,acqFrequency,dampingRatio,resonantFrequency)
11
12 L = length(P);
13
14 % Applying a fast Fourier transform and extracting one side
15
16 FFT      = fft(P,L);           % applied to signal to be corrected
17 halfFFT  = FFT(1:L/2+1);       % extracting one side
18 f        = 0:acqFrequency/L:acqFrequency/2; % creating frequency vector
19
20
21 % Calculating magnitudes and phases of second-order system
22
23 secondMags = 1./sqrt((1 - (f/resonantFrequency).^2).^2 + ...
24     (2*dampingRatio*f/resonantFrequency).^2);
25
26
27 secondPhases = -1.0*atan2(2*dampingRatio*(f/resonantFrequency), (1 - ...
28     (f/resonantFrequency).^2));
29
30
31 % Correcting magnitudes and phases in the frequency domain
32
33 for i = 1:length(f)
34
35     z          = halfFFT(i,1);
36     mag        = abs(z);
37     phase      = angle(z);
38     newMag     = mag/secondMags(1,i);
39     newPhase   = phase - secondPhases(1,i);
40     [a,b]      = pol2cart(newPhase,newMag);
41     halfFFT(i,1) = complex(a,b);
42
43 end
44
45 % Re-assembling full Fourier results for inversing
46
47 FFTleft      = halfFFT;           % left-hand complex
48 realsLeft    = real(halfFFT);     % left-hand reals
49 imagsLeft    = imag(halfFFT);     % left-hand imaginary
50 FFTright     = complex(realsLeft,-1.0*imagsLeft); % right-hand complex
51 corrFFT      = [FFTleft; flipud(FFTright(2:end-1))]; % corrected FFT
52 Pc           = real(ifftr(corrFFT,L)); % corrected signal
53
54 end
```

## Wiener Noise Estimation

```
1 % This function uses the measurements of a noise field signal to estimate
2 % the noise present in a signal that is to be noise reduced.
3 %
4 % signal_1: signal to be noise reduced
5 % signal_2: noise field signal (measured simultaneously with signal_1)
6 %     order: filter order
7 %
8 %     noise: noise present in signal_1 (subtract this off)
9
10 function [noise,w] = wienerNoiseCancel(signal_1,signal_2,order)
11
12 N     = length(signal_1);           % signal length
13
14 X     = xcorr(signal_2)/N;          % autocorrelation of signal 2
15 Rv2   = toeplitz(X(N:N+order-1));  % Toeplitz matrix of autocorrelations
16
17 X     = xcorr(signal_1,signal_2)/N; % cross-correlation between signals
18 rxv2  = X(N:N+order-1);           % cropped cross-correlation vector
19
20 w     = Rv2\rxv2;                  % filter coefficients
21
22 noise = conv(w,signal_2);          % applying filter to signal 2
23 noise = noise(1:end-order+1);      % isolating the useful part
24
25 end
```

## Wiener System Identification

```
1 % This function applies the Wiener filter to identify the impulse
2 % response and transfer function for a single-input, single-output
3 % system that is assumed to be linear
4 %
5 %     input: input to linear system
6 %     output: output from linear system
7 %     order: order of Wiener filter
8 %     acqFreq: acquisition frequency of input and output
9 %
10 %     g_io: time domain impulse response
11 %     G_io: frequency domain transfer function
12 %     f: frequencies associated with G_io
13
14 function [g_io, G_io, f] = wienerSystemID(input,output,order,acqFreq)
15
16 N    = length(input);           % signal length
17
18 X    = xcorr(input)/N;          % autocorrelation of input
19 Rv2  = toeplitz(X(N:N+order-1)); % Toeplitz matrix of autocorrelations
20
21 X    = xcorr(output,input)/N;  % cross-correlation between signals
22 rxv2 = X(N:N+order-1);         % cropped cross-correlation vector
23
24 g_io = Rv2\rxv2;               % impulse response
25 G_io = fft(g_io);              % transfer function
26 G_io = G_io(2:order/2+1);      % taking useful part
27
28 f    = 0:acqFreq/order:acqFreq/2; % convert from bins to frequencies
29 f    = f(2:end)';              % removing 0 Hz
30
31 end
```